

# **TRANSPORT OF MATERIALS IN THE DYNAMIC EARTH**

**October 2 – 6, 2001  
Kurayoshi, Japan**

## **Program Committee**

Eiji Ito (Chair) Institute for Study of the Earth's Interior, Misasa  
Masaru Kono Institute for Study of the Earth's Interior, Misasa  
Bjorn Mysen Geophysical Laboratory, Washington D.C.  
Dave Rubie Bayerisches Geoinstitut, Beyreuth  
Michael Walter Institute for Study of the Earth's Interior, Misasa

## **Local Organizing Committee**

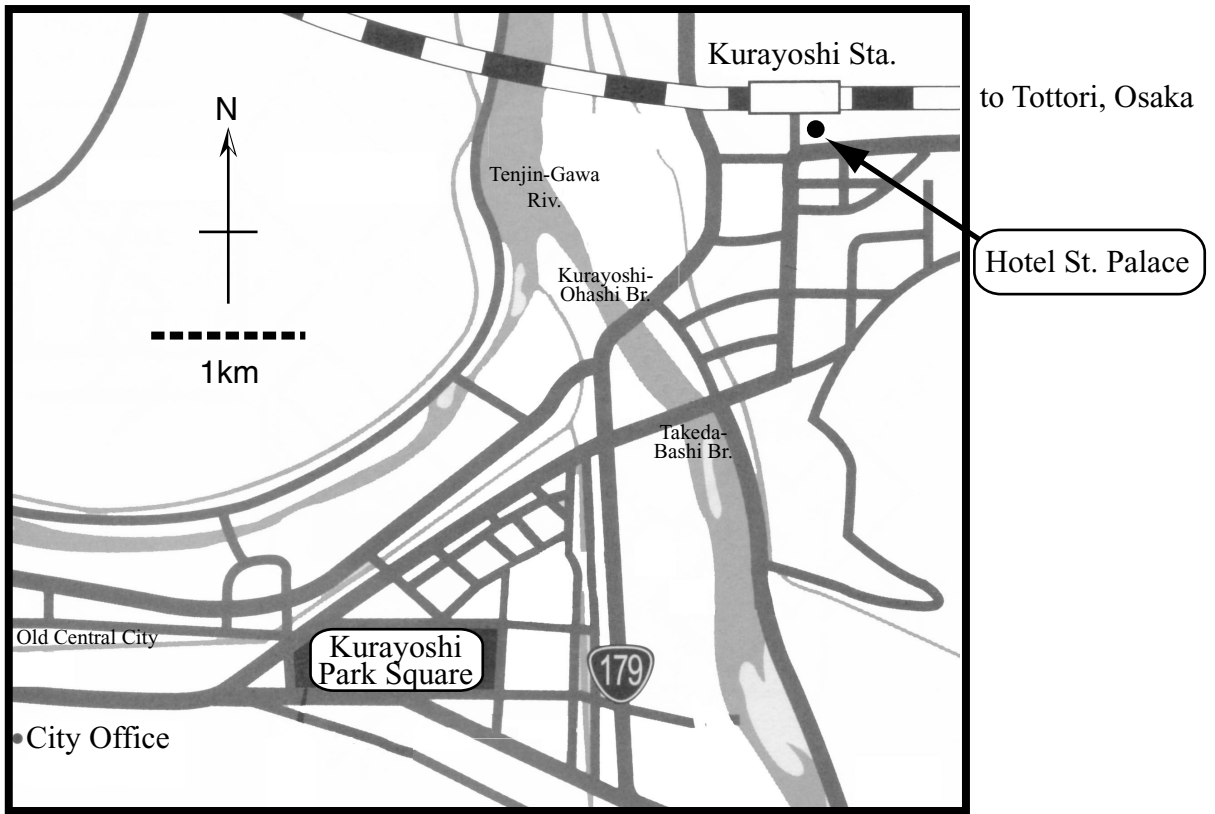
Masaru Kono (Chair), Hitoshi Chiba, Eiji Ito, Masami Kanzaki, Tomoo Katsura,  
Masako Kawata, Noriaki Kishima, Toshiro Kobayashi, Minoru Kusakabe, Yukari  
Shimizu, Michael Walter, Shigeru Yamashita, Akira Yoneda

## **Sponsors**

Ministry of Education, Culture, Sports, Science, and Technology  
Tottori Prefecture  
Kurayoshi City  
Misasa Town  
Okayama University  
Institute for Study of the Earth's Interior

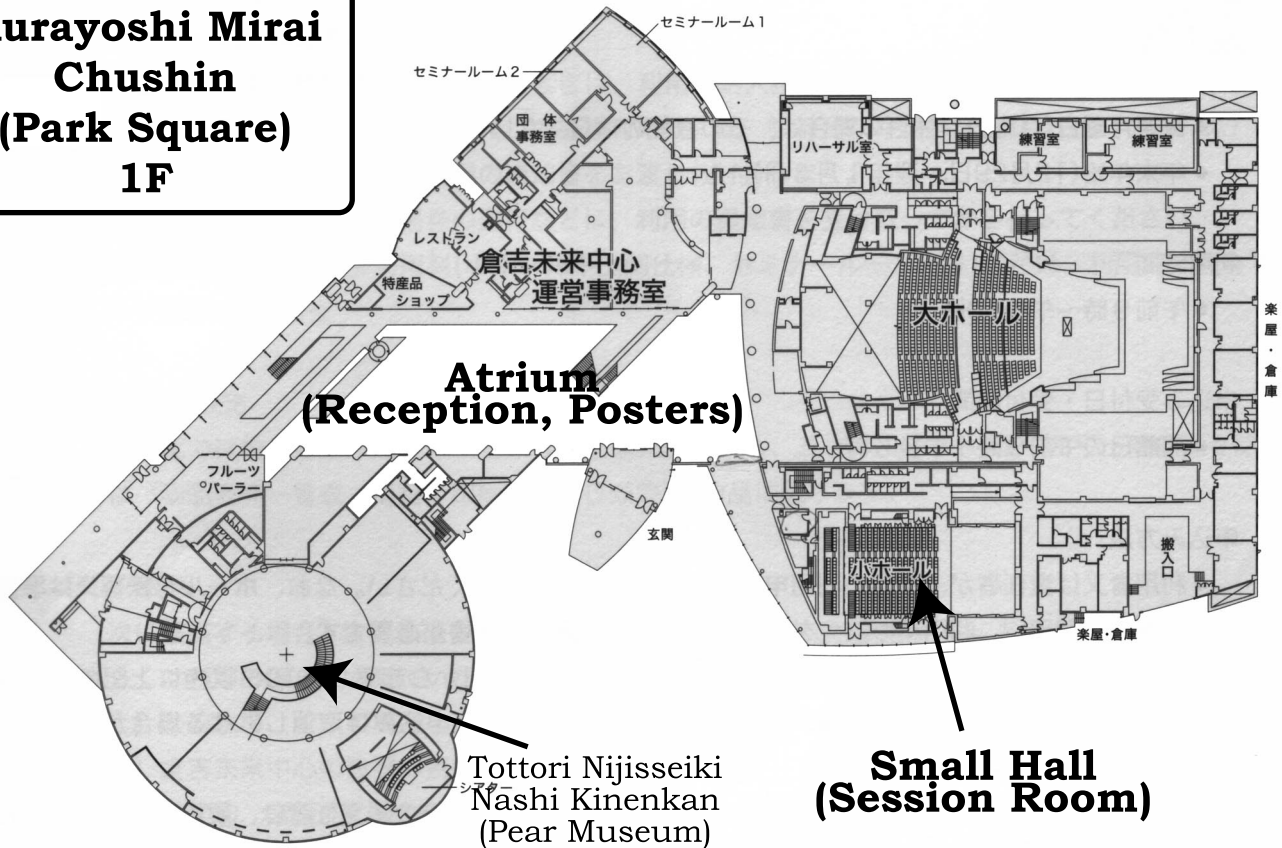
# Kurayoshi City Map

to Yonago



to ISEI, Misasa

## Kurayoshi Mirai Chushin (Park Square) 1F



## Bus Time Table

### Shuttle Bus

**Hotel** → **Meeting Site**

Oct. 3 (Wed) – 5 (Fri): Dept. at 08:30

**Meeting Site** → **Hotel**

Oct. 2 (Tue) : Dept. at 21:30

Oct. 3 (Wed) – 5 (Fri): Dept. at 18:30

### Public Bus

Carrier: Hinomaru Bus (Kurayoshi Eki (Station) ↔ Ikuta-Shako)

Nikko Bus (Kurayoshi Eki (Station) ↔ Nishi-Kurayoshi)

Nearest Bus Stop: “Kurayoshi Park Square (倉吉パークスクエア)”

Time Required: about 12 minutes.

Kurayoshi Sta. → Park Square							
Dept.	07:43	<u>08:00</u>	08:45	<u>09:40</u>	10:55	<u>12:00</u>	12:55
Arri.	07:55	<u>08:12</u>	08:57	<u>09:52</u>	11:07	<u>12:12</u>	13:07
Dept.	<u>14:10</u>	15:15	<u>16:50</u>	<u>18:10</u>	19:05		
Arri.	<u>14:22</u>	15:23	<u>17:02</u>	<u>18:22</u>	19:13		
Park Square → Kurayoshi Sta.							
Dept.	07:15	<u>09:08</u>	09:38	<u>10:48</u>	11:58	<u>13:18</u>	14:38
Arri.	07:27	<u>09:20</u>	09:50	<u>11:00</u>	12:10	<u>13:30</u>	14:50
Dept.	<u>15:48</u>	16:48	<u>17:38</u>	17:58	<u>18:53</u>	19:08	
Arri.	<u>16:00</u>	17:00	<u>17:50</u>	18:10	<u>19:05</u>	19:20	

# Scientific Program

<b>October 2</b>	Tuesday PM	
14:00–19:30	Registration	Kurayoshi Mirai Chushin (Posters can be displayed in this period)
19:00–21:00	Reception	Kurayoshi Mirai Chushin
<b>October 3</b>	Wednesday AM	<b>Session 1: Imaging the Mantle</b>
09:00	Convenor	Welcome and introduction
09:00–10:00	Yoshio Fukao	The upper and lower mantle transition region as temporal reservoirs of subducted slabs and rising plumes
10:00–10:30	Guy Masters	Seismological constraints on geochemical reservoirs?
10:30–10:50	Coffee break	
10:50–12:00	Discussion	
12:00–13:30	Lunch	(Poster preparation)
<b>October 3</b>	Wednesday PM	<b>Session 2: Formation and evolution of geochemical reservoirs</b>
13:30–14:30	Stan Hart	Formation and evolution of geochemical mantle domains
14:30–15:00	Marc Hirschmann	A petrologic view of the characteristics of mantle geochemical reservoirs
15:00–15:20	Coffee break	
15:20–16:30	Discussion	
16:30–18:00	Poster Session	
<b>October 4</b>	Thursday AM	<b>Session 3: High pressure mineral physics</b>
09:00–10:00	Takehiko Yagi	Developments and problems in laboratory high pressure experiments
10:00–10:30	Eiji Ito	Recent developments in high pressure mineral physics experiments using sintered diamond anvils
10:30–10:50	Coffee break	
10:50–12:00	Discussion	
12:00–13:30	Lunch	
<b>October 4</b>	Thursday PM	<b>Session 4: Dehydration of subducting slabs and water storage in the mantle</b>
13:30–14:30	Max Schmidt	Dehydration vs. melting vs. dissolution: Where and how to generate a mobile component during subduction
14:30–15:00	Eiji Ohtani	Circulation and Redistribution of Water in the Earth's Interior
15:00–15:20	Coffee break	
15:20–16:30	Discussion	
16:30–18:00	Poster Session	

<b>October 5</b>	Friday AM	<b>Session 5: Magmatic differentiation and the evolution of the mantle and core</b>
09:00–10:00	Eiichi Takahashi	Melt Generation in the Hawaiian Plume
10:00–10:30	Bernie Wood	Mantle composition and conditions of core formation
10:30–10:50	Coffee break	
10:50–12:00	Discussion	
12:00–13:30	Lunch	
<b>October 5</b>	Friday PM	<b>Session 6: Future Perspectives</b>
13:30–14:30	Ho-kwang Mao	Future perspectives on high-pressure experimental geophysics and geochemistry
14:30–15:00	Dave Rubie	Title to be announced
15:00–15:20	Coffee break	
15:20–16:30	Discussion	
16:30–18:00	Poster Session	
19:00–21:00	Banquet	Kurayoshi St. Palace Hotel
<b>October 6</b>	Saturday	<b>Post-conference field trip</b>
08:00	Departure	from Kurayoshi St. Palace Hotel
		Field trip to Daisen Volcano (by chartered bus)
20:00	Return	to the Hotel

Front cover: The National Treasure “Nageire-do” in Misasa Town built in 8th century on a precipitous flank of Mt. Mitoku-san.

## Table of Contents

<b>Map of Kurayoshi City</b>	<b>i</b>
<b>Bus time table</b>	<b>iii</b>
<b>Scientific Program</b>	<b>iv</b>
<b>Abstracts of Papers</b>	<b>v</b>
<b>1 Imaging the mantle</b>	<b>1</b>
1.1 Yoshio Fukao: The upper and lower mantle transition region as temporal reservoirs of subducted slabs and rising plumes . . . . .	3
1.2 Guy Masters, Gabi Laske: Seismological constraints on geochemical reservoirs? . .	4
1.3 Mamoru Kato <sup>1</sup> , and Hitoshi Kawakatsu <sup>2</sup> : Seismological <i>in situ</i> estimation of density jumps across the transition zone discontinuities beneath Japan . . . . .	5
1.4 Hitoshi Kawakatsu: Seismic discontinuities/scatterers in the lower mantle . . . . .	6
1.5 Frank D. Stacey: Thermal vs compositional interpretations of lower mantle tomography	7
1.6 Dapeng Zhao: A new global tomography of the earth: structure of mantle plumes . .	8
<b>2 Formation and evolution of geochemical reservoirs</b>	<b>9</b>
2.1 Stanley R. Hart: Formation and evolution of geochemical mantle domains . . . . .	11
2.2 M. Hirschmann <sup>1</sup> , T. Kogiso <sup>1</sup> , and Daniel J. Frost <sup>2</sup> : A petrologic view of the characteristics of mantle geochemical reservoirs . . . . .	13
2.3 Ian H. Campbell: The relationship between continental and oceanic crust formation and the development of the depleted mantle . . . . .	15
2.4 P.R. Castillo <sup>1*</sup> , R.U. Solidum <sup>1,2</sup> , and R.S. Punongbayan <sup>2</sup> : Origin of high-Nb basalts from the Sulu Arc, southern Philippines . . . . .	16
2.5 Takeshi Hanyu*, Tibor J. Dunai, Gareth R. Davies, Ichiro Kaneoka, Susumu Nohda, and Kozo Uto: Evidence for distinct primitive mantle sources; a noble gas study of the Reunion hotspot . . . . .	17
2.6 Manuel Moreira: Noble gases and the primitive reservoir . . . . .	18
2.7 Katsura Kobayashi and Eizo Nakamura: Geochemical evolution of Akagi volcano, northeast Japan: implications for interaction between island arc magma and lower crust, and generation of isotopically variable magmas. . . . .	21
2.8 Katsura Kobayashi <sup>1</sup> , Takuya Moriguti <sup>1</sup> , Ryoji Tanaka <sup>1</sup> , Kenji Shimizu <sup>2</sup> , Eizo Nakamura <sup>1</sup> : Analytical procedure for the measurement of lithium and boron isotope composition by High Resolution Secondary Ion Mass Spectrometer and its Application . . . . .	22
2.9 Takeshi Kuritani and Eizo Nakamura: A simple method for precise isotope analysis of ng-level Pb for natural rock samples . . . . .	23
2.10 Naoko Matsumoto* and Masao Kitamura: Chemical compositions of a binary dilute solid solution during growth . . . . .	24
2.11 Takuya Moriguti and Eizo Nakamura: Precise Li isotope analysis by thermal ionization mass spectrometry (TIMS) using lithium phosphate as an ion source material and highly-yield lithium separation from natural samples . . . . .	25
2.12 Takuya Moriguti and Eizo Nakamura: Li-B-Pb isotope systematic study of Izu arc volcanic rocks: implications for crust-mantle recycling at subduction zone . . . . .	26

2.13	Takuya Moriguti and Eizo Nakamura: Li isotope variation in quaternary basaltic rocks in northeastern Japan arc . . . . .	27
2.14	Chie Sakaguchi and Eizo Nakamura: Chemical and isotopic evolution of the Allende meteorite . . . . .	29
2.15	K. Shimizu <sup>1*</sup> , E. Nakamura <sup>1</sup> , and S. Maruyama <sup>2</sup> : Petrology, geochemistry and garnet and pyroxene xenocrysts of Belingwe volcanics, Zimbabwe - indisputable evidence for crustal contamination . . . . .	30
2.16	Hiroyuki Takei, Tetsuya Yokoyama, Akio Makishima and Eizo Nakamura: Formation and suppression of AlF <sub>3</sub> during HF digestion of rock samples in Teflon bomb for precise trace element analyses by ICP-MS and ID-TIMS . . . . .	32
2.17	Hiroyuki Takei and Eizo Nakamura: Origin of the ore-forming fluids in the Hishikari gold deposits. . . . .	33
2.18	Tetsuya Yokoyama, Akio Makishima, Eizo Nakamura: Evaluation of coprecipitation of incompatible trace elements with fluoride during silicate rock dissolution by acid digestion . . . . .	35
2.19	Tetsuya Yokoyama, Akio Makishima, Eizo Nakamura: Separation of thorium and uranium from silicate rock samples using two commercial extraction chromatographic resins . . . . .	37
2.20	Tetsuya Yokoyama, Akio Makishima, Eizo Nakamura: Precise analysis of <sup>234</sup> U/ <sup>238</sup> U ratio using UO <sub>2</sub> <sup>+</sup> ion with TIMS . . . . .	39
2.21	Tetsuya Yokoyama, Eizo Nakamura: Precise determination of ferrous iron in silicate rocks . . . . .	41
2.22	Tetsuya Yokoyama, Katsura Kobayashi, Takeshi Kuritani, Eizo Nakamura: Mantle metasomatism and rapid melt ascent beneath Miyakejima volcano: evidence from <sup>238</sup> U- <sup>230</sup> Th disequilibrium . . . . .	43
2.23	Tomohiro Usui <sup>1</sup> , Eizo Nakamura <sup>1</sup> , Katsura Kobayashi <sup>1</sup> , Shigenori Maruyama <sup>2</sup> and Herwart Helmstaedt <sup>3</sup> : Petrology and trace element geochemistry of eclogite xenoliths from the Colorado Plateau . . . . .	46
2.24	Tomohiro Usui, Katsura Kobayashi and Eizo Nakamura: Preparation of reliable zircon standard for U-Pb dating method by HR-SIMS . . . . .	47
2.25	Eizo Nakamura and Toshio Nakano: Trace element migration associated with evolution of metamorphic fluid during subduction zone-related metamorphism . . . . .	49
2.26	Eizo Nakamura, Masaaki Tanimoto, Takeshi Kuritani and Masako Yoshikawa: Geochemical evolution of the Horoman peridotite complex revised by incorporation of lead isotope systematics: Implications for melt extraction, metasomatism, and compositional layering in the mantle . . . . .	50
2.27	Gray E. Bebout <sup>1</sup> , and Eizo Nakamura: Record in metamorphic tourmalines of subduction-zone devolatilization and boron cycling . . . . .	51
2.28	Toshio Nakano and Eizo Nakamura: Boron isotope geochemistry of metasedimentary rocks and tourmalines in a subduction-zone metamorphic suite . . . . .	53
2.29	Akio Makishima, Mayumi Nakanishi and Eizo Nakamura: Simultaneous determination of Ru, Pd, Re, Os, Ir and Pt contents and <sup>187</sup> Os/ <sup>188</sup> Os ratios in geological samples using a new anion exchange chromatographic procedure . . . . .	54
2.30	Estelle F. Rose, A. Makishima, E. Nakamura: Major and rare earth elements geochemistry of the Icelandic Plume: an island-wide approach for source determination . . . . .	55
2.31	Sophie Alves <sup>1</sup> , Pierre Schiano <sup>2</sup> , Bernard Bourdon <sup>3</sup> , Claude J. Allègre <sup>3</sup> : Magma formation at Saba Island, Lesser Antilles: a numerical model for mantle wedge-slab mixing according to osmium data . . . . .	57
<b>3</b>	<b>High pressure mineral physics</b>	<b>59</b>

3.1	Takehiko Yagi: Developments and problems in laboratory high pressure experiments	61
3.2	Eiji Ito: Recent developments in high pressure mineral physics experiments using sintered diamond anvils . . . . .	61
3.3	Hitoshi Yamada <sup>1</sup> , Tomoo Katsura <sup>1</sup> , Toru Shinmei <sup>1</sup> , Atsushi Kubo <sup>1</sup> , Osamu Nishikawa <sup>1</sup> , Maoshuang Song <sup>1</sup> , Eiji Ito <sup>1</sup> , Kenichi Funakoshi <sup>2</sup> : In situ determination of the olivine-modified spinel phase boundary in the system Mg <sub>2</sub> SiO <sub>4</sub> - Fe <sub>2</sub> SiO <sub>4</sub> . . . . .	61
3.4	Masaki Akaogi <sup>1*</sup> , Akira Tanaka <sup>1</sup> , and Eiji Ito <sup>2</sup> : Garnet-ilmenite-perovskite transitions in the system Mg <sub>4</sub> Si <sub>4</sub> O <sub>12</sub> -Mg <sub>3</sub> Al <sub>2</sub> Si <sub>3</sub> O <sub>12</sub> : phase equilibria, calorimetry and application to the mantle . . . . .	63
3.5	Masanori Matsui: MD simulation of the density and P- and S-wave velocity jumps across the 410km and 660km seismic discontinuities . . . . .	66
3.6	Kiyoshi Fujino <sup>1*</sup> , Nobuyoshi Miyajima <sup>1</sup> , Yohei Sasaki <sup>1</sup> , Reki Odawara <sup>1</sup> , Hisayuki Ogawa <sup>1</sup> , Nagayoshi Sata <sup>2</sup> , Takehiko Yagi <sup>2</sup> : Mineralogy of the lower mantle by the combined method of a laser-heated diamond anvil cell experiment and analytical transmission electron microscopy . . . . .	67
3.7	S. Ono <sup>1</sup> , E. Ito <sup>2</sup> : Mineralogy of subducted basaltic crust (MORB) in the lower mantle	69
3.8	Tetsuo Irifune*, Yuichiro Sueda, Takeshi Sanehira, Hisanobu Naka, Toru Inoue, Yuji Higo, Takayuki Ueda, Ken-ichi Funakoshi, and Wataru Utsumi: In situ X-ray diffraction measurements for some mantle minerals to 40 GPa using a combination of synchrotron radiation and multianvil apparatus with sintered diamond anvils . . . . .	71
3.9	Atsushi Kubo, Eiji Ito, Tomoo Katsura, Toru Shinmei, Hitoshi Yamada, Osamu Nishikawa, Maoshuang Song, Kenichi Funakoshi: Exploration of $\beta$ -Fe using sintered diamond anvils . . . . .	72
3.10	Satoru Urakawa*, Masayuki Hasegawa, Junji Yamakawa, Ken-ichi Funakoshi, Wataru Utsumi: High-pressure phase relationships of FeS . . . . .	75
3.11	Yoshitaka Aizawa: Experimental determination of compressional wave velocity of olivine aggregate at 1 GPa up to 1273 K . . . . .	76
3.12	N. Mayama*, I. Suzuki, T. Katsura, A. Yoneda, I. Ohno: Temperature dependence of elastic moduli of polycrystalline wadsleyite and ringwoodite . . . . .	77
3.13	Takaya Nagai, Koichi Kittaka, Takamitsu Yamanaka: X-ray diffraction study of CaO at high pressure and temperature: equation of state of CaO . . . . .	78
3.14	Yu Nishihara, Eiichi Takahashi, Tomohiro Iguchi, Keisuke Nakayama, Kyoko Matsukage, Miki Shirasaka and Takumi Kikegawa: Thermal equation of state of an omphacite . . . . .	79
3.15	Naohisa Hirao, Tadashi Kondo, Eiji Ohtani, and Takumi Kikegawa: Static compression of Fe-Si alloy . . . . .	80
3.16	Taku Tsuchiya and Katsuyuki Kawamura: Theoretical estimations of contribution of electrons to the thermal expansion of Au and Pt metals . . . . .	81
3.17	Masahiro Osako <sup>1</sup> , Eiji Ito <sup>2</sup> and Akira Yoneda <sup>2</sup> : Thermal diffusivity and thermal conductivity of olivine and garnet under pressures up to 8 GPa and at temperatures up to 1000 K . . . . .	83
3.18	Akira Yoneda: Non-hydrostatic thermodynamics of anisotropic materials: geological implications for pressure solution . . . . .	86
3.19	Christian Holzappel <sup>1</sup> , D.C. Rubie <sup>1</sup> , S. Chakraborty <sup>2</sup> , F. Langenhorst <sup>1</sup> , D.J. Frost <sup>1</sup> : Rates of cation diffusion in olivine and silicate perovskite under mantle conditions . . . . .	88
3.20	KT Koga, MJ Walter, E Nakamura, and K Kobayashi: Carbon self-diffusion in diamond	90
3.21	Osamu Nishikawa: Stored strains and boundary characters of dynamically recrystallized quartz aggregates . . . . .	92
3.22	Masami Kanzaki: In-situ observation of plastic deformation at high pressure and temperature: A preliminary study . . . . .	93

3.23	D. Sakamoto*, A. Yoshiasa, O. Ohtaka, T. Yamanaka and K. Ota: Conduction mechanism of fayalite and gamma-Fe <sub>2</sub> SiO <sub>4</sub> : electrical conductivity jump by olivine-spinel transition . . . . .	95
3.24	Nobuyoshi Miyajima <sup>1</sup> , Falko Langenhorst <sup>1</sup> , Daniel Frost <sup>1</sup> , Dave Rubie <sup>1</sup> and Takehiko Yagi <sup>2</sup> : Electron energy-loss spectroscopy of garnet-perovskite high-pressure assemblages . . . . .	96
3.25	X. Xue*, T. Kawamoto, M. Kanzaki: NMR evidence for a new water dissolution mechanism in depolymerized silicate melts: results for hydrous diopside composition . . . . .	99
3.26	X. Xue and M. Kanzaki: Ab initio calculation of the <sup>17</sup> O and <sup>1</sup> H NMR parameters for various OH groups: Implications to the speciation and dynamics of dissolved water in silicate glasses . . . . .	100
3.27	T. Tsujimura <sup>(1)</sup> , X. Xue <sup>(2)</sup> , M. Kanzaki <sup>(2)</sup> , A. Kitakaze <sup>(1)</sup> and Y. Kudoh <sup>(1)</sup> : The effect of sulfur on silicate network structure in sodium silicate glasses . . . . .	101
3.28	Shigeru Yamashita: Water speciation in basaltic melts: constraints from water solubility measurements . . . . .	102
3.29	Tomohiro Iguchi*, Eiichi Takahashi, Yu Nishihara: Pressure dependence of the emf of thermocouples: Comparison of W-Re and Pt-Rh thermocouples with P-measurements by in situ X-ray . . . . .	103
3.30	M. Song <sup>1</sup> , K. Aoki <sup>2</sup> , H. Yamawaki <sup>2</sup> , H. Fujihisa <sup>2</sup> , and M. Sakashita <sup>2</sup> : Infrared Observation on Low Temperature Phase Transformations of Ice . . . . .	104
<b>4</b>	<b>Dehydration of subducting slabs and water storage in the mantle</b>	<b>107</b>
4.1	Max W. Schmidt: Dehydration vs. melting vs. dissolution: Where and how to generate a mobile component during subduction . . . . .	109
4.2	Eiji Ohtani: Circulation and Redistribution of Water in the Earth's Interior . . . . .	111
4.3	Ganesha Atni Venkatramiah, J.A.K. Tareen: An experimental study on the Mg-Al granulites and production of granitic melts in K <sub>2</sub> O-MgO-Al <sub>2</sub> O <sub>3</sub> -SiO <sub>2</sub> -H <sub>2</sub> O system . . . . .	112
4.4	Harry W. Green, II: Earthquakes at depth, their enabling mineral reactions, and transport of H <sub>2</sub> O into the deep mantle . . . . .	114
4.5	Dapeng Zhao: Slab dehydration and earthquakes: Seismological evidence . . . . .	116
4.6	Hikaru Iwamori: Transportation of H <sub>2</sub> O and melting in subduction zones . . . . .	117
4.7	Tomoaki Morishita*, Shoji Arai, Akihiro Tamura: Apatite concentration in the Finero phlogopite-peridotite, Italian Western Alps, as the late product of subduction-related mantle metasomatism . . . . .	118
4.8	Hiroyuki Kagi: High internal pressure retained in fluid inclusions of mantle-derived materials . . . . .	120
4.9	Tatsuhiko Kawamoto and Kyoko Matsukage: In situ observation of supercritical behaviors between H <sub>2</sub> O fluids and subduction zone magmas. . . . .	121
4.10	Robert P. Rapp <sup>1</sup> and N. Shimizu: Geochemical Consequences of Deep Subduction of Oceanic Crust: Insights from Melting Experiments on Hydrous Metabasalt at 3-16 GPa	122
4.11	Miki Shirasaka and Eiichi Takahashi: The fate of subducted carbonate within oceanic crusts . . . . .	124
4.12	Joseph R. Smyth <sup>1*</sup> , Daniel J. Frost <sup>2</sup> : An Experimental Study of the Effect of Water on the 410-km Discontinuity . . . . .	126
4.13	Toru Inoue <sup>§*</sup> , Yuji Higo <sup>†</sup> , Takayuki Ueda <sup>†</sup> , Yasutika Tanimoto <sup>†</sup> and Tetsuo Irifune <sup>§</sup> : The effect of water on the high-pressure phase boundaries in the system Mg <sub>2</sub> SiO <sub>4</sub> -Fe <sub>2</sub> SiO <sub>4</sub> . . . . .	128
4.14	G.C.M Richard*, M. Monnereau: Is the transition zone a water reservoir ? . . . . .	130
4.15	Motohiko Murakami*, Kei Hirose, Hisayoshi Yurimoto, Satoru Nakashima: Solubility of water in lower mantle minerals . . . . .	132

4.16	Tomoo Katsura <sup>1</sup> , Kiyoshi Fujita <sup>2</sup> , and Keishi Shinoda <sup>3</sup> : Electrical conductivity of hydrous materials at high pressures and high temperatures. . . . .	133
<b>5</b>	<b>Magmatic differentiation and the evolution of the mantle and core</b>	<b>135</b>
5.1	E. Takahashi <sup>1</sup> , K. Nakajima <sup>1</sup> , R. Takeguchi <sup>1</sup> , K. Shinozaki <sup>1</sup> , Ren Zhang-Young <sup>1</sup> , R. Tanaka <sup>2</sup> and E. Nakamura <sup>2</sup> : Melt Generation in the Hawaiian Plume . . . . .	137
5.2	B.J. Wood: Mantle composition and conditions of core formation . . . . .	140
5.3	Takeshi Kuritani: Boundary layer fractionation constrained by differential information from the Kutsugata lava flow, Rishiri Volcano, Japan . . . . .	141
5.4	Ulrich Faul: Constraints on Porosity in Partially Molten Regions in the Upper Mantle from Permeability Measurements and U-series Modeling . . . . .	142
5.5	Ryoji Tanaka and Eizo Nakamura: Evidence for slab tear and the related magmatism beneath the northwestern El Salvador, Central America . . . . .	144
5.6	Ryoji Tanaka <sup>1</sup> , Eizo Nakamura <sup>1</sup> , Eiichi Takahashi <sup>2</sup> : Geochemical evolution of Koolau Volcano, Hawaii . . . . .	145
5.7	Masaaki Obata*, Eiichi Takazawa: A possible discontinuous behavior of melt percolation in partially molten mantle and its implication to compositional layering in orogenic lherzolites. . . . .	146
5.8	Yuki Asahara, Eiji Ohtani: The role of water in generation of komatiite magma . . .	147
5.9	Eizo Nakamura <sup>1</sup> , Toshihiro Suzuki <sup>2</sup> , Katsura Kobayashi <sup>1</sup> , Akio Makishima <sup>1</sup> and Masaki Akaogi <sup>2</sup> : Determination of trace element partitioning between majorite and silicate melt in the primitive mantle composition at pressure of 15 GPa . . . . .	148
5.10	E. Ito, A. Kubo, T. Katsura, and M. J. Walter: Melting of peridotite under lower mantle conditions and its implication to differentiation of a deep magma ocean . . .	150
5.11	M. Walter: Core formation in a reduced magma ocean: new constraints from W, P, Ni and Co . . . . .	152
5.12	D.C. Rubie <sup>1</sup> , C. Holzappel <sup>1</sup> , J. Reid <sup>1</sup> , S. Fortenfant <sup>1</sup> , H.J. Melosh <sup>2</sup> , B.T. Poe <sup>1</sup> , D.J. Frost <sup>1</sup> , K. Righter <sup>2</sup> : Mechanisms of metal transport during formation of the earth's core: constraints from the kinetics of metal-silicate reactions . . . . .	154
5.13	H. Terasaki <sup>1</sup> , T. Kato <sup>1</sup> , S. Urakawa <sup>2</sup> , K. Funakoshi <sup>3</sup> , A. Suzuki <sup>4</sup> , K. Sato <sup>5</sup> , M. Hasegawa <sup>2</sup> : Effect of Light Elements on Viscosity of Liquid Iron-Alloy	156
5.14	Takashi Yoshino, Michael J. Walter and Tomoo Katsura: Critical melt fraction for percolation of core-forming materials . . . . .	158
5.15	Tadahiro Hatakeyama and Masaru Kono: Geomagnetic field model for the last 5 my and conditions at core-mantle boundary . . . . .	160
<b>6</b>	<b>Future Perspectives</b>	<b>161</b>
6.1	Ho-kwang Mao: Future perspectives on high-pressure experimental geophysics and geochemistry . . . . .	163
6.2	Dave Rubie: Title to be announced . . . . .	163
6.3	S. Honda <sup>1</sup> and M. Yoshida <sup>2</sup> : Mantle convection as a tool for understanding the links among the various geological phenomena . . . . .	163
6.4	Takamitsu Yamanaka*, A. Yoshiasa, O. Otaka and N. Nagai: High-pressure crystallography in mineral physics . . . . .	165
6.5	Masaru Kono: Dynamo process in the core under varying energy flow conditions . .	167
6.6	Eizo Nakamura, Akio Makishima, Takuya Moriguti, Katsura Kobayashi, Chie Sakaguchi, Tetsuya Yokoyama, Ryoji Tanaka, Takeshi Kuritani & Hiroyuki Takei: Comprehensive geochemical analyses of extremely small amounts of terrestrial and extraterrestrial materials for sample-return missions . . . . .	169

6.7	Katsura Kobayashi, Tomohiro Usui and Eizo Nakamura: Zircon age dating by dynamic multi-collection method using high resolution secondary ion mass spectrometer	170
	<b>List of Participants</b>	<b>172</b>
	<b>Author Index</b>	<b>177</b>

**October 3 (Wednesday) 08:50 — 12:00**

**Session 1**

## **Imaging the mantle**

Keynote: Yoshio Fukao, Earthquake Research Institute, U. Tokyo

Chair: Guy Masters, Scripps Institution of Oceanography, UCSD



## 1.1 The upper and lower mantle transition region as temporal reservoirs of subducted slabs and rising plumes

Yoshio Fukao

Earthquake Research Institute, Univ. Tokyo

We examined cross-sectional views across typical island arcs for several recent P and S wave tomographic models. We found that the slabs that started or restarted subduction after the Eocene tend to be now subhorizontally deflected in the upper and lower mantle transition region at depths from 400 to 1000km, and that the slabs that started subduction before the Eocene are now descending through the deep lower mantle without upward continuation to surface plates. These findings suggest that the pre-Eocene slabs were trapped in the transition region just as in the present day and that the resultant gravitational instability in the Eocene epoch induced a global fall of stagnant slabs into the lower mantle and consequently a global change in plate motion (Eocene plate reorganization).

In order to obtain sharper images of deeply subducted slabs and rising plumes, we added independent datasets in our whole mantle P-wave tomography. Addition of the first arrival time data from many Russian observatories has enabled us to obtain sharper images of deeply subducted slabs beneath the northern Kurile-Kamchatka arc and the Aleutian arc. Beneath the northern Kurile-Kamchatka arc, the subducted slab shows a complex contortion at its leading edge in a depth range below the 660-km discontinuity but above about 900-km. Beneath the Aleutian arc, the horizontal slab detached from the presently subducting slab lies just above the 660-km discontinuity. Thus, the addition of a new dataset has revealed stagnant slabs for the hitherto poorly resolved region. The upper and lower mantle transition region appears to be a temporal reservoir for subducted slabs.

Addition of the PP-P differential travel times obtained by a cross-correlation technique from broadband seismograms has improved the resolution significantly for the Hawaiian hot plume, which has been imaged as an extensive low-velocity zone confined in depth from the uppermost mantle down to about 900-km depth. The Hawaiian plume appears to have its origin in the upper and lower mantle transition region. Although the improvement of resolution by the addition of PP-P data is limited for the Pacific and African superplumes, the associated low-velocity anomalies rise all the way through the mantle to remarkably increase their intensities in the upper mantle, beneath French Polynesia and the Afar Triangle, respectively. There may be some mechanism for these rising plumes to have their pools in the upper mantle. For the African superplume, the addition of arrival time data of core-diffracted P-waves has emphasized greatly the low-velocity anomaly just above the core-mantle boundary, a feature consistent with the recent seismological studies.

## 1.2 Seismological constraints on geochemical reservoirs?

Guy Masters, Gabi Laske

Scripps Institute of Oceanography, UCSD

During the past 15 years, our view of the seismic structure of the interior of the Earth has improved immensely. There is now general consensus on the gross 3D structure of the mantle: the upper mantle and lowermost mantle are characterized by large amplitude, long-wavelength structure while the mid-mantle contains low-amplitude slab-like fast features which surround broad regions of slow velocities. Almost all the global models show some level of decorrelation of structure at or near the 660km discontinuity consistent with the presence of a weak impediment to flow (such as a phase transition or viscosity jump) but strict stratification of the mantle at this depth can be ruled out. This is also consistent with the evidence for slab “ponding” at certain locations in the transition zone.

Evidence for layering deeper in the mantle is extremely tenuous, however, several joint inversions of global seismic datasets for shear velocity and bulk sound speed suggest that there is a negative correlation between bulk and shear velocity in the bottom few hundred kilometers of the mantle. This negative correlation is difficult to explain and is unlikely to be due to subsolidus thermal effects or even partial melt. One current hypothesis is that the regions of negative correlation (under the mid-Pacific and Africa) correspond to a geochemical reservoir which is complementary to the depleted mantle above. Iron enrichment in these regions might give rise to the observed anticorrelation. On the other hand, it is unlikely that such a reservoir would be large enough to satisfy the geochemical constraints.

### 1.3 Seismological *in situ* estimation of density jumps across the transition zone discontinuities beneath Japan

Mamoru Kato<sup>1</sup>, and Hitoshi Kawakatsu<sup>2</sup>

<sup>1</sup>School of Earth Sciences, Faculty of Integrated Human Studies, Kyoto University, Kyoto 606-8501 Japan; mkato@gaia.h.kyoto-u.ac.jp,

<sup>2</sup>Earthquake Research Institute, University of Tokyo, Bunkyo, Tokyo 113-0032 Japan; hitosi@eri.u-tokyo.ac.jp

Density jumps at the transition zone discontinuities in the Earth's mantle are among the key parameters that control the style of mantle convection. How large they are is particularly of geodynamical interest, especially in modeling efficiency of mixing of the mantle. We can, on one hand, measure densities of mantle minerals at high pressure and temperature in laboratory, and seismological observations of density, especially at the transition zone discontinuities, would be valuable assets in modeling mantle mineralogy. It is, however, difficult to observe *in situ* density jumps seismologically, and most previous attempts rely on empirical scaling laws between velocities and density.

We take advantage of recent development of high-density broadband seismic networks in Japan, and estimate shear velocity and density jumps at the 410-km and 660-km discontinuities in this region. Our estimation is based on purely seismological observations such as seismic reflection and transmission coefficients at the discontinuities, and is free from any mineralogical models. We first estimate near-vertical S-to-S reflection coefficients by modeling ScS reverberation waveforms for the Izu-Japan corridor [Kato et al., 2001]. We then estimate conversion-transmission coefficients for P-to-S conversion using receiver-side converted phases that are observed as later phases to the direct *P* phase for teleseismic events. The former are controlled by both the shear velocity and density jumps at the discontinuities, and the latter are mainly controlled by the shear velocity jump, and by combining these observations we are able to overcome the trade-off among model parameters that is inherent in such seismological studies. We use AK135 as a reference model, and correct effects of anelastic attenuation with our own estimates of seismic *Q*. We take into account the associated uncertainties, and estimate acceptable ranges of shear velocity and density jumps at 410-km and 660-km discontinuities [Kato and Kawakatsu, 2001].

Our best estimates for the 660-km discontinuity ( $\Delta V_s$ ,  $\Delta\rho$  : 8.5%, 5.4%) lie slightly more than  $2\sigma$  away from AK135. The density jump at the 670-km discontinuity in PREM appears to be too large, and is less favorable to explain our observations. For the 410-km discontinuity ( $\Delta V_s$ ,  $\Delta\rho$  : 4.9%, 1.9%), the estimated density jump is smaller than both in PREM and AK135, but is more or less consistent with predictions of high-pressure mineralogical models. Our results do not agree with estimates with *PP* and *SS* precursors by Shearer and Flanagan [1999] at either discontinuity, whose model has apparently a larger impedance contrast at the 410-km than the 660-km discontinuities.

## 1.4 Seismic discontinuities/scatterers in the lower mantle

Hitoshi Kawakatsu

*Earthquake Research Institute, University of Tokyo, 1-1-1 Yayoi, Bunkyo-ku, Tokyo 113-0032, Japan; e-mail: hitosi@eri.u-tokyo.ac.jp*

Indications of lower mantle discontinuities are known for decades, but still little is known about their properties, and their origins are enigmatic. For example, in our recent studies, broad-band seismograms of deep events have been explored with the aid of a novel technique (Vinnik *et al.*, 1998, 2001). In our data there are indications of discontinuities near 860-880 km, 1010-1120 km, 1170-1250 km, 1340-1430 and 1670 - 1800 km depths, and the clearest signals are obtained from the discontinuity at a depth of 1200 km in several subduction zones. On the other hand, from the analyses of short-period array data, the presence of “mid-mantle discontinuities” at depths of 900-1100km has been shown (Kawakatsu and Niu, 1994; Niu and Kawakatsu, 1997). The presence of dipping discontinuities/scatterers in the lower mantle has been also confirmed from short-period array data (Kaneshima and Helffrich, 1998, 1999; Castle and Creager, 1999). The emerging results from the broad-band and short-period array analyses do not necessarily give a consistent picture, and the situation seems rather confusing.

In hope for clarifying the situation, results of a systematic analysis of data from the high density (& quality) broadband and short-period arrays recently deployed in Japan will be shown. We especially focus on the mid- and lower mantle structure beneath the Tonga arc. The questions to be addressed also include (1) should subducted oceanic crusts in the lower mantle all explain these discontinuities/scatterers, (2) is there any evidence for the postulated deep chemical boundary (Kellogg *et al.*, 1999)?

### References

- Castle, J. C and K. C. Creager, 1999. A steeply dipping discontinuity in the lower mantle beneath Izu-Bonin. *J. Geoph. Res.*, 104, 7279-7292.
- Kaneshima, S. and G. Helffrich, 1998. Detection of lower mantle scatterers northeast of the Mariana subduction zone using short-period array data, *J. Geoph. Res.*, 103, 4825-4838.
- Kaneshima, S and G. Helffrich, 1999. Dipping low-velocity layer in the mid-lower mantle: evidence for geochemical heterogeneity, *Science*, 283, 1888-1891.
- Kawakatsu, H., and F. Niu, 1994. Seismic evidence for a 920-km discontinuity, *Nature*, 371, 301-305.
- Kellogg, L. H., B. H. Hager, and R. D. van der Hilst, 1999, Compositional stratification in the deep mantle, *Science*, 283, 1881-1884.
- Niu, F., and H. Kawakatsu, 1997, Depth variation of the mid-mantle seismic discontinuity, *Geophys. Res. Lett.*, 24, 429-432.
- Vinnik, L., F. Niu, and H. Kawakatsu, 1998, Broad-band converted phases from midmantle discontinuities, *Earth, Planets, and Space (OHP special issue)*, 50, 987-997.
- Vinnik, L., M. Kato, and H. Kawakatsu, 2001, Search for seismic discontinuities in the lower mantle, *Geophys. J. International*, in press.

## 1.5 Thermal vs compositional interpretations of lower mantle tomography

Frank D. Stacey

CSIRO Exploration and Mining, PO Box 883, Kenmore, Qld. 4069, Australia f.stacey@cat.csiro.au

Reported variations in lower mantle seismic velocities,  $V_p$  and  $V_s$ , appear too dependent on geography to be explicable solely as thermal anomalies. Two questions arise: Are the temperature sensitivities of elastic moduli strong enough to admit temperature as the dominant effect? and, if so, can we distinguish regions where velocity variations may be entirely of thermal origin from those where compositional effects are required? These questions are addressed by a new analysis of thermoelastic properties, based on an equation of state constrained to give reliable derivative properties (Stacey and Isaak, 2001). A linear relationship between elasticities and pressure, which is well observed for the lower mantle (Stacey, 1992,1995), permits calculation not only of the Grüneisen parameter but its volume derivative as functions of depth. Then thermodynamic identities suffice to calculate the thermal expansion coefficient and the temperature dependences of elasticities.

The adiabatic Anderson-Grüneisen parameter ( $\delta S$ ) varies with depth from  $2.28 \pm 0.32$  at the top of the lower mantle to  $1.24 \pm 0.13$  at the bottom. The corresponding non-dimensional temperature-dependence of rigidity,  $\epsilon$ , varies from  $6.1 \pm 0.3$  to  $5.7 \pm 0.5$ . As other authors have noted (e.g. Isaak et al, 1992), this is constant within the uncertainties of calculation. Volume expansion coefficient decreases from  $23.3 \pm 1.2 \times 10^{-6}/K$  to  $11.3 \pm 0.1 \times 10^{-6}/K$ . The anelastic contribution to  $\epsilon$  (noted by Karato, 1993), which may be up to 15% of the total  $\epsilon$ , is included in this calculation and there is no significant anelastic contribution to  $\delta S$ . Thus these numbers convert directly to temperature dependences of seismic velocities. In the depth range 670km to 3290km the total temperature-dependences vary with depth as

$$d \ln V_s / dT = 5.9 \text{ to } 2.7 \times 10^{-5} / K$$

$$d \ln V_p / dT = -3.4 \text{ to } -1.1 \times 10^{-5} / K$$

$d \ln V_s / d \ln V_p$  increases with depth from 1.75 to 2.46 with much less uncertainty because the uncertainties in the  $V_s$  and  $V_p$  variations are correlated.

There is a general similarity to tomographic observations in the calculated  $d \ln V_s / d \ln V_p$  and its depth variation, inviting the conclusion that thermal effects dominate, even if some compositional effect is required, most obviously where there are reports of negatively correlated  $V_s$  and “bulk sound velocity” (for which  $\delta S < 1$ ). However, the gross magnitude of the thermal effect gives trouble. If we postulate an anomalous spherical volume, of radius 500 km, in the middle of the lower mantle, with a 0.5% contrast in  $V_p$  relative to its surroundings, this requires a 250K temperature contrast and consequent density contrast of  $19 \text{ kg/m}^3$ . Then, equating the buoyancy force to the Stokes flow viscous drag on its motion (Stacey, 1992, Eq.5.97) and imposing plausible limits on the heat flux implied by the convective speed, we face three alternative conclusions: (i) mid lower mantle viscosity exceeds  $10^{23}$  Pas, (ii) anomalous volumes with velocity contrast of order 0.5% are very much smaller than a 500km radius sphere, or (iii) compositional effects are more important than thermal effects.

### References

- D G Isaak et al, 1992. Geophys. Res. Lett. 19:741-744.  
 S Karato, 1993. Geophys. Res. Lett. 20:1623-1626.  
 F D Stacey, 1992. Physics of the Earth, 3rd ed., Brookfield Press, Brisbane  
 F D Stacey, 1995. Phys. Earth Planet. Inter. 89:219-245.  
 F D Stacey and D G Isaak, 2001. Geophys. J. Int. 146:143-154.

## 1.6 A new global tomography of the earth: structure of mantle plumes

Dapeng Zhao

Geodynamics Research Center, Ehime University, Matsuyama 790-8577, Japan,

<zhao@sci.ehime-u.ac.jp>

During the last two decades, seismologists have made continuous efforts to determine the three-dimensional (3-D) seismic velocity structure of the mantle. In order to better understand the Earth's deep structure and dynamics, I have attempted to develop a new model of whole mantle seismic tomography with a novel approach (Zhao, 2001). I adopted a grid parameterization instead of blocks and spherical harmonic expansions which were used in most of the global tomographic studies. Ray paths and travel times are computed with an efficient 3-D ray tracing scheme (Zhao et al., 1992). Moreover, the topography of mantle discontinuities at 410 and 660 km depths and the Moho discontinuity (Flanagan and Shearer, 1998; Mooney et al., 1998) are taken into account in the tomographic inversions. The three discontinuities exhibit lateral depth variations of tens of kilometers, which greatly affects the ray path and travel times, hence their depth changes should be taken into account in the inversions.

This new approach was applied to a large data set of travel times (P, PP, PcP, pP) which were compiled by the International Seismological Center (ISC) and were reprocessed by Engdahl et al. (1998), resulting in a new model of whole mantle P-wave tomography. For the shallow mantle, our new model contains the general features observed in the previous models: a low-velocity ring around the Pacific Ocean basins and high-velocity anomalies under the old and stable continents in the depth range of 0-400 km. One significant difference from the previous models is that stronger and wider high-velocity anomalies are visible in the transition zone depths under the subduction zone regions, which suggests that most of the slab materials are stagnant for a long time in the transition zone before finally dropping down to the lower mantle. Plume-like slow anomalies are visible under the hotspot regions in most parts of the mantle. The slow anomalies under hotspots usually do not show a straight pillar shape, but exhibit winding images, which suggests that plumes are not fixed in the mantle but can be deflected by the mantle flow. As a consequence, hotspots are not really fixed but can wander on the Earth's surface, as evidenced by the recent geomagnetic and numeric modeling studies. Wider and more prominent slow anomalies are visible at the core-mantle boundary (CMB) than most of the lower mantle, and there is a good correlation between the distribution of slow anomalies at the CMB and that of hotspots on the surface, which suggest that most of the mantle plumes under the hotspots may originate from the CMB. However, there may be some small-scaled, weak plumes originating from the transition zone depths.

### References

- Engdahl, E.R. et al. (1998) Global teleseismic earthquake relocation with improved travel times and procedures for depth determination. *Bull. Seismol. Soc. Am.*, **88**, 722-743.
- Flanagan, M. and P. Shearer (1998) Global mapping of topography on transition zone velocity discontinuities by stacking SS precursors. *J. Geophys. Res.*, **103**, 2673-2692.
- Mooney, W., G. Laske and G. Master (1998) CRUST 5.1: A global crustal model at 5 X 5. *J. Geophys. Res.*, **103**, 727-747.
- Zhao, D., A. Hasegawa and S. Horiuchi (1992) Tomographic Imaging of P and S wave velocity structure beneath northeastern Japan. *J. Geophys. Res.*, **97**, 19909-19928.
- Zhao, D. (2001) Seismic structure and origin of hotspots and mantle plumes, *Earth Planet. Sci. Lett.*, in press.

**October 3 (Wednesday) 13:30 – 16:30**

**Session 2**

**Formation and evolution of geochemical reservoirs**

Keynote: Stan Hart, Woods Hole Oceanographic Institution

Chair: Marc Hirschmann, University of Minnesota



## 2.1 Formation and evolution of geochemical mantle domains

Stanley R. Hart

Woods Hole Oceanographic Institution, Woods Hole, MA 02543

I will review our current understanding of the placement, genesis, evolution and lithologic nature of the several known geochemical mantle domains, and the dynamics of melting and melt extraction from these mantle domains. This arena has been recently subjected to several paradigm “warps”: one is the increasing evidence that mesoscale mantle heterogeneities (veins, pods, layers) may be important in creating some of the isotopic heterogeneity observed in mantle-derived melts. This in turn demands a better understanding of melting and melt transport processes. The second is the geophysically-based concept that the deepest mantle (> 1700km) may be convectively isolated from the overlying mantle by virtue of a compositional restraint on deep mantle buoyancy. This in turn demands a better understanding of the chemical and lithologic make-up of mantle plumes, as they may provide our most direct sampling of the deep mantle.

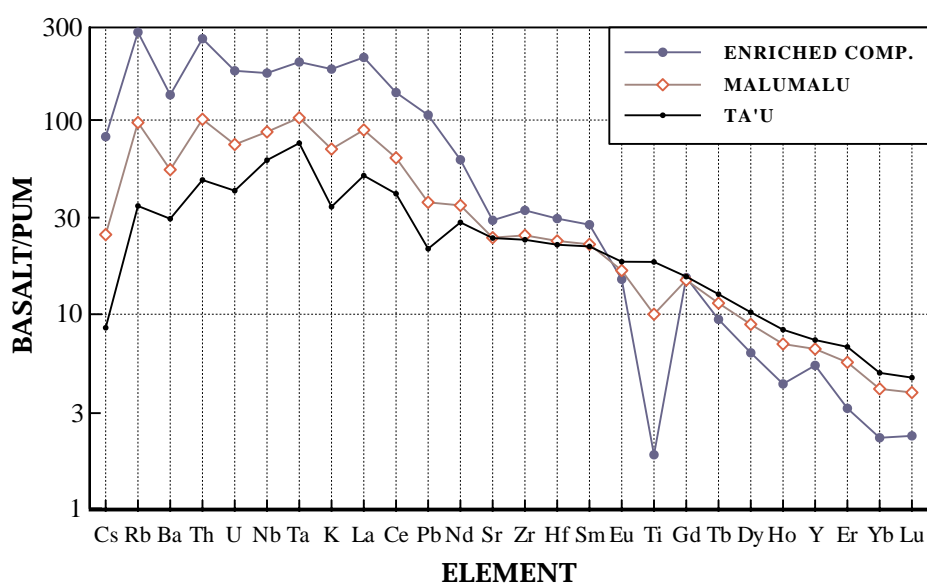


Figure 1. Spidergrams (primitive earth normalized) for basalts from Ta'u (average of 18), Malumalu (average of the two highest  $^{87}\text{Sr}/^{86}\text{Sr}$  basalts) and a model “Enriched Component.” The Malumalu samples are corrected for olivine control, so as to have the same MgO as the Ta'u average. The mixing is calculated as 75% Ta'u plus 25% EC equals Malumalu. The enriched component bears no resemblance to any typical oceanic sediment.

Several of the isotopically-defined domains in the mantle zoo are thought to be a result of lithospheric recycling, and yet we have little understanding of the parentage or lithologic expression of this material, or of its melting dynamics. We are pursuing several avenues as a means to confront this problem. One is an in-depth study of the Samoa hotspot, which is the EM2 mantle holotype. Samoa is the most enriched of the EM hotspots ( $^{87}\text{Sr}/^{86}\text{Sr} \sim 0.7089$ ), and this distinctive chemistry is conventionally ascribed to recycling of ancient lithosphere containing a terrigenous sediment component. However, no model has as yet satisfactorily accounted for many of the puzzling geochemical characteristics of EM2 hotspots (e.g. the coexistence of enriched  $^{87}\text{Sr}/^{86}\text{Sr}$ , heavy  $\delta^{18}\text{O}$ , and high  $^3\text{He}/^4\text{He}$ ). By comparing the geochemical character of basalts from Ta'u Island, Samoa, which are the least-enriched of Samoan basalts ( $^{87}\text{Sr}/^{86}\text{Sr} = 0.70464$ ) with the most-enriched material, from Malumalu seamount ( $^{87}\text{Sr}/^{86}\text{Sr} = 0.70889$ ), we are able to characterize the trace-element patterns of the “enrichment”; this is shown in the spidergram Figure 1 below. What is noteworthy is the very large negative

Ti anomaly in the enriched component, indeed suggestive of a terrigenous sediment component. However, the lack of Pb, Nb, and Ta anomalies, and the negative Ba anomaly, are difficult to reconcile with a terrigenous pedigree for the enriched component. One can simply assert that chemical processing during subduction has erased the continental fingerprint. We are exploring magic-free explanations as well, such as autometasomatism of a mixed lithology of peridotite with mafic enclaves.

The second avenue is a chemical and isotopic study of pre-aggregated melts (as captured in melt inclusions in phenocrysts) in the expectation that these will shed significant light on the melting lithologies and melt transport networks involved in hotspot volcanism. Pb isotope studies of melt inclusions from end-member EM1, EM2 and HIMU hotspots show remarkable diversity on a hand-specimen scale. Typically, the isotopic arrays are anchored at one end by compositions comparable to the bulk basalts; the other ends extend into the interior regions of the mantle isotope tetrahedron, perhaps to a FOZO-like composition. This behavior is what one might expect of melts derived from a mantle with mesoscale mafic enclaves, and is thus supportive of a lithologically diverse mantle containing recycled lithospheric domains. At the same time, it is consistent with a monolithologic peridotitic mantle, with isotopically diverse domains being serviced by a fractal melt-extraction network. In this case, disparate and remote “drainage basins” can end up with a common area of confluence, mixing and trapping, in shallow melt plumbing systems.

The debate over whole-mantle versus layered-mantle convection is nearing its 30th birthday. While the geophysical evidence for whole-mantle mass exchange appears incontrovertible, full accommodation with the geochemical evidence has been a challenging goal.

## 2.2 A petrologic view of the characteristics of mantle geochemical reservoirs

M. Hirschmann<sup>1</sup>, T. Kogiso<sup>1</sup>, and Daniel J. Frost<sup>2</sup>

<sup>1</sup>Univ. Minnesota, Dept. Geol. Geophys. Minneapolis, MN 55455 USA

<sup>2</sup>Bayerisches Geoinstitut, Universitaet Bayreuth.

The characteristics of mantle geochemical reservoirs are known chiefly from the geochemistry of oceanic basalts and particularly from the geochemistry of oceanic island basalt (OIB). OIB have received considerable attention from analytical geochemists, but relatively little from experimental petrologists. This is unfortunate, as some key problems regarding the character and origin of these reservoirs are as much petrologic as they are geochemical. Some key petrologic questions regarding the source regions of oceanic islands include:

(1) Are the lithologic carriers of exotic mantle components easier to melt than those that carry typical (depleted) mantle signatures? If so, than much of the variability we see among oceanic basalts may be related to preferential fusion of “plums” in weak plumes and dilution of heterogeneities by voluminous partial melting of depleted components in strong plumes and ridges. Additionally, the geochemical mixing spectra in OIB may be refracted through the melting relations, making it difficult to discern proportions of materials in OIB sources.

(2) Are there major element (phase equilibria) signatures associated with melting of exotic component source regions? Suggestions for such relationships have generally been attributed to the putative presence of eclogite or pyroxenite, but there are other possibilities, such as the role of enhanced volatiles.

(3) Can geochemical signatures of small-scale heterogeneities survive the partial melting and melt extraction process? This is an important question for understanding the Os isotopes of OIB source regions, as the lithologies principally associated with radiogenic Os, pyroxenites, are low in Os. If partial melts of pyroxenite mix intimately with surrounding peridotite, we would not expect to see a radiogenic Os signature in basalts derived from these sources. The question of reaction with ambient peridotite is also important for the preservation of possible major element signatures.

Ongoing research at the University of Minnesota is addressing all 3 of these questions. Here we summarize some of our results pertaining to question 2. In particular, we focus on the possible origin of alkalic lavas similar to those common in the Cook-Austral chain, which produce OIB with a range of geochemical signatures including extreme HIMU. These lavas are characteristically undersaturated alkali olivine basalts, basanites, and nephelinites.

A survey of major element characteristics of OIB from the Cook-Austral chain suggests that the parental magma is likely a magnesian alkali olivine basalt or basanite with ~15 wt.% MgO, 44-45 wt.% SiO<sub>2</sub>, ~10 wt.% Al<sub>2</sub>O<sub>3</sub>, and CaO/Al<sub>2</sub>O<sub>3</sub> >1. Such liquids have not been produced from partial melting of peridotite or carbonated peridotite at 3 GPa, though partial melts of garnet peridotite near 5 GPa (Walter, 1998) could plausibly be parental to such liquids. Partial melts of peridotite-basalt mixtures (Kogiso et al., 1998) also do not produce appropriate liquids.

Our experiments partially melting garnet pyroxenite (Mix1G garnet Mg# = 79) at 1.5-2.5 GPa produce liquids that are strongly alkalic with notable similarities to Cook-Austral lavas, but in detail these lavas are too rich in Al<sub>2</sub>O<sub>3</sub> to be parental to the OIB. New experiments at 5.0 and 7.5 GPa using a Walker-type multi-anvil apparatus at Bayerisches Geoinstitut indicate that expansion of the garnet field with increasing pressure drives partial melt compositions to lower Al<sub>2</sub>O<sub>3</sub> contents, producing liquids with 8% Al<sub>2</sub>O<sub>3</sub> and quite similar to nominal parental HIMU lavas.

Thus, partial melting of garnet pyroxenite is capable of generating lavas similar to likely HIMU parents, but the required temperatures are high (1650 °C at 5 GPa) and not much different from those needed to produce similar liquids from garnet peridotite and more importantly, may not be reconcilable with the potential temperature of the HIMU source. Further investigations, including documentation of low-melt fractions of anhydrous peridotite and pyroxenite in this pressure range, are

needed. Finally, we note that the garnet pyroxenite (Mix1G) is unlike likely compositions for pristine recycled oceanic crust. Recycled oceanic crust is thought by many to be the origin of the HIMU source, but is incapable of producing partial melts similar to the alkalic lavas seen in HIMU localities. It is unclear whether extended residence in the mantle and associated hybridization could produce garnet-pyroxenite-like compositions that would have partial melting relations similar to Mix1G.

### 2.3 The relationship between continental and oceanic crust formation and the development of the depleted mantle

Ian H. Campbell

Research School of Earth Sciences, Australian National University, Canberra, ACT, 0200, Australia  
<Ian.Campbell@anu.edu.au>

The Nb/U and Th/U of the primitive mantle are 34 and 4.04 respectively, which compare with 9.7 and 3.96 for the continental crust. Extraction of continental crust from the mantle therefore has a profound influence on its Nb/U but little influence on its Th/U. Conversely, extraction of MOR-type basalts lowers the Th/U of the mantle residue but has little influence on its Nb/U. As a consequence, variations in Th/U and Nb/U with Sm/Nd can be used to evaluate the relative importance of continental and basaltic crust extraction in the formation of the depleted (Sm/Nd enriched) mantle reservoir.

This study evaluates Nb/U, Th/U and Sm/Nd variations in suites of komatiites, picrites and their associated basalts, of various ages, in order to determine whether basalt and/or continental crust have been extracted from their source region. Emphasis is placed on komatiites and picrites because they formed at high degrees of partial melting and are expected to have Nb/U, Th/U and Sm/Nd that are essentially the same as the mantle that melted to produce them. The results show that all of the studied suites, with the exception of the Barberton, have had both continental crust and basaltic crust extracted from their mantle source region. The high Sm/Nd of the Gorgona and Munro komatiites require the elevated ratios seen in these suites to be due primarily to extraction of basaltic crust from their source regions whereas basaltic and continental crust extraction are of sub-equal importance in the source regions to the Yilgarn and Munro komatiites. The Sm/Nd of modern MORBs lies above the crustal extraction curve on a plot of Sm/Nd against Nb/U, which requires the upper mantle to have had both basaltic and continental crust extracted from it.

It is suggested that the extraction of the basaltic reservoir from the mantle occurs at mid-ocean ridges and that the basaltic crust, together with its complementary depleted mantle residue, is subducted to the core-mantle boundary. When the two components reach thermal equilibrium with their surroundings the lighter depleted component separates from the denser basaltic component. Both can return to the upper mantle in plumes, and as the counter flow to subducted slabs, but the lighter depleted component has a shorter residence time in the lower mantle than the denser basaltic component. If the difference in the recycling times for the basaltic and depleted components is about 1.0 to 1.5 Ga, a basaltic reservoir is created in the lower mantle, equivalent to the amount of basalt that is subducted in 1.0 to 1.5 Ga, and that reservoir is isolated from the upper mantle. It is this reservoir that is responsible for the Sm/Nd ratio of the upper mantle lying above the trend predicted by extraction of continental crust on the plot of Sm/Nd against Nb/U.

## 2.4 Origin of high-Nb basalts from the Sulu Arc, southern Philippines

P.R. Castillo<sup>1\*</sup>, R.U. Solidum<sup>1,2</sup>, and R.S. Punongbayan<sup>2</sup>

<sup>1</sup> Scripps Institution of Oceanography, UCSD, La Jolla, CA 92093-0212, USA

<sup>2</sup> Philippine Institute of Volcanology and Seismology, Quezon City, Philippines

\* <pcastillo@ucsd.edu>

A hallmark geochemical feature of convergent zone lavas is their distinctive depletion in high field strength elements (HFSE - e.g., Nb, Hf, Zr, Ta) relative to other trace elements. The origin of this geochemical feature is of great importance to Earth Science as it bears directly on such global problems as mass balance between material input and output along convergent margins and source of mantle plumes and/or mantle heterogeneities. Interestingly, there are rare high-Nb arc basalts with pronounced enrichment in Nb (i.e., basalts with >20 ppm Nb) and other HFSE. Understanding the petrogenesis of such high-Nb basalts will lead to a better understanding of the behavior of HFSE in convergent zone magmatism.

Lavas erupted along the Sulu Arc in southern Philippines range from typical, HFSE-depleted arc lavas to HFSE-enriched, high-Nb basalts. Sajona and others (J. Petrol. 37: 1996), using the same arguments of Defant and Drummond (Nature 347: 1990), propose that the enrichment of HFSE in high-Nb basalts is connected to the presence of slab-derived melts in the eastern segment of Sulu Arc and in the nearby island of Mindanao. Sajona and others envision that the initially subducted slab is melted beneath the Sulu Arc. Slab melt rose through the mantle wedge beneath the arc, but only a portion reached the surface; the remainder of the melt enriched the mantle wedge in HFSE through the formation of metasomatic phases such as amphibole and rutile. Later, the metasomatized mantle was dragged down to deeper portion of the wedge. The breakdown of metasomatic phases produced the different types of Nb-enriched basalts in the Sulu Arc. Implicit in their model is that the presence slab-derived melt in sub-arc mantle is one of the keys to a better understanding of the behavior of HFSE in arc lavas - the production of slab-derived melt is the trigger for the production of high-Nb basalts.

In this study, we analyze the major and trace element and Sr-Nd-Pb isotopic composition of basalts from the Sulu Arc with variable HFSE contents, from slightly- to highly-enriched in Nb. Results show that Nb and other HFSE are generally correlated with many other trace elements, producing binary mixing arrays. Lavas from off-axis seamounts in the South China Sea basin overlap with or form the extension of the high-HFSE end of the binary array. On the other hand, typical mantle-derived and slab-derived arc lavas from eastern Sulu Arc and Mindanao Island occupy the other, HFSE-depleted end of the array. These observations clearly indicate that it is highly unlikely that the HFSE content of the high-Nb and Nb-enriched basalts originated from the breakdown of HFSE-enriched metasomatic phases generated by slab-derived melt. The high-Nb basalts and seamount lavas most likely share a common mantle source which is distinct from the source of both the typical and slab-derived arc lavas. Results of previous Sr, Nd and Pb isotope investigations suggest that South China Sea seamount lavas come from an enriched-mantle source similar to that of ocean island basalts (OIB - e.g., Tu and others, Chem. Geol. 97: 1992). The Sr, Nd, and Pb isotopic ratios of high-Nb basalts form broad, but distinct correlations with their HFSE contents and these correlations also define a binary mixing relationship between an enriched-mantle and source of typical arc lavas. Thus our isotope data strengthen our conclusion that the HFSE content of the high-Nb basalts from the Sulu Arc originate from a distinct mantle source rather from a slab-derived melt.

## 2.5 Evidence for distinct primitive mantle sources; a noble gas study of the Reunion hotspot

Takeshi Hanyu\*, Tibor J. Dunai, Gareth R. Davies, Ichiro Kaneoka, Susumu Nohda, and Kozo Uto

\*Earthquake Research Institute, University of Tokyo

He, Ne and Ar isotopes were measured from two volcanoes on Reunion (Piton de la Fournaise, <0.53 Ma; Piton des Neiges, 2 Ma - 0.44 Ma) and three magmatic series from Mauritius (Older, 5-8 Ma; Intermediate, 2-3 Ma; Younger, < 1 Ma). These volcanics record 8 Myr activity of the Reunion Hotspot.  $^3\text{He}/^4\text{He}$  ratios of Piton de la Fournaise are between 12.5 and 13.5 Ra.  $^3\text{He}/^4\text{He}$  of Piton des Neiges are constant regardless of  $^4\text{He}$  concentration and sample age, and indistinguishable from those of Piton de la Fournaise. The Older Series of Mauritius, corresponding to the shield building stage, has constant  $^3\text{He}/^4\text{He}$  around 11.5 Ra, slightly lower than the ratio of Reunion. Samples from both Reunion volcanoes have higher  $^{20}\text{Ne}/^{22}\text{Ne}$  and  $^{21}\text{Ne}/^{22}\text{Ne}$  than atmospheric value (up to 12.6 and 0.0395, respectively). These data define a linear trend on a Ne three-isotope diagram with a slope between the Loihi and MORB correlation lines. There is a clear correlation between  $^{20}\text{Ne}/^{22}\text{Ne}$  and  $^{40}\text{Ar}/^{36}\text{Ar}$  (up to 4600).

The similarity of  $^3\text{He}/^4\text{He}$  and Sr-Nd isotope ratios between Piton des Neiges and Piton de la Fournaise demonstrate that the volcanoes have had a common homogeneous source over a 2 Myr period. The Older Series of Mauritius also have  $^3\text{He}/^4\text{He}$  and Sr-Nd ratios comparable to Reunion. These data suggest that both islands were produced by the same hotspot activity with almost constant  $^3\text{He}/^4\text{He}$  over an 8 Myr period.

In contrast, Intermediate and Younger Series of Mauritius and Rodrigues have  $^3\text{He}/^4\text{He}$  ratios similar to MORB and Sr and Nd isotope ratios closer to MORB than lavas from Reunion and Older Series of Mauritius. These Intermediate and Younger Series lavas therefore record a late stage thermal rejuvenation beneath Mauritius derived from a source that is unrelated to the mantle plume.

The isotopic characteristics of the source of the Reunion magmatism are relatively low  $^3\text{He}/^4\text{He}$  (13 Ra), an intermediate slope in a Ne-three isotope diagram and relatively radiogenic Sr isotope ratios. These source characteristics cannot be explained by either crustal contamination or MORB-source mixing with Loihi-type primitive mantle. Thus He-Ne-Ar-Sr-Nd isotopes demonstrate that this plume source is distinct from the Loihi and Iceland plume sources, clearly showing that the mantle contains several relatively less-degassed reservoirs and not a single primitive source.

Two possible models can account for the different isotopic signature of Reunion and Hawaii hotspots; (1) the Reunion source contains more recycled materials than Loihi source and (2) the Reunion source experienced stronger degassing/differentiation than Loihi source in the early stage of mantle evolution. In both cases a convection mode in the mantle is required that isolates several less-degassed reservoirs to maintain their distinct isotopic signature in the convectively stirred lower mantle.

## 2.6 Noble gases and the primitive reservoir

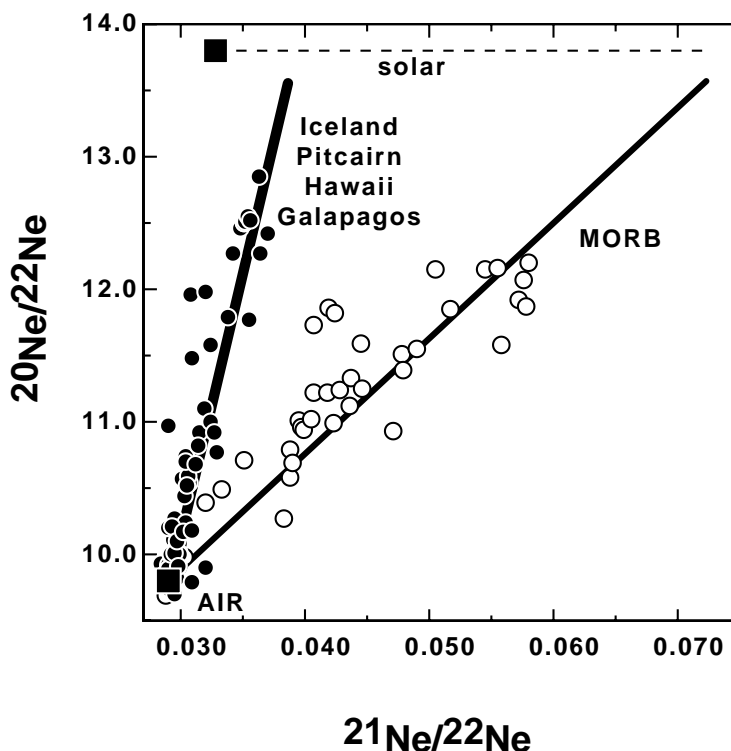
Manuel Moreira

Laboratoire de géochimie et cosmochimie, Institut de Physique du Globe de Paris, 4 Place Jussieu, 75005 Paris cedex 05, France, Email: [moreira@ipgp.jussieu.fr](mailto:moreira@ipgp.jussieu.fr)

Noble gas systematics in the mantle have been used over the past 20 years to constrain the origin of the Earth's atmosphere and the mantle dynamics. The simplest model of mantle structure obtained by noble gas systematics is a depleted-degassed upper mantle overlying a less depleted/degassed lower mantle. The origin of this model is the isotopic composition of He, Ne, Ar and Xe in MORB and OIB. We present here an overview of the noble gas systematics in MORB and in OIB.

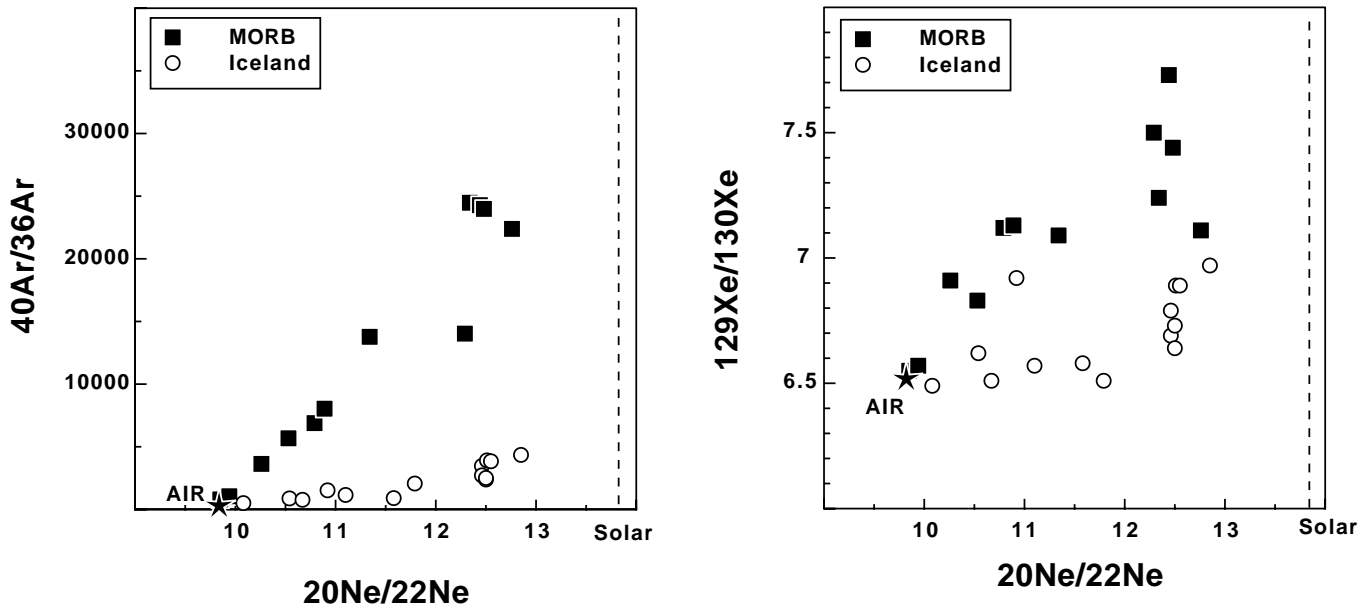
All the noble gas radiogenic isotopic ratios (e.g.  $^4\text{He}/^3\text{He}$ ,  $^{40}\text{Ar}/^{36}\text{Ar}$ , ...) are higher in MORB than in OIB. Three interpretations of such an observation are possible. -1- Higher atmospheric contamination of OIB; -2- The OIB source contains atmospheric-like noble gases; -3- The OIB source has lower parent/daughter ratios such as U/He, K/Ar.

One answer to these questions is the neon systematics. Neon has three isotopes: 20, 21 and 22. In the mantle, only the  $^{21}\text{Ne}$  changes significantly by nuclear reactions. The  $^{20}\text{Ne}/^{22}\text{Ne}$  ratio is therefore constant in the mantle. Analysis of MORB and OIB for neon have shown that the  $^{20}\text{Ne}/^{22}\text{Ne}$  is different in the mantle and in the atmosphere (Figure 1). The origin of this difference will not be discussed here but we use this property to constrain the other rare gas isotopic ratios by removing the atmospheric contamination using this neon property. The main difference between MORB and OIB is the  $^{21}\text{Ne}/^{22}\text{Ne}$  ratio (Figure 1). For similar  $^{20}\text{Ne}/^{22}\text{Ne}$ , the  $^{21}\text{Ne}/^{22}\text{Ne}$  is lower in OIB sources than in MORB source. A low  $^{21}\text{Ne}/^{22}\text{Ne}$  reflects a low  $(\text{U}+\text{Th})/^{22}\text{Ne}$  ratio.



The mantle has a  $^{20}\text{Ne}/^{22}\text{Ne}$  ratio ranging between the highest measurement (=12.6) and the solar ratio (=13.8). We will use in the following the solar value as the mantle value. It is possible to correct

all the isotopic ratios ( $^{21}\text{Ne}/^{22}\text{Ne}$ ,  $^{40}\text{Ar}/^{36}\text{Ar}$ ,  $^{129}\text{Xe}/^{130}\text{Xe}$ ) from air contamination by extrapolating the observed mixing trend to this solar ratio (Figure 2). The results of such an approach is that the OIB source does have lower radiogenic isotopic ratios ( $^{40}\text{Ar}/^{36}\text{Ar} < 10,000$ ,  $^{129}\text{Xe}/^{130}\text{Xe} < 7.2$ ). This excludes the higher contamination of OIB samples. Moreover, because the  $^{20}\text{Ne}/^{22}\text{Ne}$  ratio is identical in both MORB and OIB sources, this implies also there is negligible atmospheric noble gases subducted in the mantle. Therefore, the OIB sources have lower chemical ratios U/He, K/Ar... We will call "primitive reservoir", this reservoir with low  $^4\text{He}/^3\text{He}$ ,  $^{21}\text{Ne}/^{22}\text{Ne}$  and  $^{40}\text{Ar}/^{36}\text{Ar}$  ratios and with low U/He, U/Ne and K/Ar ratios.



We exclude a shallow origin for the OIB, therefore, the "primitive" noble gas signature has to be located below the MORB source. This could be either the whole lower mantle, the D" layer or the core itself. Wherever the OIB source is, it contains more refractory material (U, Th, K) than the depleted mantle, source of MORB (as shown by analysis of OIB). Therefore, the primitive signature reservoir has to contain a higher content of primitive rare gases ( $^3\text{He}$ ,  $^{22}\text{Ne}$ ,  $^{36}\text{Ar}$ ,  $^{130}\text{Xe}$ ) than the MORB reservoir. If this reservoir is the lower mantle, it has to be less degassed (only 10% less) than the degassed mantle. This is the simplest model. If the primitive reservoir is located in the core, to account for the high U and Th content of OIB material, subducted oceanic crust has to be involved in OIB source. However, this material is so uranium rich that it must contain high contents of radiogenic noble gases. A simple mixing equation between material coming from the core (core) with oceanic crust (OC) can be written. Using  $X=R/Ra$  :

$$X_{OIBsource} = \alpha \times X_{OC} + (1 - \alpha) \times X_{Core}$$

Where

$$\alpha = \frac{1}{1 + \frac{[4He]_{Core}}{[4He]_{OC}} \times \frac{M_{core}}{M_{OC}}}$$

Here  $X_{OC} = 0$ , therefore  $X_{OIBsource} = (1 - \alpha) \times X_{Core}$

If  $X_{Core} = 120$  (chondrites) and  $X_{OIB} = 40$  (Iceland), therefore,  $\alpha = 0.7$ . And  $\frac{[4He]_{Core}}{[4He]_{OC}} \times \frac{M_{core}}{M_{OC}} =$

0.4

Assuming  $\frac{M_{core}}{M_{OC}} = 0.1\%$ , and  $[4He]_{OC} = 10^{-5}$  ccSTP/g (1.5Ga old crust), we get  $[4He]_{Core} = 4 \times 10^{-3}$  ccSTP/g.

Estimates of the helium content in the primitive mantle is between  $10^{-4}$  and  $10^{-3}$  ccSTP/g. This leads to a silicate/iron partitioning between  $\approx 0.1$  and  $\approx 1$  for helium. This value is extremely high when compared to measured values for moderate pressures.

Similar calculation can be done for a depleted lithospheric mantle (harzburgite) that could be stored in the lower mantle and will give a similar result. A high  $^3\text{He}$  content component is necessary, which is not compatible with a residual mantle because helium is incompatible.

To conclude, the high U required by the U contents in OIB implies necessarily a high  $^3\text{He}$  (and other primordial noble gases) content component. The core seems to be an improbable component because of the helium silicate/iron partitioning. The model where the lower mantle is less depleted and degassed than the upper mantle is still the most reasonable and can best explain the data. This does not imply the lower mantle is homogeneous and less degassed at the same extent everywhere. Some parts can be highly degassed, others, where big hotspots are coming from, may be not.

## 2.7 Geochemical evolution of Akagi volcano, northeast Japan: implications for interaction between island arc magma and lower crust, and generation of isotopically variable magmas.

Katsura Kobayashi and Eizo Nakamura

Pheasant Memorial Laboratory, Institute for Study of the Earth's Interior, Okayama University at Misasa

Major and trace element, and Sr, Nd and Pb isotopic compositions were determined for whole rock samples from the “isotopically anomalous” Akagi volcano on the volcanic front of the Northeast Japan arc. Sr and Nd isotopic compositions of phenocrysts were also analyzed together with determination of major and trace element compositions. Compared with the other volcanoes from the volcanic front, the whole rock isotope compositions of Akagi show highly enriched characteristics;  $^{87}\text{Sr}/^{86}\text{Sr} = 0.7060$  to  $0.7088$ ,  $\epsilon_{Nd} = -0.40$  to  $-8.6$ , and  $^{208}\text{Pb}/^{204}\text{Pb} = 38.4$  to  $38.8$ . The REE patterns are characterized by HREE depletions with U-shaped patterns from middle to heavy REE, suggesting that amphibole fractionation was induced by a reaction between clinopyroxene and  $\text{H}_2\text{O}$ -rich magma in the lower crust. The integrated isotope and trace elements systematics, and tectonic structure beneath Akagi volcano, suggest that the lower crustal assimilation by the  $\text{H}_2\text{O}$ -rich primary magma could have been affected by the double subduction of Philippine Sea and Pacific oceanic plates. This double subduction could have supplied larger amounts of water to the magma source region in the wedge mantle than in the case of a single subduction zone.

Significant differences in isotopic compositions are observed among phenocrysts and the coexisting melts. Such isotopic disequilibrium may have been resulted from magma mixing between an isotopically-depleted aphyric and an enriched porphyritic magma in a shallow magma chamber. The geochemical characteristics of these end-member magmas were retained in the lower crust, despite differing extents of lower crustal assimilation by the  $\text{H}_2\text{O}$ -rich magmas.

## 2.8 Analytical procedure for the measurement of lithium and boron isotope composition by High Resolution Secondary Ion Mass Spectrometer and its Application

Katsura Kobayashi<sup>1</sup>, Takuya Moriguti<sup>1</sup>, Ryoji Tanaka<sup>1</sup>, Kenji Shimizu<sup>2</sup>, Eizo Nakamura<sup>1</sup>

<sup>1</sup> Pheasant Memorial Laboratory, ISEI, Okayama Univ. at Misasa

<sup>2</sup> Tokyo Institute of Technology

Lithium (Li) and boron (B) isotopes have been to be powerful tracer to understand complicate geological processes, such as mantle-crust recycling (e.g., Ishikawa & Nakamura, 1994; Moriguti & Nakamura; 1998). We have developed analytical methods for lithium and boron isotopic composition using a High Resolution Secondary Ion Mass Spectrometer (HR-SIMS), Cameca ims-1270. Our HR-SIMS are equipped 5 electron multipliers as multi-collection system, which reduces uncertainties for isotope analyses caused by the instrumental fractionation and time-drift of secondary ion intensities. This apparatus, therefore, is suitable for precise determination of isotopic compositions, such as lithium, boron, lead and oxygen, with high spatial resolution ( $\sim 10\mu\text{m}$ ) from geological materials.

In order to determine the lithium and boron isotope composition, which is comparable by conventional TIMS technique, the reliable standard to calibrate mass discrimination effect in the apparatus is much important. Therefore, we prepared five synthetic glass standards under high-pressure condition, which have different isotopic compositions of lithium and boron with same basaltic matrix. Their lithium and boron isotopic compositions of these glass standards were determined by the conventional TIMS technique. The concentrations of lithium and boron were 7 and 32  $\mu\text{g/g}$ , respectively.

On the HR-SIMS analysis, 10  $\sim$  15 nA ( $\sim 10$  to 20  $\mu\text{m}$  spot size) of O<sup>-</sup> critical illuminated (Spot) primary ion beam was adopted for both lithium and boron analyses. The acceleration voltage of the primary and secondary beam was -13 and 10 kV, respectively. In order to remove the mass interference, such as lithium hydrate and boron hydrate,  $\sim 2000$  of mass resolution ( $M/\Delta M$ ) has been applied. Typical sensitivities lithium ( $^7\text{Li}^+$ ) and boron ( $^{11}\text{B}^+$ ) on this condition were  $\sim 1000$  and  $\sim 50$  cps/ppm/nA, respectively. Counting time for each cycle was 10 sec and 55 cycles were accumulated for typical analyses. Consequently, the lithium and boron isotopic compositions of natural and synthetic basaltic glass, can be analyzed from  $\sim 10\mu\text{m}$  spots with  $\sim 1$  and  $\sim 2\%$  ( $2\sigma$ ) of reproducibility, respectively. Applying this technique to the synthetic glass standards, we obtained liner calibration curves to correct the instrumental fractionation. We are planning to investigate melt inclusions from OIB and arc volcanics to understand the material recycling process in the earth.

## 2.9 A simple method for precise isotope analysis of ng-level Pb for natural rock samples

Takeshi Kuritani and Eizo Nakamura

Institute for Study of the Earth's Interior, Okayama University

Lead isotope compositions of rock samples, as well as their strontium and neodymium data, provide important constraints on dynamic processes of the Earth's evolution. However, analytical precision and accuracy of lead isotope determination with thermal ionization mass spectrometer (TIMS) has commonly been worse compared to those of strontium and neodymium. The main reason is that the correction for the mass fractionation during measurements is not available for lead isotope analysis because only  $^{204}\text{Pb}$  is non-radiogenic in the naturally occurring isotopes. To overcome this problem and to improve analytical precision and accuracy, "double (or triple) spike technique" has been introduced in some laboratories (Hamelin et al., 1985; Woodhead et al., 1995; Todt et al., 1996; Thirlwall, 2000). However, it is still difficult for many analysts to handle spike solutions because of their high cost and relatively complicated procedures in the preparation of lead samples and estimation of error propagation through the fractionation correction.

In this presentation we show a simple technique for precise isotope analysis of lead with TIMS, including improved procedures of column chromatography, sample loading, and mass spectrometry. The mass discrimination was corrected by the method of "zero-time correction" (Tuttas and Habfast, 1982; Koide and Nakamura, 1990) followed by the conventional normalization using a pure Pb reference material (NBS 981), instead of the "double spike technique". Two-stage column chromatography using 100 and 10 ml columns enabled to minimize the amounts of impurities in separated lead samples, which dramatically improved reproducibility of mass fractionation during mass spectrometry using an ion emitter made of a mixture of silicic acid and phosphoric acid. Using the present method, analytical reproducibility of 0.02 % and 0.05 % was attained for 100 ng and 1 ng of NBS981, and also 0.02 % and 0.06 % for 100 ng and 1 ng of Pb separated from natural rock samples. Furthermore, we obtained the reproducibility of 0.1 % for GSJ JP-1 (peridotite), in which the Pb concentration is as low as 0.09 ppm. The measured isotope compositions of USGS standard rocks AGV-1 and BCR-1, along with their reproducibility, were comparable to the published values using double spike technique (Woodhead and Hergt, 2000). These observations suggest that our simple technique is highly reliable in terms of accuracy, as well as precision, in the determination of Pb isotopic compositions of natural rock samples irrespective of rock chemistry and sample sizes from 1 to 100 ng of Pb.

## 2.10 Chemical compositions of a binary dilute solid solution during growth

Naoko Matsumoto\* and Masao Kitamura

\*Institute for Study of the Earth's Interior, Okayama University

The partitioning of elements between a solid solution and its coexisting phase is one of the most important phenomena in the chemical evolution of the earth and planets. Such partitioning occurs under both equilibrium and disequilibrium conditions. In general, the chemical composition of a growing solid solution deviates from the equilibrium. Chemical heterogeneities in a solid solution formed during the growth have been widely used to derive information about crystallization history. However, no theory, other than the Rayleigh fractionation model where the growth kinetics is ignored, has been presented so far to predict the chemical composition of a growing solid solution.

The composition of a crystal growing from a mother phase is mainly influenced both by mass transfer in the mother phase and by the kinetics operating at the crystal-mother phase interface. Previous models have stressed the effects of mass transfer accompanied by the assumption of equilibrium at the interface, mainly because a comprehensive understanding of the effect of interface kinetics is lacking.

The incorporation of growth units at kink sites is essential for the interface kinetics [1-3]. Recently we propose a kink kinetic model [4] that can give both the bulk composition and the incorporating flux per kink site for a binary ideal solid solution. In the present study, we apply the kinetic model to typical growth surfaces taking into account the effect of mass transfer.

To obtain an analytical solution, we treat the growth of a dilute (A, B) solid solution, where concentrations of B are sufficiently lower than those of A. The mass transfer is treated by a volume diffusion model [5], where growth units are transferred directly to a parallel sequence of growth steps with high kink densities.

The bulk chemical compositions and the normal growth rates are expressed as functions of the supersaturation at the edge of the diffusion boundary layer, the frequencies of kink kinetic process, the diffusion coefficients, the thickness of the diffusion boundary layer, and the step-spacing. The relative role of kink kinetics and volume diffusion, the orientation dependence of chemical compositions and growth rates are discussed in terms of these parameters. For example, the phenomenological relations between chemical compositions and the normal growth rates are clarified: the growth sectors formed by surfaces with higher normal growth rate have chemical compositions more close to its equilibrium value for a given supersaturation.

The formulation of chemical compositions and the normal growth rates gives a new basis for understanding the natural crystallization quantitatively.

### References:

- [1] W. van Erk, *J. Crystal Growth* **57** (1982) 71.
- [2] A.A. Chernov, *Sov. Physics Uspekhi* **13** (1970) 101.
- [3] G.H. Gilmer and K.A. Jackson, in: E. Kaldis and H. J. Scheels (Eds.), *1976 Crystal Growth and Materials, North-Holland, Amsterdam*, 1977, p. 80.
- [4] N. Matsumoto, M. Kitamura, *J. Crystal Growth* **222** (2001) 667.
- [5] A.A. Chernov, *Soviet Physics Uspekhi* **4** (1961) 116.

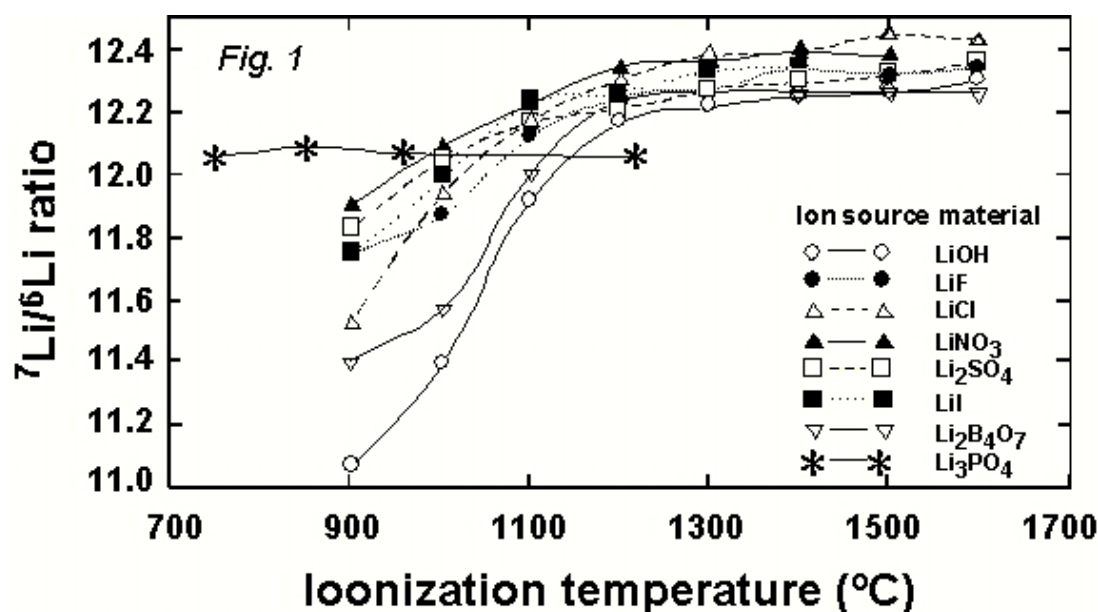
## 2.11 Precise Li isotope analysis by thermal ionization mass spectrometry (TIMS) using lithium phosphate as an ion source material and highly-yield lithium separation from natural samples

Takuya Moriguti and Eizo Nakamura

Pheasant Memorial Laboratory, Institute for Study of the Earth's Interior, Okayama University at Misasa, Tottori-ken, 682-0193, Japan

A high-precision Li isotope analysis was developed for determining the  $\text{Li}^+$  ion emitted from lithium phosphate as an ion-source material by a Re double-filament ionization method and a spot loading technique in the thermal ionization mass spectrometry. In this method, Li isotopic fractionation is distinctly less sensitive to the filament temperature than those in the previous methods, and stable and high ion beam intensity of more than  $8 \times 10^{-11}$  A for  $^7\text{Li}$  is obtained (Fig. 1). Furthermore, the sample preparation is simple and the low ionization temperature (850 °C) required by this method ensures the analysis of the isotopic composition of small amounts of Li with less influence of Li contamination to the sample, compared with the previous methods. These advantages in determining the  $^7\text{Li}/^6\text{Li}$  ratio result in the in-run precision and the analytical reproducibility of  $\pm 0.05$ - $0.08$  ‰ ( $2\sigma$  mean) and  $0.50$  ‰ (RSD), respectively for 100ng of Li, and  $\pm 0.04$ - $0.09$  ‰ ( $2\sigma$  mean) and  $0.29$  ‰ (RSD), respectively for 500ng of Li

A Highly-yield lithium separation technique for rock and aqueous samples also has been established. Four separate stages of ion-exchange chromatography were carried out using organic ion-exchange resin. An ethanol-HCl solution was used for complete separation of Li from Na at the third column stage. Total reagent volume for the entire chemical process was reduced to 42 ml and 33.3 ml for rock samples and seawater, respectively. The recovery yield and total procedural blank are 99.2 - 99.3 % and 11 pg, respectively. In this method, Rb, Sr, Sm, Nd, La and Ce can be collected after Li elution in the first column chromatography, then separated by the following specific procedures for these elements. Therefore, this method makes possible multi-isotope analysis for Li-poor and restricted small amounts of samples such as meteorites and mantle materials, extending to Li isotope geochemistry and cosmochemistry.

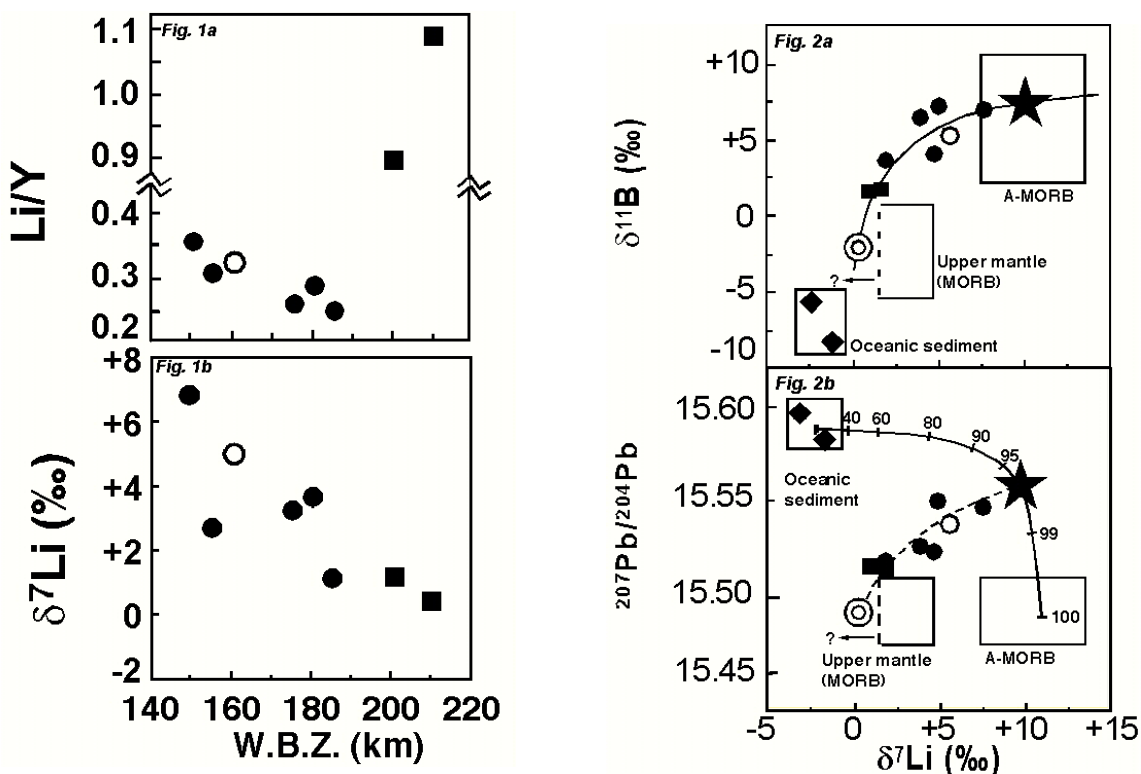


## 2.12 Li-B-Pb isotope systematic study of Izu arc volcanic rocks: implications for crust-mantle recycling at subduction zone

Takuya Moriguti and Eizo Nakamura

Pheasant Memorial Laboratory, Institute for Study of the Earth's Interior, Okayama University, Misasa, Tottori-ken, 682-0193, Japan

Li isotope systematics were applied to island arc volcanics from the Izu arc, Japan to investigate geochemical processes in subduction zones. Li isotope ratios ( $\delta^7\text{Li}$ ) and Li/Y of the arc lavas show clear across-arc variations, decreasing with increasing depth to the Wadati-Benioff zone (Fig 1a and b). This suggests that the amount of subduction component as a fluid added to the source region decreases with depth.  $\delta^7\text{Li}$ -Y/Li systematics of the arc lavas clearly indicate a simple mixing between two distinctive chemically homogenous endmembers, a subduction component and the mantle wedge. Furthermore, Li-B-Pb isotope systematics allow clear discrimination between the relative contribution of altered oceanic crust (AOC), oceanic sediment and mantle wedge to arc lavas, and suggests that AOC is the dominant subduction component, whereas the contribution of oceanic sediment is extremely small (< 5 %) (Fig 2a and b). The contrasting physicochemical properties for Li and B in mineral structures imply that Li may be less likely to migrate from the slab into the overlying mantle wedge than B. Thus the Li isotopic composition in the Earth's surface material evolved under near-surface condition could be more efficiently introduced into the deep mantle through subduction zones than the B isotopic signature, making Li isotopes a powerful geochemical tracer for better understanding of material recycling between crust and mantle.

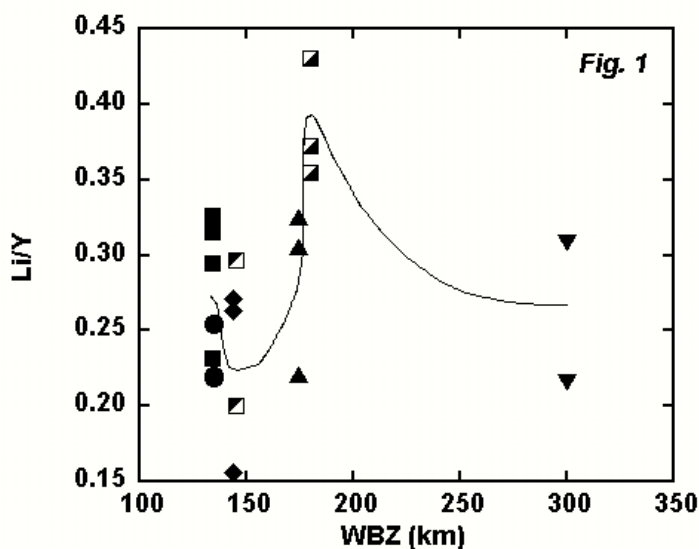


### 2.13 Li isotope variation in quaternary basaltic rocks in northeastern Japan arc

Takuya Moriguti and Eizo Nakamura

Pheasant Memorial Laboratory, Institute for Study of the Earth's Interior, Okayama University, Misasa, Tottori-ken, 682-0193, Japan

Li isotope systematics show great potential as a geochemical tracer for understanding crust-mantle recycling because of the following unique physicochemical characteristics of Li: (i) Li commonly exists as a trace element in rocks and minerals. It is a moderately incompatible element in magmatic processes such as partial melting and fractional crystallization, with incompatibility similar to that of yttrium. (ii) Li is highly mobile in fluid-related processes. (iii) Li possesses two stable isotopes,  $^6\text{Li}$  and  $^7\text{Li}$ , with an extremely large relative mass difference. Large isotopic fractionation of Li develops during low-temperature reactions associated with water at the Earth's surface, resulting in a variation in  $^7\text{Li}/^6\text{Li}$  ratio in natural samples  $> 30\text{‰}$ . In contrast, Li isotopic fractionation is extremely small when temperatures exceed  $350\text{ °C}$ , and thus, Li isotope fractionation is expected to be insignificant in magmatic processes.

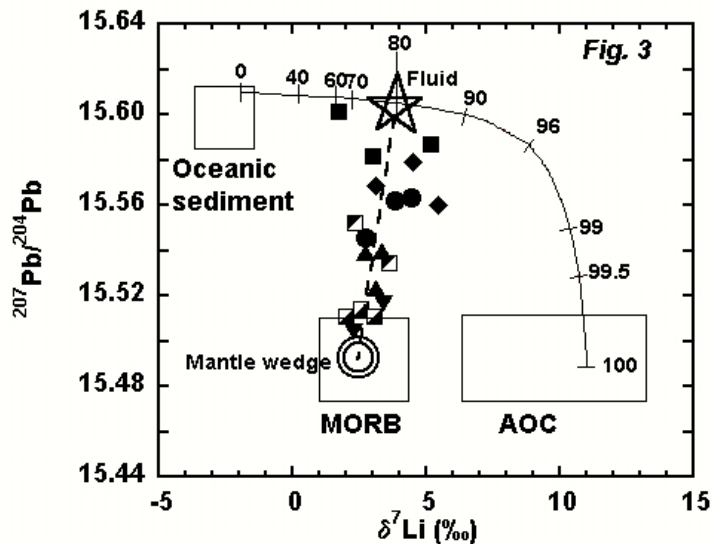
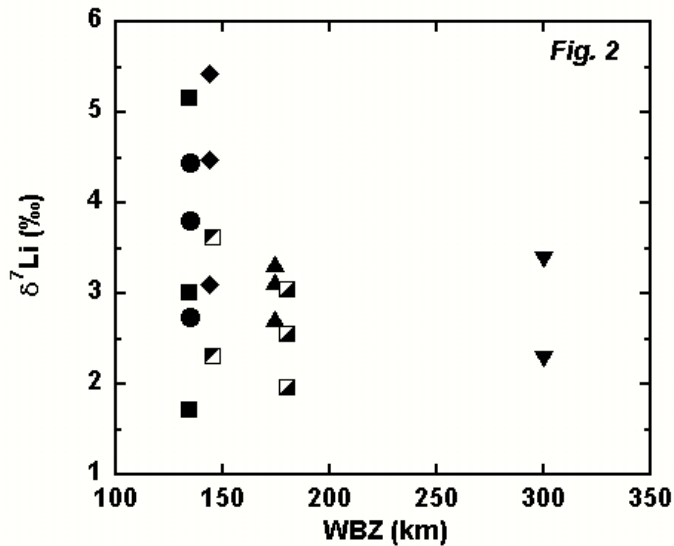


In the present study, Li isotope systematics were applied to northeastern Japan arc basalts in order to understand material recycling between crust and mantle at subduction zones, together with Pb isotope systematics. Pb/Ce and B/Nb ratios of arc basalts decrease gradually with increasing depth to the Wadati-Benioff zone (WBZ). However, Li/Y ratios do not show gradual decrease (Fig.1). Li/Y ratios decreases from 134 to 145km depths to the Wadati-Benioff zone but a positive anomaly in this ratio was found at around 180km depth to the WBZ. This across-arc profile of Li/Y ratio may reflect phase changes in the subducting slab, and the breakdown of lawsonite in the slab at  $\sim 180\text{ km}$  depth could be one explanation. In the lawsonite breakdown reaction ( $\text{lawsonite} + \text{diopside} + \text{garnet}_1 = \text{garnet}_2 + \text{coesite} + \text{H}_2\text{O}$ ) [1], Y is strongly partitioned into  $\text{garnet}_2$  and Li is strongly partitioned into  $\text{H}_2\text{O}$ . As a result of this reaction, therefore, the Li/Y ratio of the slab derived fluid could be higher at around 180 km depth, causing the positive anomaly in the Li/Y ratio of arc basalts. Sr, Nd, and Pb isotope ratios show clear across arc variation in the northeastern Japan arc lavas [2]. However, the Li isotope ratios do not show obvious across-arc variations (Fig.2). This is because the Li isotopic compositions of mixing two endmembers for arc magmas, mantle wedge and slab-derived fluids,

are extremely similar (Fig.3). The estimated Li isotopic compositions of the mantle wedge and the fluid estimated using Li and Pb isotope systematics are 2 and 4 ‰, respectively. The Li and Pb isotope systematics indicate that the proportions of the altered oceanic crust and oceanic sediment components in the slab-derived fluid are approximately 80 and 20 %, respectively. This ratio is consistent with the values previously obtained based on Sr, Nd and Pb isotope systematics [2].

[1] Schmidt, M.W. & Poli, S. *Earth Planet. Sci. Lett.* 163, 361-379 (1998)

[2] Shibata T. & Nakamura E. *J. Geophys. Res.* 102, 8051-8064 (1997)



## 2.14 Chemical and isotopic evolution of the Allende meteorite

Chie Sakaguchi and Eizo Nakamura

Institute for Study of the Earth's Interior, Okayama University

Individual chondrules and Ca-, Al- rich inclusions (CAIs) separated from Allende meteorite have been analyzed for the following; (1) trace element compositions of the bulk chondrules and CAIs, (2) the constituent minerals, and (3) Rb-Sr and Sm-Nd isotope compositions. Each chondrule was cut into two pieces; one piece was used for microprobe analyses by SEM-EDX and SIMS, and the other piece was used for bulk analyses of trace element compositions and for isotope analyses by ICP-MS and TIMS, respectively. The samples for bulk analyses were subjected to acid-leaching with diluted HCl solutions, yielding leachates and residues that were analyzed separately.

The Rb-Sr isotope systematics of chondrules show an apparent isochron age of  $4.26 \pm 0.05$  Ga with an initial  $^{87}\text{Sr}/^{86}\text{Sr} = 0.69944 \pm 44$ , and the age obtained from 4 CAIs is  $4.15 \pm 0.15$  Ga with an initial  $^{87}\text{Sr}/^{86}\text{Sr} = 0.698914 \pm 71$ . However, the Sm-Nd isotope compositions of the chondrules and CAIs plot near CHUR on the isotope evolution line of 4.56 Ga. The trace element analyses indicate that mobile elements such as the alkaline elements and Pb are enriched in the leachates relative to immobile elements such as REE, which are only slightly dissolved into the leachates with LREE enrichment. This LREE enrichment in the leachate can be explained by the preferential dissolution of mesostasis and plagioclase during acid leaching. However, it is difficult to obtain the positive Rb and Pb spikes, relative to the adjacent elements in the acid leachate trace element pattern, by the involvement of mesostasis and plagioclase.

It is known that these components, including the matrix in Allende meteorite experienced varying degrees of Fe-alkali-halogen metasomatic alteration resulting in the replacement of primary phases such as mesostasis, plagioclase, melilite and fassaite by Na-, K-, Fe- and Cl-rich phases. It is expected that Rb behaved similarly to these mobile elements during this alteration. Based on the Rb-Sr isotopic analyses, the timing of the Rb disturbance in the chondrules and in the CAIs is considered to have been the same. On the other hand, it is known that the Rb-Sr isotope compositions of the Allende matrix plot off of the isochron lines of the chondrules and CAIs, to the older-age side. Therefore, the Rb disturbance would have occurred at significantly later stage after accretion, with Rb introduced into the chondrules and CAIs from the matrix.

These observations suggest that the Rb-Sr isotope systematics and the concentrations of some mobile elements have been strongly affected by the metasomatic alteration of the Allende meteorite. This alteration apparently occurred at approximately 4Ga, coincidentally corresponding to the age of the peak of cratering on the moon.

## 2.15 Petrology, geochemistry and garnet and pyroxene xenocrysts of Belingwe volcanics, Zimbabwe - indisputable evidence for crustal contamination

K. Shimizu<sup>1\*</sup>, E. Nakamura<sup>1</sup>, and S. Maruyama<sup>2</sup>

<sup>1</sup> The Pheasant Memorial Laboratory for Geochemistry and Cosmochemistry, Institute for Study of the Earth's Interior, Okayama University at Misasa, Tottori-ken 682-0122;

<sup>2</sup> Department of Earth and Planetary Sciences, Tokyo Institute of Technology, Ookayama 2-12-1, Meguro-ku Tokyo 152-8551, JAPAN

\* <shimmy@geo.titech.ac.jp>

Belingwe greenstone belt, Zimbabwe is a large igneous province dominated by komatiitic and basaltic rocks. 2.7 Ga Komatiite from Relaince Formation in Belingwe greenstone belt is unusually fresh and well studied by many geologists, petrologists and geochemists. However, its origin and tectonic setting remain controversial. Kusky and Kidd (1992) have suggested by structural researches on the high-strain zones at the base of the volcanic sequence and discovery of ductile ultramafic mylonite from the shear zones that the thick volcanic sequence (Ngezi Group) are remnant of an Archean oceanic plateau. Trace element ratios of melt inclusions in olivine from Belingwe komatiite also support that the komatiite have extruded as oceanic plateau (McDonough and Ireland, 1993). On the other hand, Bickle et al. (1994) have argued that the volcanic sequence of the Ngezi Group stratigraphically resembles Phanerozoic flood basalt provinces extruded on continental crust. In addition, Pb and Nd isotopic correlation in Belingwe komatiites and komatiitic basalts indicates that some samples are contaminated up to 1 % of the basement of 3.5 Ga felsic gneiss (Chauvel et al., 1993). Petrology and geochemistry of Belingwe komatiites were reported by many previous workers, but those of the voluminous basaltic flows in the Zeederbergs Formation which are overlying thin komatiitic layers are not well accomplished. Studies of basaltic rocks would give important constraints on tectonic setting and petrogenesis of Archean greenstone belts. We have also focused on komatiitic basalt and basalt in Belingwe greenstone belt.

The detail microscopic observations have been done and least altered rock samples were selected. Major and trace element compositions and isotopic ratios of Nd were determined for whole rocks, residues (rock powders which are leached with 6M HCl at 80 degree Celsius for 12 hours) and clinopyroxene relicts of least altered komatiite, komatiitic basalt and basalt, and Pb isotopic ratios were determined for whole rocks.

2.7 Ga Belingwe volcanic rocks were divided into four types (komatiite, komatiitic basalt, depleted basalt and enriched basalt) by the occurrence and texture of the rocks and concentration of trace element of whole rocks. komatiites are slightly depleted ([La/Sm]N: 0.6 to 0.7) which are identical with previously published data, while that of komatiitic basalts are enriched ([La/Sm]N: 1.5). Basalts in Zeederbergs Fm. have both depleted ([La/Sm]N: 0.8) and enriched ([La/Sm]N: 1.2 to 1.6) REE patterns. Trace element compositions of clinopyroxenes in komatiite, ([La/Sm]N: ~0.1) komatiitic basalt ([La/Sm]N: ~0.4), and enriched ([La/Sm]N: ~0.3) and depleted ([La/Sm]N: ~0.1) basalt are equilibrium with those of whole rocks.

Pb-Pb ages of komatiitic basalt and enriched basalt are  $2649 \pm 89$  Ma and  $2654 \pm 24$  Ma, respectively. The obtained ages are identical to that of Chauvel et al., 1993 ( $2692 \pm 9$  Ma) within errors, but we suggest the age for Ngezi Group is 2650 Ma, because volcanics of two different types indicate almost the same age with relatively small errors. Apparent  $\mu$  values calculated with 2650 Ma are 7.9 to 8.2 for komatiite, 8.4 for komatiitic basalt, 7.7 to 8.2 for depleted basalt and 9.0 for enriched basalt.

Sm - Nd isochron for whole rocks of all rock types gives an age of  $2887 \pm 340$  Ma. Whereas, Sm - Nd isochron for clinopyroxene and residue of all rock types gives an age of  $2673 \pm 310$  Ma, which is quite close to the Pb - Pb age. However, the age error of Sm - Nd isochron is larger than that of Pb - Pb isochron. This may be caused by variety of initial  $^{143}\text{Nd}/^{144}\text{Nd}$ . The epsilon Nd at the

time of 2650 Ma have considerable variations for komatiites (-0.7 to 7.3) and depleted basalts (-1.0 to 12.8) and many of them are positive (depleted), whereas, the epsilon Nd values are negative for basaltic komatiites (-1.3 to -2.7) and enriched basalts (-3.3 to -2.3).

There are correlations among rock types and isotopic ratios of Nd and Pb. Samples with low (La/Sm)<sub>N</sub> values have high epsilon Nd and low mu values (i.e. komatiite and depleted basalt), whereas, samples with high (La/Sm)<sub>N</sub> values have low epsilon Nd and high mu values (i.e. komatiitic basalt and enriched basalt). These correlations can be generated by ~10 % contamination of the older continental crust.

Indisputable evidence for rift-related basin of Belingwe greenstone belt were also provided in this study. <100 micron garnet xenocrysts (Grs<sub>20</sub>Pyp<sub>35</sub>Alm<sub>45</sub>) were found in komatiite. Major element content and REE pattern [(Yb/Sm)<sub>N</sub> ~ 4] of the garnet xenocrysts suggest that they are garnet granulite origin. ~300 micron pyroxene xenocrysts (cpx: Wo<sub>45</sub>En<sub>51</sub>Fs<sub>4</sub>, opx: Wo<sub>1</sub>En<sub>90</sub>Fs<sub>9</sub>) were found in komatiitic basalt. Highly depleted in LREE [(La/Sm)<sub>N</sub> of cpx: 0.03, opx: 0.007] and major element characters of cpx [Na<sub>2</sub>O = 1.3 wt% and Al(6)/Al(4) = 1.8] extremely resemble to those from subcontinental mantle (tectosphere).

The remarkable variations of epsilon Nd for komatiites and depleted basalts can not be explained by contamination of older crustal rock. A possibility for these remarkable variations is that the source mantle plumes of komatiite and depleted basalt are already the heterogeneous at ca. 2.7 Ga. If the source mantle was homogeneous, there is another possibility. As the volcanic unit of Ngezi Group have extruded through thick tectosphere which is highly depleted, komatiite and depleted basalt may have assimilated with the depleted peridotite to some extent, and considerable variations of isotopic compositions in them were produced.

#### Acknowledgements

We are indebted to K. Kobayashi, C. Sakaguchi, T. Kuritani, R. Takana and all of the other PML members for their analytical support and useful discussions. We would also like to thank K. Hirose and T. Komiya for constructive discussions.

#### References

- Bickle, M.J., Nisbet, E.G., & Martin, A., 1994, Archean greenstone belts are not oceanic crust.: *Journal of Geology*, v. **102**, p. 121-138.
- Chauvel, C., Dupre, B., & Arndt, N.T., 1993, Pb and Nd isotopic correlation in Belingwe komatiites and basalts, in Bickle, M.J., & Nisbet, E.G., eds., *Rock units and stratigraphy of the Belingwe Greenstone Belt: the complexity of the tectonic setting*, Geol. Soc. Zimbabwe Spec. Pub. 2, Rotterdam, Balkema, p. 167-174.
- Kusky, T.M., & Kidd, W.S.F., 1992, Remnants of an Archean oceanic plateau, Belingwe greenstone belt, Zimbabwe: *Geology*, v. **20**, p. 43-46.
- McDonough, W.F., & Ireland, T.R., 1993, Intraplate origin of komatiites inferred from trace elements in glass inclusions: *Nature*, v. **365**, p. 432-434.

## 2.16 Formation and suppression of $\text{AlF}_3$ during HF digestion of rock samples in Teflon bomb for precise trace element analyses by ICP-MS and ID-TIMS

Hiroyuki Takei, Tetsuya Yokoyama, Akio Makishima and Eizo Nakamura

Pheasant Memorial Laboratory (PML) for Geochemistry and Cosmochemistry Institute for Study of the Earth's Interior, Okayama University at Misasa

The abundances of trace elements such as Rb, Sr, Y, Cs, Ba, REE, Pb, Th, and U in silicate rock samples provide us important information in regarding with crust and mantle evolution. Silicate rock samples are commonly decomposed using HF in the determination of trace elements by ICP-MS and TIMS. When samples contain acid resistant minerals such as zircon, the decomposition should be carried out under high temperature ( $> 200^\circ\text{C}$ ) condition in a Teflon bomb. However, we found the formation of aluminum fluoride,  $\text{AlF}_3$ , during HF digestion of felsic rock samples, when we used the Teflon bomb at high temperature and pressure. The  $\text{AlF}_3$  incorporates trace elements, and can not be decomposed by conventional methods such as evaporation with  $\text{HClO}_4$ . The production of this  $\text{AlF}_3$  results in lower yields and poor accuracy in analyses of these trace elements by ICP-MS. The formation of  $\text{AlF}_3$  is controlled by the chemical composition of the rock samples, in particular,  $\text{AlF}_3$  does not form during decomposition of mafic samples with relatively high  $(\text{Mg}+\text{Ca})/\text{Al}$  ratios. We have developed a new method to suppress the  $\text{AlF}_3$  formation, in which excess Mg is added to the sample prior to acid digestion in the bomb. This new method makes it possible to accurately determine the trace element compositions of higher-Al rock samples with lower concentrations of Mg and Ca (e.g. rhyolite and granite). In the trace element analyses by TIMS with isotope dilution techniques (ID-TIMS),  $\text{AlF}_3$  formation hinders the achievement of isotope equilibrium, resulting in erroneous results. However, the Mg-addition method removed this problem by suppression of  $\text{AlF}_3$  formation.

## 2.17 Origin of the ore-forming fluids in the Hishikari gold deposits.

Hiroyuki Takei and Eizo Nakamura

Pheasant Memorial Laboratory (PML) for Geochemistry and Cosmochemistry Institute for Study of the Earth's Interior, Okayama University at Misasa.

The Hishikari gold deposits, which are a typical low-sulfidation adularia - silica epithermal vein type deposit, are known for their extraordinarily high-grade ore and high production of gold. In this study, the origin of the ore-forming fluids responsible for the Hishikari gold deposits was investigated using the trace element concentrations and Sr, Nd and Pb isotopic compositions of the ore samples. The ore deposits occur in sedimentary rocks of the Shimanto Supergroup and/or in the unconformity overlying Quaternary volcanic rocks of Hishikari lower andesites. We collected samples from the vicinity of the Hishikari ore deposits and from the Daisen No. 5 vein in the Honko deposit, which occurs in both the Shimanto Supergroup and the Hishikari lower andesites, and the Yusen No. 4 vein in the Yamada deposit, which occurs in the Hishikari lower andesites.

The Sr and Pb isotopic compositions of the volcanic rocks and sedimentary rocks of the Shimanto Supergroup are distinct, and all of the vein samples plot in a range intermediate to compositions of those volcanic and sedimentary rocks (Fig. 1 and 2). The Sr and Pb isotopic compositions of both sets of vein samples are considered the result of two-component mixing of the Hishikari lower andesites and Shimanto Supergroup end members, although Yusen vein (Yamada deposit) occurs in the Hishikari lower andesites. Therefore, the ore-forming fluids of the Hishikari gold deposits are considered to have been hydrothermal solutions which interacted with both the Hishikari lower andesites and the sedimentary rocks of the Shimanto Supergroup independent of the location of the ore deposits.

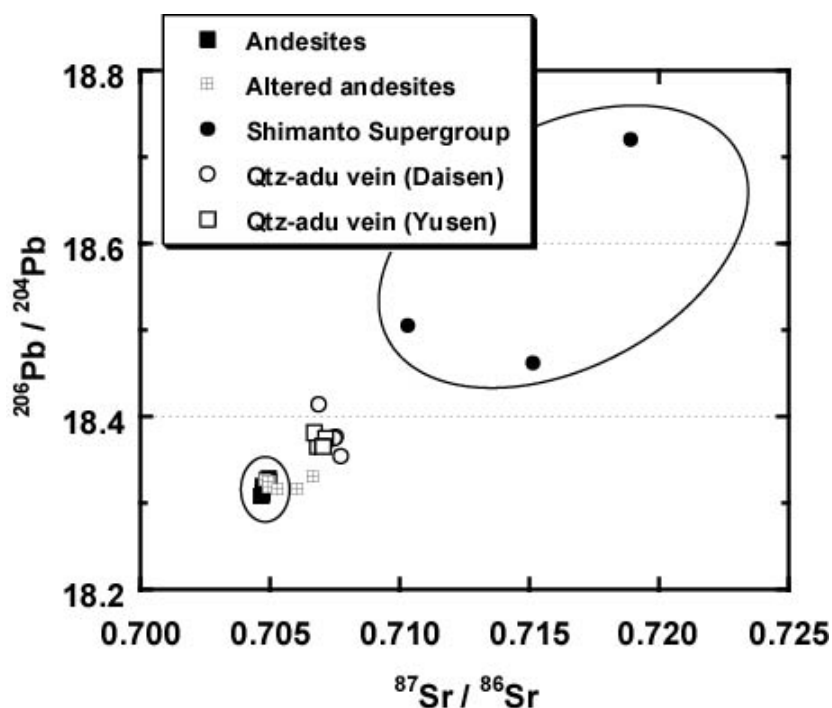


Fig. 1  $^{87}\text{Sr}/^{86}\text{Sr}$  versus  $^{206}\text{Pb}/^{204}\text{Pb}$  diagram.

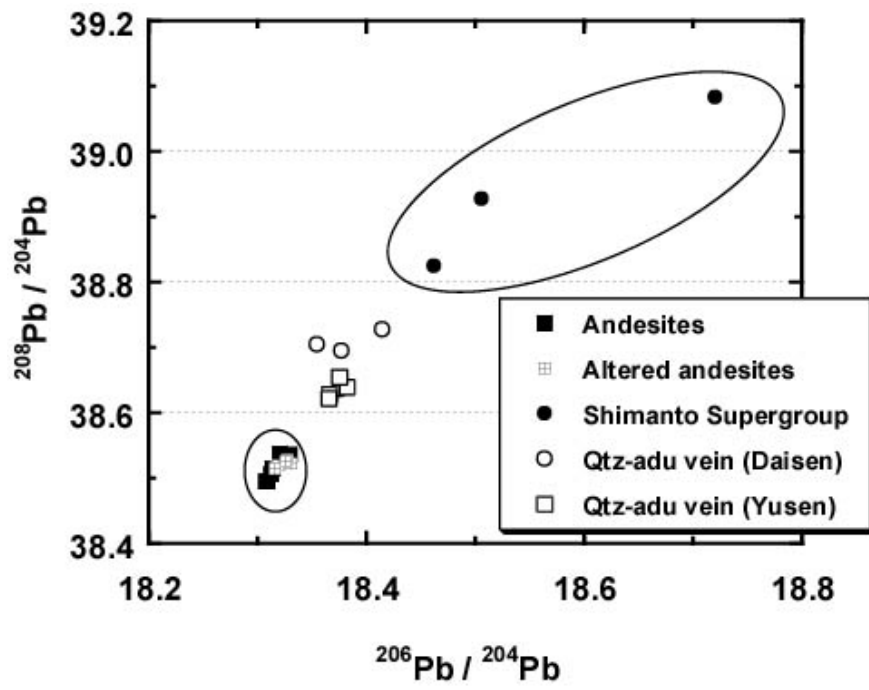


Fig. 2  $^{206}\text{Pb}/^{204}\text{Pb}$  versus  $^{208}\text{Pb}/^{204}\text{Pb}$  diagram.

## 2.18 Evaluation of coprecipitation of incompatible trace elements with fluoride during silicate rock dissolution by acid digestion

Tetsuya Yokoyama, Akio Makishima, Eizo Nakamura

PML, Institute for Study of the Earth's Interior, Okayama Univ. at Misasa

Determination of abundances of incompatible trace elements such as Rb, Sr, REE, Pb, Th and U in mafic or ultramafic rock samples (e.g. MORB, peridotites) and isotope ratios of Sr, Nd and Pb gives us direct information about chemical evolution of the mantle. Since these samples usually contain significantly lower amounts of incompatible trace elements compared to felsic rock types, decomposition of larger sample sizes (usually >100mg) is required for their precise determination. Numerous rock dissolution procedures by acid digestion have been developed and have been applied to mafic and ultramafic samples in our laboratory. However, insoluble fluorides are usually produced with sample sizes exceeding 100 mg, making it difficult to obtain homogeneous sample solutions for ICP-MS analysis and column chemistry in hydrochloric or nitric acid media.

Classical studies by Langmyhr and Kringstad (1966) and Croudace (1980) revealed that major elements (Na, Mg, Ca, Fe and Al) were incorporated into insoluble fluoride compounds such as ralsstonite ( $\text{Na}_{0.88}\text{Mg}_{0.88}\text{Al}_{1.12}(\text{F},\text{OH})_6\cdot\text{H}_2\text{O}$ ) during sample decomposition leading to erroneous results during quantitative analysis. Boer et al. (1993) analyzed Sm and Nd in rock solutions which contain such insoluble fluorides and found that the abundances were 20~50% lower and Sm/Nd ratios were systematically higher than accepted reference values. They concluded that such a difference reflected precipitation of the insoluble fluoride compounds remaining in the solution and taking up differentially Sm and Nd into their crystal structure. Such selective losses should occur to all trace elements because their affinity to fluoride compounds must be controlled by their individual character such as ionic radius and valency. Thus, analysis of trace elements in the presence of insoluble fluorides is likely to yield erroneous results and misleading conclusions especially in regard to discussion of Rb-Sr, La-Ce, Sm-Nd, U-Th-Pb systematics, or REE patterns.

In this study, we have estimated quantitatively the coprecipitation of trace elements into such fluorides, and suggest an effective method of digestion that can suppress completely fluoride precipitation. Conventional acid digestion (Methods A and B; Fig. 1) of three samples of mafic and ultramafic silicate rocks resulted in the precipitation of sticky material and very poor yields of certain trace element in the resultant solution (Fig. 2-a and b). XRD analysis indicated that the precipitates were composed of fluorides such as  $\text{CaAlF}_5$ ,  $\text{CaMg}_2\text{Al}_2\text{F}_{12}$ ,  $\text{Na}_{0.88}\text{Mg}_{0.88}\text{Al}_{1.12}(\text{F},\text{OH})_6\cdot\text{H}_2\text{O}$  and  $\text{MgF}_2$ , the formation of which depended on the major element composition of the rock sample. Coprecipitation of trace elements appeared to be strongly controlled by both ionic radius and valency of the elements as well as the species of the host fluoride precipitate, resulting in selective losses of the elements into these fluorides.

On the other hand, almost 100% of the trace elements were recovered (Fig. 2-c) using larger amounts of  $\text{HClO}_4$  than is conventionally used and evaporating the sample to dryness in a step-wise fashion (Method C; Fig. 1). Using this method, white precipitates were formed as oxides of high field strength elements after decomposition of the sample. Coprecipitation of trace elements of interest in this study with the oxides is negligible except for Th for which 0.5~3.2% by weight was coprecipitated probably as the insoluble oxide. As our method also results in negligible blank values, it can be used for both the accurate determination of trace element using ICP-MS as well as isotope analysis using TIMS.

### References

- Boer, R.H., Beukes, G.J., Meyer, F.M., Smith, C.B., 1993. Fluoride precipitates in silicate wet-chemistry: implications on REE fractionation. *Chem. Geol.* 104, 93-98.
- Croudace, I.W., 1980. A possible error source in silicate wet-chemistry caused by insoluble fluorides.

Chem. Geol. 31, 153-155.

Langmyhr, F.J., Kringstad, K., 1966. An investigation of the composition of the precipitates formed by the decomposition of silicate rocks in 38-40% hydrofluoric acid. Anal. Chim. Acta. 35, 131-135.

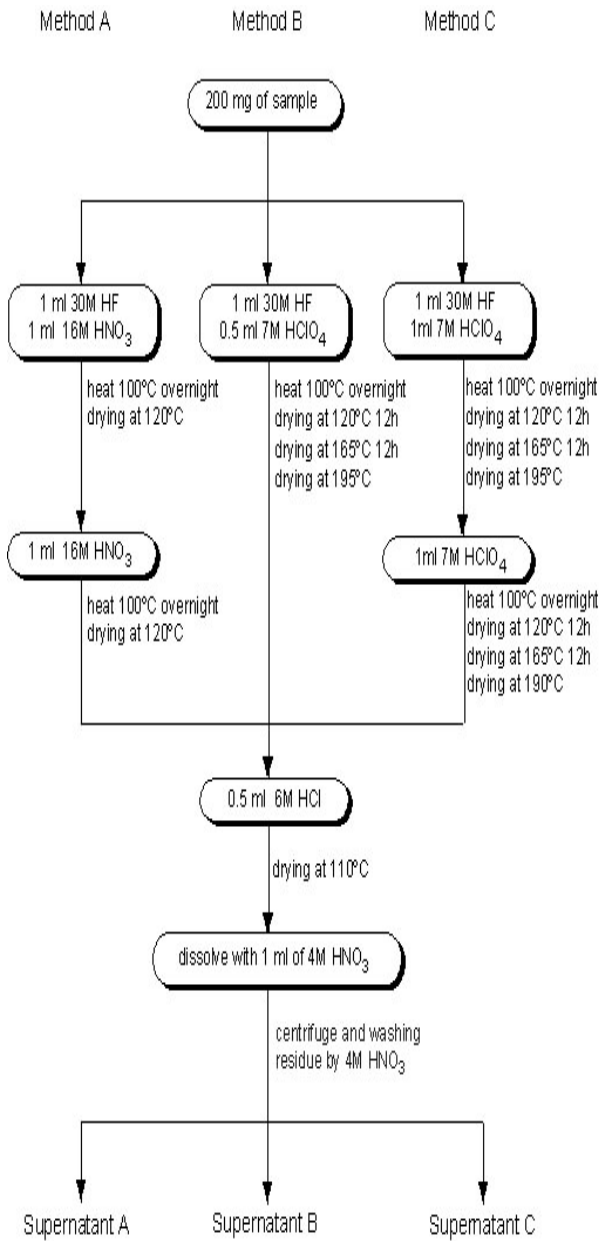


Fig. 1 Flow chart of three different sample decompositions using mixed acids

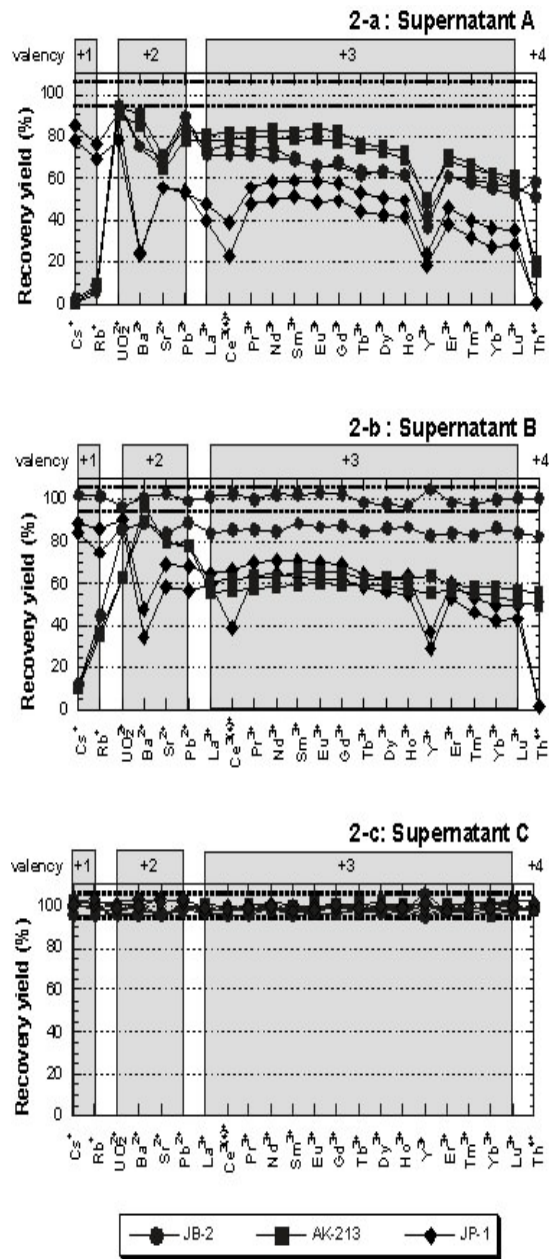


Fig. 2 Recovery yields of trace elements in Supernatants A, B and C

## 2.19 Separation of thorium and uranium from silicate rock samples using two commercial extraction chromatographic resins

Tetsuya Yokoyama, Akio Makishima, Eizo Nakamura

PML, Institute for Study of the Earth's Interior, Okayama Univ. at Misasa

U-Th disequilibrium is widely recognized as a powerful tool for the understanding of numerous geological phenomena in igneous petrology and chronology, marine geochemistry, hydrology of the earth's surface, archaeology and palaeoclimatology. Recent developments in analytical techniques have resulted in the use of TIMS as a substitute for the alpha counting method of Th and U isotope measurements. The advantages of TIMS over alpha counting includes its higher precision, smaller amount of sample, and shorter analytical procedure. In order to achieve accurate analyses, good isolation of Th and U is indispensable because ionization efficiencies of Th and U in TIMS are so low that interference by coexisting elements is a serious problem. For this purpose, ion exchange column method is generally adopted by many geochemists, and most recent separation techniques, which utilize the anion exchange resin AG1X8, are basically derived from Chen et al. (1986). However, Adriaens et al. (1992) reported that not all Fe and Pb can be separated from U using this method. Since U forms stable chloride complexes which have high distribution coefficients ( $K_d \sim 10^3$  at 9M HCl condition), purification of U is usually done in HCl media. However,  $\text{Fe}^{3+}$ ,  $\text{Co}^{2+}$ ,  $\text{Cu}^{2+}$  and  $\text{Zn}^{2+}$  also form chloride complexes similar to those of U and are adsorbed on the resin simultaneously, making it difficult to efficiently separate U in silicate samples.

Recently, two extraction chromatographic resins called U/TEVA·spec and TEVA·spec have been developed and made commercially available by Eichrom Industries Inc. Compared to AG1X8, these resins have higher selectivity towards retaining tetravalent actinides and U at lower concentrations of  $\text{HNO}_3$  or HCl. In particular, use of the U/TEVA resin avoids the problem of interference from coexisting anions because this resin is of chelate exchange type. However, only a few geological applications have been undertaken using these resins.

In this study, we present a new technique for the efficient separation of Th and U using a combination of U/TEVA and TEVA resins. Our method overcomes all the problems associated with pre-existing separation routines using AG1X8 or U/TEVA resins. In the first column procedure with U/TEVA·spec resin (Fig. 1), almost all elements except Th and U were eluted by 4M  $\text{HNO}_3$ . Th was then separated using 5M HCl, and U was finally isolated by successive addition of 0.1M  $\text{HNO}_3$ . Significant amount of Zr still remained in the Th fraction which was then further purified in the second column stage using TEVA·spec resin. In the second procedure (Fig. 2), Zr was eluted first using 2M  $\text{HNO}_3$ , then Th was collected by 0.1M  $\text{HNO}_3$ . Both the Th and U fractions obtained by these procedures were sufficiently pure for thermal ionization mass spectrometric (TIMS) analysis. Recovery yields of Th and U exceeded 90% and total blanks were <19 pg for Th and <10 pg for U.

Our method has advantages over previous methods in terms of matrix effects, tailing problems and degree of isolation. Since Th and U are effectively separated without suffering any matrix interference from coexisting cations and anions, this technique can be used not only for the analysis of igneous rock samples but also for the analysis of soils, marine sediments, carbonates, phosphates and sea, ground and surface water.

### References

- Adriaens, A.G., Fassett, J.D., Kelly, W.R., Simons, D.S. and Adams, F.C., 1992. Determination of uranium and thorium concentrations in soils: comparison of isotope dilution - secondary ion mass spectrometry and isotope dilution - thermal ionization mass spectrometry. *Anal. Chem.*, 64: 2945-2950.
- Chen, J.H., Edwards, R.L. and Wasserburg, G.J., 1986.  $^{238}\text{U}$ ,  $^{234}\text{U}$  and  $^{232}\text{Th}$  in seawater. *Earth Planet. Sci. Lett.*, 80: 241-251.

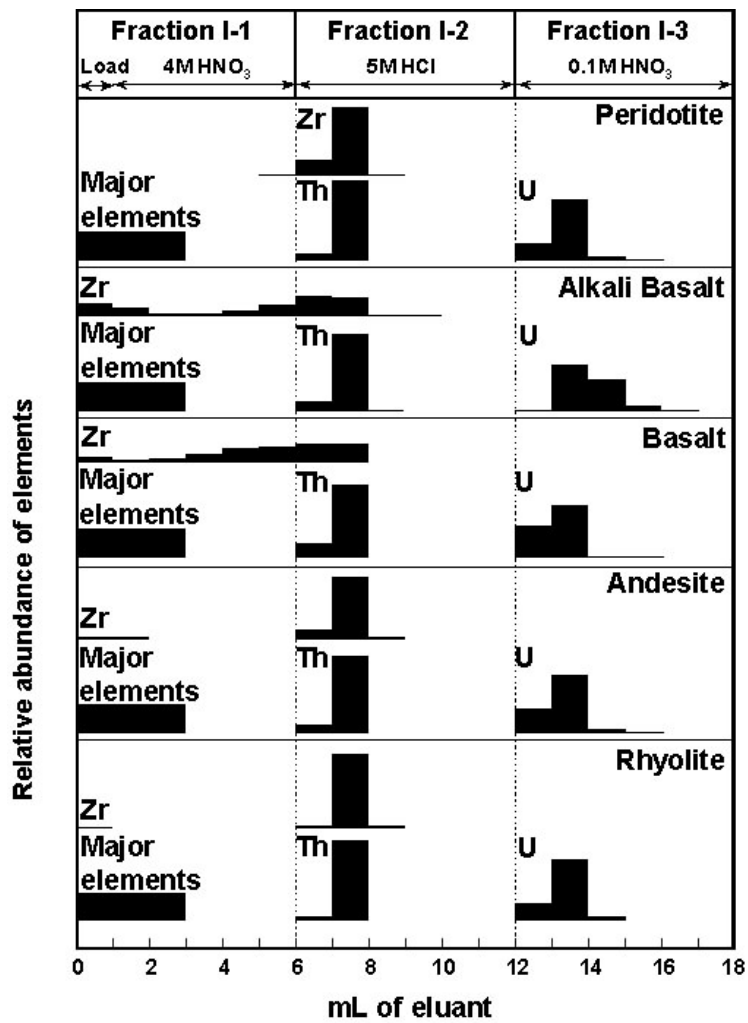


Fig. 1 Elution profile of Zr, Th, U and major elements of the first column

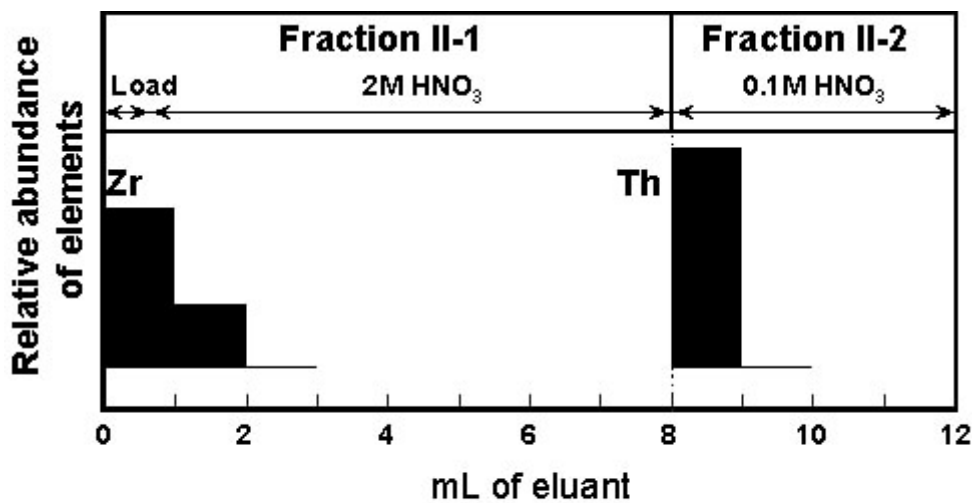


Fig. 2 Elution profiles of Zr and Th on the second column procedure

## 2.20 Precise analysis of $^{234}\text{U}/^{238}\text{U}$ ratio using $\text{UO}_2^+$ ion with TIMS

Tetsuya Yokoyama, Akio Makishima, Eizo Nakamura

PML, Institute for Study of the Earth's Interior, Okayama Univ. at Misasa

Uranium and thorium series disequilibrium is a powerful geochemical tracer especially for determining various geological processes that occur on the scales ranging from  $\sim 10^6$  years to a few days, by measuring the activity of short lived radioactive nuclides (e.g.  $^{234}\text{U}$ ,  $^{230}\text{Th}$ ,  $^{226}\text{Ra}$ ,  $^{228}\text{Th}$ , and  $^{234}\text{Th}$ ). The  $^{234}\text{U}$ - $^{238}\text{U}$  dating method has been applied to samples formed in marine environments, such as corals, ferromanganese nodules, and marine sediments because sea water is in  $^{234}\text{U}$ - $^{238}\text{U}$  disequilibrium ( $^{234}\text{U}/^{238}\text{U}$  activity ratio =  $1.144 \pm 0.002$ , Chen et al., 1986). If the system remains closed after the achievement of  $^{234}\text{U}$ - $^{238}\text{U}$  disequilibrium,  $^{234}\text{U}$ - $^{238}\text{U}$  age can be determined by the following equation:

$$\left(\frac{^{234}\text{U}}{^{238}\text{U}}\right)_{\text{present}} - 1 = \left[\left(\frac{^{234}\text{U}}{^{238}\text{U}}\right)_{\text{initial}} - 1\right] \exp(-\lambda_{234} \cdot t) \quad (\text{Eq. 1})$$

where  $\lambda_{234}$  is the decay constant of  $^{234}\text{U}$ ,  $t$  is the time from the closure of the system to present, and  $(^{234}\text{U}/^{238}\text{U})$  represents an activity ratio. It is clear from this equation that precise determination of  $^{234}\text{U}/^{238}\text{U}$  ratio in the sample is required in order to carry out precise dating. By the classical method of using  $\alpha$  counting, typical analytical uncertainties in the  $^{234}\text{U}/^{238}\text{U}$  ratio are 2~3%, resulting in a few % uncertainty in age dating thereby limiting the application for processes ranging from 0.1 ka to 100 ka.

In this study, we have developed a new, highly precise method for U isotopic analysis using a thermal ionization mass spectrometry (TIMS) by measuring  $\text{UO}_2^+$  ions emitted from a very small amount (100 ng  $\sim$  10 ng) of U. A new ionization activator, a silicic acid - diluted phosphoric acid solution, was found to be effective not only for producing a strong and stable  $\text{UO}_2^+$  ion beam, but also for keeping the mass fractionation during measurement small and constant. U isotope analysis was carried out by a "dynamic multi collection" method using three Faraday cup collectors and a secondary electron multiplier in ion counting mode with RPQ (RPQ-SEM). For precise isotope analysis, baselines of the Faraday cups and a conversion factor between Faraday cups and the RPQ-SEM were precisely determined simultaneously with U isotope collection. Analytical precision and reproducibility of  $^{234}\text{U}/^{238}\text{U}$  ratio ranged from 0.10 to 0.38% ( $2\sigma_{\text{mean}}$ ) and 0.13 to 0.31% ( $2\sigma$ ), respectively, for 100 ng to 10 ng of U extracted from a natural rhyolitic obsidian (JR-2; Fig. 1). Accuracy of our analysis was confirmed by the repeated analyses of the international U standard, NBL-145 (consistent with NBL-112A, which is formerly NIST SRM960), and we obtained no difference in the  $^{234}\text{U}/^{238}\text{U}$  ratio between previous results and this study (Table 1). The precision and reproducibility were improved compared with previous studies, and thus our method is especially useful for samples with very low abundance of U.

### References

- Chen, J.H., Edwards, R.L., Wasserburg, G.J., 1986.  $^{238}\text{U}$ ,  $^{234}\text{U}$  and  $^{232}\text{Th}$  in seawater. *Earth Planet. Sci. Lett.* 80, 241-251.
- Cheng, H., Edwards, R.L., Hoff, J., Gallup, C.D., Richards, D.A., Asmerom, Y., 2000. The half-lives of uranium-234 and thorium-230. *Chem. Geol.* 169, 17-33.
- Luo, X., Rehkamper, M., Lee, D.-C., Halliday, A.N., 1997. High precision  $^{230}\text{Th}/^{232}\text{Th}$  and  $^{234}\text{U}/^{238}\text{U}$  measurement using energy-filtered ICP magnetic sector multiple collector mass spectrometry. *Int. J. Mass Spectrom. Ion Processes* 171, 105-117.
- Stirling, C.H., Esat, T.M., McCulloch, M.T., Lambeck, K., 1995. High-precision U-series dating of corals from Western Australia and implications for the timing and duration of the Last Interglacial. *Earth Planet. Sci. Lett.* 135, 115-130.

Table 1. Comparison of analytical reproducibility of  $^{234}\text{U}/^{238}\text{U}$  measurement in the previous studies

Reference	Sample	$^{234}\text{U}/^{238}\text{U}$ ( $\times 10^{-5}$ )	Sample size	Replicates	Reproducibility ( $2\sigma$ %)	Method
Chen et al.(1986)	NIST SRM960	5.267	30 ng	6	0.5	TIMS
Stirling et al. (1995)	NIST SRM960	5.288	1000 ng	5	0.2	TIMS
Luo et al. (1997)	NIST SRM960	5.286	450 ng	8	0.12	ICP-MS
		5.284	200-600 ng	14	0.35	TIMS
Cheng et al. (2000)	NBL-112A	5.286	500-3000 ng	21	0.22	TIMS
This Study	NBL-145	5.284	50 ng	8	0.21	TIMS

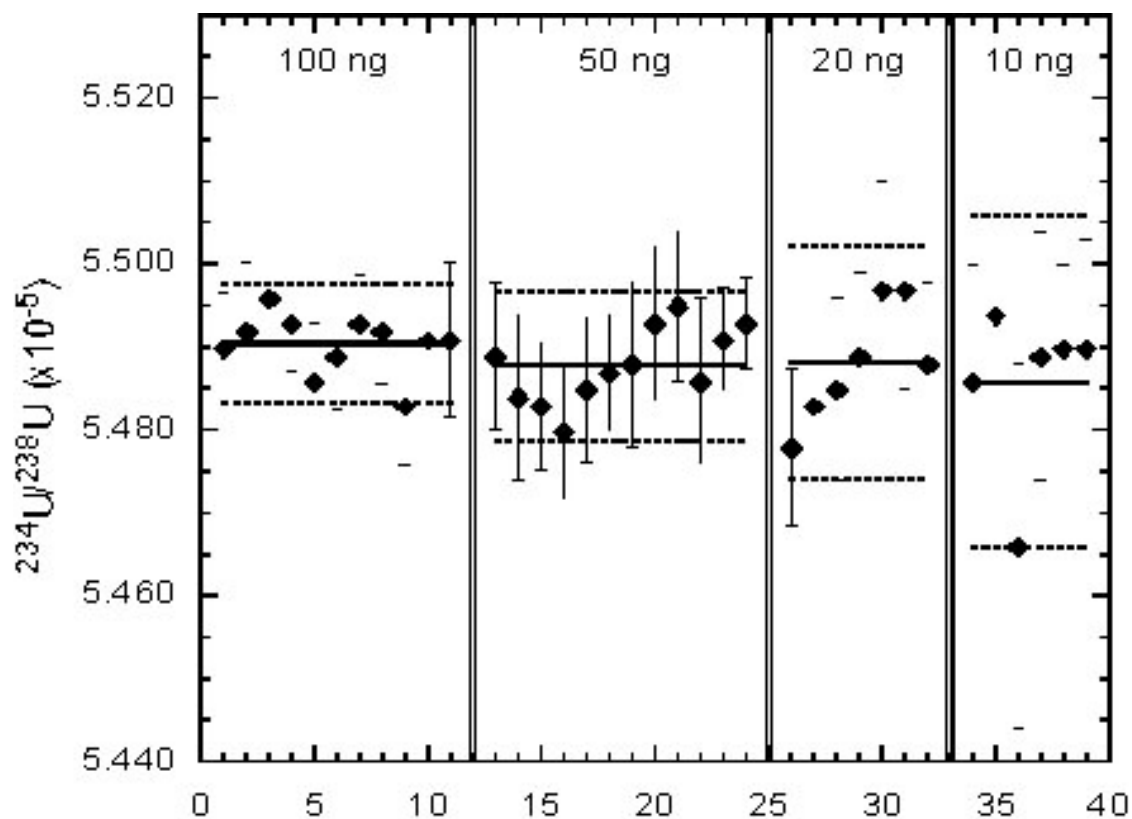


Fig. 1.  $^{234}\text{U}/^{238}\text{U}$  ratios of JR-2 obtained from different amounts of U with analytical precision ( $2\sigma_{\text{mean}}$ ). Bold lines indicate the average of different sample sizes, and dotted lines show reproducibility ( $2\sigma$ ).

## 2.21 Precise determination of ferrous iron in silicate rocks

Tetsuya Yokoyama, Eizo Nakamura

PML, Institute for Study of the Earth's Interior, Okayama Univ. at Misasa

Determination of ferrous iron ( $\text{Fe}^{2+}$ ) and  $\text{Fe}^{2+}/\text{Fe}^{3+}$  ratio in silicate rocks is important in geological, geochemical and petrological studies for evaluation of weathering, determination of oxygen fugacity in magma, and understanding chemical equilibrium between minerals and silicate melt. Recent analytical progress using XRF methods enables highly precise determination of total iron in silicate rock samples with analytical error less than 0.5 % ( $1\sigma$ ) (relative standard deviation; e.g., Takei and Nakamura, in prep.). Determination of  $\text{Fe}^{2+}$  concentrations with the same precision as that for XRF analyses of total iron would make it possible to more precisely address the above petrological issues.

Table 1.  $\text{FeO}$  (wt. %) of 15 GSJ standard rocks and their recommended or preferable (asterisked) values.

Sample	$\text{FeO}$	$1\sigma$	$1\sigma$ (%)		Recomm.	Deff. %
JB1-b	$5.15 \pm 0.01$	0.23	(n = 5)		5.16 <sup>a</sup>	-0.2
JB-2	$10.04 \pm 0.03$	0.34	(n = 5)		9.98	0.6
JB-3	$8.00 \pm 0.03$	0.35	(n = 14)		7.85	2.0
JA-2	$3.75 \pm 0.01$	0.22	(n = 5)		3.69	1.7
JA-3	$4.99 \pm 0.02$	0.49	(n = 5)		4.83	3.4
JR-1	$0.510 \pm 0$	0.80	(n = 4)		0.49	4.0
JR-2	$0.448 \pm 0.004$	0.90	(n = 5)		0.44	1.7
JR-3	$1.99 \pm 0.01$	0.38	(n = 4)		1.86	7.0
JP-1	$6.81^b \pm 0.06$	0.90	(n = 4)		5.99	13.6
JGb-1	$10.89 \pm 0.03$	0.30	(n = 4)		9.43	15.5
JGb-2	$5.54 \pm 0.02$	0.43	(n = 4)		5.41	2.4
JG1-a	$1.40 \pm 0.01$	0.92	(n = 4)		1.36	2.9
JG-2	$0.655 \pm 0.01$	0.79	(n = 6)		0.57	14.9
JG-3	$2.016 \pm 0.002$	0.09	(n = 4)		1.83	10.2
JH-1	$8.20 \pm 0.01$	0.09	(n = 4)		8.09 <sup>*</sup>	1.4

<sup>a</sup>The contribution of residual spinel is not included. See the text.

<sup>b</sup>After Terashima et al. (1998). Not recommended nor preferable value.

Although high precision analyses for  $\text{Fe}^{2+}$  is relatively easily obtained, the accuracy of these analyses is more questionable.  $\text{Fe}^{2+}$  can easily be oxidized during analytical procedures, resulting in erroneously low values. In the classical method of Pratt (Pratt, 1894), which is commonly used in many laboratories, the sample is decomposed by mixtures of HF and  $\text{H}_2\text{SO}_4$  in a covered platinum crucible that excludes atmospheric oxygen. This relatively difficult technique often yields low concentrations owing to the oxidation of  $\text{Fe}^{2+}$ . One of the most effective ways to achieve accurate determinations of  $\text{Fe}^{2+}$  is Wilson's method (Wilson, 1955) or Peters' method (Peters, 1968), in which excess  $\text{V}^{5+}$  is added to the sample before decomposition. This method is based on the following reversible reaction:



This reaction proceeds to the right side in the condition of strong acidity, and the amount of the  $\text{V}^{4+}$  reduced from  $\text{V}^{5+}$  is then the same as the amount of  $\text{Fe}^{2+}$  in the sample. Because  $\text{V}^{4+}$  is extremely

resistant to oxidation and does not back-react to  $V^{5+}$  during the analytical procedure,  $Fe^{2+}$  concentration in the sample can be determined by measuring the unreacted  $V^{5+}$  by adding excess  $Fe^{2+}$  after sample decomposition and then titrating the unreacted  $Fe^{2+}$  with  $Cr^{6+}$ .

By reevaluating the Wilson's method, we have developed a highly precise method for the determination of ferrous iron ( $Fe^{2+}$ ) in silicate rocks. With our method, which involves conditioning the sample solution with 5M  $H_2SO_4$  in a relatively small beaker (7 mL), the oxidation of  $Fe^{2+}$  or  $V^{4+}$  that leads to erroneous results can be completely avoided, even in 100-hour sample decompositions at 100°C. We have measured the concentration of FeO in fifteen standard silicate rock powders provided by the Geological Survey of Japan (GSJ; Table 1). Analytical reproducibility was better than 0.5 % ( $1\sigma$ ) for all but those samples that had small amounts of  $Fe^{2+}$  (<1.5 wt. % of FeO). Fourteen of these samples gave FeO contents significantly higher than the GSJ reference values. This likely indicates that the GSJ reference values, obtained by compiling previously published data, contain a large number of poor-quality data obtained by methods with lower recovery of  $Fe^{2+}$  caused by oxidation and/or insufficient sample decomposition during analyses. To achieve accurate determinations of  $Fe^{2+}$  in our method, several factors besides the oxidation must be considered, including: 1) long-term variations in the concentration of  $Fe^{2+}$  solution must be corrected; 2) excess use of the indicator must be avoided; and 3) the formation of inert  $FeF^+$  complex must be avoided during titration when using boric acid as a masking agent.

#### References

- Peters, A. (1968) Ein neues Verfahren zur Bestimmung von Eisen(II) oxid in Mineralen und Gesteinen. *Neues Jahrb. Mineral., Monatsh.* 3/4, 119-125.
- Pratt J. P. (1894) On the determination of ferrous iron in silicates. *Am. J. Sci.* 48, 149-151.
- Terashima S., Taniguchi M., Mikoshiba M., and Imai N. (1998) Preparation of two new GSJ geochemical reference materials: JB-1b and coal fly ash JCFA-1. *Geostand. Newslett.* 22, 113-117.
- Wilson A. D. (1955) Determination of ferrous iron in rocks and minerals. *Bull. Geol. Surv. G. B.* 9, 56-58.

## 2.22 Mantle metasomatism and rapid melt ascent beneath Miyakejima volcano: evidence from $^{238}\text{U}$ - $^{230}\text{Th}$ disequilibrium

Tetsuya Yokoyama, Katsura Kobayashi, Takeshi Kuritani, Eizo Nakamura

PML, Institute for Study of the Earth's Interior, Okayama Univ. at Misasa

$^{238}\text{U}$ - $^{230}\text{Th}$  disequilibrium of island arc volcanic rocks is a useful geochemical tracer to understand the time scales of fluid transfer, generation of melt, and its ascent in a subduction zone. Here we present  $^{238}\text{U}$ - $^{230}\text{Th}$  systematics in historic and pre-historic lavas of Miyakejima volcano, which belongs to Izu-Mariana arc located 200 km south of Tokyo. We also present major and trace element compositions as well as their Sr and Nd isotopes to estimate the time scale of magmatic processes beneath the island arc.

Volcanic rocks of Miyakejima consist of tholeiitic basalts and basaltic andesites ( $\text{SiO}_2 = 48.3\sim 62.1\%$ ) which have erupted from earlier than 7000 B.P. to 1983 A.D. Based on major and trace element compositions in this study and tephrochronological work of Tsukui and Suzuki (1998), the volcanic history of Miyakejima can be divided into four stages (Stage 1: older than 7000 B.P.; Stage 2: 7000 B.P.~2500 B.P.; Stage 3: 2500 B.P.~1154 A.D.; Stage 4: 1469 A.D.~1983 A.D.). Strong enrichment of LILE compared to HFSE, and depleted isotope ratios of Sr and Nd are observed in all stages, implying metasomatism of MORB-type mantle by fluid related processes with little contribution from a sedimentary component as observed in other Izu-arc volcanoes (Ishikawa and Nakamura, 1994; Moriguti and Nakamura, 1998).

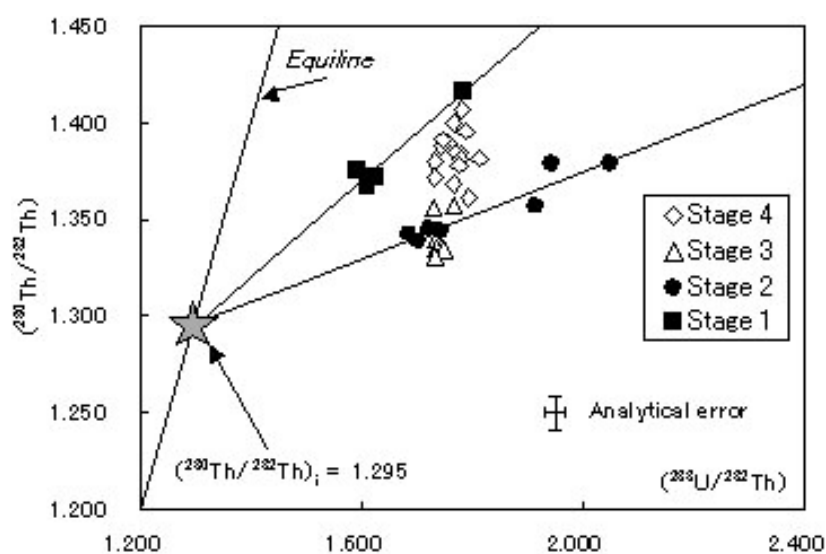


Fig. 1 U-Th diagram of Miyakejima volcano

A  $(^{230}\text{Th}/^{232}\text{Th})$  vs.  $(^{238}\text{U}/^{232}\text{Th})$  diagram (Fig. 1) shows  $^{238}\text{U}$ - $^{230}\text{Th}$  disequilibrium in eruptives from Miyakejima with large  $^{238}\text{U}$  excess ( $(^{238}\text{U}/^{230}\text{Th}) = 1.2\sim 1.4$ ), which is also obtained by the addition of fluid enriched in U relative to Th. In this diagram, samples can be distinguished into several different trends that correspond to each stage. Judging from the fact that all samples have almost constant Sr and Nd isotope ratios ( $^{87}\text{Sr}/^{86}\text{Sr} = 0.70343\sim 49$ ;  $^{143}\text{Nd}/^{144}\text{Nd} = 0.51307\sim 11$ ), they should also have had constant initial Th isotope ratio at the source region (mantle wedge) before the addition of fluid. Although the trends of Stage 1 and 2 samples can be regarded as whole-rock isochrones that have identical initial Th isotope ratio ( $(^{230}\text{Th}/^{232}\text{Th})_i = 1.295$ ), it is difficult to depict a single isochron for Stage 3 and 4 samples. Furthermore, most of the Stage 3 and 4 samples have longer

time of melt transfer (7 ~ 27 ky) than Stage 2 samples (5 ~ 11 ky), whereas Stage 2 samples erupted earlier than Stage 3 and 4 samples<sup>#1</sup>. The melt transfer time of Stage 3 and 4 samples increases as their Th contents increase, which means an increase in the degree of magma differentiation (Fig. 2). From these observations, the trend of Stages 3 and 4 in Fig. 1 is interpreted as a mixing trend between old, andesitic magma with higher Th and elevated ( $^{230}\text{Th}/^{232}\text{Th}$ ) ratio that was differentiated from Stage 1 magma, and newly injected basaltic magma with lower Th and lower ( $^{230}\text{Th}/^{232}\text{Th}$ ) ratio. This means that actual melt transfer time of Stages 3 and 4 is much shorter than apparent from the calculation above.

In other arcs, contradictions exist in the melt transfer times determined by  $^{238}\text{U}$ - $^{230}\text{Th}$  systematics (90 ky for Lesser Antilles, Turner et al. (1996); 30~50 ky for Tonga-Kermadec, Turner et al. (1997)) and  $^{230}\text{Th}$ - $^{226}\text{Ra}$  systematics (<8 ky for Lesser Antilles, Chabaux et al. (1999); ~1 ky for Tonga-Kermadec, Turner et al. (2000)). However, the minimum melt transfer time determined from our  $^{238}\text{U}$ - $^{230}\text{Th}$  systematics (5 ky) would support rapid melt transfer within several ky. In the subduction zone, therefore, channel flow in the mantle wedge is preferable for rapid melt transfer rather than conventional permeable flow. The time constraints of melt transfer determined are important for understanding physical and chemical processes in the generation of melt beneath island arcs.

#1: Here, the "melt transfer time" is the time since fluid release from the subducting slab until eruption, including residence time in the magma chamber. It is calculated by subtracting the time after eruption from  $^{230}\text{Th}$ -ingrowth time since ( $^{230}\text{Th}/^{232}\text{Th}$ ) = 1.295 to the present observed value.

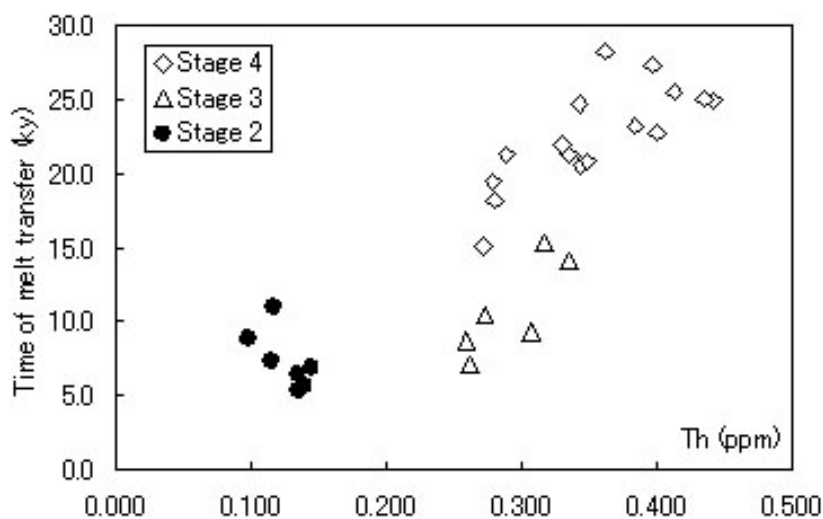


Fig. 2 Th concentration vs. melt transfer time

## References

- Chabaux F., Hemond C., Allegre C., 1999.  $^{238}\text{U}$ - $^{230}\text{Th}$ - $^{226}\text{Ra}$  disequilibria in the Lesser Antilles arc: implications for mantle metasomatism. *Chem. Geol.* 153, 171-185.
- Ishikawa, T., Nakamura E., 1994. Origin of the slab component in arc lavas from across-arc variation of B and Pb isotopes. *Nature* 370, 205-208.
- Moriguti, T., Nakamura E., 1998. Across-arc variation of Li isotopes in lavas and implications for crust/mantle recycling at subduction zones. *Earth and Planet. Sci. Lett.* 163, 167-174.
- Tsukui, M., Suzuki, Y., 1998. Eruptive history of Miyakejima volcano during the last 7000 years. *Kazan* 43, 149-166.
- Turner, S., Hawkesworth, C., Calsteren, P.v., Heath, E., Macdonald, R., Black, S., 1996. U-series isotopes and destructive plate margin magma genesis in the Lesser Antilles. *Earth and Planet. Sci. Lett.* 142, 191-207.
- Turner, S., Hawkesworth, C., Rodgers, N., Bartlett, J., Worthington, T., Hergt, J., Pearce, J., Smith, I.,

1997.  $^{238}\text{U}$ - $^{230}\text{Th}$  disequilibria, magma petrogenesis, and flux rates beneath the depleted Tonga-Kermadec island arc. *Geochim. Cosmochim. Acta* 61, 4855-4884.

Turner, S., Bourdon B., Hawkesworth, C., Evans P., 2000.  $^{226}\text{Ra}$ - $^{230}\text{Th}$  evidence for multiple dehydration events, rapid melt ascent and the time scales of differentiation beneath the Tonga-Kermadec island arc. *Earth and Planet. Sci. Lett.* 179, 581-593.

### 2.23 Petrology and trace element geochemistry of eclogite xenoliths from the Colorado Plateau

Tomohiro Usui<sup>1</sup>, Eizo Nakamura<sup>1</sup>, Katsura Kobayashi<sup>1</sup>, Shigenori Maruyama<sup>2</sup> and Herwart Helmstaedt<sup>3</sup>

1. PML, Institute for Study of the Earth's Interior, Okayama University at Misasa, Tottori 682-0193, Japan
2. Department of Earth and Planetary Sciences, Tokyo Institute of Technology, 2-12-1 Ookayama, Meguro, Tokyo 152-8551, Japan
3. Department of Geological Sciences and Geological Engineering, Queen's University, Kingston, Ontario K7L7 3N6, Canada

It is very important to characterize the trace element behavior in subducted oceanic crust for better understanding of mantle/crust recycling. Eclogite xenoliths from the kimberlite diatreme breccias on the Colorado Plateau have been thought to be fragments of subducted oceanic crust, because of their basaltic bulk compositions and mineralogical textures similar to ophiolitic eclogites from blueschist terranes (Helmstaedt and Doig, 1975). The aims of this study are to verify the hypothesis that the eclogite xenoliths are the consequence of subduction zone metamorphism, and to determine the trace element behavior during subduction of oceanic crust using the eclogite samples.

Eclogite xenoliths examined in this study mainly consist of almandine-rich garnet, Na-clinopyroxene, lawsonite, phengite, zoisite, rutile, pyrite and zircon. Additionally, coesite, which was identified by using a laser Raman microscopy, occurs as minute ( $<20\mu\text{m}$ ) inclusion in garnet. The maximum temperature deduced by the method of Ellis and Green (1979) for neighboring rims of garnet and clinopyroxene ranges from 550°C to 650°C at 2.5GPa. Garnet crystals are extremely zoned in Mn content from core ( $\sim 1.5\text{wt}\%$ ) to rim ( $\sim 0.3\text{wt}\%$ ) texture preserving growth during prograde metamorphism. The major element compositions of clinopyroxene and lawsonite occurring as inclusions in garnet indicate that the inclusions were crystallized at lower-grade metamorphic conditions than the same minerals in the matrix.

Trace element compositions of constituent minerals in the eclogite xenoliths were analyzed by an ion microprobe, Cameca ims-5f. Combining the ion microprobe data with the mineralogical observations, we evaluated the trace element behavior in the eclogite xenolith, which represents subducted oceanic crust. Based on the mass balance calculations, it is suggested that most of HREE and Zr have been preserved in garnet and zircon, both of which are stable in the eclogite facies. Moreover, approximately 97% of the LREE and 89% of the Sr in the bulk rock are retained by lawsonite, which decomposes during progressive metamorphism in the lawsonite eclogite facies. From these observations, it is inferred that: (i) migration of the HREE and Zr to the mantle wedge is significantly small; and (ii) migration of the LREE to the mantle wedge is significantly smaller than that of Sr, because LREE contents in lawsonite increase with nearly constant Sr content during progressive metamorphism.

In addition, we preliminary determined ages of the zircons in garnet of the lawsonite eclogite by a newly installed ion microprobe, Cameca ims-1270, resulting in approximately  $53.4\pm 6.3$  Ma. Throughout the course of these observations, it is finally concluded that the lawsonite eclogite xenolith is a fragment of oceanic crust subducted into more than 90km depth along a cold geotherm and with a subduction rate  $>4\text{cm/y}$ , underneath the North American continent.

#### Reference

- Helmstaedt H. H. and Doig, R., 1975. Eclogite nodules from kimberlite pipes of the Colorado Plateau - samples of Franciscan-type oceanic lithosphere. *Phys. Chem. Earth* 9, 95-111
- Ellis, D. J. and Green, D. H., 1979. An experimental study of the effect of Ca upon garnet-clinopyroxene Fe-Mg exchange equilibria. *Contributions to mineralogy and Petrology* 71, 13-22

## 2.24 Preparation of reliable zircon standard for U-Pb dating method by HR-SIMS

Tomohiro Usui, Katsura Kobayashi and Eizo Nakamura

Pheasant Memorial Laboratory, Institute for Study of the Earth's Interior, Okayama Univ.

The most outstanding advance in U-Pb dating of zircon has been achieved by the development of secondary ion mass spectrometry (SIMS). Sensitive High Resolution Ion Micro Probe (SHRIMP) can analyze Pb and U isotopic compositions in a small area ( $< 40\mu\text{m}$ ), and determines precise age to reveal the multiple growth history in a single grain (e.g. Compston et al., 1984). Recent years, a High Resolution Secondary Ion Mass Spectrometry (HR-SIMS: CAMECA ims-1270) with multi collection system in our laboratory achieved higher analytical precision and reproducibility for Pb isotopic ratios as well as higher spatial resolutions than SHRIMP (Kobayashi et al., 2001). However, one of the major problems in the SIMS analysis exists in the preparation of homogeneous zircon standard with its precise data in terms of U and Pb concentrations and Pb isotope ratios. Such data can not be obtained only by SIMS, and thus conventional Isotope Dilution method using Thermal Ionization Mass Spectrometry (ID-TIMS) is required.

More accurate determination of U/Pb ratios in zircon by SIMS demands several zircon standards with different U/Pb ratios to correct the instrumental mass fractionation inevitably arising in SIMS analysis for U-Pb zircon dating. Additionally, the zircon standard preferably has U/Pb ratios similar to an unknown sample. Since zircon is usually zoned, a reliable zircon standard requires not only precise analysis of U/Pb ratios by ID-TIMS method but also the precise extracting technique that can pick out small and homogeneous zircon fragments from a single zircon crystal. However, conventional extracting methods such as mechanical abrading (Krogh, 1982) and simple zircon crushing do not have any abilities for such a precise extraction of zircon fragments, because their methods are intended for the production of zircon standard for SIMS. In contrast with a remarkable progress of SIMS techniques that has been applied to many geological events (e.g. Whitehouse et al., 1999), there has been no study focusing on making reliable zircon standard that is essential part in precision and accuracy of SIMS analysis.

In order to surmount these shortcomings, we used automatic precision dicing saw in our laboratory (DAD522, Disco ES Ltd.) can separate a crystal into  $\sim 50\mu\text{m}$  patches under the optical microscope, which can avoid any inclusions and crack in the crystal. This method enables simultaneous extraction of two fragments with clear spatial relationships from a single zircon crystal for SIMS and TIMS works, respectively. Recent TIMS technique (Kuritani and Nakamura, 2001) that enabled precise analysis of Pb isotopes with 1~10ng of Pb is used to make our zircon standards small enough to achieve homogeneity. By combining these techniques, we prepared zircon standards for U-Pb dating by HR-SIMS, and examined the reliability of our method than previous studies.

In this study, we used two zircon standards that have different U/Pb atomic ratios in order to correct the instrumental mass fractionation during SIMS analysis. The first one was 91500 fragment, a zircon standard donated by Harvard Mineralogical Museum in Cambridge (USA), which is thought to be crystallized at 1065 Ma (Wiedenbeck et al., 1995). Another zircon was from Sri Lanka that is estimated to be crystallized at  $\sim 560$  Ma. Each zircon was cut into two pieces ( $\sim 700\mu\text{m}$  cubic) using the automatic precision dicing saw. One part from each zircon was mounted with petropoxy154 (Palouse Petro Products), and was polished for HR-SIMS standard. This was characterized regarding their homogeneity by a optical microscope, SEM-EDX (Hitachi S-3100H, Horiba EMAX 7000) and HR-SIMS. These analyses suggest that our zircon standards are homogeneous with respect to their major element compositions as well as U/Pb atomic ratios within analytical errors. These observations suffice their possibility for the use of the standards of precise U-Pb dating with HR-SIMS.

For ID-TIMS work, another part was decomposed in a Teflon bomb following the technique described by Krogh (1973) after the addition of the  $^{205}\text{Pb}$  and  $^{233}\text{U}$  spikes. The zircon solution subsequently underwent anion exchange column chemistry with a little modification of Manhès et al. (1984)

for separation of Pb and U, resulting in >95% of Pb and U recoveries without any material destabilizing their ionization in the mass spectrometry. Pb and U concentration and Pb isotopic compositions were then determined by ID-TIMS following the techniques described by Kuritani and Nakamura (2001) and Yokoyama et al. (2001). Analytical precision and reproducibility of  $^{207}\text{Pb}/^{206}\text{Pb}$  ratio were 0.002% ( $2\sigma_m$ ) and  $\sim 0.03\%$  ( $2\sigma$ ), respectively, for 10ng of Pb extracted from natural zircon. Analytical reproducibility of Pb and U concentrations ranged from 0.1% to 0.5% ( $2\sigma_m$ ) for 10ng of Pb and 100ng of U. The total procedural blank of Pb varied from 60pg to 250pg (average:  $\sim 160\text{pg}$ ), whereas that of U was  $\sim 2.0\text{pg}$ . Taking into account the effect of observed blank and the precisions of Pb and U measurements, our analytical uncertainties are 0.41% for  $^{207}\text{Pb}/^{235}\text{U}$  and 0.36% for  $^{206}\text{Pb}/^{238}\text{U}$  ( $1\sigma$ ), which are comparable to those in the other leading laboratories. These errors are approximately ten times lower than those in the HR-SIMS analysis.

U-Pb analysis of the 91500 yielded the radiogenic atomic ratios of  $0.07491\pm 3$  for  $^{207}\text{Pb}/^{206}\text{Pb}$ ,  $1.8314\pm 76$  for  $^{207}\text{Pb}/^{235}\text{U}$  and  $0.17731\pm 64$  for  $^{206}\text{Pb}/^{238}\text{U}$  ( $1\sigma$ ), and the  $^{207}\text{Pb}/^{206}\text{Pb}$  apparent age of  $1066\pm 2\text{Ma}$  ( $1\sigma$ ). Our result is consistent with that described in Wiedenbeck et al. (1995). On the other hand, U-Pb analysis of the zircon from Sri Lanka yielded the radiogenic atomic ratios of  $0.05887\pm 2$  for  $^{207}\text{Pb}/^{206}\text{Pb}$ ,  $0.7220\pm 30$  for  $^{207}\text{Pb}/^{235}\text{U}$  and  $0.08892\pm 32$  for  $^{206}\text{Pb}/^{238}\text{U}$  ( $1\sigma$ ), and the  $^{207}\text{Pb}/^{206}\text{Pb}$  apparent age of  $561\pm 2\text{Ma}$  ( $1\sigma$ ), resulting in 2% discordance from the calculated concordia age of 561Ma.

As described above, we have precisely determined Pb and U contents, and Pb isotopes of two zircon standards by ID-TIMS with analytical errors comparable to previous studies. Moreover, we carefully extracted the pristine zircon fragments for ID-TIMS and SIMS work in a single zircon crystal, and separately checked the homogeneity of the standards by SEM-EDX, HR-SIMS and optical microscope. Therefore, it is concluded that our zircon standards are much more reliable than those prepared in previous studies.

## References

- Compston, W., Williams, I. S. and Meyer, C., 1984. *Journal of Geophysical Research* **89**, B525-534
- Kobayashi, K., Usui T., Nakamura, E., 2001. International Symposium "Transport of Material in the Dynamic Earth", Kurayoshi, October 2-5, 2001
- Krogh, T. E., 1973. *Geochimica et Cosmochimica Acta* **37**, 485-494
- Krogh, T. E., 1982. *Geochimica et Cosmochimica Acta* **46**, 637-649
- Kuritani, T. and Nakamura, E., 2001. Submitted to *Chemical Geology* (revised)
- Manhes, G., Allegre, C. J. and Provost, A., 1984. *Geochimica et Cosmochimica Acta* **48**, 2247-2264
- Wiedenbeck, M., Alle, P., Corfu, F., Griffin, W. L., Meier, M., Oberli, F., von Quadt, A., Roddick, J. C. and Spiegel, W., 1995. *Geostandards Newsletter*, **19**, 1-23
- Yokoyama, T., Makishima, A. and Nakamura, E., 2001. *Chemical Geology* (in press)
- Whitehouse, M. J., Kamber, B. S. and Moorbath, S., 1999. *Chemical Geology*, **160**, 201-224

## 2.25 Trace element migration associated with evolution of metamorphic fluid during subduction zone-related metamorphism

Eizo Nakamura and Toshio Nakano

The Pheasant Memorial Laboratory for Geochemistry & Cosmochemistry (PML), Institute for Study of the Earth's Interior, Okayama University at Misasa, Tottori 682-0193, Japan

Fluids probably carry components from the slab (oceanic crust and sediment) to the mantle wedge in deep-seated portions of subduction zones and induce partial melting of the mantle wedge to form island arcs. Based on multi-isotope systematics including boron and lithium, island arc volcanics are believed to originate through addition of oceanic slab components to island arc basalt sources by aqueous fluids released from the subducting slab (e.g., Shibata and Nakamura, 1997; Moriguti and Nakamura, 1998). Subduction zone metamorphic processes may also affect the trace element compositions and isotope compositions of rocks subducted to greater depths in the mantle beyond arcs (e.g., Hofmann & White, 1982). It is, therefore, important to characterize the trace element behavior in the metamorphic fluid liberated by the devolatilization of the slab. There are, however, few constraints on the behavior of trace elements in fluids during high-P/T metamorphism, making it difficult to quantitatively model mantle/crust recycling through subduction zones.

Boron isotope and trace element compositions of metabasites from the Sambagawa Metamorphic Belt, representing the chlorite, garnet and biotite zones, were investigated as a function of distance from a boundary between metasedimentary and metabasite rocks. The B isotopic compositions of metabasites near the boundary are similar to those estimated for the metamorphic fluids derived from the sedimentary layers, and the  $\delta^{11}\text{B}$  values increase with decreasing B concentration and increasing distance from the boundary. Most trace element abundances in the metabasites also decrease with increasing distance from the boundary, correlate with changing REE patterns in the metabasites in relation to metamorphic grades. Estimates of REE mobility in fluid by subtraction of REE in the lower grade rocks from those in the higher grade rocks indicate that REE in the metamorphic fluids are controlled by the dissociation of specific mineral phases in the surrounding metasediments.

These observations suggest that most of the trace elements are transferred by infiltrating aqueous fluid during metamorphism as released by devolatilization, and that the trace element compositions of the metamorphic fluids are dependent upon the stability of important carrier minerals (e.g., garnet, chlorite, mica and rutile) during metamorphism.

## 2.26 Geochemical evolution of the Horoman peridotite complex revised by incorporation of lead isotope systematics: Implications for melt extraction, metasomatism, and compositional layering in the mantle

Eizo Nakamura, Masaaki Tanimoto, Takeshi Kuritani and Masako Yoshikawa

The Pheasant Memorial Laboratory for Geochemistry and Cosmochemistry (PML), Institute for Study of the Earth's Interior, Okayama University at Misasa, Tottori 682-0193, Japan

The Horoman peridotite complex is one of the freshest orogenic peridotite complexes. On the basis of detailed petrologic and geochemical studies, it has been inferred that this complex suffered similar chemical fractionation processes, such as melt extraction, metasomatism, and subsolidus mineral breakdown, as did other peridotite complexes [e.g., Niida, 1974, 1984; Obata and Nagahara, 1987; Frey *et al.*, 1991; Takahashi, 1991a, b, 1992; Takazawa *et al.*, 1992, 1995, 1996; Yoshikawa, 1993; Nakamura and Yoshikawa, 1995; Ozawa and Takahashi, 1995; Takazawa, 1996]. Thus this complex should be suitable for resolving the origin and timing of chemical and isotopic variations in the peridotites, because their compositions have not been significantly disturbed by secondary alteration near the surface.

Major and trace element compositions and isotopic ratios of Sr and Nd were determined for bulk rocks and their constituent clinopyroxenes from the Horoman peridotite complex, Japan.  $\text{Al}_2\text{O}_3$ , CaO, and heavy rare earth elements (HREE) contents of peridotites generally decrease from plagioclase lherzolite through spinel lherzolite to spinel harzburgite, indicating simple melt extraction from a single source. However, the extremely large variations in isotopic ( $^{87}\text{Sr}/^{86}\text{Sr} = 0.7019$  to  $0.7066$ ,  $\epsilon_{\text{Nd}} = +110$  to  $-10$ ,  $^{206}\text{Pb}/^{204}\text{Pb} = 17.56$  to  $18.25$ ,  $^{207}\text{Pb}/^{204}\text{Pb} = 15.34$  to  $15.52$ ,  $^{208}\text{Pb}/^{204}\text{Pb} = 36.82$  to  $38.22$ ) and trace element compositions ( $[\text{Ce}/\text{Yb}]_N = 0.006$  to  $4.0$ ) cannot be explained by a simple melt extraction mechanism. The samples can be divided into two groups: one suite has depleted isotopic and light REE (LREE) characteristics (DP), while the other suite shows enriched isotopic and LREE signatures (EP). Sm-Nd isotope systematics of whole-rock DP samples yield an isochron age of  $833 \pm 78$  Ma with an initial  $^{143}\text{Nd}/^{144}\text{Nd}$  ratio of  $0.5119 \pm 2$ , which is identical to the isotopic composition of mid-ocean ridge basalt (MORB) source mantle at that time. The relationship between MgO and Yb abundances of whole rocks shows that melt extraction was initiated at pressures near the garnet and spinel lherzolite transition. Peridotites that formed at different depths presently occur in close proximity to each other, sometimes within tens of meters. The chemical and isotopic signatures of the EP samples can be explained by mixing between mantle residue and an isotopically and more incompatible element enriched fluid derived from a subducted slab. This is strongly supported by Pb isotope systematics indicating that such a metasomatic fluid have been mostly derived from subducted sediments presumably corresponding to Hidaka accretionary complex, which consists of a large amount of terrigenous sediments derived from an intracontinent collision zone. These observations suggest that the small-scale compositional layering observed in the complex may have formed in a wedge mantle by water-enhanced thinning and folding of metasomatized peridotites which had previously developed large-scale simple stratification as a result of melt extraction beneath a mid-ocean ridge. Final uplift from the upper mantle occurred as a result of the uplift of the Hidaka metamorphic belt arising from the collision between the Eurasian and North American plates at approximately 20 Ma as suggested by Yoshikawa *et al.* (1993). In conclusion, these observations imply that the Horoman peridotite complex is not a piece of normal convecting mantle, but is a fragment of wedge mantle extensively deformed and metasomatized under water-bearing conditions associated with subducted sediments.

## 2.27 Record in metamorphic tourmalines of subduction-zone devolatilization and boron cycling

Gray E. Bebout<sup>1</sup>, and Eizo Nakamura

The Pheasant Memorial Laboratory for Geochemistry and Cosmochemistry (PML), Institute for Study of the Earth's Interior, Okayama University at Misasa, Tottori-ken 682-0193 Japan; (<sup>1</sup> permanent address: Department of Earth and Environmental Sciences, Lehigh University, USA; e-mail: geb0@lehigh.edu)

Boron partitioning among fluids, tourmaline, and micas (and other B-rich phases) dictates the extent and location, and isotopic composition, of B loss in subducting slabs (and any additions to arc sources or the deeper mantle), but the scarcity of information regarding mineral-fluid fractionation limits efforts to quantitatively model B isotopic evolution. To clarify tourmaline's role in B redistribution during devolatilization of subducting sediments, we have analyzed tourmaline  $\delta^{11}\text{B}$  in several HP and UHP suites, employing high-precision ( $2\sigma_{\text{mean}} = 0.5\text{-}0.8\text{‰}$ ) ion microprobe methods.

Catalina Schist and Sambagawa Belt metasediments (sub-blueschist to amphibolite facies, <1.2 GPa) show contrasting systematics in whole-rock B content and tourmaline abundance. The Sambagawa shows uniform whole-rock B across grade, but an increasing proportion of B in tourmaline and a decreasing proportion in micas at higher grades (Nakano and Nakamura, 2001). Catalina Schist rocks contain less tourmaline, and at higher grades show up to 75 percent decrease in whole-rock B (Bebout et al., 1999) with correlated decreased mica B. In both suites, some higher-grade (~epidote-amphibolite) rocks contain abundant, zoned, dravitic tourmaline. In these rocks, tourmaline cores have lower  $\text{Mg}/(\text{Mg}+\text{Fe}^{+2})$  and  $\text{Ca}/(\text{Ca}+\text{Na})$  and higher  $\delta^{11}\text{B}$  SRM951 (up to +1.6‰, mostly -6 to -2‰), and tourmalines show increased  $\text{Mg}/(\text{Mg}+\text{Fe}^{+2})$  (up to 0.825) and  $\text{Ca}/(\text{Ca}+\text{Na})$  and decreased  $\delta^{11}\text{B}$  (approaching -15‰) toward rims. These variations are consistent with significant prograde tourmaline growth. Some higher-grade tourmalines have thin outermost zones compositionally similar to cores and attributed to retrogradation. The  $\delta^{11}\text{B}$  of less-abundant tourmaline in lower-grade rocks (-7 to +4.5‰) overlaps with, or is higher than, that of tourmaline cores in higher-grade rocks, and some cores in low- and high-grade rocks are regarded as detrital. Lago di Cignana UHP metasediments (peak 2.7-2.9 GPa; Reinecke, 1998, and van der Klauw et al., 1997, who reported coesite inclusions in tourmaline) contain dravitic tourmaline zoned in  $\text{Mg}/(\text{Mg}+\text{Fe}^{+2})$ ,  $\text{Ca}/(\text{Ca}+\text{Na})$ , and  $\delta^{11}\text{B}$ . We tentatively associate cores with garnet and rutile inclusions,  $\text{Mg}/(\text{Mg}+\text{Fe}^{+2})$  up to 0.95, and  $\delta^{11}\text{B}$  as low as -16‰ with prograde, high-P/T metamorphism, and rims with clinozoisite and quartz inclusions, lower  $\text{Mg}/(\text{Mg}+\text{Fe}^{+2})$ , and higher  $\delta^{11}\text{B}$  up to +4.3‰ with overprinting during exhumation.

The HP suites illustrate contrasting B evolution reflecting the significance of sedimentary processes, bulk-rock/fluid chemistry, or kinetic factors (e.g., need for sedimentary or lower-grade metamorphic "seed crystals") in controlling the presence and further growth of tourmaline at higher-grades. In the absence of tourmaline, devolatilization can reduce whole-rock B (Catalina), whereas tourmaline growth may serve to retain whole-rock B lost from micas and minimize change in whole-rock  $\delta^{11}\text{B}$  (Sambagawa). At Lago di Cignana, tourmaline (with  $\delta^{11}\text{B} = -16$  to  $-9\text{‰}$ ) was apparently stable to depths of ~90 km, and correlated major element and B isotope zoning (>16‰) demonstrates tourmaline's ability to preserve complex metamorphic history spanning extremely large P-T ranges.

Based on our results, and taking into account other recent studies of B isotope fractionation, the B lost during devolatilization from subducting sedimentary rocks (and mica-bearing altered oceanic crust) is thought to be isotopically heavier than the residual B in the micas. This heavier B could be sequestered by growing tourmaline (particularly in sedimentary lithologies), in which it could be subducted to and released at even greater depths, or could be released into and mobilized in metamorphic fluids. These metamorphic fluids (containing B released from micas in subducting sediment and altered oceanic crust) would appear to be capable of imparting the observed, relatively high- $\delta^{11}\text{B}$  signatures observed in most arc lavas and producing the across-arc trends of decreasing  $\delta^{11}\text{B}$  observed

in several arcs.

## 2.28 Boron isotope geochemistry of metasedimentary rocks and tourmalines in a subduction-zone metamorphic suite

Toshio Nakano and Eizo Nakamura

The Pheasant Memorial Laboratory for Geochemistry & Cosmochemistry (PML), Institute for Study of the Earth's Interior, Okayama University at Misasa, Tottori 682-0193, Japan

Boron is considered to be an excellent tracer of the recycling of subducted oceanic sediment and/or altered oceanic crust at convergent margins (Morris et al., 1990; Palmer, 1991; Ishikawa and Nakamura, 1994). This is because of its extremely high mobility during both magmatic and fluid-related processes (e.g., Seyfried et al., 1984; Ryan and Langmuir, 1993) and its extreme enrichment in the subducted oceanic sediments and altered oceanic crust compared with unaltered mid-ocean ridge basalts (MORB) and upper mantle materials (Spivack and Edmond, 1987; Ishikawa and Nakamura, 1992; 1993). However, B isotopic fractionation behavior during progressive metamorphism is not well understood making it still difficult to interpret B isotope systematics of island arc and oceanic island volcanics in relation to mantle/crust recycling through subduction zones.

In order to understand the behavior of boron (B) and its isotope fractionation during subduction zone metamorphism, B contents and isotopic compositions together with major element compositions were determined for metasedimentary rocks and tourmalines from the Sambagawa Metamorphic Belt, central Shikoku, Japan. No systematic changes in whole-rock B content and isotope composition of the metasediments were observed among the different metamorphic grades, indicating the lack of a bulk fluid-rock B-isotope fractionation as a result of devolatilization.

Both modal abundance and grain size of tourmaline increase with increasing metamorphic grade. In contrast, B contents in muscovite and chlorite decrease with increasing metamorphic grade. These observations combined with mass balance calculations of B suggest the formation of tourmaline during progressive metamorphism from metamorphic fluids containing B mainly derived from muscovite and subordinately from chlorite without allowing significant net removal of B from the metasedimentary rocks. Tourmalines in the higher-grade metasedimentary rocks have zonal structure of B isotope and major element composition with decreasing  $\delta^{11}\text{B}$  and increasing  $\text{Mg}/(\text{Mg}+\text{Fe})$  from the inner rim (core) to the outer rim. The change of  $\text{Mg}/(\text{Mg}+\text{Fe})$  in the tourmalines with increasing grade is paralleled by similar variation in chlorite. These observations suggest that the growing tourmalines record the progressive evolution of the B isotopic composition of the metamorphic fluid, in the outermost rims preserving the isotope signature of peak metamorphic P-T-fluid conditions.

Based on the above observations, the  $\delta^{11}\text{B}$  of the tourmaline is thought to have been nearly identical to that of the metamorphic fluid resulting in the "apparent" B isotopic fractionation factor between metamorphic fluid and whole rock ( $\alpha = (^{11}\text{B}/^{10}\text{B})_{\text{fluid}} / (^{11}\text{B}/^{10}\text{B})_{\text{wholerock}}$ ) which decreases from  $1.007 \pm 0.003$  to  $1.001 \pm 0.003$  from chlorite to biotite zone metamorphism. Such results together with the formation of tourmaline from (and sequestering of) B in metamorphic fluids may lead to less B-isotopic fractionation as a result of subduction-zone devolatilization than noted in suites containing less tourmaline. This, therefore, makes it possible to transport B isotopic signatures, which ultimately reflect Earth's surficial materials to the deep mantle, perhaps resulting in mantle B isotope anomalies near convergent margins.

## 2.29 Simultaneous determination of Ru, Pd, Re, Os, Ir and Pt contents and $^{187}\text{Os}/^{188}\text{Os}$ ratios in geological samples using a new anion exchange chromatographic procedure

Akio Makishima, Mayumi Nakanishi and Eizo Nakamura

The Pheasant Memorial Laboratory for Geochemistry and Cosmochemistry (PML), Institute for Study of the Earth's Interior, Okayama University at Misasa, Misasa, Tottori-ken 682-0193, Japan

We have developed a new group separation method of Ru, Pd, Os, Ir and Pt (PGEs) and Re in silicate samples employing less hazardous reagents and procedures. A silicate sample and isotope spikes were mixed, and digested with HF-HBr in a Teflon bomb at 518 K after the in situ generated  $\text{Br}_2$  treatment. Then the sample was dried and redissolved with 0.1 M HBr. After separation of fluoride residues by centrifugation, Re and PGEs were adsorbed on a 0.1 ml TEVA anion exchange resin, which has distribution coefficients ( $K_{ds}$ ) of 2200, 16000, 1600, 5500, 4000 and 17000 for Ru, Pd, Re, Os, Ir and Pt, respectively [Makishima, Nakanishi and Nakamura, Anal. Chem., in press]. Re and PGEs were recovered into Re and Os fractions, by combination of HCl, HBr and HI with total recovery yields of >90 % for Ru, Pd, Os and Ir, and >70 % for Re for ~1g silicate sample. The Re fraction was further purified by 0.1 ml cation exchange resin, AG 50W-X8, and Re and PGE concentrations were determined by isotope dilution (ID) ICP-MS with detection limit of <4 pg g<sup>-1</sup> except Os. The Os fraction was purified by the micro-distillation technique, and its  $^{187}\text{Os}/^{188}\text{Os}$  ratio was measured with negative thermal ionization mass spectrometry (N-TIMS). Total blanks were 2~3 pg for Ir and Os, 8 pg for Re, and 12~14 pg for Pd and Pt. This technique, therefore, enables us to determine simultaneously sub ng g<sup>-1</sup> levels of Ru, Pd, Re, Os, Ir and Pt and the Os isotope ratio in silicate samples. Furthermore, common distillable acids were used, Sr, Ce, Nd and Pb isotope ratios should be easily determined from the same sample. In addition, S can be also measured simultaneously by simply adding S-spike before sample digestion.

### 2.30 Major and rare earth elements geochemistry of the Icelandic Plume: an island-wide approach for source determination

Estelle F. Rose, A. Makishima, E. Nakamura

Institute for Study of the Earth's Interior, Okayama University at Misasa, 682-0193 Tottori-ken, Japan

The principal distinguishing feature of Iceland among other plume-fed ocean island is its location on the Mid-Atlantic Ridge (MAR). The geochemical variations in basalts from Iceland and the Reykjanes Ridge have for a long time been attributed to mixing between two endmembers (1) the depleted mid-ocean ridge basalt (MORB) source and (2) the enriched Iceland mantle plume (Shilling, 1973; Hart et al., 1973; Sun et al., 1975). In contrast, the occurrence of some Iceland basalts with relatively depleted incompatible trace element ratios and low Pb and Sr isotope ratios compared to normal MORB (NMORB) have been interpreted as an indicator that the Iceland mantle plume transports both geochemically enriched and depleted material from the lower mantle into the upper mantle and that the depleted MORB source does not contribute significantly to the generation of the Iceland basalts (Thirlwall, 1995; Hards et al., 1995; Kerr et al., 1995; Fitton et al., 1997; Kempton et al., 1998; Nowell et al., 1998). More recently it has been proposed that no depleted Iceland plume component existed but rather an enriched low  $^{206}\text{Pb}/^{204}\text{Pb}$  EM1-like component which could correspond to entrained subcontinental lithospheric material embedded in the North Atlantic depleted MORB source (Hanan et al., 2000). On the other hand, another recent study showed that no MORB component was necessary to explain the range of chemical and isotopic compositions of Icelandic lavas. It could all be explained by melting different sections of an old oceanic crust (Chauvel and Hémond, 2000).

In this study we analyzed major and rare earth elements. By looking at samples from various locations, we propose to correct for the common mantle process that affect those lavas and decipher some constraints on the magma sources. We present here preliminary results of this island-wide approach, since contrary to previous studies, we do not pre-select the rocks neither according to their type or location, nor to their "primitive" chemical characteristics.

The samples from east (Snaefellsnes Volcanic Zone), south-east (Reykjanes Rift Zone) and south Iceland (South Iceland Volcanic Zone) as well as from center-north Iceland (North Iceland Rift Zone, were collected by T. Koyaguchi and A. Makishima in 1993 and 1994).

6 samples are alkali-basalts, 3 from the Snaefellsnes Peninsula SN4, SN5, SN6, and 3 from Heimaey Island HE1, HE2, HE3. 3 others are basaltic andesites from Hekla HL1, HL2, HL3. All the other samples are tholeiitic basalts.

In this sample set, no correlation was found between index of differentiation ( $\text{SiO}_2$  and  $\text{Fe}/(\text{Fe}+\text{Mg})$ ) and many incompatible trace element ratios were found. Therefore it is considered that certain trace element ratios reflect information other than crustal processes such as crystal fractionation and assimilation. For example, we find that Icelandic lavas are characterized by large excess Sr, Ba and Rb relative to trace elements with similar chemical behavior, which is in good agreement with previous study (Chauvel and Hémond, 2000). However we notice an additional feature which is a Cs positive anomaly for 8 samples that seems to correlate with an U positive anomaly (SN6, SN8, SN9, HE1, TV1, TV2, MY2, GR1). While Rb/Cs might be expected to vary in fluid-derived deposits, we can determine two groups of sample with constant Rb/Cs with an average of  $89 \pm 7$  and  $3 \pm 0.3$ , respectively. The first value is consistent with mantle derived volcanic values (McDonough et al., 1992) and is similar to what has been previously described for other Iceland rocks (Chauvel and Hémond, 2000). The second, much lower value, has never been described in Icelandic lavas and can not be interpreted as a mixing with any other reservoir because Rb/Cs is lower than any ratio known. Therefore it could represent (1) different melting conditions during the formation of the lava or (2) an original heterogeneity of the magma source which needs to be identified. Since this is a new observation for Icelandic lavas we will focus on characterizing this endmember in more details.

The partition coefficients of Rb and Cs between cpx and melt are too close ( $D^{\text{cpx}}(\text{Rb}) = 0.0010 -$

0.0041 and  $D^{cpx}(Cs) = 0.00035 - 0.0063$ ; Shimizu, 1974) to account for the significant fractionation of Rb/Cs by melting. As for the partition coefficient for these elements between plagioclase and melt  $D^{plagio}(Rb) = 0.13 - 0.3$  and  $D^{plagio}(Cs) = 0.13 - 0.14$ ; Villemant et al., 1988. If a source containing plagioclase and with an initial Rb/Cs=89 undergoes melting, the lowest possible Rb/Cs ratio obtainable is 39. This is much higher than the observed Rb/Cs  $\approx 3$ . Overall, the ratio  $D^{rock}(Cs)/D^{rock}(Rb)$  has to be more than 30 to fractionate Rb/Cs significantly, and such partition coefficients are not reported in mantle silicate phases. Different melting conditions that possibly could fractionate Rb/Cs are therefore ruled out.

Such low Rb/Cs ratio have been reported in a few xenoliths from Australia (Wilkinson and Taylor, 1980) but further constraints of these sources can be obtained by principal component analysis (PCA).

This is an ongoing study and our preliminary results should be strengthened by Nd, Sr, Pb isotopic analysis.

#### References

- Chauvel C. and Hemond C. (2000) *Geochem. Geophys. Geosyst.*
- Fitton J. G., Saunders A. D., Norry M. J., Hardarson B. S. and Taylor R. N. (1997) *Earth and Planet. Sci. Lett.* 153, 197-208.
- Hanan B. B., Blichert-Toft J., Kingsley R. and Schilling J.-G. (2000) *Geochem. Geophys. Geosyst.*
- Hards V. L., Kempton P. D. and Thompson R. N. (1995) *Journal of Geological society of London* 152, 1003-1009.
- Hart S. R. and Schilling J.-G. (1973) *Nature Phys. Sci.* 246, 104-107.
- Kempton P. D., Fitton J. G., Saunders A. D. and Nowell G. M. (1999) *LIP Reader* April.
- Kempton P. D., Nowell G. M., Fitton J. G., Saunders A. D. and Taylor R. N. (1998) *Mineral. Mag.* 62A, 759-760.
- Kerr A. C., Saunders A. D., Tarney J. and Berry N. H. (1995) *Geology* 23, 843-846.
- Makishima A. (1995). Icelandic Volcanic Rocks No.1, ISEI.
- Rudnick R. L., McDonough W. F., McCulloch M. T. and Taylor S. R. (1986) *Geochim. et Cosmochim. Acta* 50, 1099-1115.
- Schilling J.-G. (1973) *Nature* 242, 565-571.
- Shimizu N. (1974) *Geochim. et Cosmochim. Acta* 38, 1789-1798.
- Sun S. S., Tatsumoto M. and Schilling J.-G. (1975) *Science* 190, 143-147.
- Thirwall M. F. (1995) *J. Geol. Soc. London* 152, 991-996.
- Villemant B. (1988) *Contrib. to Mineral. and Petrol.* 98, 169-183.
- Wilkinson J. F. G. and Taylor S. R. (1980) *Contrib. to Mineral. and Petrol.* 75, 225-233.

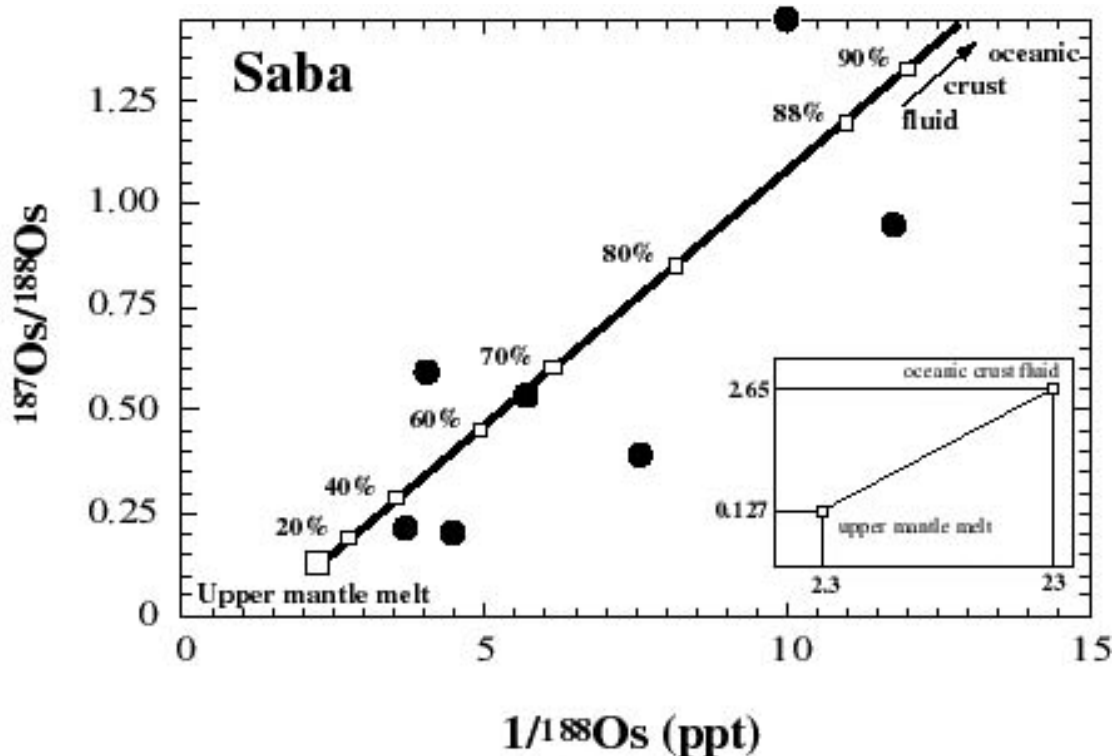
### 2.31 Magma formation at Saba Island, Lesser Antilles: a numerical model for mantle wedge-slab mixing according to osmium data

Sophie Alves<sup>1</sup>, Pierre Schiano<sup>2</sup>, Bernard Bourdon<sup>3</sup>, Claude J. Allègre<sup>3</sup>

<sup>1</sup>ISEI, <sup>2</sup>University Blaise Pascal, Clermont-Ferrand, France, <sup>3</sup>IPG-Paris, France

We have studied the osmium isotopic characteristics of samples from Saba Island, Northern Lesser Antilles. Os concentrations are low (0.7-2.1 ppt) and isotopic ratios are very high ( $^{187}\text{Os}/^{188}\text{Os} = 0.198 - 1.443$ ). When the isotope ratios are plotted versus the inverse of the concentration, the data forms a positive trend, which can be interpreted as a mixing relationship. Trace element ratios (such as Ba/Th) and Sr, Nd and Pb isotope ratios suggest that Saba lavas are not affected by continental or sediment material neither from the down-going slab nor from the crustal basement. We then concluded that high Os isotope ratios in lavas may be imparted by the subducting oceanic crust contribution in the mantle source. In order to evaluate such a hypothesis, we conducted calculations to model mantle and oceanic osmium contributions to the composition of the Saba lavas.

For the model, we considered a binary mixing process between mantle melt and oceanic crust derived fluid, both contributing Os to the lava. Parameters such as Os concentration and isotope ratio in the subducting crust and Os partition coefficient during mantle melting and oceanic crust dehydration are not well known and the initial range of possible values for these parameters were chosen very large (e.g., for partition coefficients during melting and dehydration, respectively 0-5000 and 0-1000). The calculation shows that it is possible to fit the data with such a calculated mixture and that we can estimate statistically likely values for Os partition coefficients:  $D^{\text{Os}}$ (mantle melting  $\approx 1000$ ;  $D^{\text{Os}}$ (crust dehydration)  $\approx 50$ ). These high partition coefficients suggest that Os is more efficiently mobilized in the crustal fluid than in the mantle melt. The following figure displays the best model obtained from the calculation and shows that 30 to 90% of the osmium occurring in the Saba lavas must come from the subducting oceanic crust.





**October 4 (Thursday) 09:00 — 12:00**

**Session 3**

**High pressure mineral physics**

Keynote: Takehiko Yagi, Institute for Solid State Physics, U. Tokyo

Chair: Eiji Ito, Institute for Study of the Earth's Interior, Okayama U.

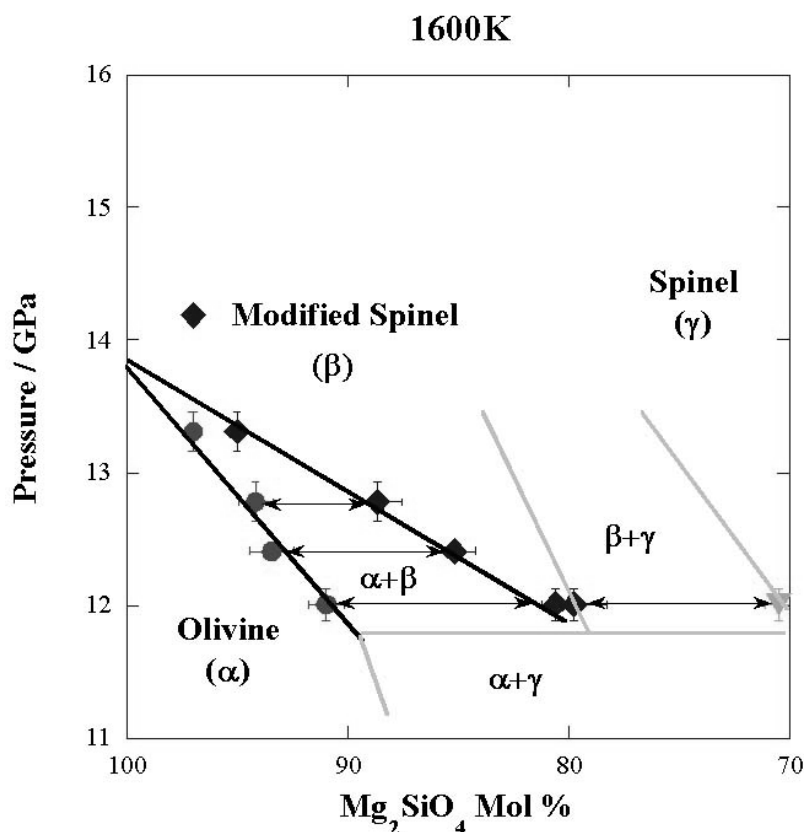


### 3.3 In situ determination of the olivine-modified spinel phase boundary in the system $\text{Mg}_2\text{SiO}_4$ - $\text{Fe}_2\text{SiO}_4$

Hitoshi Yamada<sup>1</sup>, Tomoo Katsura<sup>1</sup>, Toru Shinmei<sup>1</sup>, Atsushi Kubo<sup>1</sup>, Osamu Nishikawa<sup>1</sup>, Maoshuang Song<sup>1</sup>, Eiji Ito<sup>1</sup>, Kenichi Funakoshi<sup>2</sup>

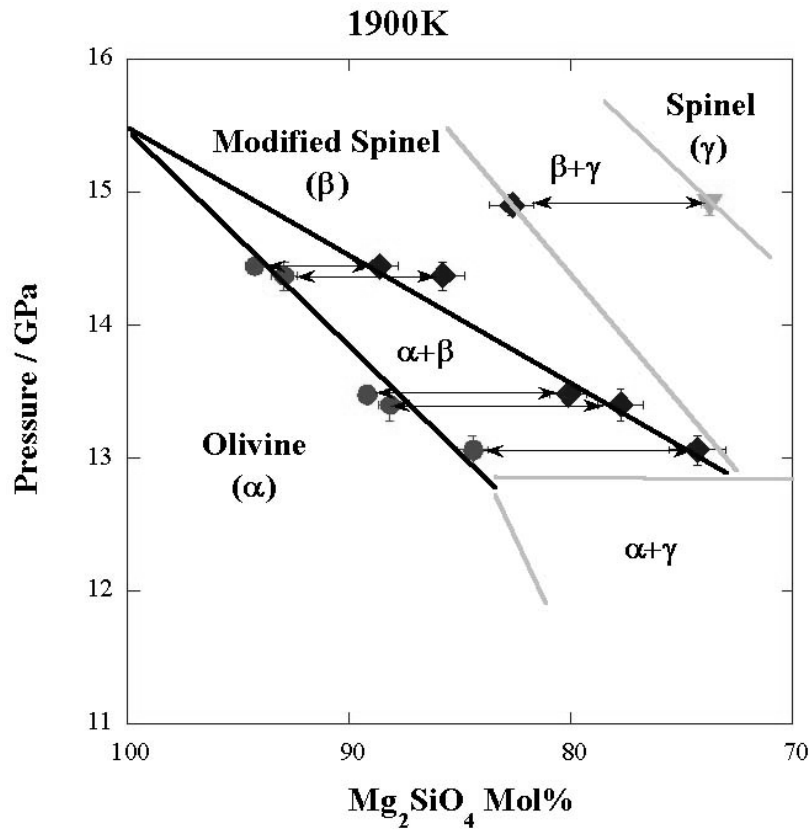
1: Institute for Study of the Earth's Interior, Okayama University ,  
2: Japan Synchrotron Radiation Research Institute

The 410-km seismic discontinuity is usually attributed to the phase transition of olivine to modified spinel in  $(\text{Mg}, \text{Fe})_2\text{SiO}_4$ . From this reason, we have reinvestigated detailed phase relations of this transition in detail by combination of high P-T in situ X-ray diffraction and compositional analysis. Starting materials were olivine solid solutions with compositions of  $(\text{Mg} \times \text{Fe} 1-x)_2\text{SiO}_4$  ( $x = 0.97, 0.95, 0.93, 0.90, 0.85, 0.80, 0.70$ ). High P-T experiments were conducted using a 6-8 type multi-anvil press "SPEED-1500" at SPring-8. Pressures were calculated from the unit cell volume of MgO pressure maker and temperature primarily using EOS of MgO proposed by Jamieson et al. (1982). We compressed the sample at ambient temperature, and then heated to 1600 or 1900K. We kept the temperature with taking X-ray diffraction. After that, we quenched the sample. Compositions of coexisting olivine and modified spinel in the recovered samples were determined using electron microprobe analyzer.



The olivine and modified spinel coexisting loops at temperatures of 1600K and 1900K are found to be located at pressure range of 12.0~13.8GPa and 13.0~15.4GPa, respectively. The  $dP/dT$  slope of the transition in  $\text{Mg}_2\text{SiO}_4$ , which is estimated by extrapolation of the binary loop, is found to be steeper than that given by Katsura and Ito (1989). The phase relations obtained here suggest that the temperature at the 410km depth should be 1850K. However, because of uncertainty of EOS, we

still have 100K uncertainty of temperature estimation. The depth interval of olivine-modified spinel coexisting regions in the mantle should be 20km if the composition of mantle olivine is  $(\text{Mg}_{0.89}\text{Fe}_{0.11})_2\text{SiO}_4$ . The seismic observations showing less than 10km thickness of the 410km discontinuity cannot be simply explained by applying the phase diagram of olivine-modified spinel transition obtained here.



### 3.4 Garnet-ilmenite-perovskite transitions in the system $\text{Mg}_4\text{Si}_4\text{O}_{12}$ - $\text{Mg}_3\text{Al}_2\text{Si}_3\text{O}_{12}$ : phase equilibria, calorimetry and application to the mantle

Masaki Akaogi<sup>1\*</sup>, Akira Tanaka<sup>1</sup>, and Eiji Ito<sup>2</sup>

<sup>1</sup> Dept. of Chem., Gakushuin Univ., Toshima, Tokyo 171-8588

<sup>2</sup> ISEI, Okayama Univ., Misasa, Tottori 682-0193

#### 1. Introduction

Recent high-pressure phase equilibrium experiments in simple systems and natural mantle rocks showed that at normal mantle temperature majorite garnet transforms to perovskite in pyrolitic mantle at the depth of the uppermost lower mantle (Irifune et al., 1996; Wood, 2000; Kubo and Akaogi, 2000). However, phase transition of majorite at lower temperature regime such as in subducting slabs is not fully clarified. We have examined phase relations at 1000 °C in the system  $\text{Mg}_4\text{Si}_4\text{O}_{12}$ (En)- $\text{Mg}_3\text{Al}_2\text{Si}_3\text{O}_{12}$ (Py) which represents a model system for majorite garnet in the mantle. Post-garnet transitions of  $\text{Mg}_3\text{Al}_2\text{Si}_3\text{O}_{12}$  pyrope have been studied at temperature down to 800 °C. Enthalpies of ilmenite solid solutions in the En-Py system have also been measured to calculate the phase relations among garnet, ilmenite and perovskite. These results are used to examine stability of ilmenite solid solution in the mantle, particularly in subducting slabs.

#### 2. Experimental Methods

High-pressure phase equilibrium experiments were carried out using multianvil apparatus. Starting materials were glasses of  $(1-x)\text{MgSiO}_3$ - $x\text{Al}_2\text{O}_3$  compositions ( $x=0, 0.05, 0.1, 0.15, 0.2, 0.25$ ) and crystalline pyrope. The experimental pressure and temperature ranges were 19-27 GPa and 800-1000 °C, respectively, and run duration was 3-6 hrs. The recovered samples were examined by microfocus X-ray diffraction technique, and lattice parameters of ilmenite solid solutions were measured by powder X-ray diffraction method. Calorimetric measurements were performed using a Calvet-type microcalorimeter at 978 K. Enthalpies of  $(1-x)\text{MgSiO}_3$ - $x\text{Al}_2\text{O}_3$  ilmenite solid solutions ( $x=0, 0.1, 0.2, 0.25$ ) were measured by differential drop-solution calorimetry method in lead borate solvent.

#### 3. Results and Discussion

The results of phase equilibrium experiments on  $\text{Mg}_3\text{Al}_2\text{Si}_3\text{O}_{12}$  have shown that pyrope dissociates into perovskite solid solution and corundum solid solution at about 26 GPa at temperature above about 1100 °C, while pyrope first transforms to ilmenite and subsequently to perovskite below about 1100 °C. At 1000 °C,  $\text{MgSiO}_3$  ilmenite is stable at 20-24 GPa and  $\text{Mg}_3\text{Al}_2\text{Si}_3\text{O}_{12}$  ilmenite at about 25-27 GPa. These two endmembers form single phase ilmenite solid solution in the whole compositional range of the En-Py system at about 20-27 GPa at 1000 °C (Fig. 1). Garnet solid solution and perovskite solid solution are stable, respectively, below and above the stability field of ilmenite. The stability of ilmenite solid solution at 1000 °C in the entire compositional range is very different from that at 1600 °C by Kubo and Akaogi (2000) in which ilmenite is stable only in the En-rich composition. This indicates that stability of ilmenite solid solution is very sensitive to temperature and its field expands rapidly with decreasing temperature.

Enthalpies of ilmenite solid solutions measured by differential drop-solution calorimetry increase with  $\text{Al}_2\text{O}_3$  content in ilmenite. By combining the data of ilmenite solid solutions in this study with those of garnet and perovskite solid solutions (Akaogi and Ito, 1999), enthalpies of garnet-ilmenite and ilmenite-perovskite transitions in  $\text{Mg}_3\text{Al}_2\text{Si}_3\text{O}_{12}$  are estimated to be 150.16 and 99.27 kJ/mol, respectively. Using the above enthalpy data of  $\text{Mg}_3\text{Al}_2\text{Si}_3\text{O}_{12}$  and those of  $\text{MgSiO}_3$  (Akaogi and Ito, 1993), the phase relations in the En-Py system have been calculated. The calculated phase boundaries are generally consistent with those by the experimental determination, and it is confirmed that the ilmenite stability field expands to Py-rich composition with decreasing temperature.

Here we assume that mantle composition is pyrolite and that transformations of majorite garnet in the mantle can be approximated by those of the En-Py system. We choose two adiabatic temperature

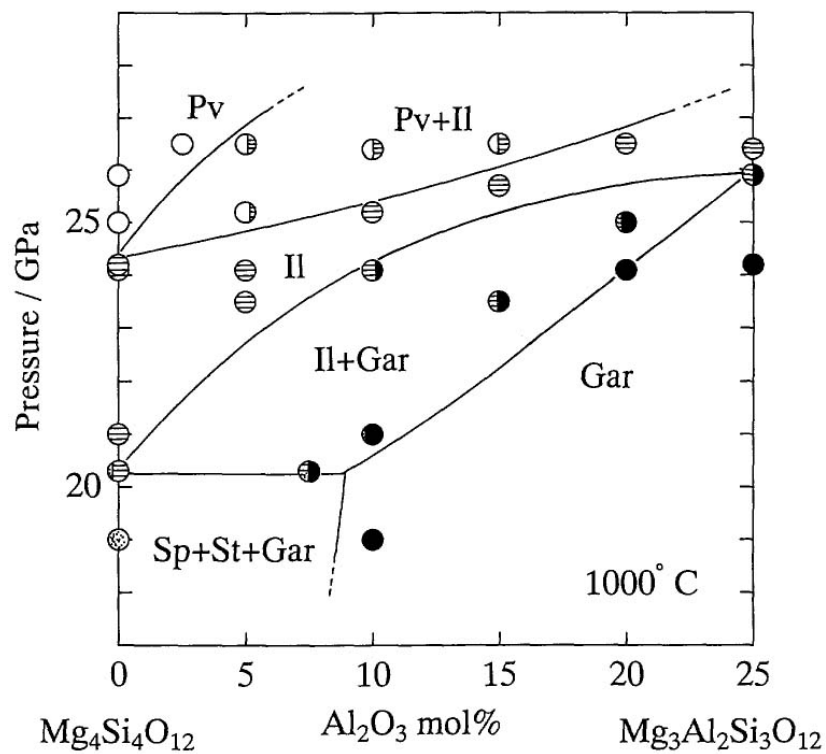


Fig. 1. Phase relations in the En-Py system at 1000 °C.

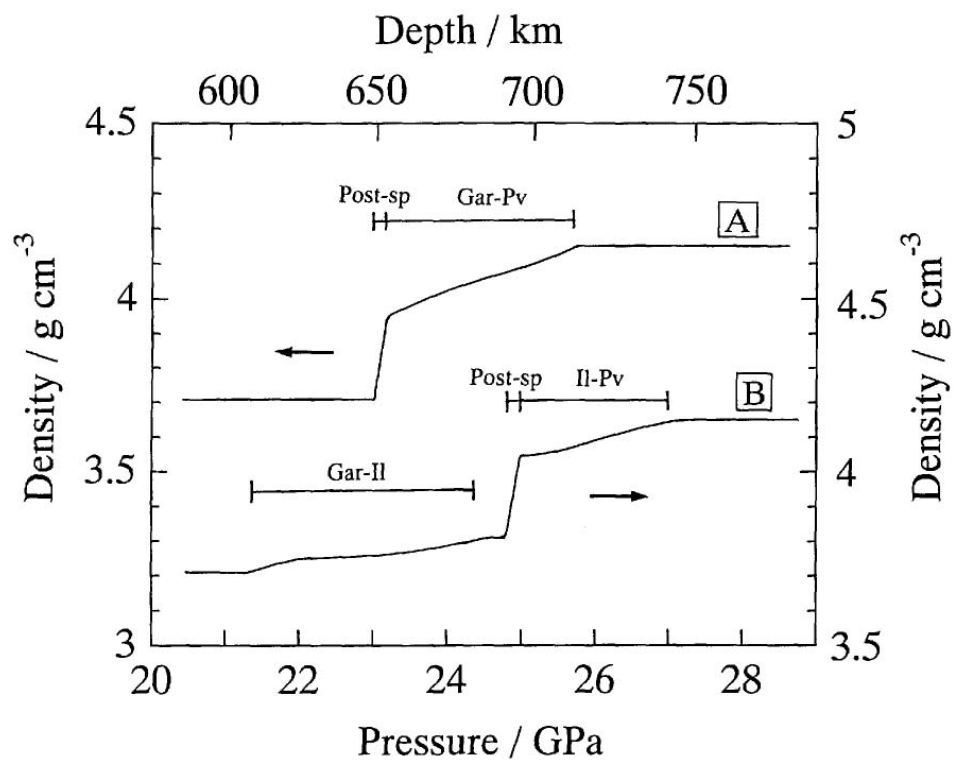


Fig.2. Zero-pressure density vs. depth.

distributions in which temperature at the 660 km depth is 1600 °C in the normal mantle and 1000 °C in descending slab. Based on the phase relations of the En-Py system at 1600 °C (Kubo and Akaogi, 2000), it is suggested that majorite transforms to perovskite at about 660-720 km depth in the normal mantle (Fig. 2(A)). In contrast, the present results on En-Py system at 1000 °C suggest that majorite first transforms to ilmenite at about 610-680 km, and subsequently to perovskite at about 700-740 km. As shown in Fig. 2(B), in the descending slab, a sharp density increase associated with the post-spinel transition exists at about 690 km and two broad regions of density increase, one above and the other below the post-spinel transition are observed.

#### References

- Akaogi, M. and Ito, E. (1993) *Geophys. Res. Lett.*, **20**, 1839-1842.  
Akaogi, M. and Ito, E. (1999) *Phys. Earth Planet. Inter.*, **114**, 129-140.  
Irifune, T., Koizumi, T. and Ando, J. (1996) *Phys. Earth Planet. Inter.*, **96**, 147-157.  
Kubo, A. and Akaogi, M. (2000) *Phys. Earth Planet. Inter.*, **121**, 85-102.  
Wood, B. J. (2000) *Earth Planet. Sci. Lett.*, **174**, 341-354.

### 3.5 MD simulation of the density and P- and S-wave velocity jumps across the 410km and 660km seismic discontinuities

Masanori Matsui

Faculty of Science, Himeji Institute of Technology

The seismic wave discontinuities near 410 and 660 km depths in the mantle have been attributed to the pressure-induced phase transformations from  $(\text{Mg,Fe})_2\text{SiO}_4$  olivine to  $(\text{Mg,Fe})_2\text{SiO}_4$  modified-spinel, and from  $(\text{Mg,Fe})_2\text{SiO}_4$  spinel to  $(\text{Mg,Fe})\text{SiO}_3$  perovskite plus  $(\text{Mg,Fe})\text{O}$  magnesiowustite, respectively. In recent publications (Matsui, 1999; Matsui et al., 2000; Matsui, 2000), we have shown that the molecular dynamics (MD) simulation with realistic potential models, including the breathing shell model for O ions, is very successful in reproducing accurately the observed crystal structures and elastic constants of MgO periclase (Pc), the three  $\text{Mg}_2\text{SiO}_4$  polymorphs, olivine (Ol), modified-spinel (Ms) and spinel (Sp), and  $\text{MgSiO}_3$  perovskite (Pv) over wide T and P ranges, including those found in the deep Earth. Here we apply MD simulation to predict the density and P- and S-wave velocity jumps between  $\text{Mg}_2\text{SiO}_4$  Ol and Ms, and between  $\text{Mg}_2\text{SiO}_4$  Sp and  $\text{MgSiO}_3$  Pv plus MgO Pc at the high-T and high-P conditions corresponding to the 410 and 660 km discontinuities, respectively. We then compare these simulated density and P- and S-wave velocity jumps with representative seismological models reported for the 410 and 660 km discontinuities, to study the mineral composition for the mantle, and to assess the seismological models.

For both the 410km and 660 km discontinuities, the MD simulation for mineral composition models containing about 50 to 60 vol%  $(\text{Mg,Fe})_2\text{SiO}_4$  component is found to be compatible with a recent model SF99 (Shearer and Flanagan, 1999) within nearly 1 sigma limit of SF99 for all density and P- and S-wave velocity jumps. However, for both the 410km and 660 km discontinuities, our MD computed density jumps, either for the pyrolite or the piclogite composition, are substantially smaller than the values by the PREM (Dziewonski and Anderson, 1981) or the ak135 model (Kennett et al., 1995).

#### References

- Dziewonski, A.M., Anderson, D.L., 1981. *Phys. Earth Planet. Inter.* **25**, 297-356.  
Kennett, B. L. N., Engdahl, E. R., Buland, R., 1995. *Geophys. J. Int.* **122**, 108-124.  
Matsui, M., 1999. *Phys. Earth Planet. Inter.* **116**, 9-18.  
Matsui, M., 2000. *Phys. Earth Planet. Inter.* **121**, 77-84.  
Matsui, M., Parker, S.C., Leslie, M., 2000. *Am. Mineral.* **85**, 312-316.  
Shearer, P. M., Flanagan, M. P., 1999. *Science* **285**, 1545-1548.

### 3.6 Mineralogy of the lower mantle by the combined method of a laser-heated diamond anvil cell experiment and analytical transmission electron microscopy

Kiyoshi Fujino<sup>1\*</sup>, Nobuyoshi Miyajima<sup>1</sup>, Yohei Sasaki<sup>1</sup>, Reki Odawara<sup>1</sup>, Hisayuki Ogawa<sup>1</sup>,  
Nagayoshi Sata<sup>2</sup>, Takehiko Yagi<sup>2</sup>

<sup>1</sup>Hokkaido University, <sup>2</sup>ISSP, University of Tokyo

\* <fujino@ep.sci.hokudai.ac.jp>

#### 1. Introduction

For the study on mineralogy of the Earth's lower mantle, a laser-heated diamond anvil cell (DAC) experiment is indispensable because it is almost the only method to produce static high pressures corresponding to the Earth's lower mantle. However, characterization of the synthesized materials is not easy because these materials are very small in amount and very fine in grain size. Analytical transmission electron microscopy (ATEM) is suitable for characterization of such materials. With ATEM we can analyze both structures and chemistries of these materials in a nanometer scale. Therefore, the combined method of a laser-heated DAC experiment and ATEM is very powerful for the mineralogy of the lower mantle. However, both techniques have several problems to be improved. We present the outline of a newly installed YLF-laser heated DAC system and the attempts to overcome problems in AEM analyses of ultrahigh pressure materials, along with the preliminary results on the mineralogy of the lower mantle.

#### 2. Newly installed YLF laser-heated DAC system

The newly installed DAC system consists of double-sided laser heating by a YLF laser and spectroradiometric temperature measurement. The YLF laser is operated in TEM<sub>01</sub>(donut) mode with output power of maximum 53 W. The laser-heated spot size ranges from 20 to 150 micrometer in diameter. Temperature profiles of the heated sample are displayed nearly in real time by fitting the thermal radiation to the Plank radiation function. More detailed data of the heating stability, the precision of measured temperatures and temperature profiles will be given in the meeting.

#### 3. Analytical transmission electron microscopy

Although ATEM is very powerful to analyze synthetic ultrahigh pressure materials by DAC [1] and also natural ultrahigh pressure minerals [2], analyses by ATEM have problems as follows [3];

- 1) Ultrahigh pressure materials are very weak against an electron beam and easily become amorphous.
- 2) In ion-thinning to prepare ATEM foils of these materials, elements are selectively removed from the surface area of the foils.
- 3) A properly spread (weak) electron beam must be used to prevent the selective removal of elements from the foil during the measurement of characteristic X-ray intensities.

To overcome the problem 1), we are installing a high-sensitive TV camera system for electron microscope by which we can observe electron images and diffraction patterns of the ultrahigh pressure materials under the very weak electron beam.

To resolve the problem 2), we proposed to use the experimentally determined k-factors to calculate compositions [3]. We are now examining another way to resolve this, ultramicrotomy instead of ion-thinning to prepare ATEM foils. Ultramicrotomy was originally developed to prepare ultrathin TEM

foils in biology. In this method samples embedded in polymeric resin are sectioned into very thin foils with a diamond knife. So far, the DAC samples could be sectioned into 40 nm thick foils, and EDS analyses of  $\text{MgSiO}_3$  perovskite showed an nearly ideal chemical formula.

#### 4. Preliminary results on the mineralogy of the lower mantle

To explore the solubility relations between  $(\text{Mg,Fe})\text{SiO}_3$ - and  $\text{CaSiO}_3$ - perovskites under the lower mantle conditions, phase relations of the system  $\text{CaMgSi}_2\text{O}_6$ - $\text{CaFeSi}_2\text{O}_6$  under the lower mantle conditions and chemical compositions of the product phases have been examined.

In the analyses of the recovered samples synthesized at 20-40 GPa and 1700-2300 K by a laser-heated DAC using diopside-hedenbergite solid solutions as starting materials,  $\text{MgSiO}_3$  perovskite coexists with  $\text{CaSiO}_3$  perovskite in the diopside composition. Their EDS analyses showed that the Ca content in  $\text{MgSiO}_3$  perovskite was within 1 mol%, but the reliable composition of coexisting  $\text{CaSiO}_3$  perovskite has not yet been obtained. The obtained Ca content of  $\text{CaSiO}_3$  perovskite is far lower than that of the ideal chemical formula.

#### References

- [1] Miyajima, N., Fujino, K., Funamori, N., Kondo, T., and Yagi, T. (1999) Garnet-perovskite transformation under the Earth's lower mantle conditions: An analytical transmission electron microscopy study. *Phys. Earth Planet. Inter.*, **116**, 117-131.
- [2] Tomioka, N. and Fujino, K. (1997) Natural  $(\text{Mg,Fe})\text{SiO}_3$ -ilmenite and -perovskite in the Tenham meteorite. *Science*, **277**, 1084-1086.
- [3] Fujino, K., Miyajima, N., Yagi, T., Kondo, T., and Funamori, N. (1998) Analytical electron microscopy of the garnet-perovskite transformation in a laser-heated diamond anvil cell. Proceedings of the U.S.-Japan Seminar, AGU, Washington, 409-418.

### 3.7 Mineralogy of subducted basaltic crust (MORB) in the lower mantle

S. Ono<sup>1</sup>, E. Ito<sup>2</sup>

<sup>1</sup>IFREE, JAMSTEC, <sup>2</sup>ISEI, Okayama Univ.

#### 1. Introduction

Recent seismological studies [1-3] indicate the presence of seismic structures in the lower mantle. Laboratory experiments indicate that the pressure-induced phase transitions of the olivine component of the mantle occur at about 13.5 GPa and 23.5 GPa, these phase transitions being thought to be responsible for the seismic discontinuities at 410 km and 660 km depths. However, an adequate explanation of the seismic observations has not yet been forthcoming. Peridotitic material converts to an assemblage of Mg-rich and Ca-rich perovskites and magnesiowtite by a depth 750 km, and this lithology probably persists deep in the lower mantle [4]. Therefore, we explore experimentally whether phase transitions in subducted oceanic crust (MORB) might be responsible for the deeper seismic observations.

Recently, we have developed a multianvil apparatus using sintered diamond anvils, which provides stable conditions for long-duration runs to 50 GPa and 3000 K. Here we report an experimental study on the phase relations in MORB composition over a pressure range from 25 to 37 GPa, i.e. depths of 700-950 km in the mantle. The results provide insight into seismic observations and dynamics of deeply subducted slabs in the lower mantle.

#### 2. Experimental methods

Sintered diamond anvils with truncated edge length of 2 mm were used in combination with magnesia octahedron. Pressure calibration was carried out using several fixed points up to higher than 33 GPa. We further confirmed pressures up to 40 GPa at room temperature, based on equations of states of Au and MgO (used as pressure markers) by means of in situ X-ray diffraction using a synchrotron radiation source, SPring-8. High temperature generation was performed by putting a small cylindrical rhenium heater in the pressure medium of magnesia together with a thermal insulator of LaCrO<sub>3</sub>. Powdered sample of the MORB composition was put directly into the rhenium heater. After loading to the desired pressure, the sample was heated at 1973 K for at least 3 hours. The recovered sample was polished and examined by an electron probe-micro analyzer (EPMA). The lattice parameters of the phases were measured by micro-focused X-ray diffractometry.

#### 3. Results and discussion

Runs were conducted at 25-37 GPa and 1973 K in a multianvil press. The mineral assemblage observed at 25 GPa was majoritic garnet + stishovite + Ca-perovskite. We confirm that at 30 GPa majoritic garnet completely disappeared, and the MORB composition crystallized into an assemblage of Mg-perovskite + Ca-perovskite + stishovite + aluminous phase with the calcium ferrite type structure. At pressures between 30 and 37 GPa we encountered no further phase changes. These results are generally consistent with those of Kesson et al. [5], who examined the high pressure and temperature mineral chemistry of the MORB by transmission electron microscopy on run products from the diamond anvil cell.

We estimated that the change in proportions of major phases in the MORB composition for depths from 200 to 1000 km in the mantle [6]. A conspicuous change in the mineral assemblage occurs at depths of 700-800 km, where, corresponding to the disappearance of majoritic garnet, Mg-perovskite and the aluminous phase appear as major phases and the proportions of Ca-perovskite and stishovite also increase rapidly. It should be noted, however, that in the region beyond 800 km, no further change

in the mineralogical constitution of MORB was encountered.

The density of MORB under lower mantle conditions was calculated for various temperatures with an appropriate equation of state using suitable thermoelastic parameters. The average mantle is denser than MORB at the top of the lower mantle owing to the transition of spinel to a dominantly perovskitic lithology at the 660 km discontinuity. However, the density of the MORB increases rapidly at 700-750 km as a consequence of the change from a majoritic garnet-dominant assemblage to one dominated by perovskite, which is then denser than surrounding average mantle.

The density profile of MORB is definitely expected to intersect the average mantle density at depths between 1500 and 2000 km (depending on the temperature within the subducted slab). The density crossover indicates the presence of a neutral buoyancy region, and the MORB portion of the subducted slab might stagnate at that depth. Indeed, static neutrally buoyant oceanic crust might also be responsible for the recently observed transition in seismological heterogeneity at a depth around 1600 km. To derive more definite conclusions as to the fate of the entire subducted slab deep in the lower mantle, however, we have to carry out density calculations for the whole slab, including the layers of depleted peridotite and sediment.

#### References

- [1] H. Kawakatu, F. Niu, Seismic evidence for a 920-km discontinuity in the mantle, *Nature* **371** (1994) 301-305.
- [2] R. D. van der Hilst, H. Kàrason, Compositional heterogeneity in the bottom 1000 kilometers of Earth's mantle: toward a hybrid convection model, *Science* **283** (1999) 1885-1888.
- [3] S. Kaneshima, G. Helffrich, Dipping low-velocity layer in the mid-lower mantle: evidence for geochemical heterogeneity, *Science* **283** (1999) 1888-1891.
- [4] S. E. Kesson, J. D. Fitz Gerald, J. M. Shelley, Mineralogy and dynamics of a pyrolite lower mantle, *Nature* **393** (1998) 252-255.
- [5] S. E. Kesson, J. D. Fitz Gerald, J. M. Shelley, Mineral chemistry and density of subducted basaltic crust at lower-mantle pressures, *Nature* **372** (1994) 767-769.
- [6] S. Ono, E. Ito, and T. Katsura, Mineralogy of subducted basaltic crust (MORB) from 25 to 37 GPa, and chemical heterogeneity of the lower mantle, *EPSL* **190** (2001) 57-63.

### 3.8 In situ X-ray diffraction measurements for some mantle minerals to 40 GPa using a combination of synchrotron radiation and multianvil apparatus with sintered diamond anvils

Tetsuo Irifune\*, Yuichiro Sueda, Takeshi Sanehira, Hisanobu Naka, Toru Inoue, Yuji Higo, Takayuki Ueda, Ken-ichi Funakoshi, and Wataru Utsumi

\*Geodynamics Research Center, Ehime University, 2-5 Bunkyo-cho, Matsuyama, Ehime 790-8577 Japan

Phase transformations in some mantle minerals have been studied at pressures 20 - 40 GPa and temperatures to 1800K using SPEED-1500 at SPring-8. High pressure generation was performed using sintered diamond (SD) cubes of 14 mm edge length, manufactured by Sumitomo Electric Industries Co. Ltd. In situ X-ray diffraction measurements were made by the energy dispersive system equipped at the BL04B1 beamline of SPring-8. Pressure was monitored by unit cell changes of Au using an adequate equation of state, while the temperature measurement was based on e.m.f. of W97Re3-W75Re25 thermocouple. Twin sheet heaters of Re was used, and the sample was directly enclosed in MgO pressure medium. We made several such in situ X-ray diffraction measurements for  $\text{MgAl}_2\text{O}_4$  and  $\text{Ca}_{0.5}\text{Mg}_{0.5}\text{SiO}_3$ , which are both important constituents of the upper mantle peridotite, as the first attempt in our SD experiments at SPring-8.

$\text{MgAl}_2\text{O}_4$  spinel was found to transform to  $\text{CaFe}_2\text{O}_4$ -type phase at pressures above 25 GPa via an assemblage of MgO periclase and  $\text{Al}_2\text{O}_3$  corundum at lower pressures. No evidence for the formation of the  $\text{CaTi}_2\text{O}_4$  phase, which was reported recently on the basis of diamond anvil cell experiments, was obtained at pressures to 40 GPa and temperatures to 1800K in the present experiments. The presence of  $\epsilon\text{-MgAl}_2\text{O}_4$  reported earlier was also not confirmed, and it is thus most likely that the  $\text{CaFe}_2\text{O}_4$  phase is the only stable phase under these P/T conditions.

$\text{Ca}_{0.5}\text{Mg}_{0.5}\text{SiO}_3$  diopside transformed to an assemblage of  $\text{CaSiO}_3$  and  $\text{MgSiO}_3$  perovskites at pressures to about 35 GPa and temperatures to 1500K, confirming our recent results based on both quench and in situ X-ray diffraction measurements at lower pressures (<25 GPa). The bulk moduli (K) of both of these perovskites were estimated based on the present and some existing in situ X-ray diffraction data, avoiding the effects of the deviatoric stress produced in the sample. The preliminary data analyses yield the  $K_0$  values of 230 GPa for  $\text{CaSiO}_3$  perovskite and 260 GPa for  $\text{MgSiO}_3$  perovskite, respectively.

### 3.9 Exploration of $\beta$ -Fe using sintered diamond anvils

Atsushi Kubo, Eiji Ito, Tomoo Katsura, Toru Shinmei, Hitoshi Yamada, Osamu Nishikawa,  
Maoshuang Song, Kenichi Funakoshi

Institute for Study of the Earth's Interior, Okayama University

Based on experiments using the laser-heated diamond-anvil cells (DAC), a new polymorph of Fe, called  $\beta$  phase, was reported [1, 2]. As to the structure of  $\beta$ -Fe, Saxena et al. [3] have claimed the double hexagonal closest packing (dhcp), while Andrault et al. [4] have persisted the orthorhombic (space group Pbcm). Both groups [3, 4], however, reported almost the same P-T stability field for  $\beta$ -Fe; i.e., higher than 35 GPa and ca. 1500K. On the other hand, Yoo et al. [5] observed the dhcp structure under the conditions of 15 - 40 GPa and 1300 - 2000 K. Shen et al. [6] reported that the dhcp phase was never found at high temperature but found in temperature-quenched product at pressures lower than 60 GPa. In order to clarify if the  $\beta$  phase is really existent, it is desirable to do experiments using a multi anvil apparatus (MAA), which is superior to DAC in terms of larger sample volume, smaller deviatoric stress, and less temperature gradient through the sample. Funamori et al. [7] first studied P-T stability of Fe by in situ X-ray diffraction using MAA, and concluded that  $\beta$  phase was not found up to 32 GPa and 1500K. In the present study, we explored  $\beta$ -Fe by in situ X-ray observation up to conditions higher than 40 GPa and 1900 K using MAA equipped with sintered diamond (SD).

Cubic SD anvil assembly was squeezed by a press SPEED-1500 installed at SPring-8. The SD cubes used in the present study were of 14 mm edge length with truncated edge length (TEL) of 1.5 or 2.0 mm. Several experimental runs were carried out. Figure 1 shows a cross section of a representative cell assembly. A fine powder mixture of Fe + MgO (1:1 in wt.) was put into a semi-sintered MgO sleeve of 0.6 mm outer diameter (OD), 0.3 mm inner diameter (ID) and 0.5 mm length. The sleeve was set at the center of a cylindrical Re heater of 0.7 mm OD, 0.65 mm ID and 1.85 mm length. Very fine powder (< 1 micron) of diamond was packed into the remaining spaces inside the heater. The Re heater was placed inside a LaCrO<sub>3</sub> thermal insulation sleeve that was embedded in an octahedral pressure medium made of MgO + 5 wt% Cr<sub>2</sub>O<sub>3</sub>. Temperature was monitored using W97%/Re3%-W75%/Re25% thermocouple in contact with the central surface of the Re heater. High-pressure in situ X-ray diffraction study was performed by energy-dispersive method using synchrotron radiation X-ray. Incident white X-ray cut to 0.05 mm in horizontal and 0.1 or 0.2 mm in vertical was irradiated to the sample from the direction parallel to the axis of the Re cylindrical heater (Fig. 1). The press position was adjusted to make incident X-ray shoot the sample and the MgO sleeve independently. The horizontally diffracted beam was introduced to the Ge-SSD through the collimator of 0.05 mm width to ensure the diffraction angle  $2\theta = 6.0^\circ$ . By this method, diffraction patterns of the sample together with weak reflections from diamond powder were collected (Fig. 2). The generated pressure was determined by measuring the volume of MgO of the sample sleeve based on the pressure scale of Jamieson et al. [8]. Diffraction patterns of MgO sleeve and the sample were acquired alternatively at the same press load and temperature for typically 5 and 10 minutes, respectively. The recovered samples were polished to make chemical analyses by electron probe micro analyzer (EPMA).

Here we describe the results of a typical run S614 (TEL 2.0 mm). The heating and cooling cycles were performed up to 1700 and 1900 K at press loads of 662 and 803 tonf, respectively.

In the first cycle at 662 tonf, Fe initially assumed  $\epsilon$  phase at 37.7(4) GPa and 300 K. On heating,  $\gamma$  phase appeared at 1400 K and 38.4(2) GPa. The peaks from  $\gamma$  phase intensified in accord with weakening of those from  $\epsilon$  phase to 1700 K. However, the peaks of  $\epsilon$  phase still survived at 1700K presumably due to temperature gradient in the sample. On cooling, the diffraction peaks of  $\gamma$  phase began to weaken accompanying with the increase of  $\epsilon$  peaks at 1300 K and 36.9(1) GPa. However, the diffraction peaks of  $\gamma$  phase still remained even at 300K and ca. 34 GPa. In addition to the above observation, many small peaks were noticed on increasing temperature higher than 1100K that were

thoroughly assigned to diffraction peaks of either FeO (wüstite) or Fe<sub>3</sub>C (cementite) [9].

On isothermal compression from 662 to 803 tonf at 300 K,  $\gamma$  phase was always observed with  $\epsilon$  phase. The diffraction pattern of FeO slightly changed at 675 tonf and 300 K; i.e., the (111) and (220) reflections became weak and broad presumably due to splitting of these peaks while the intensity of (200) reflection unchanged. These changes indicate phase transition of FeO from B1 to the rhombohedral structure [10].

The second heating cycle at 803 tonf was started from 300K and ca. 36 GPa. On heating, no change in diffraction pattern was observed up to 1300 K. However, the growth of reflections from  $\gamma$  phase was recognized at 1600K and 41.1(2) GPa, associating with the reduction of  $\epsilon$  phase, and became prompt with increasing temperature (Fig. 2). It should be noted that the diffraction patterns in Fig. 2 show the larger thermal expansivity of  $\epsilon$  than that of  $\gamma$ . Phase transition in FeO (rhombohedral to B1) was also observed at 1000 K and 39.1(4) GPa. The sample was quenched at 42.2(3) GPa and 1900 K.

EPMA analyses of the run products revealed that Fe grains and MgO in the sleeve remained as pure Fe and MgO, respectively. However, marginal portion of MgO grains in the sample changed to ferropericlasite (Fp) showing chemical zoning of 0 - 19 mol% FeO. The FeO component of Fp should have derived by oxidation of the outer layer near the surface of Fe grains. Existence of Fe<sub>3</sub>C was confirmed in the very limited region between the sample and diamond powder by analyzing the product after aluminum coating.

The results obtained in the present study indicate that the  $\epsilon - \gamma$  boundary is approximated by  $T$  (K) =  $670 + 18P$  (GPa) over pressures from 14 to 42 GPa. We obtained no evidence for the presence of  $\beta$  phase with the dhcp or the orthorhombic Pbcm structure up to 42.2(3) GPa and ca. 1900 K. Therefore, the present study do not support the stability of  $\beta$  phase under conditions higher than 35 GPa and ca. 1500 K claimed by DAC experiments [1-5].

#### References

- [1] Saxena et al., Science 260, 1312 (1993)
- [2] Boehler, Nature 363, 534 (1993)
- [3] Saxena et al., Science 269, 1703 (1995)
- [4] Andrault et al., Science 278, 831 (1997)
- [5] Yoo et al., Science 270, 1473 (1995)
- [6] Shen et al., GRL 25, 373 (1998)
- [7] Funamori et al., GRL 23, 953 (1996)
- [8] Jamieson et al., in High-Pressure Research in Geophysics, pp. 27-48, CAPJ, Tokyo (1982)
- [9] Scott et al., GRL 28, 1875 (2001)
- [10] Fei and Mao, Science 266, 1678 (1994)

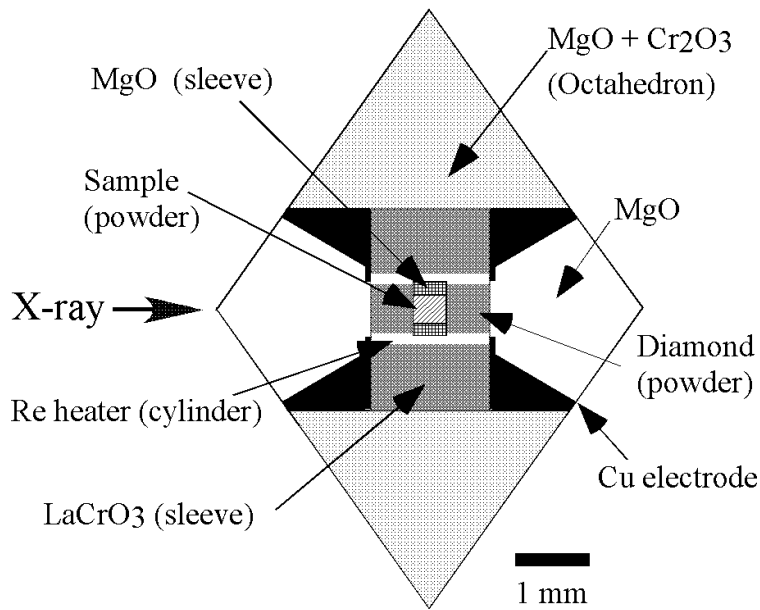


Fig. 1 A schematic drawing of the sample assembly used in the run S614.

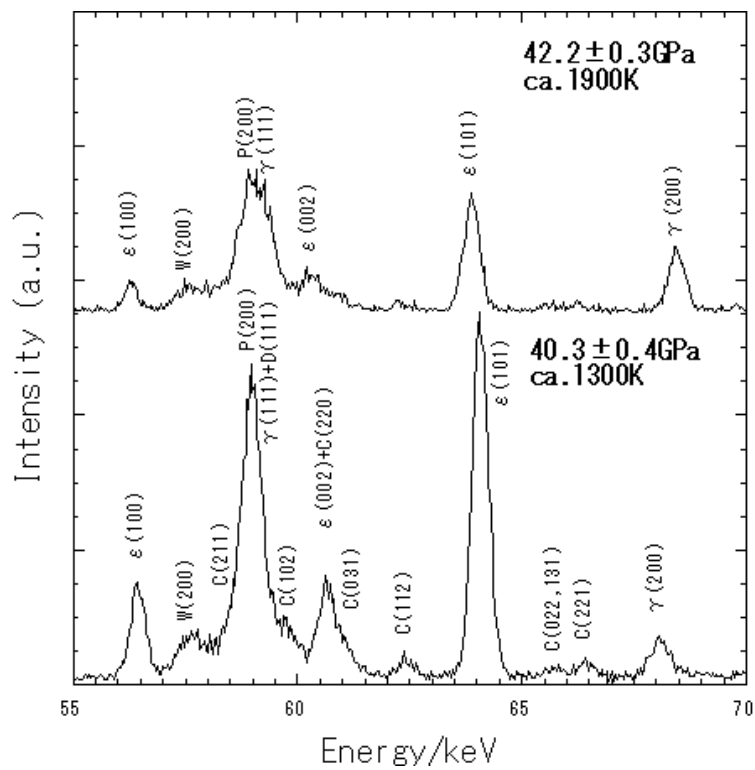


Fig. 2 Diffraction patterns obtained at 803 tonf and 1300K (lower) and 1900K (upper). P: periclase, D: diamond, C: cementite, W: wüstite.

### 3.10 High-pressure phase relationships of FeS

Satoru Urakawa\*, Masayuki Hasegawa, Junji Yamakawa, Ken-ichi Funakoshi, Wataru Utsumi

\*Department of Earth Science, Okayama University

Phase relationships for FeS polymorphs have been studied at the pressure of 16-20 GPa and the temperature of 300-1350 K by in situ X-ray observation. Experiments were carried out by an energy dispersive X-ray diffraction method using SPEED-1500 system at BL04B1 of SPring-8. FeS transforms from monoclinic phase to NiAs-type phase via hexagonal phase, with increasing temperature at 16-20 GPa. Contrary to Fei's prediction [1], we found that NiAs-type phase of FeS is stable at 18 GPa. The stability fields will extend the higher pressure than 20 GPa. Our results correspond with the NiAs-hexagonal phase boundary determined by Kusaba et al [2, 3]. Assuming the straight NiAs-hexagonal phase boundary, we evaluate the location of the NiAs-hexagonal-liquid triple junction at 39.5 GPa and 2300 K.

#### References

- [1] Fei, Y. et al., *Science*, **268**, 1892, 1995.
- [2] Kusaba, K. et al., *Geophysical Monograph* **101**, 297, 1998.
- [3] Kusaba, K., et al., *Journal of Physics and Chemistry of Solids*, **59**, 945, 1998.

### 3.11 Experimental determination of compressional wave velocity of olivine aggregate at 1 GPa up to 1273 K

Yoshitaka Aizawa

Institute for Study of the Earth's Interior, Okayama University , aizawa@misasa.okayama-u.ac.jp

The velocity of the compressional wave ( $V_p$ ) was measured for olivine aggregate at temperatures up to 1273 K at 1 GPa using a piston-cylinder high-pressure apparatus. The samples used in the present study were hot-pressed olivine aggregate with uniform chemical composition. The value of  $V_p$  at 1 GPa and an ambient temperature is 8.42 km/s, which is identical to that in previous measurements of olivine single-crystals. The temperature derivative of  $V_p$  ( $dV_p/dT = -4.7 \times 10^{-4}$  km/s/K) obtained from the present experiments at 1 GPa is smaller than the previously reported value at an ambient pressure. The temperature gradient for constant velocity  $(dT/dZ)_c$  allowing the effect of anelasticity is calculated to be 4 K/km. Taking the temperature gradient in the upper mantle into account (15 K/km within the lithosphere and 0.6 K/km within the asthenosphere), it is suggested that the low velocity zone in the upper mantle could be caused by a drastic change in the temperature gradient at the lithosphere/asthenosphere boundary.

### 3.12 Temperature dependence of elastic moduli of polycrystalline wadsleyite and ringwoodite

N. Mayama\*, I. Suzuki, T. Katsura, A. Yoneda, I. Ohno

\*Earth Science, Okayama University

We synthesized and sintered polycrystalline specimens of wadsleyite (beta-phase) and ringwoodite (gamma-phase) using the San Carlos olivine with composition of  $(\text{Mg}_{0.91}\text{Fe}_{0.09})_2\text{SiO}_4$  at high P/T conditions. We measured the resonance frequencies of the sphere specimens of beta- and gamma-phases for 13 and 8 isotropic oscillatory modes at ambient condition, and the 9 and 6 modes in them were traced up to 700K. We obtained the adiabatic bulk modulus,  $K_S=167.7(2)\text{GPa}$  and shear modulus,  $G=106.13(4)\text{GPa}$  for beta-phase, and  $K_S=185.0(1)\text{GPa}$ ,  $G=118.10(5)\text{GPa}$  for gamma-phase, respectively at 298K. The average slope of the moduli were found to be  $dK_S/dT= -0.0176(1)\text{ GPa/K}$ ,  $dG/dT= -0.0156(3)\text{ GPa/K}$  for beta-phase and  $dK_S/dT= -0.0188(1)\text{ GPa/K}$ ,  $dG/dT= -0.0155(3)\text{ GPa/K}$  for gamma-phase, respectively. The numerals in parentheses indicate probable errors in the last place.

The compressional ( $v_p$ ) and shear ( $v_s$ ) wave velocities of the high pressure specimens as well as the olivine phase under upper mantle conditions were calculated with the aid of the modified Watchman's equation. Comparing these results with seismic Earth models, we estimated the olivine content around the 410km-discontinuity, to be about 60 and 45 volume % for  $v_p$  and  $v_s$ , respectively. With the same way, the olivine content was also estimated from 30 to 50 volume % for shear wave at 520km-discontinuity. If olivine content is uniform below 410km-depth and has the volume ratio estimated above, the jumps of seismic velocities and acoustic impedance at 520km-discontinuity were estimated to be about 1.5% and 2.5%, though some of seismic Earth models do not indicate discontinuity at 520km-depth.

### 3.13 X-ray diffraction study of CaO at high pressure and temperature: equation of state of CaO

Takaya Nagai, Koichi Kittaka, Takamitsu Yamanaka

Department of Earth and Space Science, Osaka University, 1-1 Machikaneyama, Toyonaka, Osaka 560-0043, JAPAN

Pressure-volume measurements have been performed for CaO at  $P=0-73$  GPa and  $T=295-643$  K using an externally heated diamond anvil cell and angular dispersive X-ray diffraction method. Heating was accomplished with a Pt/Rh-resistance coil heater placed surrounding diamond anvils and temperature was measured by almel-chromel thermocouple attached to the surface of a diamond anvil. Temperature difference between sample and thermocouple was calibrated and it should be within  $\pm 3$  K. More homogeneous temperature distribution in sample chamber can be expected rather than laser heating method. Pressure was determined by ruby fluorescence method at 295 K and by the equation of state of gold (Anderson et al., 1989) at high temperatures. Silicon grease was used as pressure-transmitting media and pre-indented rhenium gasket was used. Angular dispersive X-ray diffraction measurements were carried out using a 12 kW Molybdenum-target rotating anode X-ray generator with a graphite monochromator (Rigaku RU-200) and an imaging plate system (Rigaku Raxis IV<sup>++</sup>) as a detector. The lattice parameters of CaO and gold (pressure marker) were determined by a profile-fitting method, since some diffraction lines of CaO and gold are partially overlapped.

It has been known that the pressure-induced phase transition occurs from the B1 to the B2 structure on CaO. We confirm that the transition is reversible and the transition pressure is between 61 and 63 GPa and at 295 K. We also confirm that the transition pressure is almost independent of temperature and this can be explained that the B1-B2 transition is driven by elastic instability rather than by thermal activation as discussed in Tsuchiya and Kawamura (2001).

Room temperature equation of state parameters of the B1 phase are identified as  $K_{T0} = 117(1)$  GPa with  $K'_{T0} = 4$  (fixed), whereas the third-order Birch-Murnaghan equation of state yields  $K_{T0} = 125(2)$  GPa and  $K'_{T0} = 3.6(1)$ . These parameters are in good agreement with those of Richet et al.(1988). High temperature data sets at 488, 584 and 643 K were analyzed by high-temperature Birch-Murnaghan equation of state.  $K'_{T0} = 3.6$  was assumed constant and zero-pressure thermal expansion  $\alpha(0, T)$  of Okajima (1978) was used. We obtained  $(\partial K_{T0}/\partial T)_p = -0.0114(4)$  GPaK<sup>-1</sup> and this value is comparable with the value  $(\partial K_{T0}/\partial T)_p = -0.0147(4)$  GPaK<sup>-1</sup> of the molecular dynamics simulation (Matsui, 1998).

#### References

- Anderson, O.L., D.G. Isaak and S. Yamamoto (1989) *J. Appl. Phys.*, vol.65, 1534-1543.  
 Matsui, M. (1998) *J. Chem. Phys.*, vol.108, 3304-3309.  
 Okajima, S. (1978) *Master thesis of Okayama University*.  
 Richet, P., H.K. Mao and P.M. Bell (1988) *J.Geophys.Res.*, vol.93, no. B12, 15279-15288.  
 Tsuchiya, T. and K. Kawamura (2001) *J. Chem. Phys.*, vol.114, 10086-10093.

### 3.14 Thermal equation of state of an omphacite

Yu Nishihara, Eiichi Takahashi, Tomohiro Iguchi, Keisuke Nakayama, Kyoko Matsukage, Miki Shirasaka and Takumi Kikegawa

Earth and Planetary Sciences, Tokyo Institute of Technology

Omphacite is one of the most abundant minerals in subducted mid oceanic ridge basalt (MORB) at the pressure condition of 3 - 15 GPa. In order to understand the behavior of MORB in the deep mantle, knowledge about physical properties of omphacite would be impotent. In situ synchrotron X-ray diffraction experiments were conducted on an omphacite, which was synthesized at 5 GPa and 1773 K, at simultaneous high-pressures and high-temperatures by using multi-anvil apparatus MAX-III, and pressure-volume-temperature data were collected up to 10 GPa and 1000 K. A fit to the high-temperature Birch Murnaghan equation of state yielded, isothermal bulk modulus  $K_{T0} = 120(2)$  GPa, with assumed pressure derivative of bulk modulus  $K'_T = 5.0$ , temperature derivative of bulk modulus  $(dK_T/dT)_P = -0.014(5)$  GPa  $K^{-1}$ , and volumic thermal expansivity with  $\alpha = a + bT$  with values of  $a = 1.6(4) \times 10^{-5} K^{-1}$  and  $b = 0.9(7) \times 10^{-8} K^{-2}$ , when equation of state of NaCl by Brown (1999) is adopted for pressure scale. The derived  $K_{T0}$  value is consistent with the linear interpolations from those of diopside and jadeite in literatures.

### 3.15 Static compression of Fe-Si alloy

Naohisa Hirao, Tadashi Kondo, Eiji Ohtani, and Takumi Kikegawa

Tohoku University

Seismic data indicate that the density of the Earth's outer core is about 10% lower than the density of iron at the core pressures and temperatures (e.g., (1, 2)). Light alloys with iron are assumed to be present to account for the density deficit of the core. H, C, O, S, and Si are considered as the candidates of the light elements (e.g., (3)). Therefore, the properties of iron compounds at high pressures provide constraints on the composition of the Earth's inner core as well as outer core. However, there are little experimental data at the core pressures on the properties of these iron compounds. Static compression experiment on Fe-Si alloy was carried out up to 50 GPa at room temperature (4). We have conducted high pressure experiments to clarify the structure and stability of Fe-Si alloy,  $\text{Fe}_{2.3}\text{Si}$ , under high pressures.

High pressure experiments for  $\text{Fe}_{2.3}\text{Si}$  have been conducted to the pressures above 70 GPa at room temperature by a Mao-Bell diamond anvil cell (DAC). Angle dispersive x-ray diffraction experiments at high pressure were performed using a synchrotron radiation source and an imaging plate detector at the BL-13A beamline of PF. The sample was loaded directly into the hole of a rhenium gasket. No pressure medium was used in experiments to obtain the maximum sample volume. Pressure was determined by the equation of state for rhenium to evaluate the pressure of the exposure area in x-ray experiments (5).

$\text{Fe}_{2.3}\text{Si}$  alloy has a metallic DO3 structure of  $\text{Fe}_3\text{Si}$  showing a body-centered-cubic (bcc) phase. No evidence for the phase transition was obtained at pressures to 74 GPa in this study. Using the second-order Birch-Murnaghan equation of state with a pressure derivative of bulk modulus, 4, the 300 K bulk modulus of  $\text{Fe}_{2.3}\text{Si}$  yields the value of 190 GPa.

#### References

- (1) Birch, F., J. Geophys. Res., 69 4377, 1964.
- (2) Dziewonski and Anderson, Phys. Earth Planet. Int., 25, 297, 1981.
- (3) Poirier, J. P., Phys. Earth Planet. Int., 85, 319, 1994.
- (4) Knittle and Williams, Geophys. Res. Lett., 22, 445, 1995.
- (5) Vohra et al., Phys. Rev. B, 36, 9790, 1987.

### 3.16 Theoretical estimations of contribution of electrons to the thermal expansion of Au and Pt metals

Taku Tsuchiya and Katsuyuki Kawamura

Dept of Earth and Planetary Sci., TITech, JAPAN

## Introduction

Au and Pt are often used as the pressure calibration standard in high-temperature high-pressure in-situ experiments. However, some recent studies suggest that the pressure values measured in high- $TP$  in-situ experiments are not in agreement with those determined in quench experiments.<sup>1-3</sup> As the origin of this discrepancy, uncertainty of pressure effect on a thermocouple, deficiency of used pressure scale itself, etc. are inferred. Especially, in the case that the equation of state of metal constructed only using low-temperature experimental data is used as a pressure scale under high- $TP$  conditions, there is possibility of some underestimation of pressure value. The fact that the effect of the electron expected to become important under high temperature is hardly taken in these equations of state causes the underestimation.

However, this electronic effect to the thermal expansion of Au and Pt and its pressure dependence have never been studied at all. It is quite important to clarify whether this effect is negligible or not under the temperature pressure conditions of the Earth's mantle. In the present study based on the solid state physics and the electronic structure calculation method, we predict contributions of electrons to the thermal pressures of gold and platinum and discuss the necessity for possible improvement of the known equations of state under high- $TP$  conditions.

## Theory and calculation

According to the solid state physics,<sup>4</sup> the contribution of electrons to the thermal pressure in metals is represented based on the volume dependence of electronic free energy as follows,

$$P_e(V, T) = \frac{1}{2} \gamma_e \beta \left( \frac{T^2}{V} \right). \quad (2)$$

Here,  $\beta$  and  $\gamma$  are the electronic specific heat coefficient and the electronic Grüneisen parameter, respectively. These are written as

$$\beta = \frac{1}{3} \pi^2 k_B^2 N(E_F) \quad (3)$$

$$\gamma_e = \frac{\partial \ln \beta}{\partial \ln V}. \quad (4)$$

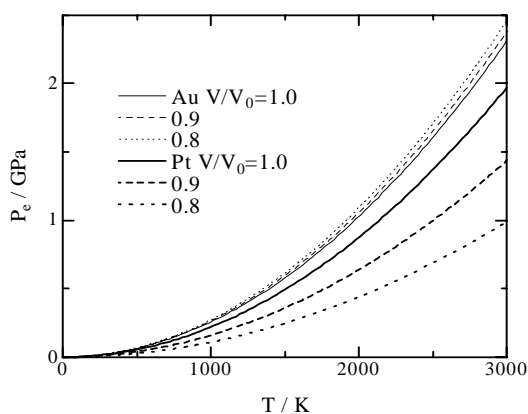
And  $N(E_F)$  is density of states (DOS) at the fermi level. Consequently,  $P_e(V, T)$  can be estimated from volume  $V$  and  $N(E_F)$  which can be calculated by the electronic structure of metal. In this study electronic structures of Au and Pt were calculated by the first principles method within the density functional theory (DFT) and the local spin density approximation (LSDA). It is known that the relativistic effect of valence electrons becomes important in the heavy element after the 5th period. In this study full-relativistic calculations were performed to correctly include the effect of spin-orbit coupling. The pressure values at 0K were determined by least-squares fitting of calculated static lattice energies and volumes to the third-order  $E$ - $V$  Birch-Murnaghan equation of state.

## Results and discussion

Calculated thermal pressures of Au and Pt are  $249.1(V/V_0)^{-0.3}T^2$  Pa (Au) and  $(379.4-39.2\ln V)(V/V_0)^{6.2-0.7\ln V}$  Pa (Pt), respectively.  $T$  dependencies of  $P_e$  at  $V/V_0 = 1.0, 0.9$  and  $0.8$  are drawn in the figure, which indicate some interesting and important results. (1)Au has larger electronic thermal pressures than those of Pt under all volume ranges that  $V/V_0 < 1$ . (2)The volume dependence of  $P_e$  is positive in gold but negative in platinum. This difference can be explained by the position of Fermi levels. Since all  $5d$  orbitals are full in gold, the Fermi level exists in the  $s$  band above the  $d$  band and the pressure dependence of  $P_e$  is small. On the other hand,  $5d$  orbitals are not full of platinum and the Fermi level crosses the  $d$  band. This results in the large pressure dependence of  $P_e$ . (3)At high-temperature corrections of  $P_e$  to the known equations of state may be important. Estimated values of  $P_e$  at 1500K and 25 GPa are 0.39 GPa and 0.59 GPa, respectively. However, these are not so large enough to explain the deviation of pressure values of in situ observations and quench experiments.

## References

1. Irifune et al. (1998)
2. Ono et al. (2000)
3. Hirose et al. (2001)
4. Ashcroft and Mermin *Solid State Physics* (Harcourt)



### 3.17 Thermal diffusivity and thermal conductivity of olivine and garnet under pressures up to 8 GPa and at temperatures up to 1000 K

Masahiro Osako<sup>1</sup>, Eiji Ito<sup>2</sup> and Akira Yoneda<sup>2</sup>

<sup>1</sup>National Science Museum, Tokyo <sako@kahaku.go.jp>

<sup>2</sup>Institute for Study of the Earth's Interior, Okayama University

To contribute toward study on the dynamic aspects of the Earth, we have measured the thermal conductivity and the thermal diffusivity of mantle candidate minerals under high pressures and at high temperatures.

A pulse method using one dimensional heat flow has been applied to simultaneous thermal diffusivity and thermal conductivity measurements. The sample, made in the form of three identical thin disks, is instantaneously heated by a pulse current in a thin heater inserted into one joint of the stacked disks. Change of temperature is observed on the other joint by a thermocouple. Thermal diffusivity is determined from decay time of the temperature profile, and thermal conductivity is calculated from the rise of temperature and an power of the current.

Experiments were performed using a uniaxial split-sphere high-pressure apparatus (USSA-1000) at ISEI. A magnesia octahedron with a edge length of 18 mm was used as a pressure medium in tungsten carbide anvils with a truncation of 11 mm. Dimensions of the sample were 4 mm in diameter and 1 mm in height. A furnace composed from a pair of metallic planar heater was installed in the octahedron for high temperatures. Fig. 1 shows the sample assembly.

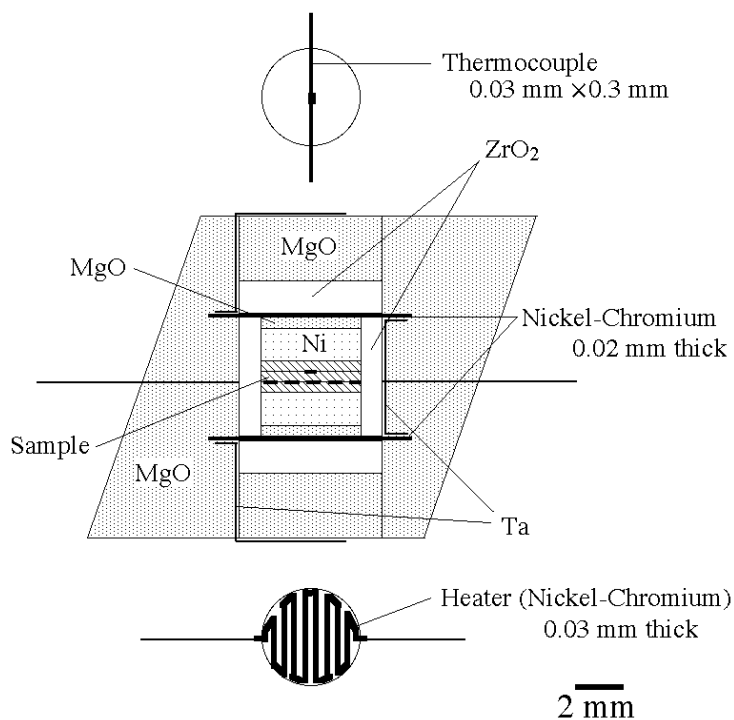


Fig. 1. Sample assembly used in this work.

Measurements were made on garnet and olivine single crystals under pressures up to 8.2 GPa. The garnet sample from Bahia, Brazil, has a composition of 73 % almandine and 25 % pyrope in molar fractions. This kind of garnet belongs to the cubic crystal system and reveals no heterogeneity in thermal conductivity, however, the sample disks were cut so that the end of their surface was perpendicular to one crystallographic axis. The olivine sample from northern Pakistan shows a idomorphic shape and has a composition of 93% forsterite and 7% fayalite in molar fraction. Olivine reveals high anisotropy in thermal conductivity or thermal diffusivity (Fig. 2), therefore, we need to prepare sets of disk specimens for the three different crystallographic axes.

Fig. 3 shows the thermal diffusivity and thermal conductivity of the olivine for b-axis under high pressures at room temperature. Error bars come from uncertainty of the thickness of specimens (0.001 mm) and from limits of resolutions for time and emf on the temperature profile. Extrapolated values of thermal conductivity or thermal diffusivity to zero pressure agree with those obtained by other methods. Reproducibilities of measurements are within 7 per cent for thermal diffusivity and within 15 per cent for thermal conductivity. In the case of olivine for the direction of b-axis the pressure dependences on thermal diffusivity and thermal conductivity is 5 per cent increase per 1 GPa. On the other hand the garnet is shown that the pressure derivatives of thermal diffusivity and thermal conductivity tend to decrease as pressure increases, whereas the olivine does not reveal such tendency. At 5 GPa the garnet has a pressure dependence of 2 per cent a 1 GPa for thermal diffusivity and 3 per cent a 1 GPa for thermal conductivity.

High temperature measurements of thermal diffusivity and thermal conductivity up to 1000 K were made at 8.2 GPa, the terminal pressure in this experiments. The thermal diffusivity or the thermal conductivity of garnet decreases moderately with temperature increase unlike normal insulators in the T-inverse law of thermal conductivity. The same effect on garnet is seen in previous measurements under zero pressure.

From our results, we can estimate the thermal diffusivity or the thermal conductivity of major constituents in the upper mantle. In the uppermost mantle garnet could have a thermal diffusivity of  $0.9 \sim 1.0 \times 10^{-6} \text{m}^2 \text{s}^{-1}$  and a thermal conductivity of  $2.6 \sim 2.8 \times \text{W/mK}$ . Those values would become  $0.8 \sim 0.9 \times 10^{-6} \text{m}^2 \text{s}^{-1}$  and  $2.8 \sim 3.5 \times \text{W/mK}$  at around 400 Km depth, the bottom of the upper mantle.

#### References

- [1] L. D. Dzhavadov. *High Temp.-High Pressures*, **7**: 49-54 (1975).
- [2] M. Osako. *Bul. Natl. Sci. Mus.*, **Ser E**, **20**: 1-7 (1997).
- [3] H. Fujisawa, N. Fujii, H. Mizutani, H. Kanamori and S. Akimoto. *J. Geophys. Res.*, **73**: 4727-4733 (1968).
- [4] T. Katsura. *Geophys. J. Int.*, **122**: 63-69 (1995).
- [5] A. E. Beck, D. M. Dabha and H. H. Schloessin. *Phys. Earth Planet. Inter.*, **17**: 35-53 (1978).
- [6] G. H. Schaermeri. In: W. Schreyer (Ed.), *High Pressure Researchs in Geoscience*, E. Schweizerbart'sche Verlangsbuchbandlung, Stuttgart, pp. 349-373 (1982).

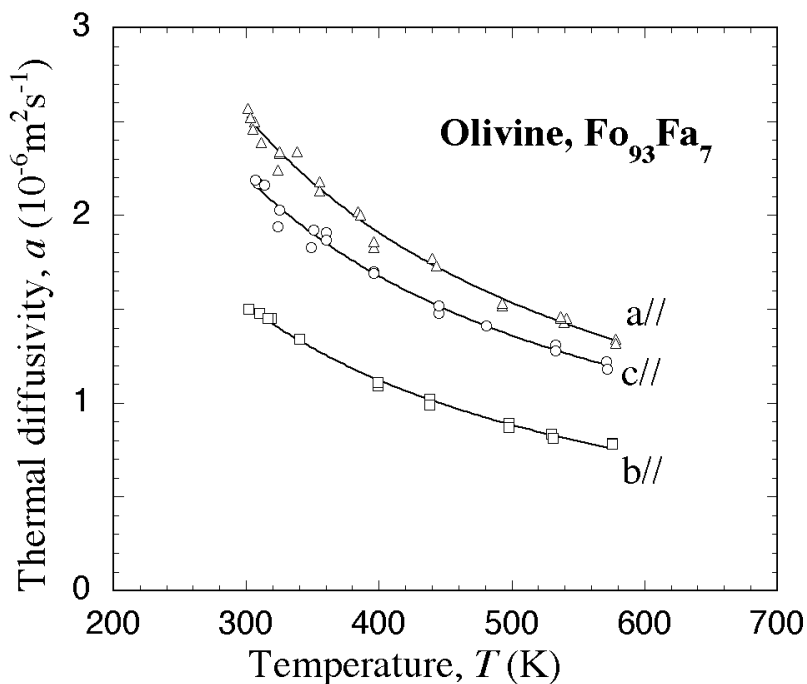


Fig. 2. Anisotropic thermal diffusivity of olivine at ambient pressure measured by an Angstrom method [2].

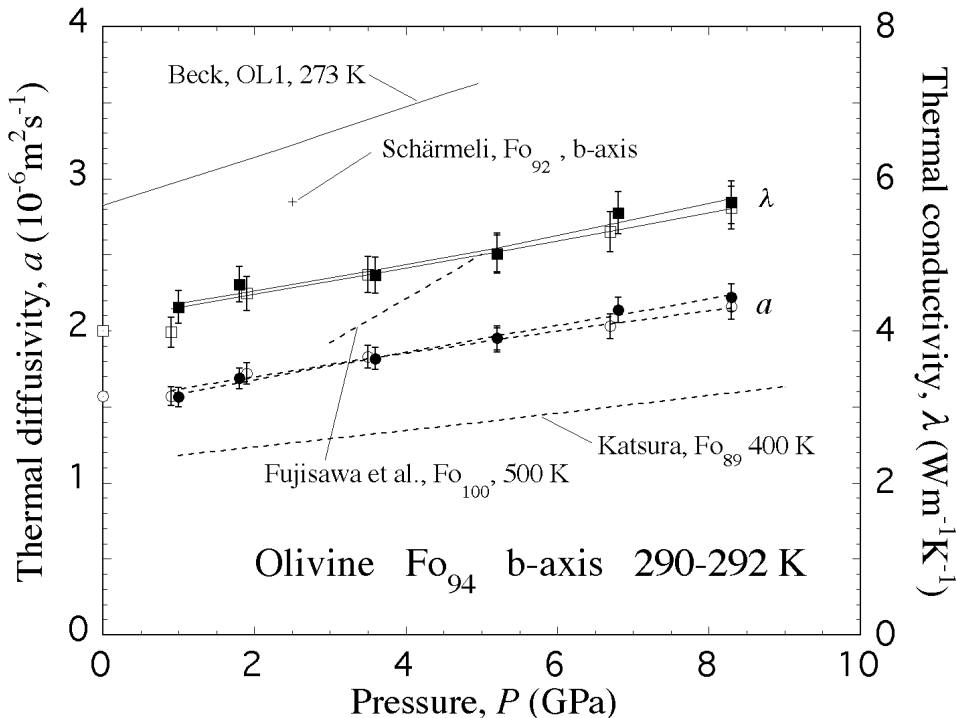


Fig. 3. Thermal diffusivity and thermal conductivity of olivine (parallel to b-axis) versus pressure compared with other results [3][4][5][6]. Circles and dotted lines denote thermal diffusivity, and squares, solid lines and cross denote thermal conductivity. Dotted symbols on the zero-pressure line are the thermal diffusivity in Fig. 1 and the calculated thermal conductivity.

### 3.18 Non-hydrostatic thermodynamics of anisotropic materials: geological implications for pressure solution

Akira Yoneda

Institute for Study of the Earth's Interior, Okayama University, Misasa, Tottori-ken 682-0193, Japan

#### Introduction

The occurrence of earthquakes and presence of highly deformed rock textures are unequivocal lines of evidence that non-hydrostatic stress and strain play an important role in geological processes. Despite its significance in geoscience, the basic thermodynamic theory for systems in a non-hydrostatic state has not been fully constructed yet, because the current formulation of Gibbs free energy,  $G$ , under non-hydrostatic stress has been debated for many years (Macdonald 1957; Kamb 1961; Kumazawa 1963; Ito 1966; Ida 1969; Paterson 1973; Robin 1974; Bayly 1987; Dahlen 1992; Shimizu 1992). In this paper, I present a new formulation of  $G$  in a non-hydrostatic stressed state within the elastic region or thermodynamically reversible region. The formulation is then applied to interpreting the pressure solution process (e.g., Evans and Kohlstedt 1995).

#### Formulation

The Gibbs free energy,  $G$ , under non-hydrostatic stress is formulated uniquely as

$$G = F - \sigma_{ij} \cdot \omega_{ij} \omega_{ij} = V \left( K_T S_{ijkl} \delta_{kl} + \Delta \epsilon_{ij}^+ \right),$$

where  $F$  is the Helmholtz free energy,  $\sigma_{ij}$  the stress,  $\omega_{ij}$  the tensorized volume newly defined,  $V$  the volume,  $K_T$  the isothermal bulk modulus,  $S_{ijkl}$  the elastic compliance, and  $\Delta \epsilon_{ij}^+$  the isochoric strain. For the first-order approximation, the above equation can be further simplified as

$$dG = -K_T dV,$$

where  $dV$  is the volume change for any given thermodynamically reversible process, including both hydrostatic and non-hydrostatic processes. An experimental result regarding a geological process of pressure solution supports the present formulation quantitatively. Further, the present formulation is successfully used to explain thermodynamic equilibrium in pressure solution process.

#### An experimental result supporting the present formulation

Elias and Hajash (1992) conducted a quantitative experiment controlling confining pressure and pore-fluid pressure on compaction of quartz sand; they determined chemical potential of quartz component in fluid from its concentration. Figure 1 compares their result with theoretical predictions. In their work, effective stress,  $P_e$ , is defined by subtraction of pore fluid pressure,  $P_f$ , from confining pressure,  $P_c$ , or  $P_e = P_c - P_f$ . Therefore positive  $P_e$  yields compressive state for quartz grains. During the experiment,  $P_f$  was kept constant at 345 bar and temperature at 150°C.  $P_e = 0$  bar, or,  $P_c = 345$  bar was the reference state to measure chemical potential change. The Gibbs-Kamb theory cannot explain experimental results at all. At lower stress, experimental result is in good agreement with prediction by uni-axial stress, while at higher stress it approaches to that by hydrostatic pressure. It is quite probable that stress state evolves from uni-axial state to tri-axial state with proceeding compaction caused by increasing effective stress. It is obvious that their result is consistent with the present formulation, at least in order of magnitude, and definitely against the Gibbs-Kamb theory.

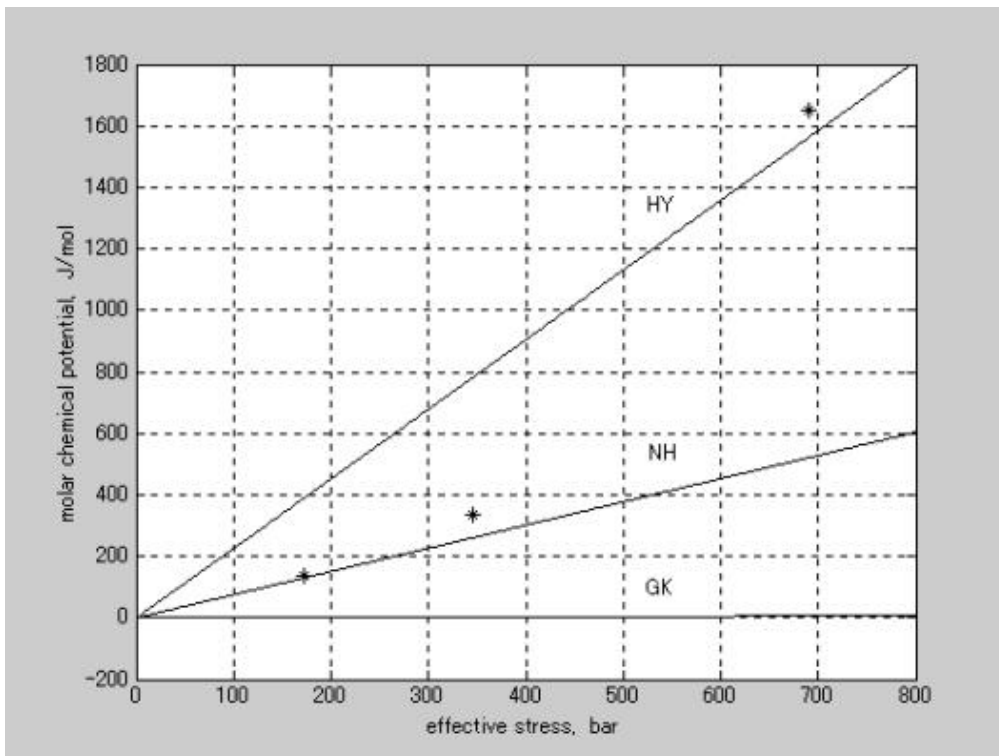


Figure 1 Molar chemical potential, or Gibbs free energy, variation induced by increasing effective stress; \*: experimental data; GK: prediction by Gibbs-Kamb theory,  $d\mu^* = P_f dV + dF$ ; NH: that by the present formulation for uni-axial stress,  $dG = -K_T dV = (1/3)V dP_e$ ; HY: that by hydrostatic compression,  $dG = -K_T dV = V dP_e$ .

### 3.19 Rates of cation diffusion in olivine and silicate perovskite under mantle conditions

Christian Holzzapfel<sup>1</sup>, D.C. Rubie<sup>1</sup>, S. Chakraborty<sup>2</sup>, F. Langenhorst<sup>1</sup>, D.J. Frost<sup>1</sup>

<sup>1</sup> Bayerisches Geoinstitut, Universität Bayreuth, 95440 Bayreuth

<sup>2</sup> Institut für Geologie, Mineralogie und Geophysik, Ruhruniversität Bochum, Universitätsstr. 150, 44780 Bochum

Determining the kinetics of mineral reactions and phase transformations is essential to understand dynamic and geochemical processes occurring in the Earth. One important area of study in this respect is the determination of the rate of chemical diffusion in mineral phases because slow diffusion rates in oxides and silicates often control reaction kinetics and can result in compositional zoning during chemical exchange. From measured chemical zonation patterns it is in principle possible to deduce information about the time scales of processes, temperatures and pressures. In this study we investigate diffusional behavior in olivine and (Mg,Fe)SiO<sub>3</sub> perovskite at high pressures and temperatures using the multianvil apparatus.

To investigate diffusion in olivine, single crystal diffusion couples were employed consisting of pure synthetic forsterite (Mg<sub>2</sub>SiO<sub>4</sub>) and natural San Carlos olivine ( (Mg<sub>1.88</sub>,Fe<sub>0.12</sub>)SiO<sub>4</sub>), contained in Au and Ni capsules. The oxygen fugacity was either directly buffered at the Ni-NiO buffer (Ni capsules) or was calibrated (Au capsules) by comparison with experiments at known oxygen fugacity. Observed diffusion profiles are 8 to 25 μm long and can be measured with high accuracy with the electron microprobe. In a first set of experiments we determined diffusion coefficients at a constant temperature of 1400°C and at pressures between 6 and 12 GPa and in a second set at a constant pressure of 12 GPa and temperatures between 1350°C and 1550°C. An activation volume of 5.5 cm<sup>3</sup>/mole was determined for Fe-Mg exchange, valid along the Ni-NiO buffer up to the upper pressure limit of olivine stability, which is consistent with former studies at lower pressure [1, 2]. We determine an activation energy of 282(47) kJ/mole at 12 GPa which is consistent with previous estimates at 1 bar. Over the range of investigated conditions, no change of slope of either ln *D* vs 1/*T* or ln *D* vs *P* was observed, suggesting a single diffusion mechanism in the investigated pressure-temperature regime. For Ni diffusion the activation volume is 6(1) cm<sup>3</sup>/mole and the activation energy is 352(72) kJ/mole. Mn diffusion coefficients are similar in magnitude to those for Fe-Mg exchange but a direct evaluation of the activation volume is difficult because of large analytical scatter due to low Mn concentrations. These results confirm that divalent cations with similar ionic radii have similar diffusional properties.

Although (Mg,Fe)SiO<sub>3</sub> perovskite is the dominant phase of the lower mantle and therefore probably the most abundant mineral in the Earth, there has been only one previous study of diffusion in this phase (Si self-diffusion in MgSiO<sub>3</sub>) [3]. In this study we have investigated Fe-Mg interdiffusion in polycrystalline perovskite diffusion couples at 24 GPa and 1750-2100°C. Samples with different iron contents (*X*<sub>Mg</sub> = 0.95 and 0.90) have been synthesized prior to the diffusion experiments. Experiments were performed at low *f*O<sub>2</sub> in the presence of metallic Fe. Because of extreme slow diffusion, concentration profiles are typically only 100 to 600 nm long. For analysis we use analytical transmission electron microscopy which, in addition to determining the diffusion profile, also allows a direct structural observation of the diffusion zone. In one sample an apparent influence of subgrain boundaries on the diffusion profile was observed. Samples at very high temperatures (> 1800°C) are intensively twinned, but so far line measurements and elemental maps show no effect of twin lamellae crossing the interface on diffusion profiles. At 1750°C and 24 GPa a diffusion coefficient of 3.66 × 10<sup>-20</sup> m<sup>2</sup>/sec is derived from our measurements. To explore possible effects of oxygen fugacity we are currently performing experiments at higher *f*O<sub>2</sub> in Re capsules

#### References

- [1] Farber et al. (2000):JGR 105(1), 513-529

[2] Misener (1974), In Hoffmann et al.: *Geochemical Transport and Kinetics*, 117-129, Carnegie Inst

[3] Yamazaki et al.(2000): Toriumi (2000): *Phys Earth Planet Int* 119, 299-309

### 3.20 Carbon self-diffusion in diamond

KT Koga, MJ Walter, E Nakamura, and K Kobayashi

*ISEI, Okayama University at Misasa, Misasa, Tottori, Japan*

The formation ages of diamonds have been inferred from various observations, yet they are not conclusive (Richardson et al., 1984, Rudnick et al., 1993; Shimizu and Sobolev, 1995; Pearson et al., 1998). Notable differences in estimated ages are 1 to 2 billion years old using a Sm-Nd model isochron determined for silicate inclusions in diamonds (Richardson et al., 1984), and less than 120 million years old inferred from the trace element zoning in garnet inclusions in diamonds (Shimizu and Sobolev, 1995). Advances in micro analytical techniques demonstrated that carbon isotopic ratio in diamond can show heterogeneity down to the tens of microns (Harte and Otter, 1992, and Hauri et al., 1998). Experimental determination of carbon diffusivity in diamond adds a strong constraint to the duration for which carbon isotopic zoning can persist under the pressure-temperature conditions of cratonic lithosphere. We have conducted the diffusion experiments at 10GPa and 1800°C. Our initial result of a carbon self-diffusion coefficient is approximately  $3 \times 10^{-21} \text{ m}^2/\text{s}$  in IA diamond annealed for 24 hours.

Experiments are designed and conducted as follows. The starting material is a small chip of natural IA diamond which was used as an anvil for DAC apparatus. To minimize the deformation related crystallographic imperfection, we have used undeformed, faceted girdle portion of a diamond. A thin, approximately 600°, isotopically enriched  $^{13}\text{C}$  is vapor deposited on top of polished diamond surface.

Experimental conditions were obtained using a split sphere-type multi-anvil apparatus at ISEI. Octahedral shaped MgO+5%Cr<sub>2</sub>O<sub>3</sub> was used as a pressure medium, and 50μm thick Re foil was used as a cylindrical heater. A  $^{13}\text{C}$  coated diamond piece was then packed with in MgO powder and MgO spacers in the central part of the Re heater. The temperature was monitored by a  $W_{74}\text{Re}_{26} - W_{95}\text{Re}_5$  thermocouple. After the anneal, the diamond surface was recovered by dissolving MgO in HCl. The diamond was mounted and surface roughness was determined by a Dektak surface profilometer.

The Diffusion profiles were determined by Cameca 5f at PML, ISEI, Okayama University. We have used the depth profiling technique on diamond, which is to raster the ion beam from a direction parallel to the direction of diffusion, to obtain a high resolution diffusion profile. Focused oxygen beam was rastered over 50μm square area and electronic gate was used to collect the signal from the central, approximately 35μm square, region. The spattered secondary ions were accelerated to 4.5kV and an electron multiplier counted the  $^{12}\text{C}^+$  ions for 1s and  $^{13}\text{C}^+$  ions for 4s. No energy filtering was applied, and the mass resolution was approximately 500. Molecular interference of  $^1\text{H}^{12}\text{C}^+$  to  $^{13}\text{C}^+$  was insignificant in our measurements since the range of  $^{13}\text{C}/^{12}\text{C}$  ratio for diffusion experiments far exceeds that of nature. We also have obtained approximately natural level abundance ratio of  $^{13}\text{C}/^{12}\text{C}$  in a natural, untreated diamond.

The largest uncertainty of the diffusion experiments is due to mixing of diffusant layer caused by topography at the diamond surface. Over a distance of 100μm along the surface, a range of 40nm high frequency topography is common. This topography prevents the determination of diffusion coefficient from a profile shorter than 40nm long. Thus the diffusion profiles determined from short duration, and/or low temperature experiments does not provide significant information. Our 24h annealing at 1800°C produced a diffusion profile over 120nm in depth while the surface topography ranged over 60nm. The minimum possible diffusivity is  $7 \times 10^{-23} \text{ m}^2/\text{s}$  which is calculated from a profile only due to surface mixing. Considering small differences between depth profile range and surface topography, the present result needs to be confirmed with longer duration experiments and with significantly longer diffusion profile than the surface topography. Until those determination, we only infer the value as an initial estimate.

The implication to the age of diamond from this result is limited since there is no understanding of the activation energy of diffusion from one data point. However, using the results of ab initio cal-

culations for the energy of vacancy formation and migration (Swalin, 1961; Bernholc et al., 1988; Bernholc et al., 1992), it is possible to extrapolate the initial result to the condition of subcontinental lithosphere which is around 800-1200°C. Using 750kJ/mol activation energy from above estimate, diffusivity is about 7 to 17 order of magnitude smaller than  $3 \times 10^{-21} \text{m}^2/\text{s}$  reported here. In one billion years, the equilibration distance will be from  $3 \mu\text{m}$  to 30pm. Thus, according to the current inference, the reported carbon isotope zoning in diamond could persist for durations on the order of the age of the Earth.

- Bernholc J., Antonelli A., Del Sole T. M., Bar-Yam Y., and Pantelides S. T. (1988) Mechanism of self-diffusion in diamond. *Phys.Rev.Lett.* 61, 2689-2692.
- Bernholc J., Kajihara S. A., Wang C., and Antonelli A. (1992) Theory of native defects, doping and diffusion in diamond and silicon carbide. *J.Mater.Sci.Eng.* B11, 265-272.
- Harte B. and Otter M. (1992) Carbon isotope measurements on diamonds. *Chem.Geol.* 101, 177-183.
- Hauri E., Pearson D., Dulanova G., and Milledge H. (1998) Microscale variations in C and N isotopes within mantle diamonds revealed by SIMS. *7thInternationalKimberliteConference*, 317-319.
- Pearson D. G., Shirey S. B., Harris J. W., Carlson R. W., (1998) Sulphide inclusions in diamonds from the Koffiefontein kimberlite, S Africa: constraints on diamond ages and mantle Re-Os systematics. *EarthPlanet.Sci.lett.*, 160, 311-326.
- Richardson S. H., Gurney J. J., Erklank A. J., and Harris J. W. (1984) Origin of diamonds in old enriched mantle. *Nature* 310, 198.
- Rudnick, R. L., Elderidge, C. S., and Bulanova, G. P. (1993) Diamond growth history from in situ measurement of Pb and S isotopic compositions of sulfide inclusions. *Geology*, 21, 13-16.
- Shimizu N., and Sobolev N. V., (1995) Young peridotitic diamonds from the Mir kimberlite pipe. *Nature*, 375, 394-397.
- Swalin R. A. (1961) Theoretical calculations of the enthalpies and entropies of diffusion and vacancy formation in semiconductors. *J.Phys.Chem.Solids* 18, 290-296.

### 3.21 Stored strains and boundary characters of dynamically recrystallized quartz aggregates

Osamu Nishikawa

Institute for Study of the Earth's Interior, Okayama University

The strain energy and grain boundary misorientation recorded in the growing and the consumed grains during dynamic recrystallization process are fundamental information, respectively about the driving force of the grain boundary migration and the grain boundary character. I have investigated strains stored in grains and grain boundary misorientations for naturally sheared and recrystallized quartz aggregates (Hatagawa mylonite) on the basis of detailed analyses of the crystallographic orientations and the microstructures.

Analysis of crystallographic orientation distribution patterns using a SEM-EBSP system and TEM observations revealed that  $\{10\bar{1}1\}\langle a \rangle$  slip system was dominantly operated, and  $(0001)\langle a \rangle$  and  $\{10\bar{1}0\}\langle a \rangle$  slip systems also operated subordinately during deformation. Grain sizes and shapes in quartz aggregates exhibit bimodal distributions: coarse ribbon grains of which their long axes oriented parallel to mylonitic lineation forming banding structures, and fine equant grains which are prevailed in highly strained portions. Serrated grain boundaries are well developed in ribbon grains. The grains favorably oriented for  $\{10\bar{1}1\}\langle a \rangle$  and  $\{10\bar{1}0\}\langle a \rangle$  slip tend to grow to large ribbon grains. Microstructural features of these grains are smooth boundary and low intra-grain misorientation (lower than  $5^\circ$ ), which is regarded as strain free. These observations suggest that grains favorably oriented for active slip systems ( $\{10\bar{1}0\}\langle a \rangle$  and  $\{10\bar{1}1\}\langle a \rangle$ ) rapidly grew at the expense of differently oriented neighboring grains during deformation.

Strains stored in grains have been investigated in more detail by analyzing dislocation sub-structures using a TEM. Free dislocation densities and mean subgrain size throughout the samples are  $10^8 \text{ cm}^{-2}$  orders and  $1.5 \mu\text{m}$  respectively, and no significant differences are found among grains by their orientation. However, misorientations at the subgrain boundaries are significantly dependent on the crystallographic orientation of host grains. Grains favorably oriented for  $\{10\bar{1}0\}\langle a \rangle$  and  $\{10\bar{1}1\}\langle a \rangle$  slips have the subgrain boundaries with small misorientation by  $2^\circ$ , while larger misorientation exceeding several degree are common in other grains. The results of TEM observations indicate that once dislocation density exceeds a certain critical value, for example  $10^8 \text{ cm}^{-2}$  orders in the present case, newly multiplied dislocations are absorbed into subgrain boundaries with rotation of subgrain. Therefore, the difference of strain energy stored in grains could describe only by those of subgrain boundary energy, which depends on degree of misorientation.

Misorientations between neighboring grains have been calculated in order to investigate the grain boundary characters. For the grains favorably oriented for  $\{10\bar{1}0\}\langle a \rangle$  and  $\{10\bar{1}1\}\langle a \rangle$  slips, in addition to frequent occurrence of low angle boundaries, those close to Dauphiné twin relationship whose twined parts are related by a rotation of  $180^\circ$  around  $c$ -axis are also found very often. It has been believed that Mechanical Dauphiné twinning are frequently introduced in  $\alpha$ -quartz during plastic deformation, and cause  $r\{1011\}$  poles to orient parallel to the compression axis rather than  $z\{0111\}$  pole. However, no preferred orientation of  $r$  and  $z$  poles was found in the samples. Therefore, it is concluded that grain boundary characters in the present samples are completely controlled by  $a$ - and  $c$ -axes preferred orientations, and not by mechanical twinning.

### 3.22 In-situ observation of plastic deformation at high pressure and temperature: A preliminary study

Masami Kanzaki

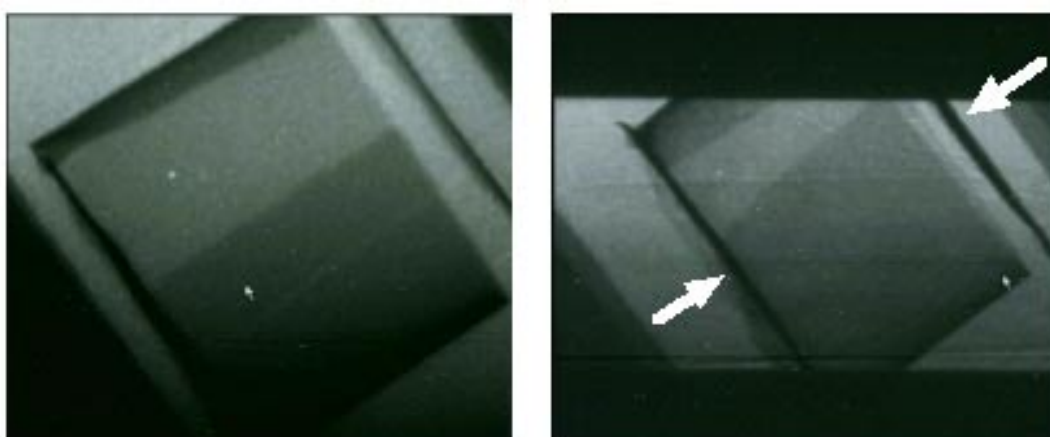
Institute for Study of the Earth's Interior, Okayama Univ., Misasa, Tottori 682-0193 Japan;  
mkanzaki@misasa.okayama-u.ac.jp

#### 1. Introduction

Deformation experiment utilizing multi-anvil apparatus is difficult, because strain and stress can not be measured directly by conventional techniques. Therefore no quantitative deformation experiment has been conducted to date. In this study, we developed in-situ sample strain measurement technique based on X-ray radiography under high pressure and temperature conditions. In order to test this technique, we measured deformation of polycrystalline forsterite ( $\text{Mg}_2\text{SiO}_4$ ) under compression.

#### 2. Experimental

Experimental setup for X-ray radiography is similar to our in-situ viscosity measurement (Kanzaki et al, 1998). SPEED1500 press at SPring-8 was employed to generate high pressure and temperature. 18M MgO cell was used. Rod shaped sample ( $d=1.9\text{mm}$ ,  $l=1.9\text{mm}$ ) was obtained by sintering polycrystalline forsterite at 1 atm and  $1500^\circ\text{C}$ . Pair of hard alumina pistons is placed at top and bottom of the sample. The sample is covered by 25 micron thick platinum foil. Since platinum absorbs more X-ray compared to silicate, it acts as a sample shape marker for radiography. In this way, we could monitor sample shape during the experiment (see Fig. 1). With increasing pressure, part of sample is eclipsed by WC anvils. Nevertheless, we can observe not only height but also diameter, so sample volume can be calculated. The cell was first compressed to 3 GPa at room temperature. Then it was heated up to  $1200^\circ\text{C}$ . After annealing the sample for 2 h, the sample is isothermally compressed to 6.5 GPa (3.5GPa/8h). During the experiment, X-ray image of the sample has been recorded in digital video tape. We also monitored guide block displacement and anvil gap length during the experiment.



**Before**

**After compression**

*X-ray radiographs of sample before (left) and after (right) the compression. Inclined rectangular area at the center is forsterite sample. Arrows show compressional stress directions by hard alumina pistons. Note that significant reduction of sample length by compression.*

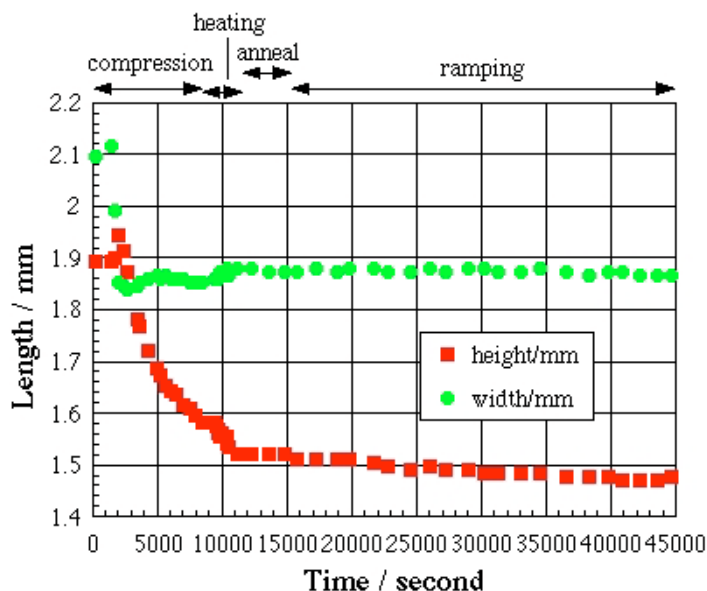
### 3. Results and Discussion

Fig. 2 shows change in sample shape during the deformation experiment. At initial compression at room temperature, the sample length reduced up to 20%. We noted that there is no significant change in diameter. Therefore reduction in length is mostly due to reduction of sample porosity. During the heating, sample length reduced slightly with increase of diameter. So at this stage, deformation without volume change has been taking place. At ramping stage, we observed sample length reduction, but it was much smaller than that of initial compression. Part of this reduction should be due to elastic deformation. Judging from bulk modulus of forsterite, sample strain due to plastic deformation at whole ramping stage would be about 1%.

Our preliminary study shows that by directly observing the sample shape, quantitative information of deformation can be obtained. This is significant improvement over previous indirect studies. Previous studies relied on guide block displacement as an indicator of sample length change. However, our data revealed that guide block displacement is not good indicator at all, especially at heating stage. Present result showed that plastic deformation at ramping stage is very small. This result is already predicted by Durham and Rubie (1998), from their analysis of recovered MgO pressurized medium. In order to obtain better strain data at ramping stage, high resolution CCD camera and better sample arrangement such as employed by Karato and Rubie (1997) must be employed. We observed small but real deformation at heating stage. This is not reported before, but stress relaxation of sample during heating by diffraction technique has been reported. Thus combining stress and strain measurements, stress relaxation behavior as a function of temperature could be fully explored.

#### References:

- Durham and Rubie (1998) in "Properties of Earth and Planetary Materials", AGU.  
 Kanzaki et al. (1998) SPring-8 User Experimental Report No.2, 1998A, p78.  
 Karato and Rubie (1997) J. Geophys. Res., 102, 20111-20122.



Height and width (diameter) changes during the compression of polycrystalline forsterite. Data at very initial stage ( $t \leq 2000$ s) contain large error. Note large height reduction at initial compression and following small change at ramping.

### 3.23 Conduction mechanism of fayalite and gamma-Fe<sub>2</sub>SiO<sub>4</sub>: electrical conductivity jump by olivine-spinel transition

D. Sakamoto\*, A. Yoshiasa, O. Ohtaka, T. Yamanaka and K. Ota

\*Earth and Space Science, Graduate School of Science, Osaka University

Fayalite and gamma-Fe<sub>2</sub>SiO<sub>4</sub> are an end member of (Mg<sub>1-x</sub>Fe<sub>x</sub>)<sub>2</sub>SiO<sub>4</sub> olivine and ringwoodite solid-solutions, respectively. Bradley et al. (1963) mentioned that the electric conductivities of fayalite and gamma-Fe<sub>2</sub>SiO<sub>4</sub> were induced by electron hopping, Fe<sup>2+</sup> = Fe<sup>3+</sup> + e.

Xu et al. (1998) measured the electric conductivities of olivine, wadsleyite and ringwoodite under upper-mantle conditions. The 2 orders of conductivity jump was found at the olivine-wadsleyite transition, while the conductivity jump was not found at the wadsleyite-ringwoodite transition. It has not been solved yet why ringwoodite (or gamma-Fe<sub>2</sub>SiO<sub>4</sub>) exhibits higher conductivity than olivine (or fayalite).

In this study the difference in conduction mechanism of fayalite and gamma-Fe<sub>2</sub>SiO<sub>4</sub> was examined by in-situ measurement of electric conductivity and Seebeck coefficient under high pressure. Noted that an electron (or hole) mobility can be estimated by electric conductivity and Seebeck coefficient. The mobility is important factor to decide conduction mechanism, because a small polaron has a low mobility (Emin 1975).

Electric conductivities of fayalite and gamma-Fe<sub>2</sub>SiO<sub>4</sub> at 6.2 GPa were fitted to the above equation and the fitting results yield the values of =1.99(0.02) and Ea=0.396(0.002) eV (376~670K) for fayalite =1.99(0.02) and Ea=0.396(0.002) eV (534~1057K) for gamma-Fe<sub>2</sub>SiO<sub>4</sub>, respectively.

A hole mobility of gamma-Fe<sub>2</sub>SiO<sub>4</sub> at 500K, 1000K and 1500K can be estimated as  $8.53 \times 10^{-8} \text{m}^2 \text{V}^{-1} \text{S}^{-1}$ ,  $1.32 \times 10^{-6} \text{m}^2 \text{V}^{-1} \text{S}^{-1}$  and  $3.29 \times 10^{-6} \text{m}^2 \text{V}^{-1} \text{S}^{-1}$ , respectively. These values are much lower than  $8 \times 10^{-5} \text{m}^2 \text{V}^{-1} \text{S}^{-1}$  (Emin 1975). This feature shows the hopping conduction is dominant conduction mechanism in gamma-Fe<sub>2</sub>SiO<sub>4</sub> (spinel). It is assumed that an electric conductivity of fayalite exhibits intermediate character between hopping conduction and band conduction. On the other hand, it is considered an electric conductivity of gamma-fayalite exhibits hopping conduction. Hence, it is concluded that conductivity jump between ringwoodite (or gamma-Fe<sub>2</sub>SiO<sub>4</sub>) and olivine (or fayalite) is caused by a difference of conduction mechanism.

### 3.24 Electron energy-loss spectroscopy of garnet-perovskite high-pressure assemblages

Nobuyoshi Miyajima<sup>1</sup>, Falko Langenhorst<sup>1</sup>, Daniel Frost<sup>1</sup>, Dave Rubie<sup>1</sup> and Takehiko Yagi<sup>2</sup>

<sup>1</sup> Bayerisches Geoinstitut, Universitat Bayreuth, D-95440 Bayreuth, Germany  
(Nobuyoshi.Miyajima@uni-bayreuth.de)

<sup>2</sup> Institute for Solid State Physics, University of Tokyo, Kashiwa 277-8581, Japan

**Introduction:** The valences of iron and its cation sites in (Mg,Fe)SiO<sub>3</sub>-Al<sub>2</sub>O<sub>3</sub> perovskite are generally considered to have significant effect on the physical properties of the earth's lower mantle (e.g., electrical conductivity and cation diffusion). Recently, the high relative Fe<sup>3+</sup> concentration in (Mg,Fe)(Si,Al)O<sub>3</sub> perovskite was determined in the relation to the Al content and the possibility of a significant concentration of oxygen vacancies was demonstrated, using Mössbauer spectroscopy [McCammon, 1997] and electron energy-loss spectroscopy (EELS) [Lauterbach et al, 2000 & Gloter et al., 2000]. The latter has much potential for determination of redox states and coordination of chemical elements in high-pressure samples in which nanometer spatial resolution is often required due to the small size of the coexisting phases. In this study, iron oxidation states in garnet-perovskite transformation have been investigated using analytical transmission microscope (ATEM) equipped with parallel electron energy-loss spectrometer (PEELS). We discuss the Fe<sup>3+</sup> / ∑Fe ratio and the substitution mechanism of trivalent species of aluminous silicate perovskite.

**Experimental:** A natural orthopyroxene and two natural garnets with different chemical compositions were used as starting material (Table 1). The synthesis of a (Mg,Fe)(Si,Al)O<sub>3</sub> perovskite and majorite assemblage from natural orthopyroxene has been performed at 24.5 GPa and 2223 K using multi-anvil apparatus (for orthopyroxene starting material, run no. H1488). On the other hand, the high-pressure transformations from garnet to perovskite have been carried out at about 35 GPa (for pyrope, no. Prp01) and 65 GPa (for almandine, no. Alm01) using laser-heated diamond anvil cells. The Fe L<sub>2,3</sub>-edge electron energy-loss near-edge structure (ELNES) of product phases has been examined by ATEM operating at 200kV with PEELS and energy-dispersive X-ray spectrometer (EDS). Fe L<sub>2,3</sub> ELNES is a sensitive probe of the Fe<sup>3+</sup> / ∑Fe ratio which can be measured with a small electron probe, enabling the separate acquisition of spectra of silicate perovskite and the coexisting phases in a mixed assemblage. Quantification of the spectra followed the procedure described by van Aken et al. (1998), using an empirically calibrated universal curve.

Table 1. Composition of the phases for measurement of Fe-L<sub>2,3</sub> ELNES spectrum (NA not analysed)

Phase	Fe / (Fe + Mg +Ca)	Al <sub>2</sub> O <sub>3</sub> mol%	Fe <sup>3+</sup> / Total Fe
Orthopyroxene starting material for run of perovskite-majorite assemblage, no. H1488	0.09(1)	4.1(1)	< 6
Perovskite in two-phase assemblage, no. H1488	0.071(3)	2.6(1)	48
Majorite in two-phase assemblage, no. H1488	0.090(5)	10(2)	12
Pyrope starting material for run of garnet-perovskite transformation, no. Prp01	0.17*	23*	28
Perovskite, no. Prp 01	0.23(9)	19.6(9)	56
Almandine starting material for run of garnet-perovskite transformation, no. Alm01	0.78*	25*	NA
Silicate LiNbO <sub>3</sub> phase transformed metastably from perovskite, no. Alm 01	0.61	26.8	53

Note: Values in parentheses are experimental uncertainties by ATEM analysis. \* analyzed using a secondary electron microprobe.

**Results and Discussions:** The chemical composition and Fe<sup>3+</sup> / ∑Fe ratio of all analyzed samples are summarized in Table 1. A typical Fe L<sub>2,3</sub> ELNES spectrum for silicate perovskite and coexisting majorite from multi-anvil samples are illustrated in Fig. 1. Based on a simple fingerprint technique using a reference Fe<sup>2+</sup> spectrum of the starting material orthopyroxene, the Fe L<sub>2,3</sub> edge spectrum for majorite consists mainly of Fe<sup>2+</sup> and perovskite indicates primarily a mixed iron valence compound of Fe<sup>2+</sup> and Fe<sup>3+</sup>. This result suggests that in the silicate perovskite-majorite assemblage of

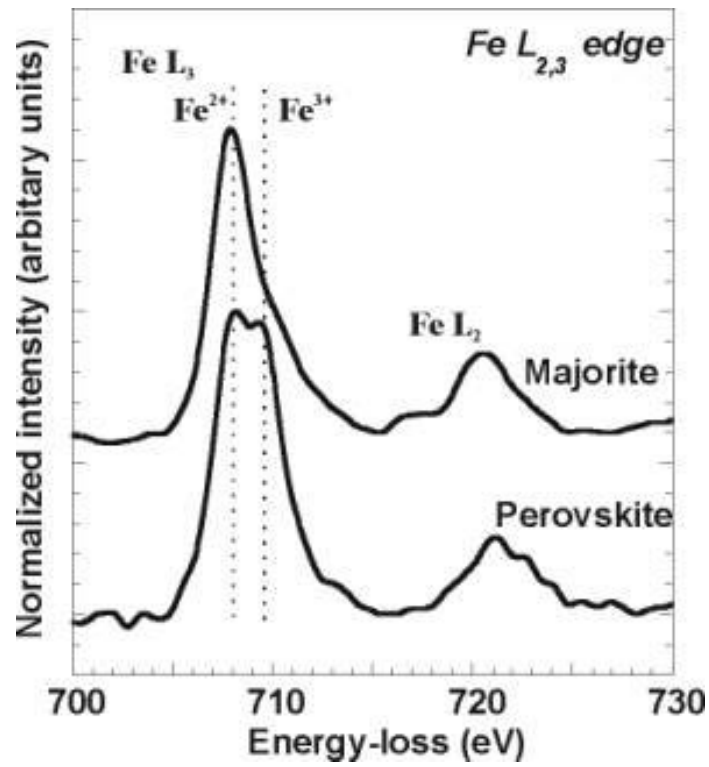


Fig. 1. Typical Fe  $L_{2,3}$ -edge ELNES of silicate perovskite and majoritic garnet.

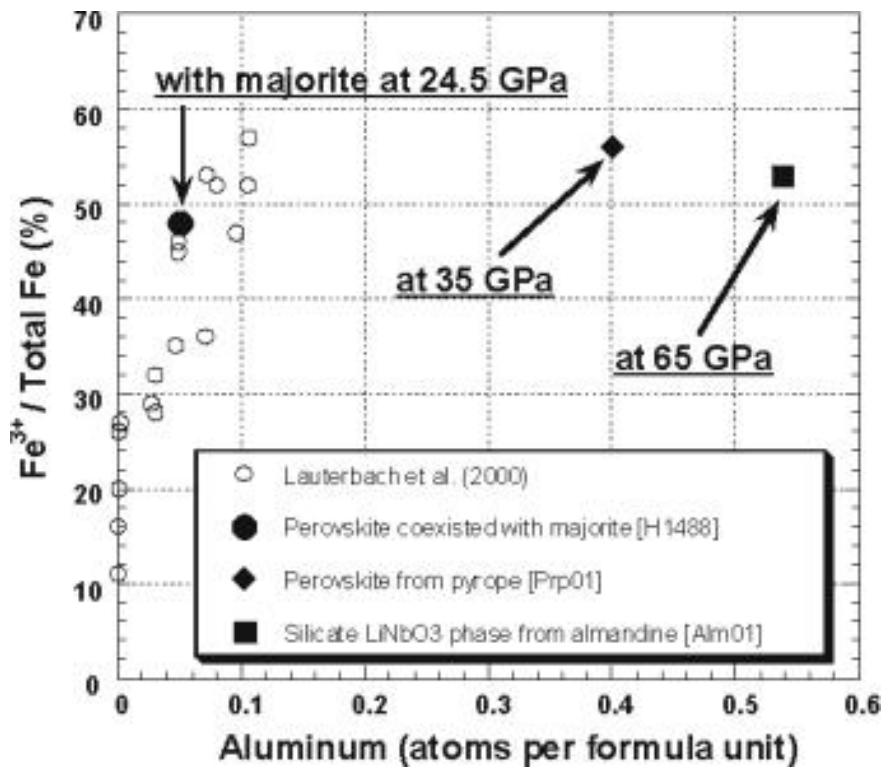


Fig. 2. Relation between  $Fe^{3+} / \sum Fe$  and Al composition for silicate perovskite.

(Mg,Fe)SiO<sub>3</sub>-Al<sub>2</sub>O<sub>3</sub> system, Fe<sup>3+</sup> has strong affinities with the perovskite phase under the same pressure, temperature and oxygen fugacity. Perovskites transformed from two garnets also contains the high relative Fe<sup>3+</sup> concentration, compared with the starting material garnets. In order to elucidate the relation between Fe<sup>3+</sup> / ∑Fe and Al composition for Al-rich perovskite, the compositions were plotted on Fig. 2, followed the Fig. 6 in Lauterbach et al. (ibid). Although the relative low Al-perovskite coexisted with majorite is plotted in a linear trend with their data, Al-rich perovskites are plotted out of the trend. This preliminary result might suggest a significant change of the following two mechanisms of incorporation of trivalent species into MgSiO<sub>3</sub> perovskite: (1)  $2\text{Si}_B^{4+} = 2(\text{Al}^{3+}, \text{Fe}^{3+})_B + \text{V}_O$  and (2)  $\text{Mg}_A^{2+} + \text{Si}_B^{4+} = \text{Fe}_A^{3+} + \text{Al}_B^{3+}$ . Which mechanism of Eq. (1) or (2) becomes favorable for Al<sup>3+</sup> and/or Fe<sup>3+</sup> in the lower mantle under the conditions of much higher pressure and the different bulk compositions such as silica-rich bulk composition (e.g., subducted slab) or MgO-rich composition? We are therefore currently examining samples in Fe-free system of MgSiO<sub>3</sub>-Al<sub>2</sub>O<sub>3</sub> for comparison.

#### References

- Gloter, A., Guyot, F., Martinez, I. & Colliex, C. (2000): Electron energy-loss spectroscopy of silicate perovskite-magnesiowustite high-pressure assemblage. *American Mineralogist*, 85, 1452-1458.
- Lauterbach, S., McCammon, C.A., van Aken, P., Langenhorst, F. & Seifert, F. (2000): Mössbauer and ELNES spectroscopy of (Mg,Fe)(Si,Al)O<sub>3</sub> perovskite: a highly oxidized component of the lower mantle. *Contrib Mineral Petrol*, 138, 17-26.
- McCammon, C.A. (1997): Perovskite as a possible sink for ferric iron in the lower mantle. *Nature*, 387, 694 - 696.
- van Aken P.A., Liebscher, B., Styrsa, V.J. (1998): Quantitative determination of iron oxidation states in minerals using Fe L<sub>2,3</sub>-edge electron energy-loss near-edge structure spectroscopy. *Phys Chem Minerals*, 25, 323-327.

### 3.25 NMR evidence for a new water dissolution mechanism in depolymerized silicate melts: results for hydrous diopside composition

X. Xue\*, T. Kawamoto, M. Kanzaki

\*Institute for Study of the Earth's Interior, Okayama University, Misasa, Tottori 682-0193 Japan

The dissolution of water in silicate melts significantly affects their phase relations, and physical/thermodynamic properties. The mechanism of water dissolution is thus a subject of intensive interest in earth sciences and has been studied by various spectroscopic techniques. However, almost all the studies thus far have been on relatively polymerized systems, from fully polymerized silicates (e.g.  $\text{SiO}_2$ ) to disilicate compositions (e.g.  $\text{Na}_2\text{Si}_2\text{O}_5$ ). These studies have shown that water is dissolved in either molecular  $\text{H}_2\text{O}$  or  $\text{SiOH}$  at least for Al-free systems. More depolymerized silicate melts, such as metasilicate compositions are also geologically important, because mantle-derived magmas are known to become less silica-rich with depth of generation. Such magma could be particularly important during the early evolution of the earth's mantle.

We have studied a hydrous diopside ( $\text{CaMgSi}_2\text{O}_6$ ) glass (quenched melt) using  $^{29}\text{Si}$  and  $^1\text{H}$  NMR in an attempt to understand the water dissolution mechanism in a depolymerized system. The sample contains about 3.85 wt%  $\text{H}_2\text{O}$  and has been synthesized at 1 GPa and 1500C in a piston cylinder apparatus. Both single-pulse  $^{29}\text{Si}$  and  $^1\text{H}$ - $^{29}\text{Si}$  cross-polarization (CP) MAS NMR yield a single, asymmetric peak near -82 ppm, resembling that of anhydrous diopside glass. The  $^1\text{H}$ - $^{29}\text{Si}$  CP time constant has been found to be 0.39 ms, similar to those of  $\text{SiOH}$  in other hydrous silicate glasses and crystals. Thus at least some of the dissolved water are in the form of  $\text{SiOH}$ . The  $^1\text{H}$  NMR spectra (both single pulse and spin-echo) contain two partially resolved peaks at 1.3 and 4.5 ppm. The 4.5 ppm peak is broader and asymmetric with a broad shoulder near 14 ppm. This peak and its shoulder are similar to those observed in more polymerized hydrous silicate glasses, such as  $\text{BaSi}_2\text{O}_5$ , and can be ascribed to  $\text{SiOH}$  and/or molecular  $\text{H}_2\text{O}$  with a range of H-bonding strengths. The 1.3 ppm peak is narrower and somewhat taller than the 4.5 ppm peak. The chemical shift of this peak indicates that it is due to OH groups that are not hydrogen-bonded. Peaks at this position has not been observed in any Al-free hydrous silicate glasses thus far and are not likely to be due to  $\text{SiOH}$  or molecular  $\text{H}_2\text{O}$ . On the other hand,  $\text{MgOH}$  in low-pressure hydrous magnesium silicates, such as talc, and  $\text{CaOH}$  in calcium silicate hydrates (CSH) are known to yield similar  $^1\text{H}$  NMR chemical shifts. We may thus assign this peak to  $\text{MgOH}/\text{CaOH}$ , suggesting that a substantial part of the dissolved water are in the form of free OH. Therefore the water dissolution mechanisms in silicate melts/glasses seem to change from molecular  $\text{H}_2\text{O}+\text{SiOH}$  in more polymerized systems to free OH groups plus  $\text{SiOH}/\text{molecular H}_2\text{O}$  in metasilicate compositions. Any model for water dissolution in depolymerized silicate melts/glasses must take this fact into consideration.

### 3.26 Ab initio calculation of the $^{17}\text{O}$ and $^1\text{H}$ NMR parameters for various OH groups: Implications to the speciation and dynamics of dissolved water in silicate glasses

X. Xue and M. Kanzaki

Institute for Study of the Earth's Interior, Okayama Univ., Misasa, Tottori 682-0193 Japan;  
mkanzaki@misasa.okayama-u.ac.jp

Ab initio molecular orbital calculations have been carried out for silicate, aluminosilicate and aluminate clusters, in order to study the NMR characteristics of various types of hydroxyls (OH) that are possibly present in hydrous silicate glasses and melts. The clusters have been optimized with the density functional theory (B3LYP/6-311+G(2df,p)), and their NMR parameters calculated at HF/6-311+G(2df,p). Our calculations suggest that the  $^{17}\text{O}$  and  $^2\text{H}$  quadrupolar coupling constants ( $C_q^O$ ,  $C_q^H$ ) and  $^1\text{H}$  chemical shift ( $\delta_i^H$ ) of SiOH, AlOH and bridging OH's (SiOHAl, AlOHAl) all show good correlation with the O-H and O-H...O distances. The calculated  $C_q^O$ ,  $C_q^H$  and  $\delta_i^H$  values agree well with those of experimental data for OH groups with similar O-H...O distances in crystalline phases. Our calculation suggests that hydroxyls with stronger hydrogen-bonding tend to yield smaller  $C_q^O$ ,  $C_q^H$ , and larger  $\delta_i^H$ . SiOH and bridging OH's of comparable hydrogen-bonding strengths give similar  $^{17}\text{O}$  and  $^1\text{H}$  ( $^2\text{H}$ ) NMR parameters. AlOH have a tendency not to form strong Al-O-H...O type hydrogen-bonding, and thus give relatively large  $C_q^O$ ,  $C_q^H$  and small  $\delta_i^H$ . On the basis of these calculation results, together with information for hydrogen-bonding strengths estimated from experimental vibrational spectra and  $^1\text{H}$  NMR data, we were able to predict  $^{17}\text{O}$  NMR parameters for hydroxyls in hydrous silicate glasses. The observed  $^{17}\text{O}$  NMR peaks for silica gel and hydrous albite glass, that have been attributed to SiOH, are significantly narrower than expected from  $C_q^O$ , suggesting that at least some of the SiOH, if present, must be non-rigid. The observed broad  $^{17}\text{O}$  NMR peaks for hydrous albite and alkali silicate glasses, originally attributed to molecular  $\text{H}_2\text{O}$ , could equally well be ascribed to rigid hydroxyls with no or weak hydrogen-bonding.

### 3.27 The effect of sulfur on silicate network structure in sodium silicate glasses

T. Tsujimura<sup>(1)</sup>, X. Xue<sup>(2)</sup>, M. Kanzaki<sup>(2)</sup>, A. Kitakaze<sup>(1)</sup> and Y. Kudoh<sup>(1)</sup>

(1) Department of Mineralogy, Petrology and Economic Geology, Graduate School of Science, Tohoku University, Sendai, 980-8943, Japan

(2) Institute for Study of the Earth's Interior, Okayama University, Misasa, Tottori, 682-0193, Japan

When the sulfur contents in silicate melts exceed the saturation limit, an immiscible sulfide melt segregates from silicate melts. Chalcophile elements partition preferentially into the sulfide melt effecting major changes in the trace and minor element distributions of the silicate melt and possibly generating metal-sulfide deposits (Naldrett et al., 1978; Ohmoto and Goldhaber, 1997). Thus, sulfur plays a crucial role in magmatic system although its contents in silicate melts are less than 1 wt.% (Poulson and Ohmoto, 1990; Tsujimura and Kitakaze, in prep.). Information about the effect of sulfur on the silicate melt network is therefore necessary in order to understand their physical and chemical properties. <sup>29</sup>Si magic angle spinning nuclear magnetic resonance spectroscopy (MAS NMR) work has demonstrated that the technique is useful in characterizing silicon coordination environment (Stebbins, 1988; Maekawa et al., 1991). The purpose of this study is to provide constraints on the effects of sulfur on the structure of sodium silicate glasses (quenched melts) using <sup>29</sup>Si and <sup>23</sup>Na MAS NMR.

Starting glasses of (Na<sub>2</sub>O<sub>(40)</sub>SiO<sub>2(60)</sub> and Na<sub>2</sub>O<sub>(30)</sub>SiO<sub>2(70)</sub>) compositions were prepared from reagent grade Na<sub>2</sub>CO<sub>3</sub> and SiO<sub>2</sub> at ambient pressure. Mixed starting materials were carefully melted in Pt crucible at 1000°C for 5 h and then quenched in water. All samples were clear glasses. 0.2 wt. % Gd<sub>2</sub>O<sub>3</sub> was added in all glasses to reduce the relaxation time of the <sup>29</sup>Si nucleus. For the sulfur-containing glass syntheses, the silicate glass and native sulfur were well mixed and sealed in an Au capsule with graphite powder. The ratio of the silicate glass to sulfur is 90:10 in weight. The samples were melted at 1000°C and 1-2 kbar and then quenched to glasses in an Ar-mediated internally heated pressure vessel with a rapid quenching device at Tokyo Institute of Technology (SMC-2000). We made MAS NMR measurements with a Varian UNITY-INOVA400NB spectrometer and a 5mm Jakobsen-type MAS probe at a Larmor resonance frequency of 79.5 and 105.9 MHz for <sup>29</sup>Si and <sup>23</sup>Na respectively. External chemical shift standards of tetramethyl-silane (TMS) for <sup>29</sup>Si and 1M aqueous NaCl for <sup>23</sup>Na were used.

For the Na<sub>2</sub>O<sub>(40)</sub>SiO<sub>2(60)</sub> composition, the <sup>29</sup>Si MAS NMR spectrum of the starting, sulfur-free glass consists mainly of two partially resolved peaks centered at -77.2 and -86.8 ppm, that are attributable to Q<sup>2</sup> and Q<sup>3</sup> species, respectively. Whereas in the spectrum of the sulfur-bearing glass, the intensity of the Q<sup>2</sup> peak decreases markedly. For the Na<sub>2</sub>O<sub>(30)</sub>SiO<sub>2(70)</sub> composition, the <sup>29</sup>Si MAS NMR spectrum of the starting, sulfur-free glass consists of a main peak centered at -89.3 ppm, attributable to Q<sup>3</sup> species, and a shoulder on the low frequency (more negative chemical shift) side, attributable to Q<sup>4</sup>. Whereas for the spectrum of the sulfur-bearing glass, the relative intensity of the shoulder due to Q<sup>4</sup> species increases compared with that of the sulfur-free glass. Changes in the <sup>23</sup>Na MAS spectra upon sulfur dissolution are subtle. These results suggest that the dissolution of a small amount of sulfur (< 1 wt.%) into silicate melts result in a marked increase in the degree of polymerization of the silicate network.

#### References:

- Maekawa et al. (1991) *J. Non-Cryst. Solids*, 127, 53-64.  
Naldrett et al. (1978) *Can. J. Earth Sci.*, 15, 715-728.  
Ohmoto and Goldhaber (1997) in "Geochemistry of Hydrothermal Ore Deposits" VIII, 517-611.  
Poulson and Ohmoto (1990) *Chem. Geology*, 85, 57-75.  
Stebbins (1988) *J. Non-Cryst. Solids*, 106, 359-369.

### 3.28 Water speciation in basaltic melts: constraints from water solubility measurements

Shigeru Yamashita

shigeru@misasa.okayama-u.ac.jp, Institute for Study of the Earth's Interior, Okayama University, Misasa, Tottori 682-0193, Japan

Water is a major volatile component dissolved in magmas at depth, and its presence can promote a significant change in the physicochemical properties of silicate melts. Many spectroscopic studies have shown that water is dissolved into quenched silicate melts (glasses) as both OH groups and molecular H<sub>2</sub>O, through a coupled reaction: (1) H<sub>2</sub>O (vapor) = molecular H<sub>2</sub>O (melt) and (2) molecular H<sub>2</sub>O (melt) + O (melt) = 2OH (melt) (e.g., Stolper, 1982). However, recent advance in the understanding of relaxation kinetics of hydrous silicate melts has revealed that the relaxation rates are so fast that the water speciation measured by spectroscopy in quenched glasses represents, to some degree, rapid re-equilibration upon quenching (e.g., Dingwell & Webb, 1990).

Here I present results from an indirect approach to investigate the water speciation in basaltic melts along the solubility surface for total water (both OH groups and molecular H<sub>2</sub>O as H<sub>2</sub>O) in the melts at magmatic temperature. Basaltic melt (Izu-Oshima volcano, ~53 wt% SiO<sub>2</sub>) was equilibrated with pure water vapor at 1473 K and at pressure between 10 and 80 MPa in an internally heated pressure vessel, and the total water content in the quenched glass was determined by IR spectroscopy. This dataset can be modeled adequately on the basis of ideal mixing of quasi-chemical oxygen species in the system OH (melt) - molecular H<sub>2</sub>O (melt) - O (melt). In combination with available volumetric data of water (Ochs & Lange, 1999), I used an iterative approach to fit the  $K_{(2)}$  value (equilibrium constant of water speciation reaction (2) defined by  $X_{OH}^2 / (X_{mol.H_2O} X_O)$ ) to the solubility data. The iteration converged upon  $\ln K_{(2)} = 0.32 \pm 0.22$ , and with this optimum value, the model reproduces the solubility data over the pressure range studied. The  $\ln K_{(2)}$  value obtained in basaltic melts is ~1.7 magnitude greater than that obtained by the same procedure in rhyolitic melts (~77 wt% SiO<sub>2</sub>) at 1473K and at pressure between 22 and 100 MPa ( $\ln K_{(2)} = -1.38 \pm 0.18$ , Yamashita, 1999). This implies that a greater fraction of dissolved water has been converted to OH groups in more basic silicate melt.

#### References

- Dingwell, D. B. & Webb, S. L. (1990). Relaxation in silicate melts. *Eur. J. Mineral.* 2, 427-449  
Ochs, F. A. & Lange, R. A. (1999). *Science* 283, 1314-1317  
Stolper, E. M. (1982). *Contrib. Mineral. Petrol.* 81, 1-17  
Yamashita, S. (1999). *J. Petrol.* 40, 1497-1507.

### **3.29 Pressure dependence of the emf of thermocouples: Comparison of W-Re and Pt-Rh thermocouples with P-measurements by in situ X-ray**

Tomohiro Iguchi\*, Eiichi Takahashi, Yu Nishihara

Department of Earth and Planetary Sciences, Tokyo Institute of Technology

One of the serious problems in high-temperature-high-pressure studies is the pressure dependence of the emf of thermocouples. When two different kinds of thermocouples exposed to identical temperatures and elevated pressures, there is a discrepancy in temperature reading. We measured the temperature discrepancy and the pressure using the in situ X-ray observations. Experiments were performed using a DIA-type, cubic-anvil apparatus. Experimental results were obtained in the pressure and temperature ranges of  $P=1.8-10.6\text{GPa}$  and  $T=26-1000\text{C}$ . W5%Re/W26%Re thermocouples recorded 12C higher temperature than Pt/Pt13% Rh thermocouples at 10.6GPa and 1000C.

### 3.30 Infrared Observation on Low Temperature Phase Transformations of Ice

M. Song<sup>1</sup>, K. Aoki<sup>2</sup>, H. Yamawaki<sup>2</sup>, H. Fujihisa<sup>2</sup>, and M. Sakashita<sup>2</sup>

<sup>1</sup> Core Research for Evolutional Science and technology Japan Science and technology Corporation, Kawaguchi, Saitama 332-0012, Japan

<sup>2</sup> National Institute of Materials and Chemical Research 1-1 Higashi, Tsukuba, Ibaraki 305-8565, Japan

Ice exhibits a very rich phase diagram with 12 known crystalline phases and many metastable and amorphous phases. The high pressure behavior of ice is of fundamental importance to condensed matter physics and planetary sciences. Many intriguing phenomena of ice have been revealed in recent years, such as pressure-tuned amorphization, hydrogen-bond symmetrization, Fermi resonance, soft-mode behavior. In the low temperature and low-pressure region, the physical behavior of ice becomes extremely unusual. When pressed at 77 K, ice Ih transformed into high-density amorphous (HDA) ice at 1.0 GPa [1], and then HDA ice will further transform into a ice VII-like phase at about 4 GPa at 80K [2], which is confirmed by a neutron diffraction measurement to be metastable phase quenchable to ambient pressure below 100K [3]. This particular phase-metastable ice VII exists at temperature below 180 K in the thermodynamic stable field of ice VIII [2, 3]. When compressed at below 150 K, ices II, VI also transit into metastable ice VII [4, 5]. The orientation disorder in metastable ice VII is speculated to be static [3], completely different from that dynamical one in ice VII. When heated at ambient pressure, metastable ice VII will transit into LDA ice and then ice Ih [3]. Metastable ice VII transited into ice VIII upon heating above 2 GPa [2, 3], but Raman measurements of metastable ice VII up to 30 GPa at 77 K showed no phase transformation [2], although theoretical calculation predicted that under isothermal compression metastable ice VII should finally transform into ice VIII [6]. The phase stability of metastable ice VII is still not completely determined. Here we employ low-temperature infrared absorption technique to study the stability of this phase. A detailed study of metastable ice VII may shed light on our understanding of the structures of ice VII and VIII, and provides new refinements on the potentials of ice.

Infrared spectroscopic absorption observation of ice was performed in a P-T range of 40-300 K and 0.2-50 GPa. The pressure of sample was around 3-10 GPa at ambient temperature after sampling. We cooled down sample to 230-240 K in a cryostat with KBr windows, and then unloaded pressure to 0.1-1.5 GPa to get ice VI, V, II, Ih. The IR spectra of ice Ih, II, V, VI, VII, VIII were carefully observed and compared with previous studies. Both ice II, VI were successfully cooled down below 150 K. When compressed at temperature below 120 K, ices II and VI transformed into metastable ice VII probably due to mechanical instability as ice Ih-HAD transformation [7]. The metastable ice VII show an IR absorption profile almost same as that of ice VII at ambient temperature. Under isobaric heating, metastable ice VII transits in to ice VIII and shows a general trend to decrease the phase transition temperature by about -2 K/GPa from about 170K at 6GPa to 120 K at 24 GPa. This confirms that the intensification of dipole-dipole interaction in ice contribute to the reorientation of water molecules in metastable ice VII to form an orientationally-ordered antiferroelectric configuration of ice VIII. Under isothermal compression below 100 K, metastable ice VII shows a temperature-insensitive phase transition into ice VIII at 30 GPa. The mechanisms of ice II, VII-metastable VII-VIII remains to be further studied by theoretical calculation and experiment.

#### References

- [1] O. Mishima, L. D. Calvert & E. Whalley, 'Melting ice' I at 77 K and 10 kbar: a new method of making amorphous solids. *Nature* **310**, 393-395 (1984).
- [2] R. J. Hemley, L. C. Chen & H. K. Mao, New transformations between crystalline and amorphous ice. *Nature* **338**, 638-640 (1989).
- [3] S. Klotz, J.M. Besson, G. Hamel, R.J. Nelmes, J.S. Loveday & W.G. Marshall, Metastable Ice VII at Low Temperature and Ambient Pressure, *NATURE* **398**, 681 (1999).

- [4] J. L. Finney, C. Lobban, S. Klotz & J. M. Besson, In *Collected Abstracts of the XVII Congress and General Assembly* (ed. Griffin, J. F.) C-534 (IUCr, Seattle, 1996).
- [5] Finney, J. L., Lobban, C., Klotz, S., Besson, J. M. & Hamel, G. in *ISIS 96-Rutherford Appleton Laboratory Report RAL 96-050* (ed. Taylor, A. D.) Vol. A17 (Chilton, UK, 1996).
- [6] J. S. Tse, and M.L. Klein, *Phys. Rev. Lett.* **58**, 1672-1675 (1987).
- [7] J.S. Tse and D.D. Klug, C. A. Tulk, I. Swainson, E. C. Svensson, C.-K. Loong, V. Shpakov, V. R. Belosludov, R. V. Belosludov & Y. Kawazoe, The mechanisms for pressure-induced amorphization of ice Ih. *Nature* **400**, 647 (1999).



**October 4 (Thursday) 13:30 – 16:30**

**Session 4**

**Dehydration of subducting slabs and water storage in  
the mantle**

Keynote: Max Schmidt, CNRS, Clermont-Ferrand/ETH Zürich

Chair: Eiji Ohtani, Tohoku University



#### 4.1 Dehydration vs. melting vs. dissolution: Where and how to generate a mobile component during subduction

Max W. Schmidt

Institute for Mineralogy and Petrology, ETH, Sonneggstr.10, Zuerich 8092 Switzerland;  
max.schmidt@erdw.ethz.ch

Prograde metamorphism of subducting lithosphere causes a series of mineralogical reactions which commonly result in a mobile phase. The mobile phase is either a low-density fluid or a high-density, possibly supercritical fluid or a silicate or carbonatite melt. This contribution reviews the generation (conditions and amounts) of the various mobile phases and also examines the restite(s) to be subducted to large depths.

Somewhat simplifying, 5 different regimes can be recognized to depth-equivalents of 10 GPa:

- (i) Low to medium P, low T ( $< 650$  C,  $< 2.5$  GPa) where hydrous phases are abundant and dehydration reactions are often perpendicular to typical subduction P-T paths, thus, dehydration rates are high. Any subducted lithosphere will go through this first stage.
- (ii) Low to medium P, high T where amphibole and biotite are the principal hydrous phases to melt at fluid absent conditions. Adakitic magmas (slab melts,  $\text{Na} > \text{K}$ ) are likely to origin at such conditions (1-2.5 GPa, 800-1000 C).
- (iii) Medium to high P, low T (500-800 C, 2.5-10 GPa) where hydrous phases are already largely reduced in volume and dehydration reactions are often subparallel to possible P-T paths. In this range fluids become increasingly rich in dissolved matter.
- (iv) Medium P, high T ( $> 700$ -800 C, 2.5-5 GPa) where phengite is the principal hydrous phase to melt and melts have  $\text{K} > \text{Na}$ .
- (v) High P, high T ( $> 800$  C,  $> 5$  GPa) where the solvus between fluid and melt is closed and a supercritical fluid might dissolve hydrous phases. Above 10 GPa (8 GPa in metasediments) phengite decomposes to the anhydrous phase K-hollandite, however at such pressures potassium could already be extracted by melting or by supercritical fluids.

Most dehydration and decarbonatization reactions are continuous and, in a given bulk composition, result in a combination of continuous and stepwise devolatilization. In the real world, the following factors contribute to the continuous nature of the devolatilization signal: highly variable bulk compositions in the sedimentary and mafic layers as well as possibly different degrees of depletion in the peridotitic layer(s); inhomogeneous distribution of carbonates vs. hydrates resulting in an inhomogeneous  $\text{X}(\text{CO}_2)$  in the fluid phase, high temperature gradients within the subducting lithosphere, and finally, possible kinetic hindering of reactions and thus widening of reaction zones.

Contrasting the above petrological effects, a mechanism of fluid/melt ascent through channeled flow or hydrofractures could focus a broadly distributed fluid. These latter mechanisms are largely in discussion.

Although the exact pressures and temperatures for the closure of the solvus between fluid and melt are poorly defined, there is little doubt that at high pressures the solvus closes and the mobile phase becomes supercritical. Especially potassium may entirely dissolve in small quantities of fluid and it is doubtful that much of the potassium could reach large depths. The transport properties of supercritical fluids for key trace elements is expected to differ significantly from low-pressure, low-density fluids but little experimental data are available.

Carbonates present within the subducting oceanic crust influence dehydration reactions but contrary to what is intuitively believed, often enlarge the stability field of hydrous phases. This is especially true in mafic and pelitic compositions where melting reactions are generally shifted to higher temperatures in the presence of carbonates. Carbonates may remain stable in a siliceous melt and with increasing temperature form a carbonatite melt coexisting with a silicate melt. At low temperatures fluids from carbonate-saturated lithologies are generally CO<sub>2</sub>-poor (especially with magnesite or dolomite X(CO<sub>2</sub>) is mostly < 15%) and the only efficient decarbonatization processes are either flushing with aqueous fluids from below or melting at relatively high temperatures.

The layered structure of an oceanic lithosphere originating from fast spreading ridges (i.e. the entire circum-pacific and thus most actual subduction zones) and temperature gradients within the subducting lithosphere define the relation between amount and depth range of dehydration in the mafic and ultramafic layer and possible melting of the sedimentary and mafic layers. In particular, the layered structure causes fluid:rock ratios in the sedimentary layer (as fluids from the underlying mafic and peridotitic layers must rise through the sediments) of >1:1 (integrated from 10 to 70 km depth) before melting temperatures are reached. Thus, some of the trace elements commonly considered to be only efficiently mobilized by melts (e.g. Be, Th) can also be quite effectively mobilized by fluids. The layered structure is likely to cause significant amounts of fluid to be present in the sedimentary layer to ca. 70 km depth. To this pressure, fluid-present sediment melting is likely to dominate over fluid-absent sediment melting, however at larger depths, dehydration below the sediments is generally insufficient to saturate significant amounts of sedimentary melt.

## 4.2 Circulation and Redistribution of Water in the Earth's Interior

Eiji Ohtani

Institute of Mineralogy, Petrology, and Economic Geology, Tohoku University, Aza-Aoba, Aramaki, Aoba-ku, Sendai 980-8578 Japan; ohtani@mail.cc.tohoku.ac.jp

Water stored in descending slab is transported into the depths greater than 200 km when the slab temperatures are lower than c.a. 600°C at around 6 GPa (e.g., (1)). In cold slabs with local water enrichment greater than 1 wt.% of the bulk rock, hydrous wadsleyite and hydrous ringwoodite are the main water reservoirs and excess water is stored in superhydrous phase B  $\text{Mg}_{10}\text{Si}_3\text{O}_{14}(\text{OH})_4$  in the transition zone. Phase Egg,  $\text{AlSiO}_3\text{OH}$  is also a candidate for water reservoir in the sediment component in slabs in the transition zone. Our high pressure experiments revealed that a decomposition reaction of superhydrous phase B into phase G(=D) and periclase;  $\text{Mg}_{10}\text{Si}_3\text{O}_{14}(\text{OH})_4 = (5/3)\text{Mg}_{1.2}\text{Si}_{1.8}\text{H}_{2.6}\text{O}_6 + 8\text{MgO}$  at 30 GPa and 1000~1100°C, and a decomposition of phase Egg into delta-AlOOH and stishovite,  $\text{AlSiO}_3\text{OH} = \text{AlOOH} + \text{SiO}_2$  at 23 GPa and about 1000°C. delta-AlOOH is a new high pressure polymorph of AlOOH with a structure similar to delta-FeOOH (2). No water release occurs by these reactions. Hydrous phases, phase G and delta-AlOOH, are not stable under the normal geotherm conditions, and are stable only in the cold slabs descending into the lower mantle. These phases can play a crucial role for water transport into the lower mantle by slab subduction.

We can expect two dehydration zones in the descending slabs; a shallow dehydration zone in the 200km depth, and a deep dehydration zone in the depths around 900~1200 km, where dehydration is originated from decomposition of superhydrous phase B, phase G, and delta-AlOOH. There is a layered structure in the water storage potential along the normal mantle geotherm; i.e., the upper and lower mantles have a relatively low water storage potential (e.g., (3)), whereas wadsleyite and ringwoodite in the transition zone have a larger potential. Thus, the fluid formed in the deep dehydration zone will move upwards and will be stored in the transition zone.

We have clarified the boundary the reaction  $3\text{Fe} + \text{H}_2\text{O} \rightarrow \text{FeO} + 2\text{FeH}$  using the diamond anvil cell. FeO and FeH is stable at temperatures above 1000°C at 35 GPa, and the phase boundary of the reaction has a positive slope. The reaction indicates that iron hydrite FeH is important during the accretional stage of the Earth. We observed that Fe and water is stable at relatively lower temperatures and higher pressures, whereas FeO and FeH are stable at higher temperatures. This observation indicates that iron and water reacted to form FeO and FeH in the hot accretional stage of the early Earth, and FeH can be transported into the core by the reaction (e.g., (4,5)). On the other hand, during cooling stage of the core, dissolved FeH and FeO in the core can react to form Fe and water.  $\text{H}_2\text{O}$  may be formed by this process at the core mantle boundary.

Thus two processes, i.e., water transport from ocean to the mantle by slab subduction and supply of water from the core to the mantle provide re-distribution of water from the ocean and core to the mantle transition zone during secular cooling of the Earth.

### References

- (1) T. Kawamoto et al. (1996). *Earth Planet. Sci. Lett.*, **142**, 587-592.
- (2) A. Suzuki et al. (2000). *Phys. Chem. Minerals*, **27**, 689-693.
- (3) Bolfan-Casanova et al. (2000). *Earth Planet. Sci. Lett.*, **182**, 209-221.
- (4) Fukai, Y. (1992). in *High-Pressure Research: Application to Earth and Planetary Sciences*, edited by Y. Syono and M.H. Manghnani, pp. 373-385, TERRABUB/AGU, Tokyo/Washington D. C..
- (5) Okuchi, T. (1997). *Science*, **278**, 1781-1784.

### 4.3 An experimental study on the Mg-Al granulites and production of granitic melts in K<sub>2</sub>O-MgO-Al<sub>2</sub>O<sub>3</sub>-SiO<sub>2</sub>-H<sub>2</sub>O system

Ganesha Atni Venkatramiah, J.A.K. Tareen

Department of Geology, University of Mysore, MYSORE-570 006, INDIA

<ganmysore@hotmail.com>

Ultrahigh Temperature (UHT) crustal metamorphism has been considered as that type of metamorphism which occurs at P-T conditions of more than 7 kb and 900°C respectively. The key minerals represent this UHT metamorphism includes sapphirine, spinel, cordierite, orthopyroxene, sillimanite, garnet, osumilite and the worldwide occurrence of these has been discussed in detail [1]. Experimental work on dehydration melting of biotite in natural system shows that large amount of granitic melt produces depending on the starting bulk composition [2-5]. The stability of biotite in KFMAS(H) system has been studied experimentally [6-9] and hitherto there are no reports on the dehydration melting of phlogopite in Fe-free KMASH system above 950°C/6 kb. We report here the composition of melts along with restites obtained by vapour-absent melting of phlogopite in the P-T range of 6-9 kb and 1000-1250°C respectively.

All experiments were carried out in KMASH system using bulk composition 2Phl-6Sil-9Qtz\*, corresponding to Mg-Al granulite. The starting mineral phases used were synthetic ideal phlogopite, sillimanite and natural quartz in the ratio of 2:6:9 respectively. Experiments were conducted using Internally Heated Pressure Vessel under vapour-absent condition and the water available in the system was solely from the structural water of phlogopite. Table-1 lists the bulk composition, experimental details, mineral phases encountered and composition of melts.

The major mineral phases obtained in the given P-T range are Spr-Crd(H)-Al.En-Os. Sapphirine is of 221 type and enstatite is highly aluminous (up to 14 wt% of Al<sub>2</sub>O<sub>3</sub>). Interestingly, an hexagonal cordierite instead of orthorhombic cordierite was observed as new phase. The melts obtained is highly silicic (up to 75 wt% of SiO<sub>2</sub>) and overall chemical analysis are comparable and consistent with the reported melts [2,4]. The melts of the present study show positive trend in MgO, Al<sub>2</sub>O<sub>3</sub> and negative trend in SiO<sub>2</sub> with respect to increasing temperature. Further, there is an inverse correlatin between MgO and Al<sub>2</sub>O<sub>3</sub> vs SiO<sub>2</sub>. The clustering and overlapping of melts obtained and that of the reported melts [2,4] on (Al<sub>2</sub>O<sub>3</sub>+K<sub>2</sub>O)-MgO-SiO<sub>2</sub> triangular diagram (Fig-1) indicates that 'granitic melts' would be produced from pelitic rocks irrespective of XMg in biotite. But, the quantity of melt and restites at given P-T condition definetely varies with the bulk composition and water in the system.

\*Abbreviations are after Kretz (1983), Os-Osumilite

Table-1. Experimental details and composition of melts and bulk.

Expt. No.	Temp (°C) Pressure (kb)	Duration (Hours)	Product K <sub>2</sub> O	Oxide%				
				MgO	Al <sub>2</sub> O <sub>3</sub>	SiO <sub>2</sub>	Total	
BULK COMPOSITION: 2Phl-6Sil-Qtz (+H <sub>2</sub> O-1.27)				4.01	9.81	30.29	53.97	99.35
				Melt Composition				
48	1150/7.40	24	Spr-Crd(H)-En-Os-L	7.34	1.75	13.77	72.00	94.86
49	1050/8.00	46	Spr-Crd(H)-Sil-En-L-Os	5.62	2.55	14.91	73.46	96.54
26B	1190/9.00	24	Spr-Crd(H)-En-Os-L	7.04	2.06	13.88	75.13	98.11
40	1200/6.00	34	Spr-Crd(H)-En-Os-L	6.81	2.82	14.61	73.31	97.55
35	1050/6.00	24	Spr-Crd(H)-Sil-En-Qtz-L	7.24	2.59	14.94	70.42	95.19
43	1200/7.00	64	Spr-Crd(H)-En-Os-L	8.34	1.86	14.26	73.48	97.94
37A	1250/6.00	24	Spr-Crd(H)-L	5.61	4.85	15.93	69.95	96.34

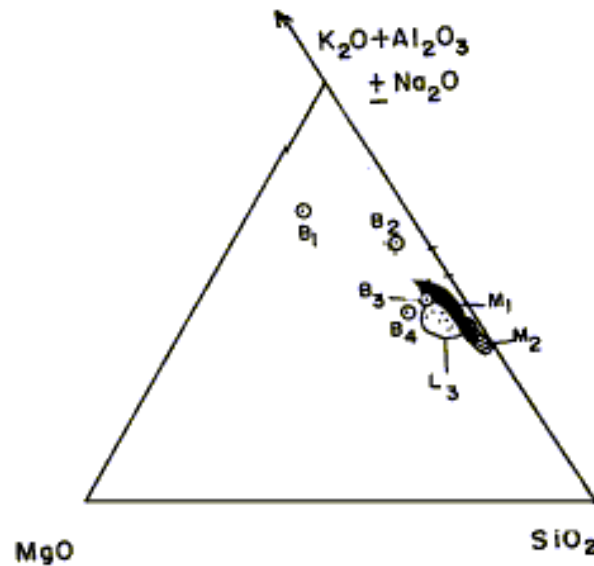


Fig-1: ( $\text{Al}_2\text{O}_3\text{-K}_2\text{O}$ )- $\text{MgO-SiO}_2$  diagram showing starting bulk composition and experimental melts. B1: Starting bulk of the present study. B2, B3 and B4 are bulk used for experimentation by previous workers [2,4,7]. L3 denotes melts of present study. M1 and M2 are melts of previous workers in the natural systems [2,4]. Note the overlapping of melts [2,3] on the present study in the KMAH system.

#### References

- [1] Harley, S.L, Geol.Soc.London Spec.Publ., 138, 81-107 (1998)
- [2] Vielzeuf, D. and Holloway, J.R., Contrib.Mineral.Petrol., 98, 257-276 (1988)
- [3] Patino Douce, A.E. et al., Earth Plan.Sci.Letter, 97, 290-315 (1990)
- [4] Patino Douce, A.E. and Johnston, A.D., Contrib.Mineral. Petrol., 107, 202-218 (1991)
- [5] Rutter, J.M. and Wyllie, P., Nature, 331, 159-160 (1988)
- [6] Carrington, D.P. and Harley, S.L., Contrib.Mineral.Petrol., 120, 270-291 (1995a)
- [7] Carrington, D.P. and Harley, S.L., J.Met.Geol., 13, 613-625 (1995b)
- [8] Audibert, N. et al., J.Met.Geol., 13, 331-344 (1995)
- [9] Motoyoshi et al., Eur.J.Mineral., 5, 439-440 (1993)
- [10] Kretz, R., Am., Mineral., 68, 277-279 (1983)

#### 4.4 Earthquakes at depth, their enabling mineral reactions, and transport of H<sub>2</sub>O into the deep mantle

Harry W. Green, II

Institute of Geophysics and Planetary Physics and Department of Earth Sciences, University of California, Riverside, CA 92521 USA  
<harry.green@ucr.edu>

Over the last decade, extraordinary progress has been made in visualizing the interior of the earth using seismic wave speeds and tomographic inversion techniques. However, we still know relatively little about the mechanism(s) by which earthquakes can be triggered and propagate at depth. Only two mechanisms have been experimentally verified as potential earthquake trigger mechanisms at high pressure: dehydration embrittlement and transformation-induced faulting. During this period, many aspects of the latter have been worked out in the laboratory, hence reasonably stringent tests on the viability of this mechanism can be made. However, the former mechanism has been little studied since its discovery in the 1960s; discussions of its potential importance as an earthquake mechanism have been qualitative and uncertain. Both mechanisms require enabling mineral reactions under stress that produce local pockets of low-viscosity "fluid" that lead to mechanical instability. Dehydration embrittlement, potentially capable of explaining all earthquakes at depth, requires hydrous phases that dehydrate under conditions appropriate to explain the continuous distribution of earthquakes with depth in subduction zones. Only recently have candidate high-pressure hydrous phases been identified and their stability fields mapped out but still only in simple systems and whether hydrous phases exist to sufficient depth in subducting lithosphere is unknown. Similarly, transformation-induced failure can only function under conditions of metastable transformation of olivine to wadsleyite and ringwoodite in the mantle transition zone, yet evidence for the presence of metastable olivine in the cores of subduction zones has been equivocal. Therefore, it is not clear whether or not the necessary enabling mineralogy for either mechanism is present under all conditions where it might operate.

Several subduction zones have clearly defined double seismic zones at intermediate depths, with the lower zone located as much as 40 km below the top of the slab. Hydration of the oceanic lithosphere at ridges is unlikely to extend below 10-12 km and only a very small percentage of xenoliths from oceanic islands contain even small crystals of hydrous phases. Therefore, if the lower seismic zone is a result of dehydration, there must be a mechanism operating at or near oceanic trenches that introduces water to sufficient depth. Although there is no direct evidence of such a mechanism, it has been proposed that fault zones of great normal faults outboard of trenches might provide a pathway for introduction of water and consequent growth of hydrous phases. Moreover, the correlation is now quite striking between the stability field of antigorite, the hydrous phase most likely to be present at depth in the oceanic lithosphere, and models of subduction zones. In particular, the convergence of double seismic zones at 200-250 km is readily fit by thermal models to the breakdown of antigorite to olivine + enstatite + H<sub>2</sub>O. This evidence, although indirect, is a powerful suggestion that these earthquakes may be triggered by this reaction. If antigorite does exist at least discontinuously distributed in the subducting lithosphere and if the cold core of the subduction zone remains at a temperature of less than ~600 °C at 200 km, then the part of the slab colder than that will pass into the stability field of Phase A, the first of a succession of increasingly dense hydrous phases. However, the earthquake generating power of these phases is questionable because all of the reaction boundaries likely to be crossed by a particle path in a subduction zone result in increasingly hydrous phases, hence fluid could be released only transiently during the reaction, an unlikely process. The disappearance of double seismic zones at ~250 km and the very low frequency of all earthquakes at depths of 300-400 km may be a consequence of this fact. Thus, the combination of the phase equilibria of hydrous peridotite and the presence of earthquakes deep in slabs at intermediate depths suggest that H<sub>2</sub>O is present in many subducting slabs and that however much H<sub>2</sub>O makes it to 200 km is likely to be

carried undisturbed into the deep mantle.

New evidence that may indicate extensive preservation of metastable olivine in the transition zone of the Fiji region (Chen and Brudzinski, *Science*, 2001) reinforces the transformation-induced faulting hypothesis for triggering of earthquakes below 400 km. However, in hydrous slabs thermal consequences of transformation-induced faulting, perhaps enhanced by shear heating, could raise the temperature in the growing fault/slip zone and activate brucite dehydration at depths greater than 500 km. Thus, earthquakes below 500 km could be composite, potentially explaining the very large very deep earthquakes about which there has been controversy over the last several years. This two-step process for these earthquakes would also be consistent with the observations that they occur in warmer slabs and are frequently double events, with a smaller event preceding the larger event. In this model, even though the Phase D + brucite dehydration boundary extends to pressures appropriate for the lower mantle, earthquakes would stop at the base of the transition zone because the transformation-induced trigger would cease to operate at that boundary.

The model of composite earthquakes is testable in the laboratory whereas the inferred presence of hydrous phases in shallow subducting lithosphere should be testable by seismological methods.

#### 4.5 Slab dehydration and earthquakes: Seismological evidence

Dapeng Zhao

Geodynamics Research Center, Ehime University, Matsuyama 790, Japan

<zhao@sci.ehime-u.ac.jp>

A growing body of evidence suggests that fluids (water, magma, and gases) are intimately linked to a variety of earthquake faulting processes. These include the nucleation, propagation, arrest and recurrence of earthquake ruptures, fault creep or slow earthquakes, and the long-term structural and compositional evolution of fault zones. In this report I present seismological evidence for the influences of fluids and magma on the generation of large earthquakes in the crust and the subducting oceanic slabs under the Japan Islands. The relationship between seismic tomography and large crustal earthquakes (M 5.7-8.0) in Japan during a period of 116 years from 1885 to 2000 is investigated and it is found that most of the large crustal earthquakes occurred in or around zones of low seismic velocity. The low-velocity zones may represent weak sections of the seismogenic crust. The crustal weakening is closely related to the subduction process in this region. Along the volcanic front and in back-arc areas, the crustal weakening may be caused by active volcanoes and arc magma resulting from the convective circulation process in the mantle wedge and dehydration reactions in the subducting slab. In the forearc region of southwest Japan, fluids are detected in the 1995 Kobe earthquake source zone, which may have contributed to the rupture nucleation. The fluids may originate from the dehydration of the subducting Philippine Sea slab. The recent 2001 Geiyo earthquake (M 6.8) occurred at 50 km depth within the subducting Philippine Sea slab, and it may be also related to the slab dehydration process. A detailed 3-D velocity structure is determined for the northeast Japan forearc region using data from 598 earthquakes that occurred under the Pacific Ocean with hypocenters well located with sP depth phases. The results show that strong lateral heterogeneities exist along the slab boundary, which may represent asperities and results of slab dehydration and may affect the degree and extent of the interplate seismic coupling. These results indicate that large earthquakes do not strike anywhere, but only anomalous areas which may be detected with geophysical methods. The generation of a large earthquake is not a pure mechanical process, but is closely related to physical and chemical properties of materials in the crust and upper mantle, such as magma, fluids, etc.

#### References

- Zhao, D., H. Kanamori, H. Negishi, D. Wiens, 1996. Tomography of the source area of the 1995 Kobe earthquake: Evidence for fluids at the hypocenter? *Science* **274**, 1891-1894.
- Zhao, D., H. Negishi, 1998. The 1995 Kobe earthquake: Seismic image of the source zone and its implications for the rupture nucleation. *J. Geophys. Res.* **103**, 9967-9986.
- Zhao, D. T. Mizuno, 1999. Crack density and saturation rate in the 1995 Kobe earthquake region. *Geophys. Res. Lett.* **26**, 3213-3216.
- Zhao, D., F. Ochi, A. Hasegawa, A. Yamamoto, 2000. Evidence for the location and cause of large crustal earthquakes in Japan. *J. Geophys. Res.* **105**, 13579-13594.

## 4.6 Transportation of H<sub>2</sub>O and melting in subduction zones

Hikaru Iwamori

Department of Earth and Planetary Sciences, University of Tokyo

### Abstract

Recent knowledge concerning the phase relationships of hydrous peridotitic and basaltic systems allows us to model fluid generation and migration in subduction zones. Here I present (1) numerical models for the transportation of H<sub>2</sub>O and melting in subduction zones, in which generation and migration of aqueous fluid, its interaction with the convecting solid, and melting are considered, based on the phase relationships, (2) predictions of the corresponding seismic structures based on the calculated distribution of the fluids (aqueous fluids and melts), (3) comparison between the model predictions and 3-D seismic tomographic images beneath the Japanese islands, and (4) analyses on distribution of the volcanoes and the volcanic chains.

The model calculation suggests that in northeast Japan, nearly all the H<sub>2</sub>O expelled from the subducted Pacific plate is hosted by serpentine and chlorite just above the plate, and is brought down to ~150 km. Breakdown of serpentine and chlorite at these depths results in the formation of a fluid column through which H<sub>2</sub>O is transported upwards, and results in the initiation of melting in the mantle wedge beneath the backarc (Iwamori, 1998). The seismic tomographic studies suggest the existence of such a melting region beneath the backarc (Iwamori and Zhao, 2000). In central Japan, the subducted Philippine Sea plate overlaps the subducted Pacific plate. This geometry causes slow thermal recovery of the subducted Pacific plate, resulting in dehydration reactions at levels (200-300 km) deeper than in northeast Japan, and deflection of the volcanic chain towards the backarc side (Iwamori, 2000). The model also suggests that, beneath central Japan, a part of H<sub>2</sub>O subducted is carried to depths greater than 300 km by phase A. In contrast, in southwest Japan, where a relatively hot part of the Philippine sea plate (Shikoku basin) subducts, the dehydration reactions are predicted to occur at relatively shallow levels (<100 km depth). The seismic tomographic image supports well the predicted distribution of the fluids beneath the volcanic front to the forearc region (Zhao et al., 2000). These comparisons between the model predictions and the observations suggest that the thermal structure (determined by age and subduction velocity) of the subducting plate strongly controls the distribution of the aqueous fluids and melts in subduction zones through the position of the dehydration reactions.

References: Iwamori, EPSL 160, 65-80, 1998; Iwamori, EPSL 181, 41-46, 2000; Iwamori, EPSL 181, 131-144, 2000; Iwamori and Zhao, GRL 27, 425-428, 2000; Zhao et al., GRL 27, 2057-2060, 2000.

#### 4.7 Apatite concentration in the Finero phlogopite-peridotite, Italian Western Alps, as the late product of subduction-related mantle metasomatism

Tomoaki Morishita\*, Shoji Arai, Akihiro Tamura

\*Earth Sciences, Kanazawa University

##### Introduction

The Finero phlogopite-peridotite is thought to be an example of highly metasomatized peridotite by slab-derived melts (or fluids) (Zanetti et al., 1999; Prouteau et al., 2001). The Finero phlogopite-peridotite is, therefore, very important to understand evolution of mantle wedge due to interaction with slab-derived melts or fluids. We found apatite concentrations in the Finero phlogopite-peridotite. Here we present occurrence of apatite and other petrographical characteristics, and discuss the origin of the apatite concentrations in the context of mantle metasomatism on a mantle wedge.

##### Petrography

The phlogopite-peridotite consists of harzburgite and dunite with small amounts of chromitite and clinopyroxenite. Apatite and carbonate are randomly distributed in the phlogopite-peridotite (Zanetti et al., 1999). Apatite concentration was found in thin (< 1 cm in thickness) layers being relatively white in color. The host peridotite has a granoblastic texture consisting mainly of olivine, amphibole, orthopyroxene and spinel with minor amount of clinopyroxene, phlogopite and sulfide minerals. Very weak foliation is recognized in the host peridotite by elongation of amphibole. The thin layers are slightly oblique to the foliation of the host.

The thin layers consist of fine-grained minerals (a few to 100  $\mu\text{m}$  in size), olivine, orthopyroxene, amphibole, spinel, phlogopite, apatite, carbonate and sulfide minerals. Each apatite grain is 10-100  $\mu\text{m}$  in size and concentrates as veins parallel to the thin layers. Apatite concentration exceeds more than 10 modal % in locally. Carbonate minerals are commonly found in the apatite-rich vein. The thin layers are rich in fine-grained orthopyroxene (< 50  $\mu\text{m}$ ). Distinctive low-Al, Ca orthopyroxene locally occurs as a thin film, < 10  $\mu\text{m}$  in width, to be network at the grain boundary of fine-grained olivine grains (50  $\mu\text{m}$ ). Orthopyroxenes characterized by low Al contents were also reported from apatite-bearing domains in the Finero (Zanetti et al., 1999). Cr-spinels in the thin layers are chemically heterogeneous within each grain ( $\text{Cr}_2\text{O}_3$  &  $\text{Fe}_2\text{O}_3$ -poor part and  $\text{Cr}_2\text{O}_3$  &  $\text{Fe}_2\text{O}_3$ -rich part).

##### Discussion

The presence of low-Al orthopyroxenes was reported in peridotite xenoliths, which are thought to be subarc upper mantle metasomatized by slab-derived fluids (Blatter & Carmichael, 1998; Smith et al., 1999, Arai & Kida, 2000; McInnes et al., 2001). The thin layers with apatite concentration was formed through a very local reaction between peridotite with ( $\text{CO}_2 + \text{H}_2\text{O}$ )-bearing melts (or fluids), probably derived from a subducted slab. Composition of localized melts (or fluids) may evolve in local situation where amphibole or phlogopite are precipitating with loss of  $\text{K}_2\text{O}$ ,  $\text{Al}_2\text{O}_3$  and increasing of  $\text{CO}_2/\text{H}_2\text{O}$  ratio from the primary melts (or fluids), leading to be unmixing of  $\text{SiO}_2$ -rich and  $\text{CO}_2$ -rich melts (or fluids) (Zanetti et al., 1999). Apatite and carbonate were precipitated from  $\text{CO}_2$ -rich varieties. Crystallization of orthopyroxene, representing addition of silica to mantle peridotite is a mechanism for metasomatic alteration of mantle wedge peridotite.

##### Reference

- Arai, S. & Kida, M. (2000). *The Island Arc*, **9**, 458-471.  
Blatter, D. L., & Carmichael, I. S. E. (1998). *Geology*, **26**, 1035-1038.

- McInnes, B. I. A., Gregoire, M., Binns, R. A., Herzig, P. M. & Hannington, M. D. (2001). *Earth Planet. Sci. Lett.*, **188**, 169-183.
- Prouteau, G., Scaillet, B., Pichavant, M., Maury, R. (2001). *Nature*, **410**, 197-200.
- Smith, D., Riter, J. C. A. & Mertzman, S. A. (1999). *Earth Planet. Sci. Lett.*, **165**, 45-54.
- Zanetti, A., Mazzucchelli, M., Rivalenti, G. & Vannucci, R. (1999). *Contrib. Mineral. Petrol.*, **134**, 107-122.

#### 4.8 High internal pressure retained in fluid inclusions of mantle-derived materials

Hiroyuki Kagi

Laboratory for Earthquake Chemistry, Graduate School of Science, University of Tokyo

Mantle-derived geological samples give us direct information on the physicochemical state of fluid of mantle origin. In this talk, our recent studies on the excess internal pressure of fluid inclusions in natural diamond and in mantle xenolith will be introduced.

Natural minerals of high-pressure origin have the potential to retain high internal pressures on materials trapped within these crystals. Inclusions in natural diamonds, as demonstrated from the blue shift in vibrational spectra, retain several gigapascals of high pressure (Kagi et al. (2000), *Min. Mag.*, 64, 1089-1097, and references therein.). The internal pressure retained in inclusions gives us a clue to decipher the depth where the inclusions were trapped. Some kinds of natural diamonds contain “mantle-derived” fluid inclusions. It is essential problem to discuss the depth (pressure) where the fluids were trapped for understanding chemistry of mantle-fluids. We investigated NIR-IR spectroscopic properties of water contained as fluid inclusions of cuboid diamonds. The results indicated that a cuboid diamond contained two kinds of water; ice VI retaining approximately 1.9 GPa and liquid water at ambient pressure. Recently, we have measured mapping analysis of infrared absorption spectra on the thinly sliced cuboid diamonds. The preliminary results demonstrated that the high-pressure bearing fluid distribute heterogeneously in the crystal suggesting that the diamond trapped mantle-fluid at different growth stage of diamond. Natural diamonds trap fluids at mantle depth (pressure) where diamond is thermodynamically stable, but some part of fluid might be trapped at shallower depth during the growth stage of the diamond.

Internal pressure of fluid inclusions can serve as a sensitive strength-marker for mantle minerals. Recently, we investigated fluid inclusions in mantle xenolith from Far Eastern Siberia (Yamamoto et al., *EPSL* submitted) by micro-Raman spectroscopy and microthermometry. The samples contained pure CO<sub>2</sub> inclusions and melt inclusions. We measured Raman spectra for each CO<sub>2</sub> inclusion after separating to mineral species. Two lines are observed approximately at 1286 cm<sup>-1</sup> and 1388 cm<sup>-1</sup> on Raman spectra of CO<sub>2</sub>. Both the intensity ratio (R) and energy difference ( $\Delta$ ) between these two peaks are known to show pressure dependence. The changes in two parameter with pressure are very subtle for natural samples, however, Raman barometry for CO<sub>2</sub> inclusions have not been established for geological purpose. We determined R and D precisely by applying the numerical resolution enhancement technique, then Raman barometer was calibrated with conventional homogenized temperature using cryogenic microthermometry. The results indicated that retained pressure in the CO<sub>2</sub> inclusions showed surprisingly systematic gradation dependent to mineral species;  $\text{sp} > \text{opx} \sim \text{cpx} > \text{ol}$ . The difference in the pressure reflects the deformations of minerals at mantle condition after trapping fluid inclusions. This is a direct observation of strength of mantle minerals to plastic deformation which was projected onto the retained pressure of fluid inclusions.

#### 4.9 In situ observation of supercritical behaviors between H<sub>2</sub>O fluids and subduction zone magmas.

Tatsuhiko Kawamoto and Kyoko Matsukage

Institute for Geothermal Sciences, Kyoto University, Beppu, 874-0903, Japan,  
kawamoto@bep.vgs.kyoto-u.ac.jp, matsukage@bep.vgs.kyoto-u.ac.jp

Visual observation of melting relationships between H<sub>2</sub>O fluids and natural andesitic and rhyolitic melts were conducted in a range of pressure from 0.4 to 1.8 GPa and temperature up to 1050 degree C. The experiments were conducted with a Bassett type externally heated diamond anvil cell (Bassett et al., 1993, Rev. Sci. Inst.). Starting materials were the Fuji 1707 andesite and rhyolite glasses that are geochemically characterized by calc-alkaline rock series and medium K andesites, and represent typical felsic magmas erupted in subduction zones. Supercritical behavior was observed in a range of chemical composition between andesite (62 wt. % SiO<sub>2</sub>) and rhyolite (70 wt. % SiO<sub>2</sub>). The available experimental data suggest a higher supercritical temperature at equivalent pressure between andesite and H<sub>2</sub>O fluids than that between rhyolite and H<sub>2</sub>O fluids. This is in contrast to the suggestion by Bureau and Keppler (1999, Earth Planet. Sci. Lett.) based on their data in the system of H<sub>2</sub>O fluid and nepheline (39.4 wt. % SiO<sub>2</sub>), jadeite (58.8 wt. % SiO<sub>2</sub>), and haplogranitic melts (73.6 wt. % H<sub>2</sub>O) with two exceptions of albite (65.3 wt. %) and Ca bearing haplogranitic melts (71.6 wt. % SiO<sub>2</sub>).

Chemical fractionation between H<sub>2</sub>O-rich fluids and silicate-rich melts with respect to silicate components were determined by electron microprobe analysis of silicate glasses quenched from silicate-rich melts. Na<sub>2</sub>O and K<sub>2</sub>O are likely to enter the H<sub>2</sub>O-rich fluid and CaO, MgO and FeO are preferentially partitioned into silicate-rich melt. The same preferential distribution of Na<sub>2</sub>O was also observed between albite melt and H<sub>2</sub>O fluids and in this case SiO<sub>2</sub> is preferentially partitioned in the H<sub>2</sub>O-fluid. Chemical transport of Na<sub>2</sub>O and K<sub>2</sub>O by H<sub>2</sub>O-rich fluid in H<sub>2</sub>O-saturated magma chamber was suggested based on dynamic degassing experiments in andesite system (Sakuyama and Kushiro, 1979, Contrib. Mineral. Petrol.). The knowledge of partitioning coefficients of trace elements between H<sub>2</sub>O fluid and silicate melts can be investigated with the present method.

#### 4.10 Geochemical Consequences of Deep Subduction of Oceanic Crust: Insights from Melting Experiments on Hydrous Metabasalt at 3-16 GPa

Robert P. Rapp<sup>1</sup> and N. Shimizu

<sup>1</sup>Department of Geosciences and Mineral Physics Institute, State University of New York at Stony Brook, ESS Building, Stony Brook, New York 11794-2100 USA

Subduction transports hydrated, geochemically-altered basaltic oceanic crust through the island-arc and back-arc regimes, into and sometimes through the mantle transition zone at 660 km depth, to be incorporated into the deep mantle source region for so-called 'HIMU' ocean island basalts, suggesting that crustal recycling occurs on a whole-mantle scale. Along the way, breakdown of hydrous minerals in the slab release fluids which contribute to island arc volcanism and metasomatism of the sub-arc and back-arc mantle, while transforming the slab to a large-ion lithophile (LILE) element-depleted, ultrarefractory crystalline residue. Experimental studies have shown that minerals such as phengite and lawsonite can be stable in basaltic compositions up to pressures of 10-11 GPa (Schmidt, 1996); given the broad diversity in the dynamics of subduction, a broad range in slab geotherms ought to be expected, so that fluid release associated with the breakdown of hydrous minerals can take place at depths up to 300 km (e.g., "hot slabs" will undergo dehydration at lower pressure than "cold slabs").

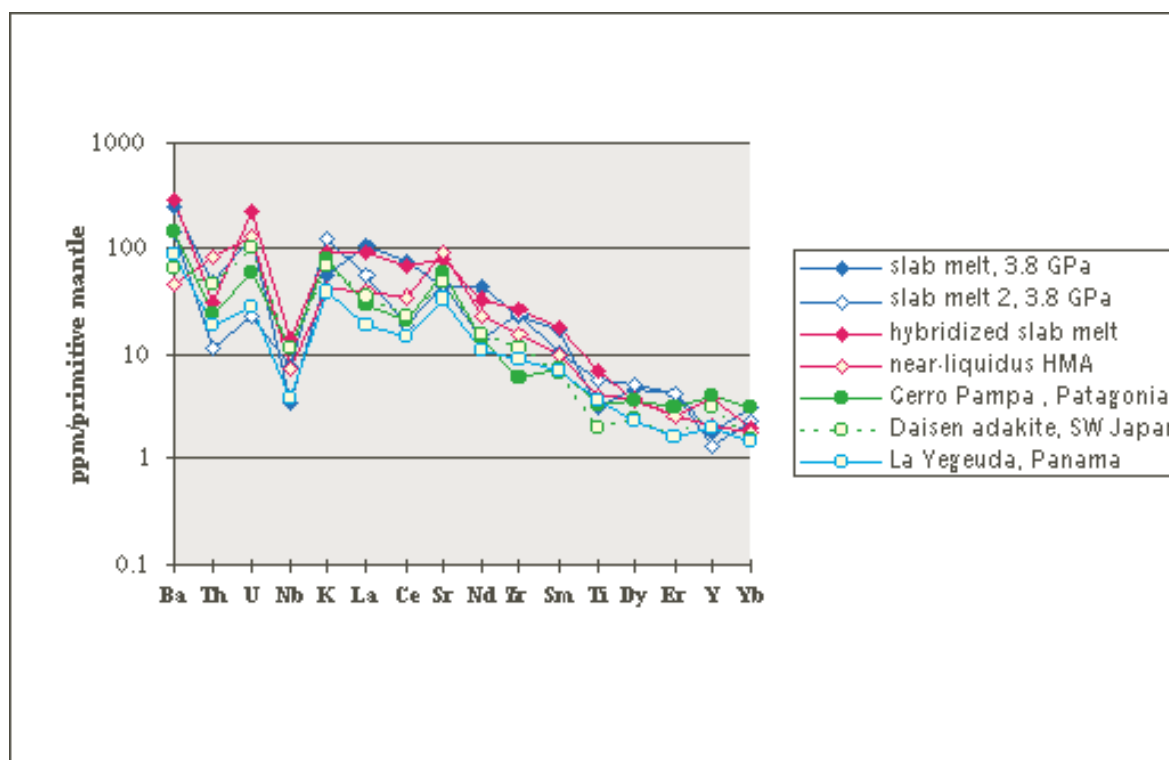


Figure 1. Primitive-mantle normalized trace element abundance patterns for "pristine" and "mantle-hybridized" slab melts, produced experimentally, and selected adakite arc lavas.

It can be readily demonstrated that dehydration reactions that involve low-degree partial melting of the slab are far more efficient at mobilizing and fractionating trace elements than dehydration reactions taking place under sub-solidus conditions (e.g., Kogiso et al., 1997 and this study). We have conducted a series of dehydration melting experiments on a natural, altered MORB composition, attempting to track along the solidus for dehydration melting at 3-11 GPa, using the ion microprobe to characterize the geochemical characteristics of low-degree slab melts and their crystalline residues as a function of pressure. Dehydration melting at pressures less than 4-5 GPa are controlled

by the breakdown of amphibole and zoisite, and produce Na-rich granitoid liquids in equilibrium with eclogite residues containing rutile; low-degree partial melts closely resemble “adakite” arc lavas in “hot” subduction zones (Fig. 1).

The characteristic depletions in such elements as Ti, Nb and Ta in the experimental “slab melts” at < 4 GPa are attributable to the low solubility of rutile at temperatures less than 1100°C. Hybridization of “pristine” slab melts by reaction with mantle peridotite in the overlying wedge produces Mg-rich adakites with trace element abundance patterns parallel to those of the (low-Mg#) adakites. These lavas form a compositional continuum with high-Mg andesites (HMA), which we interpret either as superheated hybridized adakites, or the product of partial melting of adakite-metasomatized sub-arc mantle.

At pressures between 5 and 11 GPa, dehydration melting reactions are controlled by the breakdown of lawsonite and phengite (Schmidt, 1996; Ono, 1998); low-degree melting of the slab in this pressure range produces K-rich granitoids, due to the preferential partitioning of Na in residual clinopyroxene with increasing pressure. Rutile is not part of the residual assemblage, and as a result Nb and Ta abundances in low-degree slab melts increase sharply above 5 GPa. Liquids at 5-11 GPa are strongly enriched in incompatible trace elements such as Rb, Ba, U, Th, Sr, and the LREEs, and strongly depleted in HREEs and Y; as a consequence the eclogitic residues of melting are nearly completely stripped of LILEs (including U and Th) by the time they reach depths of 300 km or so. It is these chemically-depleted, ultrarefractory residues that would be incorporated into the OIB source region. At pressures of 14-16 GPa, tenuous supercritical fluids coexist with majorite garnet and clinopyroxene assemblages (i.e., not garnetite); with trace element partitioning behavior between hydrous fluid and these crystalline residues remain wholly unconstrained.

#### References

- Defant, M.J., Richerson, P.M., DeBoer, J.Z., Stewart, R.H., Maury, R.C., Bellon, H., Drummond, M.S., Feigenson, M.D. and T.E. Jackson (1991) Dacite genesis via both slab melting and differentiation: petrogenesis of the La Yeguada volcanic complex, Panama. *J. Petrology* **32**, 1101-1142.
- Kay, S.M., Ramos, V., and M. Marquez (1993) Evidence in Cerro Pampa volcanic rocks for slab melting prior to ridge-trench collision in southern South America. *Jour. Geol.* **101**, 703-714.
- Kogiso, T., Tatsumi, Y., and S. Nakano (1997) Trace element transport during dehydration processes in the subducted oceanic crust: 1. Experiments and implications for the origin of ocean island basalts. *Earth Planet. Sci. Lett.* **148**, 193-205.
- Morris, P.A. (1995) Slab melting as an explanation of Quaternary volcanism and aseismicity in southwest Japan. *Geology* **23**, 395-398.
- Ono, S. (1998) Stability limits of hydrous minerals in sediment and mid-ocean ridge basalt compositions: implications for water transport in subduction zones. *J. Geophys. Res.* **103**, 18253-18267.
- Schmidt, M.W. (1996) Experimental constraints on recycling of potassium from subducted oceanic crust. *Science* **272**, 1927-1930.

#### 4.11 The fate of subducted carbonate within oceanic crusts

Miki Shirasaka and Eiichi Takahashi

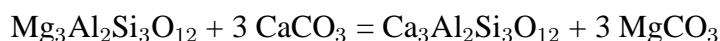
Tokyo Institute of Technology

The Carbonate-bearing eclogite and marble in the UHP metamorphic belt suggest that the sedimentary carbonate goes down to at least 100 km (c.f. Schertl and Okay, 1994) and it probably reaches to about 200 km depth (Shirasaka et al., 2001). If the subducted carbonate melts, the CO<sub>2</sub>-rich melt occurs and is probably affect the magmatism and metasomatism in arc system. On the other hand, the solid carbonate is a probable carrier of CO<sub>2</sub> into the deep mantle. In order to investigate the fate of carbonate within slabs, we carried out a series of experiments in MORB-CaCO<sub>3</sub> system at 2.7-8.0 GPa.

The phase relation of MORB-CaCO<sub>3</sub> system is shown in Figure 1. The solidus lies between 1200°C and 1300°C at 2.7-3.0 GPa, falls to 900-1000°C at 4-5 GPa, and increases in temperature with increasing pressure at 5-8 GPa. As the reaction Clinopyroxene + Aragonite = Garnet + Dolomite shifts to the right with increasing pressure, the solidus markedly decreases at 3.5-4.0 GPa.

The carbonatitic melt coexists with clinopyroxene + garnet + coesite + rutile at >3.5 GPa. The melt changes its composition with increasing temperature (increase in Ca, Si contents and decreases in Mg content). In suprasolidus above 4.0 GPa, the melt composition is Ca-enriched dolomite, Ca/(Ca+Mg+Fe) = 0.6-0.7, and less SiO<sub>2</sub> (< 1 wt.%), Al<sub>2</sub>O<sub>3</sub> (< 1 wt.%) and Na<sub>2</sub>O (< 0.1 wt.%) contents. Although the melt composition at far solidus is undefined, it seems to have higher SiO<sub>2</sub>, K<sub>2</sub>O and Na<sub>2</sub>O contents than those at lower temperature.

Carbonate phase in subsolidus changes with increasing pressure. At 2.7-3.5 GPa and <1100°C, aragonite or calcite is stable. Above ~3.5 GPa, dolomite is stable at higher temperatures, and it decomposes to aragonite + magnesite with increasing pressure and/or with decreasing temperature. Moreover a portion of aragonite decreases with increasing pressure. As the exchange reaction



shifts to the right with increasing pressure, the carbonate composition changes.

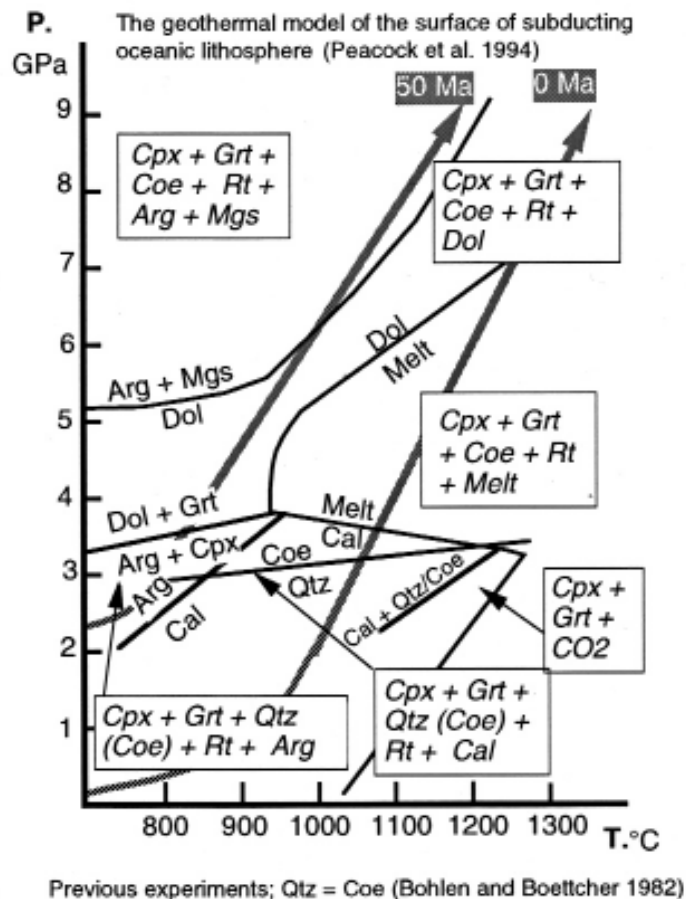
The phase relation in the present study indicates the following geological implications. (1) If the carbonate sedimentary rocks within a relatively 'Hot' oceanic plate subducts, the Ca-enriched dolomitic melt is produced at ~120 km. Gorrington and Kay (2000) reported that the calcite-bearing peridotite xenolith experienced carbonatitic metasomatism in Southern Patagonia. This xenolith came from back-arc basin related with the subducting hot oceanic plate. We considered that this carbonatitic melt was occurred in a slab, and then changed its composition to Ca-rich to react with wall-rock (peridotite) during ascending (Dalton and Wood, 1993). (2) If the carbonate sedimentary rocks within a relatively 'Cold' oceanic plate subducts, the carbonate changes in order calcite, dolomite, aragonite + magnesite with increasing depth. Aragonite within eclogite seems to decrease or disappear because of the reaction with garnet, and finally magnesite is stable in the upper mantle.

#### References

- Bohlen, S. R. and Boettcher, A. L. (1982) The quartz-coesite transformation: a pressure determination and the effects of other components. *J. Geophys. Res.*, 87, 7073-7078.
- Dalton and Wood (1993) The composition of primary carbonate melt and their evolution through wallrock reaction in the mantle. *Earth Planet. Sci. Let.*, 119, 511-525.
- Gorrington, M. L. and Kay, S. M. (2000) Carbonatite metasomatized peridotite xenoliths from southern Patagonia: implications for lithospheric processes and Neogene plateau magmatism. *Contrib. Mineral. Petrol.*, 140, 55-72.

- Peacock, S. M., Rushmer, T. and Thompson, A. B. (1994) Partial melting of subducting oceanic crust. *Earth Planet. Sci. Lett.*, 121, 227-244.
- Schertl, H. P. and Okay, A. I. (1994) A coesite inclusion in dolomite in Dabie Shan, China: petrological and rheological significance. *Eur. J. Mineral.*, 6, 995-1000.
- Shirasaka, M., Takahashi, E., Nishihara, Y., Matsukage, K. and Kikegawa, T. (2001) In situ X-ray observation of the reaction dolomite = aragonite + magnesite at 900-1300 K. *American Mineralogist*, submitted

Figure 1. Phase relation in the system MORB-CaCO<sub>3</sub>



#### 4.12 An Experimental Study of the Effect of Water on the 410-km Discontinuity

Joseph R. Smyth<sup>1\*</sup>, Daniel J. Frost<sup>2</sup>

<sup>1</sup>Department of Geological Sciences, University of Colorado, Boulder, CO 80309 USA; and

<sup>2</sup>Bayersches Geoinstitut, Universität Bayreuth, Bayreuth, D94550 Germany.

\* <joseph.smyth@colorado.edu>

The H content of the Earth is one of the most poorly constrained compositional variables for the planet. The nominally anhydrous olivine and spinelloid phases thought to compose the bulk of the upper mantle and transition zone may contain many times the amount of H and O that reside in the hydrosphere. The seismic discontinuities at depths of 410 and 660 kilometers, which bound the Transition Zone, are generally thought to be due to phase changes in an olivine-dominated mantle composition. The discontinuity at 410 kilometers corresponds to the olivine-wadsleyite transition with an increase in both density and S-wave velocity of about five percent. Wood (1995) suggested that the presence of H<sub>2</sub>O in the transition zone would extend the stability of wadsleyite to lower pressures and broaden the two-phase region. To test this hypothesis, we have conducted a series of synthesis experiments in the multi-anvil press on hydrous and anhydrous peridotite compositions and characterized the products by electron microprobe and single-crystal X-ray diffraction.

Three preliminary experiments were conducted in a hydrous olivine system. Starting material was formulated from powdered natural Fo<sub>90</sub> olivine, brucite, quartz, and wite to achieve a composition of Fo<sub>90</sub> plus 3 wt percent H<sub>2</sub>O with a slight excess of silica. Three additional experiments were conducted in a hydrous peridotite system. The starting material was formulated from powdered natural Fo<sub>90</sub> olivine, plus synthetic brucite, quartz, pyrope and wite to achieve a composition of Fo<sub>90</sub> plus 3 wt percent H<sub>2</sub>O with a sufficient excess of silica and alumina to give approximately 10 normative percent each of pyroxene and pyrope-almandine garnet. The results of our synthesis experiments are consistent with the prediction of Wood (1995) that the presence of H<sub>2</sub>O extends the stability of wadsleyite to 0.6 to 1.0 GPa lower pressure and would necessarily broaden the two-phase loop to 18 or as much as 30 km.

We have characterized the olivine and wadsleyite products by single-crystal X-ray diffraction. Kohlstedt et al. (1996) reported that olivine can accept 2000 ppm by weight H<sub>2</sub>O at pressures in excess of 10GPa. We have refined the atom position parameters and unit cells of five hydrous and anhydrous olivines. We observe a significant expansion of the unit cell volume and the M2 polyhedral volume in the hydrous samples indicating that H incorporation occurs in association with M2 cation vacancies. The volume expansion is large enough to have a significant effect on seismic velocities.

Trivalent cations and H are strongly partitioned to wadsleyite. We have refined the atom position parameters and unit cells of six hydrous and anhydrous wadsleyites. Those that contain the largest proportions of trivalent cations show the greatest deviations from orthorhombic symmetry. Although olivine cannot accept nearly as much H as wadsleyite, it has a larger volume of hydration than wadsleyite.

In all of our hydrous runs containing both olivine and wadsleyite, there appears a sharp boundary between the regions of olivine and wadsleyite. The texture of the run thus does not appear to be a simple chemical equilibrium, but rather a diffusion-controlled boundary. Hydrogen is known to diffuse very rapidly in these materials (Mackwell and Kohlstedt, 1990). This raises the possibility that diffusion of H might control the texture and may affect the sharpness of the boundary in the natural system.

Hydrous wadsleyite is still about five percent more dense than anhydrous olivine. In a hypothetical two-phase region consisting of olivine and wadsleyite plus lesser amounts of garnet and clinopyroxene extending over a depth 20 km in a hydrous system, gravitational equilibrium may be approached by rapid diffusion of H. This would enrich the lower parts of the two-phase region in wadsleyite and the upper part in olivine, thus sharpening the boundary. This mechanism could easily sharpen the

apparent boundary to four kilometers or less as indicated in some seismic studies (Benz and Vidale 1993; Yamazaki and Hirahara, 1994; Vidale et al., 1995). Because diffusion of H is considerably more rapid than convection it might cause the transition zone to serve as a trap for H in the Earth.

In summary, our experimental results are consistent with the prediction of Wood (1995) that the presence of H would move the olivine-wadsleyite transition to 0.6 to 1.0 GPa lower pressure and would expand the two phase region to 20 km or more. Although olivine can accept only up to about 2000 ppm by weight H<sub>2</sub>O whereas wadsleyite can accept 30,000 ppm, olivine has the larger volume of hydration. Both hydrous olivine and hydrous wadsleyite are expected to be significantly slower than their anhydrous equivalents, but in both the hydrous and anhydrous systems wadsleyite is still about five percent more dense than olivine. Because H diffusion is rapid relative to convection it is possible that H diffusion at the boundary may reduce the two-phase transition interval to approach gravitational equilibrium. So the 410-km discontinuity in a hydrous system is likely to appear sharper, shallower, and slower than in an anhydrous system.

#### References

- Benz, H. M. and Vidale, J. E. (1993) *Nature* 365, 147.  
Kohlstedt, D.L., et al. (1996) *Contrib. Mineral. Petrol.*, 123, 345.  
Mackwell, S. J. and Kohlstedt, D.L. (199) *J. Geophys. Res.* 95, 5079.  
Neele, F., (1996) *Geophys. Res. Lett.* 23, 419-422.  
Vidale, J.E., et al. (1995) *Geophys. Res. Lett.* 22, 2557.  
Wood, B.J. (1995) *Science* 268, 74.  
Yamazaki, A. and Hirahara, K. (1994) *Geophys. Res. Lett.* 21, 1811.

### 4.13 The effect of water on the high-pressure phase boundaries in the system $\text{Mg}_2\text{SiO}_4\text{-Fe}_2\text{SiO}_4$

Toru Inoue<sup>§\*</sup>, Yuji Higo<sup>†</sup>, Takayuki Ueda<sup>†</sup>, Yasutika Tanimoto<sup>†</sup> and Tetsuo Irifune<sup>§</sup>

<sup>§</sup>Geodynamics Research Center, Ehime Univ., Matsuyama 790-8577, Japan,

<sup>†</sup>Dept. Earth Sciences, Ehime Univ., Matsuyama 790-8577, Japan

\* <inoue@sci.ehime-u.ac.jp>

#### 1. Introduction

$\text{H}_2\text{O}$  is an important volatile material in the Earth, which may be transported to the Earth's deep mantle by subducting slab [e.g. Irifune et al., 1998; Ono, 1998; Okamoto and Maruyama, 1999]. Recent experiments clarified that wadsleyite( $\beta$ ) and ringwoodite( $\gamma$ ), which are high pressure polymorphs of olivine( $\alpha$ ) and the major high pressure phases constituting the transition zone (410-660 km), can accommodate significant amounts of  $\text{H}_2\text{O}$  (~2-3 wt%) in their crystal structures [Inoue et al., 1995; Kohlstedt et al., 1996; Inoue et al., 1998; Yusa et al., 2000; Ohtani et al., 2000]. Such  $\text{H}_2\text{O}$  should affect the nature of the phase transformation of olivine polymorphs, as it changes the densities and the thermodynamic parameters of the anhydrous forms.

We have conducted high pressure experiments to clarify the effect of  $\text{H}_2\text{O}$  on the  $\alpha$ - $\beta$ - $\gamma$  and postspinel phase boundaries. On the basis of these experimental data, we discuss the nature of the seismic discontinuities in the mantle transition zone.

#### 2. Experimental procedure

High pressure experiments were conducted using an MA8-type high pressure apparatus in Ehime University. The pressure calibration was done on the basis of the anhydrous experiments of  $\alpha$ - $\beta$ - $\gamma$  phase transitions [Katsura and Ito, 1989; Akaogi et al., 1989], and the postspinel transition [Irifune et al., 1998]. Temperature was measured with a W97Re3-W75Re25 thermocouple, whose hot junction was placed in the center of the furnace assembly. The fluctuation of temperature throughout the run was kept within  $\pm 5$  °C in each condition, but no pressure correction was made for the emf of the thermocouple.

Three starting materials ( $\text{Mg}_2\text{SiO}_4$ ,  $(\text{Mg}_{0.9}\text{Fe}_{0.1})_2\text{SiO}_4$  and  $(\text{Mg}_{0.8}\text{Fe}_{0.2})_2\text{SiO}_4$ ) with 1 wt%  $\text{H}_2\text{O}$  were prepared in the  $\alpha$ - $\beta$ - $\gamma$  phase transitions; these were made as mechanical mixtures of the oxides ( $\text{SiO}_2$  and  $\text{MgO}$ ), hydroxide ( $\text{Mg}(\text{OH})_2$ ) and  $\text{Fe}_2\text{SiO}_4$  in adequate proportions. For anhydrous starting material, we used the mixture of forsterite and fayalite. In the postspinel transition, three hydrous starting materials ( $\text{Mg}_2\text{SiO}_4$  + 1, 2 and 3 wt%  $\text{H}_2\text{O}$ ) were prepared.

In most experiments, two capsules containing hydrous and anhydrous starting materials were placed in one cell assembly to directly compare the difference between the two materials under the same pressure and temperature condition. In some experiments, two starting materials with different  $\text{H}_2\text{O}$  contents were also used for comparison.

In high-pressure and high-temperature experiments, pressure was applied first to the target ram loads and then the temperature was kept for mainly 30 minutes, and then the run was quenched by turning off the electric power.

The polished section of the recovered run product was prepared to identify the phases present and to measure their chemical compositions. A wave-dispersive electron probe microanalyser (EPMA) and a microfocused X-ray diffractometer were used for these purposes.

#### 3. Results and discussion

In the  $\alpha$ - $\beta$ - $\gamma$  phase transitions, the experiments were conducted in a pressure range from 11 to 21 GPa at a constant temperature of 1400 °C in the system  $\text{Mg}_2\text{SiO}_4$ - $\text{Fe}_2\text{SiO}_4$  with 1 wt%  $\text{H}_2\text{O}$ . The phase boundary between  $\alpha$  and  $\beta$  in hydrous condition shifted to low pressure side comparing with the anhydrous boundary; this result is consistent with that reported by Chen et al. (in preparation). While in the  $\beta$ - $\gamma$  transition, the boundary shifted to high pressure side comparing with the anhydrous boundary.

In the postspinel transition, the experiments were conducted in a pressure range from 21 to 22 GPa at a constant temperature of 1600 °C in the system  $\text{Mg}_2\text{SiO}_4$ - $\text{H}_2\text{O}$  1, 2 and 3 wt%. The boundary of postspinel transformation shifted to high pressure side comparing with the anhydrous boundary.

The interpretation of the above results can be made by the partition behavior of  $\text{H}_2\text{O}$  between  $\alpha$ - $\beta$ - $\gamma$  and perovskite(Pv)+periclase(Pc), i.e. ( $\text{H}_2\text{O}$  in  $\alpha$ ) < ( $\text{H}_2\text{O}$  in  $\beta$ ) > ( $\text{H}_2\text{O}$  in  $\gamma$ ) > ( $\text{H}_2\text{O}$  in Pv and Pc). Details of the present results are discussed in our presentation.

#### References

- Akaogi, M., E. Ito, and A. Navrotsky, *J. Geophys. Res.*, **94**, 15671-15685, 1989.  
Chen, J., T. Inoue, H. Yurimoto, and D.J. Weidner, submitted to *Science*.  
Inoue, T., H. Yurimoto, and Y. Kudoh, *Geophys. Res. Lett.*, **22**, 117-120, 1995.  
Inoue, T., D.J. Weidner, P.A. Northrup, and J.B. Parise, *Earth Planet. Sci. Lett.*, **160**, 107-113, 1998.  
Irifune, T., N. Kubo, M. Isshiki, and Y. Yamazaki, *Geophys. Res. Lett.*, **25**, 203-206, 1998.  
Irifune, T., N. Nishiyama, K. Kuroda, T. Inoue, M. Isshiki, W. Utsumi, K. Funakoshi, S. Urakawa, T. Uchida, T. Katsura, and O. Ohtaka, *Science*, **279**, 1698-1700, 1998.  
Katsura, T. and E. Ito, *J. Geophys. Res.*, **94**, 15663-15670, 1989.  
Kohlstedt, D.L., H. Keppler, and D.C. Rubie, *Contrib. Mineral. Petrol.*, **123**, 345-357, 1996.  
Ohtani, E., H. Mizobata, and H. Yurimoto, *Phys. Chem. Minerals*, **27**, 533-544, 2000.  
Okamoto, K., and S. Maruyama, *Am. Mineral.*, **84**, 362-373, 1999.  
Ono, S., *J. Geophys. Res.*, **103**, 18253-18267, 1998.  
Yusa, H., T. Inoue, and Y. Ohishi, *Geophys. Res. Lett.*, **27**, 413-416, 2000.

#### 4.14 Is the transition zone a water reservoir ?

G.C.M Richard\*, M. Monnereau

Laboratoire de Dynamique Terrestre et Planétaire, UMR 5562, Observatoire Midi-Pyrénées, 14 Avenue Edouard Belin, 31400 Toulouse, France

\* email: Guillaume.Richard@cnes.fr

Water is present everywhere in the Earth's mantle today, albeit sometimes at the parts per million (p.p.m) level. Earth's mantle total water content is estimated to be close to actual hydrosphere's water content. Numerous studies have been devoted to determination of water solubility in mantle rocks [1, 2, 3]. They all show strong solubility variation from one mineral phase to another. Principally, water partitioning have made the transition zone a probable water-trap of the Earth's mantle. Nevertheless, water distribution within the mantle is still debated to date.

Here we have investigated the effects of mantle dynamics on water distribution in a 2D cartesian box. The model takes into account water partitioning between mantle transition zone and upper and lower mantle (i.e between resp. Olivine-Spinel and Spinel-PostSpinel ). That leads, in absence of advection to an equilibrium state with 100 ppm, 1000 ppm, 10 ppm respectively in the upper mantle, transition zone and lower mantle. We have modelled mantle temperature field using depth-dependent viscosity and plate like surface conditions. Water injection at trench has also been simulated.

Numerical experiments suggest that diffusivity of water has to be very high, at least two orders of magnitude higher than the one experimentally determined [1] to influence significantly water distribution in Earth's mantle (Fig. 1). Infact, the diffusion process is not efficient enough to balance the mixing due to mantle dynamics and to keep water into the transition zone. We find that the distribution of water should be quite homogeneous in the whole mantle. Therefore, water amount deeper than the transition zone would be in excess according to the lower mantle rocks solubility. This addresses the stability of free water in the lower mantle and its mobility by percolation process.

## References

- [1] J. Ingrin, H. Skogby, Hydrogen in nominally anhydrous upper mantle minerals: Concentration levels and implications, *Eur. J. Mineral.* 12 (2000) 543-570.
- [2] D. L. Kohlstedt, H. Keppler, D. C. Rubie, Solubility of water in the alpha, beta and gamma phases of  $(\text{Mg,Fe})_2\text{SiO}_4$ , *Contributions to mineralogy and petrology* 123(4) (1996) 345-357.
- [3] N. Bolfan-Casanova, H. Keppler, D. C. Rubie, Water partitioning between nominally anhydrous mminerals in the  $\text{MgO-SiO}_2\text{-H}_2\text{O}$  system up to 24 GPa: implications for the distribution of water in the Earth's mantle, *Earth Planet. Sci. Lett.* 182 (2000) 209-221.

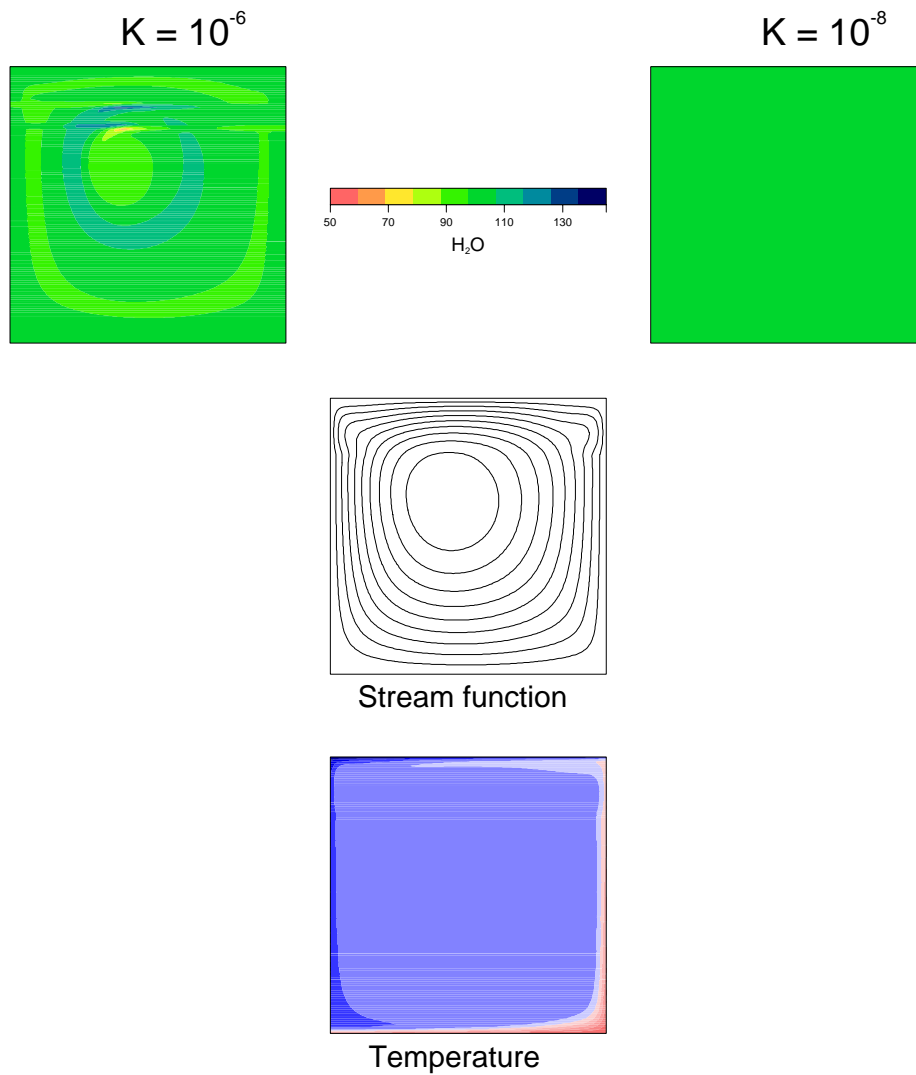


Fig. 1 Effect of water diffusivity on Earth's mantle water distribution. Stream (central box) created by bottom heating (bottom box) is applied to an homogeneous water content mantle. Snapshots of the water content in ppm after convergence is supplied for different water diffusivities (top boxes). Concentration variation in the high diffusivity case  $K = 10^{-6} m^2 \cdot s^{-1}$  (left hand side) reach a factor two, but stay too low to be discernable in this range in the low diffusivity case  $K = 10^{-8} m^2 \cdot s^{-1}$  (right hand side)

#### 4.15 Solubility of water in lower mantle minerals

Motohiko Murakami\*, Kei Hirose, Hisayoshi Yurimoto, Satoru Nakashima

\*Tokyo Institute of Technology

The maximum solubilities of water in the representative lower mantle minerals, MgSiO<sub>3</sub>-rich perovskite, magnesiowustite, and CaSiO<sub>3</sub>-rich perovskite, were determined using secondary ion mass spectrometry. They were synthesized in the peridotitic compositions by the multianvil apparatus at 23.5 GPa under water-saturated conditions. We found that Mg-perovskite and magnesiowustite dissolved about 0.2 wt% H<sub>2</sub>O and Ca-perovskite dissolved about 0.4 wt% H<sub>2</sub>O, respectively. The OH absorption bands in Mg-perovskite and magnesiowustite were also confirmed using microscopic FT-IR, and the water content estimated from these OH absorption bands is consistent with that from SIMS analysis. These results suggest that lower mantle in itself can storage considerable amounts of water, and thus could provide essential implications for the physical properties of the Earth's lower mantle.

#### 4.16 Electrical conductivity of hydrous materials at high pressures and high temperatures.

Tomoo Katsura<sup>1</sup>, Kiyoshi Fujita<sup>2</sup>, and Keishi Shinoda<sup>3</sup>

1: Institute for Study of the Earth's Interior, Okayama University

2: Faculty of Sciences, Kobe University

3: Faculty of Sciences, Osaka City University

Hydrogen plays important roles in electrical conduction in the Earth. For example, electrical conduction in the upper crust is essentially controlled by fluid phases interstitially present in rocks. It is possible that hydrogen is important for electrical conduction also in the mantle and lower crust. From this reason, we are measuring electrical conductivity of hydrous materials at high pressures. Here, we report results of measurement for brucite and granulite.

Electrical conductivity was measured using sinusoidal signal with 10 mHz frequency and 10 V<sub>p-p</sub> amplitude. Reference resistance from 10<sup>4</sup> to 10<sup>6</sup> Ω was connected to the sample in a series. The sample impedance was calculated from reference resistance and voltages on the reference resistance and whole circuit. Effect of capacitance was reduced by assuming that capacitance is connected with sample resistance in parallel. High pressures and temperatures are generated using 6-8 type and DIA-type apparatuses. To avoid decomposition of hydrous minerals or escape of a fluid phase, measurement has to be conducted at relatively low temperatures, typically up to 1000 K, in which minerals and rocks usually have very low electrical conductivity. To obtain high insulation resistance, high-pressure cells were composed of boron nitride, magnesia, thermocouples, and metallic heater system, resulting in *ca.* 10 GΩ insulation resistance up to 1000 K.

Brucite contains Mg, O, and H, but not transition metals. Therefore, hydrogen ion (proton) should be a carrier of electrical conduction in brucite. Pressure and temperature conditions of measurement were 3, 6, 9 and 12 GPa and from 300 to 700 K, respectively. In each pressure step, measurement was carried out in the heating and cooling cycles. The activation energy is decreased with elevated pressure: from 0.99 eV at 3 GPa to 0.75 eV at 12 GPa. This is probably because distance from hydrogen to the neighboring site becomes shorter with compression. On the contrary, the pre-exponential term is nearly constant of 5 × 10<sup>3</sup> S/m, indicating no change of population of the electrical carrier (proton)

Another measurement was conducted for garnet-cordierite-biotite-granulite from Hidaka metamorphic belt, Hokkaido, Japan. It is considered that this granulite was formed at 1000-1100 K and 1 GPa. It was ground into powder, loaded in a Pt capsule, and sintered at 1025 K and 1 GPa for 1 hour. The sintered sample with 2.5 mm diameter and 1.1 mm thickness was set in a pressure cell for electrical conductivity measurement and compressed to 1 GPa. First we heated to 500 K to purge water in a pressure medium, and decreased temperature to *ca.* 300 K. After that, we conducted measurements in two heating cycles: heating from 300 K to 900 K and cooling to 300K, and heating from 300K to 1000 K and cooling to 1000 K. The conductivity was decreased by one order of magnitude at low temperatures by the heating from 300 to 900 K, which is probably due to annealing of the sample. The conductivities measured at in the cooling from 900 K to 300 K and the heating from 300 to 1000 K are identical, indicating that conductivity values measured in these paths are essential to the granulite. The activation energy and pre-exponential term of this intrinsic conductivity are 0.39 eV and 8 × 10<sup>-3</sup> S/m, respectively. The conductivity varies by more than 3 orders of magnitude in the first cooling, first heating, and second heating paths in the present temperature range. However, after reaching 1000 K, conductivity does not varies with cooling, is almost constant of 1 × 10<sup>-4</sup> S/m. This high and constant conductivity could be attributed to a fluid phase formed by dehydration.



**October 5 (Friday) 09:00 — 12:00**

**Session 5**

**Magmatic differentiation and the evolution of the  
mantle and core**

Keynote: Eiichi Takahashi, Tokyo Institute of Technology

Chair: Bernie Wood, University of Bristol



## 5.1 Melt Generation in the Hawaiian Plume

E. Takahashi<sup>1</sup>, K. Nakajima<sup>1</sup>, R. Takeguchi<sup>1</sup>, K. Shinozaki<sup>1</sup>, Ren Zhang-Young<sup>1</sup>, R. Tanaka<sup>2</sup> and E. Nakamura<sup>2</sup>

1: Magma Factory, Earth & Planet Sci., Tokyo Inst. of Tech., 2-12-1 Ookayama Meguroku, Tokyo 152, Japan

2: ISEI, Okayama Univ., Misasa Japan

Genesis of magmas in large hot spot is very important to understand the temperature, chemical composition of the hot mantle plume. Compared with the magmatism under the mid oceanic ridges and those in the subduction zones, magma genesis related to mantle plumes is poorly understood. In order to study the origin and dynamics of mantle plumes, we have carried out both field works and experimental work on several volcanoes in Hawaii which is the most magma productive hot spot on our planet.

### 1. Reconstruction of Koolau volcano

Among Hawaiian shield volcanoes, Koolau shows very silica-enriched trend ( $\text{SiO}_2=53-55$  wt% at  $\text{MgO}=7-5$  wt%, see Fig.1). The Koolau tholeiites are also peculiar in that they show enriched isotope signatures in Sr, Nd and Pb (Roden & Frey, 1994). Based on co-variation in major elements and isotopes among Hawaiian shield volcanoes, Hauri (1996) proposed that the high-silica Koolau tholeiite may contain ca. 10% of dacitic melt derived from former oceanic crusts entrained in the plume. In order to constrain the primary magma composition for Koolau volcano, Takeguchi & Takahashi (2001) studied 250 rock specimen collected from subaerial part of Koolau which covers wider stratigraphic units than previous works (Frey et al.1994; Jackson et al., 1999). In addition, Takahashi & Shinozaki (2001) studied submarine portion of the volcano (ca. 200 rock samples recovered by JAMSTEC submersibles) where much of its deep interior is exposed by the giant Nuanu landslide (Moore et al., 1989, AGU Monograph on Hawaii, 2001) A sharp transition in lava chemistry and isotope ratios was observed at a low stratigraphic horizon of Koolau volcano (first noted by Jackson et al., 1999) where high-silica Koolau type lava changes to mildly silica-enriched normal Hawaiian tholeiite (similar to Mauna Loa and Kilauea). This transition in lava chemistry accompanies with large changes in Sr, Nd and Pb isotope ratios from EM-1 like Koolau values to those of modern Mauna Loa and Kilauea. We have shown for the first time that a Hawaiian shield volcano recorded shift in tholeiite magma composition from one to the other and the silica-rich Koolau tholeiite represents only the final growth stage (Makapuu stage) of the volcano (Shinozaki et al., 2001; Tanaka et al., 2001).

### 2. Primary Koolau magma composition

Picrites are occasionally found in Hawaiian shield volcanoes as well as in Koolau. Implication of the picrites, however, depends on the researchers. Some argues that olivine-rich picrites represent primary magma composition of the Hawaiian hot spot. Presence of kink banding in many olivine crystals in picrite (e.g., Heltz, 1987; Garcia, 1996), however, casts some doubt for the simple high pressure phenocryst hypothesis. Kink banding is common in mantle peridotite with subsolidus deformation. Many of olivine crystals in mantle peridotite, however, do not show kink banding. Presence of olivine xenocrysts with kink banding implies that there may be more olivine xenocrysts in the Hawaiian picrite which do not show kink banding.

In order to discriminate olivine xenocrysts, we carried out dislocation mapping analysis for four picrite specimens from Koolau volcano (Takeguchi & Takahashi, 2001). Polished rock chips were heated at 800°C for 1 hr in air for oxidation, and then the dislocation density was calculated by point counting technique using petrologic microscope. At least three areas were counted within an olivine crystal and the results were averaged. In some picrite, olivine crystals were divided into two distinct types by the dislocation density; type-A, with dislocation density  $10^6-10^9$  /cm<sup>2</sup>; type C,  $10^0-10^3$  /cm<sup>2</sup>. The type-A crystals are enriched in MgO and NiO than type C olivine. Judging from the bulk chemical

composition of the picrite, the type C crystals can be in equilibrium with the host magma but the type-A crystals are difficult. In some picrite, olivine crystal with marginal dislocation density occurs; type-B ( $10^4$ - $10^6$  /cm<sup>2</sup>). Type-B crystals may also be xenocrystic origin but have been annealed in the host magma for longer time. Based on our dislocation mapping it was found that olivine crystals with Fo>85% are xenocrystic origin in Koolau volcano. Conduit zone of the gigantic Hawaiian shield volcanoes penetrate more than 70km thick Pacific plate. These highly strained olivine xenocrysts may originate from the conduit zone where high temperature deformation of the rocks take place due to successive intrusion of hot basaltic magma.

After carefully eliminating the effect of olivine xenocrysts, we concluded that primitive magma of Koolau volcano has a basaltic andesite composition (SiO<sub>2</sub>=53 wt%, MgO=7 wt%). Picrites are present in Koolau but they are mixtures of this primitive melt and olivine xenocrysts (Takeguchi & Takahashi, 2001).

### 3. Experiments to understand the melting process in the Hawaiian Plume

In order to understand the condition of melting and the source rocks for the various primary Hawaiian magmas, we carried out melting experiments with MORB/peridotite and Archean-basalt/peridotite sandwich starting materials (Takahashi & Nakajima, 2001). It was found that Koolau type primitive melts can be produced by extensive partial melting of basaltic source rock alone at 2.5-3.0 GPa and 1350-1400°C; conditions slightly below the dry solidus of mantle peridotite. At conditions on or above the peridotite solidus, melts become saturated with olivine and are similar to picritic magma in Kilauea. Accordingly, we propose that the high-silica Koolau primary magma are produced by almost entirely from the recycled oceanic crust (cf. ca.10% by Hauri, 1996). Changing isotope compositions found in Koolau volcano may indicate variety of mixing ratio between eclogite derived melt and the ambient peridotite derived melt.

In the basalt/peridotite sandwich melting experiments, melt proportion within the basalt domain decreases as temperature increase near the peridotite solidus. This is due to the enhanced chemical reaction between the basalt domain and the ambient peridotite. Due to this effect, bulk melt proportion in the sandwich starting material records minimum at a temperature near the peridotite solidus. Accordingly, melts produced in the peridotite at temperatures above the peridotite solidus are more enriched in incompatible elements K, Ti and LREE than those produced at lower temperatures in the basalt domain. This might explain the difference in trace element characters of Koolau and Kilauea.

Based on the melting experiments and the field observation, we propose a model that the Hawaiian plume had a potential mantle temperature (PMT) of only 1350-1400°C in the Koolau stage (ca 2.5 Ma). This PMT is much lower than the estimate for the modern Hawaiian plume by Watson & McKenzie (1991, PMT=1558°C) assuming homogeneous peridotite source. Our experiments show that only slight increase in PMT (10-50deg) will shift the Koolau type melts to the parental Mauna Loa and Kilauea type melts (SiO<sub>2</sub>=49, MgO=14) in the plume head.

### 4. Phase relation of eclogite and its effect on bulk density

The important role of recycled old oceanic crust in magma genesis in large hot spots (particularly that in Hawaii has become clear in our study. The mismatch in size of the tomographic image of the mantle plume and their magma production rate has been discussed by Zhao et al (2001) and they proposed that it could be explained by the different amount of eclogite entrainments inside the plume. Distribution of the once subducted eclogite blocks in the deep mantle and their entrainment mechanism, therefore, is essentially important to understand the mantle plume related magmatism.

According to Irifune & Ringwood (1987, 1993) eclogite of MORB composition consists of garnet and omphacite at pressures below 15 GPa and becomes almost monomineralic majorite rock at higher pressures. This is reconfirmed in our experiments. The proportion of pyroxene/garnet, however, was found to change significantly with temperature at given pressure. The amount of garnet in Irifune & Ringwood's experiments were found to be underestimated (as much as 20-50%) due to metastable

growth of aluminous pyroxenes. The amount of coesite and stishovite in eclogite was underestimated because of the same reason. Increase in the amount of garnet and stishovite increase the bulk density of eclogite dramatically.

Due to the combined effect of higher amount of garnet and stishovite, calculated zero-pressure bulk density of MORB eclogite equilibrated at 10 GPa and 1200°C increased from 3.6 g/cc (Irifune & Ringwood, 1987) to 3.75 g/cc (Nishihara, Aoki and Takahashi, in preparation). The density difference between the eclogite and fertile peridotite (KLB-1) is 0.1-0.3 g/cc at temperatures of 1200-1800°C in the upper mantle (<400km depth) whereas it decreases to less than 0.1 g/cc in the mantle transition zone (400-700km depth) at temperatures above 1800°C.

Equation of state of majoritic garnet synthesized from natural abyssal basalt was determined up to 16GPa and 1000°C by in situ X-ray diffraction using a single-stage, cubic multi-anvil apparatus MAX-90 and a double stage SPEED apparatus. The MORB majorite was synthesized from a starting material at 19 GPa and 1900°C using 6-8 type multi-anvil apparatus. The bulk modulus for the MORB majorite was obtained by the third-order Birch-Murnaghan equation of state. The obtained value (160.9 GPa) is much smaller than MORB-majorite (226.2GPa) by Faust & Knittle (1995) but is consistent with majorite in Mg-Al-Si system by Yagi et al (1987) (Nishihara et al., 2001)

- E. Takahashi and K. Nakajima (2001) Melting Process in the Hawaiian plume: An experimental study *In Evolution of Hawaiian Volcanoes: recent progress in deep underwater research*, Amer. Geophys. Union, Monograph, (in press)
- K. Shinozaki, Zhong-Yuan Ren and E. Takahashi (2001) Geochemical and Petrological Characteristics of Nuuanu and Wailau landslide blocks, *In Evolution of Hawaiian Volcanoes: recent progress in deep underwater research*, Amer. Geophys. Union, Monograph, (in press).
- R. Tanaka, E. Nakamura and E. Takahashi (2001) Geochemical Characteristics of Koolau volcano and Nuuanu and Wailau landslide deposits, Hawaii, *In Evolution of Hawaiian Volcanoes: recent progress in deep underwater research*, Amer. Geophys. Union, Monograph, (in press).
- D. Zhao, F. Ochi and E. Takahashi (2001) Seismic images of mantle plumes under hotspot regions, *In Evolution of Hawaiian Volcanoes: recent progress in deep underwater research*, Amer. Geophys. Union, Monograph, (in press).
- R. Takeguchi and E. Takahashi (2001) Primary magma composition at the final growth stage of Koolau volcano, Hawaii. Submitted to *Geochimica Cosmochimica Acta*.

## 5.2 Mantle composition and conditions of core formation

B.J. Wood

University of Bristol

A major, defining event in the history of the earth was the separation, within about 80 Ma of accretion of its iron-rich core. The profound chemical fractionation associated with this event segregated into the core most of the earth's Fe and 'siderophile' elements (Ni, Co, W, Re etc) together with about 10% of one or more 'light' elements. This resulted in characteristic patterns of depletion in the silicate earth of siderophile (removed to the core) and volatile (possibly incompletely accreted) elements relative to primitive chondritic material. The 'light' element, in reality a mixture of light elements, is probably dominated by S, with Si and C as potentially important minor components. The pattern of siderophile element depletion in the silicate earth cannot be explained by low pressure equilibrium between metallic core and a silicate melt of mantle composition because siderophile element abundances in the mantle are too high. This observation has led to two competing models of core formation. In one model the earth accreted heterogeneously and began to melt when it was about 25% of the current size due to the energies of impact. Core segregation would begin and continue near the surface of the accreting planet and metal-silicate fractionation patterns be established at low pressure (about 1 GPa). In order to explain the high contents of siderophile elements in the mantle conditions would have had to become more oxidising as accretion progressed. Most of the mantle abundances of the highly siderophile elements would then have been added as a 'late veneer' of oxidised material after core formation. The alternative model relies on the observation that the metal-silicate partition coefficients for some siderophile elements (e.g Ni, Co, Re) decrease with increasing pressure such that there is a theoretical pressure-temperature condition of about 30 GPa and 2500°C where the current mantle abundances of these elements could be explained by single-stage equilibrium between core and mantle. In this model it is postulated that descending droplets of liquid metal equilibrated with the silicate at the base of a 750 km deep magma and established most of the current pattern of siderophile element depletion in a single event. Distinguishing between the two models is difficult, but we believe that weakly siderophile elements such as V, Cr, Si and Nb provide the best constraints.

The silicate earth is substantially depleted in V and Cr relative to CI chondrites, depletions frequently ascribed to dissolution in the core. In contrast, refractory lithophile elements such as Ca, Sc and the rare earth elements (REE) are known to be present in the same proportions in the silicate earth as in chondritic meteorites. Nb has always been treated as lithophile and refractory, yet at 25 GPa and plausible temperatures for core segregation, Nb rather than being lithophile, exhibits almost identical siderophile character to V and Cr. Thus V, Cr and Nb have approximately the same ratios of (core concentration)/(silicate earth concentration). This means either that the depletions of the upper mantle in V and Cr were not due to core segregation or that Nb is also depleted in the upper mantle. Geochemical data suggest that a slight Nb depletion is plausible. In either case strongly reducing conditions would lead to too great a depletion of the mantle in Nb, so a large part of core formation under such conditions can be excluded. Si is known to dissolve readily in Fe at low pressures and has been proposed as being a major part of the light element component of the core (e.g Allre et al. *Earth Planet. Sci. Lett.* 134, 1995). Si remains substantially more lithophile than Nb under all conditions we have investigated (2.5-25 GPa, 1750-2300°C), however. This means that Si cannot be part of the light element inventory of the core unless extreme conditions of temperature and pressure were involved (40 GPa, 3600K or higher).

### 5.3 Boundary layer fractionation constrained by differential information from the Kutsugata lava flow, Rishiri Volcano, Japan

Takeshi Kuritani

Institute for Study of the Earth's Interior, Okayama University  
<kuritani@misasa.okayama-u.ac.jp>

Detailed investigation of an erupted magma with limited compositional diversity provides instantaneous information on incremental magma differentiation processes in a magma chamber. Kutsugata lava, a suitable target of such study, is a Quaternary alkali basalt (51.3-53.2 wt% in SiO<sub>2</sub>) from Rishiri Volcano, northern Japan. Despite the narrow range in the whole rock compositional variation, chemical and modal compositions of mineral phases crystallized in the magma chamber vary systematically with the whole rock composition. In the North lava (51.3-51.9 wt% in SiO<sub>2</sub>) the less differentiated portion of the Kutsugata lava, most crystals which include low-Ni olivine and plagioclase were derived from the mushy boundary layer. The main part of the magma body was principally aphyric (< 0.5 vol% crystals). Estimated chemical compositions of fractionated mineral phases during differentiation of the magma coincide with the observed compositions of low-Ni olivine and plagioclase crystals. This indicates that the main magma was differentiated by separation of crystals grown in the mush zone. The low-density interstitial melt is suggested to have been extracted from the floor mush zone with average crystallinity of > 30 vol% by such mechanisms as compaction and compositional convection. This fractionated melt was mixed with the overlying main magma, causing differentiation of the Kutsugata magma. The average temperature of the extracted melt is 1010°C, significantly lower than 1100°C estimated for the main magma. A quantitative model of magmatic differentiation, which includes thermal and compositional evolution of a mushy boundary layer, can successfully reproduce the observed compositional trends of the North lava.

#### 5.4 Constraints on Porosity in Partially Molten Regions in the Upper Mantle from Permeability Measurements and U-series Modeling

Ulrich Faul

Research School of Earth Sciences, The Australian National University, Canberra

The amount of melt present (porosity) in regions of the upper mantle undergoing melting depends on the physical properties of solid matrix and melt. A critical parameter is the permeability of the matrix, which is determined by the geometry of the intergranular melt distribution. While experimental observations indicate that basaltic melt in a peridotitic matrix is interconnected at all melt fractions, this does not automatically equate to high permeability and hence low residual porosity. High permeability is predicted for self-similar models such as cylinders on a cubic grid and the isotropic equilibrium model consisting of triple junction tubules at the edges of tetrahedral grains. Permeability measurements on texturally equilibrated calcite and quartz (Wark and Watson, *EPSL*, 164, 591-605, 1998) show that natural systems deviate significantly from the ideal models, with lower than predicted permeabilities at low porosities. SEM and TEM observations of the melt distribution in partially molten dunite indicate the existence of wetted two-grain boundaries, which become more numerous as the melt fraction increases. Modeling of the evolution of permeability with increasing porosity (melt fraction) suggests that the permeability will be very low until the wetted two-grain boundaries become abundant enough to interconnect, at which point the permeability increases by orders of magnitude.

The porosity in a 1D melting column can be calculated from a fluid dynamics model based on conservation of mass and Darcy's law (e.g. Spiegelman and Elliot, *EPSL*, 118, 1-20, 1993). Besides permeability, the density difference between matrix and melt and the viscosity of the melt influence the mobility of the melt and hence porosity. Figure 1 shows the porosity distribution in an 85km deep melting column for different permeability models and measurements. Only if the permeability in partially molten upper mantle were equal to that of cylinders on a cubic grid (and hence the melt geometry would have to be that of cylinders on a cubic grid) would the porosity in the melting column be substantially below 1%, as inferred from a range of geochemical models. With Wark and Watson's measured permeabilities the porosity quickly exceeds 1%.

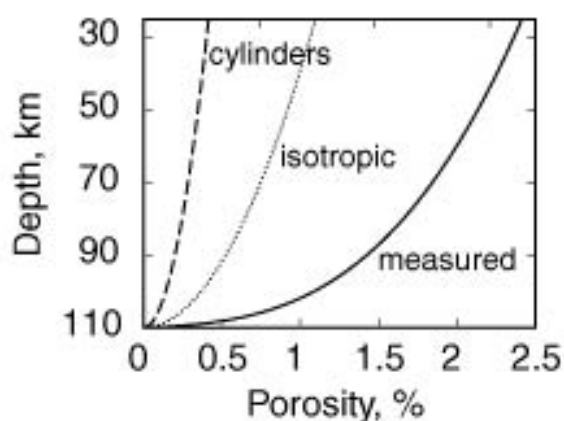


Fig 1. Porosity distribution calculated for a 1D melting column with a solid matrix upwelling velocity of 3 cm/year, density difference melt-matrix of  $500\text{kg/m}^3$  and a melt viscosity of 1 Pas. Melt production begins at 100km depth and ends at 25 km depth, melt productivity is constant at  $0.4\%/km$ . The different permeability models are indicated by dashed lines (cylinders on a cubic grid), dotted (isotropic equilibrium model) and solid (measured, Wark and Watson). The porosities calculated with the measured permeabilities indicate that melt is present at the percent level in partially molten upper mantle.

The calculated porosities allow calculation of U-decay series disequilibria with the equilibrium porous flow model developed by Spiegelman and Elliot (1993) and Spiegelman (Geochem. Geophys. Geosyst. **1**, 1999 6C 000030, 2000). The differences between the permeability models above are larger than possible variations in permeability expected due to variations in phase proportions in different parts of the upper mantle. The same permeability model should therefore be used to calculate isotopic excesses due to melting at mid-ocean ridges and ocean islands. Observed isotopic excesses in MORBs are often quite large, while OIBs generally have small excesses except for Th in relatively low degree melts. To reproduce the mid-range of measured isotopic disequilibria at mid-ocean ridges with moderate spreading rates, the permeability of peridotite has to be that of the cylinder model, which is the most permeable model that can be physically realized. Maximum porosities of the order of 0.1% necessary to satisfy high Ra excesses in depleted MORBs imply substantially higher permeability. In contrast, when used for modeling OIBs the cylinder model predicts excesses that are too high for the low degree melts. With the threshold model mid-range excesses for the longer lived isotopes Th and Pa are calculated for MORBs when a small amount of volatile-rich melt with low viscosity and density is present below the anhydrous peridotite solidus, and melt accumulation is rapid. Similarly, observed excesses at Hawaii can be reproduced when the different melt properties are taken into account. Because of the near 'instantaneous' decay of Ra at porosities above 0.1% on the time scale of physically realistic melt transport models, Ra excesses are likely to be due to processes close to the eruption site of the magmas.

## 5.5 Evidence for slab tear and the related magmatism beneath the northwestern El Salvador, Central America

Ryoji Tanaka and Eizo Nakamura

PML, ISEI, Okayama Univ., Misasa, Japan

Large felsic magmatism, volcano-plutonic complexes, back-arc side alkaline volcanoes, and high sulfidation type mineralization are often distributed at regular intervals along volcanic arc systems. In order to explain such a geographical distribution, existence of large-scale tectonic segmentations has been proposed for some volcanic arcs. Tectonic segments and segment boundaries are defined by the offset of along-arc volcanic alignment or seismic discontinuity. It is very critical in the genesis of arc magmas whether the subducting slab is torn or not, because heat and material exchange between supra and sub-slab asthenospheric mantle could occur through the torn "slab window".

A cinder cone field in NW El Salvador has been geochemically studied in order to clarify the magma genesis related to the unique segment boundary in Central America. This area was chosen for the following reasons: (1) hypocenters deeper than 120km depth are not observed in this area, (2) Quaternary volcanoes exist successively in the across-arc direction towards the back-arc side, and (3) there is a seismic offset of the Wadati-Benioff zone beneath the area. Volcanoes are divided into four groups according to distance from the volcanic front toward the back-arc side; VF (volcanic front), BVF (behind volcanic front)-A, BVF-B, and BVF-C. The trace element ratios and Sr, Nd, and Pb isotopic ratios discriminate two across-arc geochemical trends. The two trends for each isotopic ratio cross at BVF-A lavas when plotted against the distance from the volcanic front. The B/Nb and the Pb and Nd isotopic ratios indicate that Trend I (from VF to BVF-A) can be attributed to the successive depletion of a slab derived fluid component in the magma source toward the back-arc side. On the other hand, Trend II (from BVF-A to BVF-C) shows the high Zr/Hf, La/Yb and the positive correlation between Zr/Hf and Pb isotopic ratios. Lavas in Trend II have higher SiO<sub>2</sub>, Ni, Cr contents for a given value of MgO contents than those in Trend I. Among the BVF-A lavas, the most magnesian and nepheline-normative lava from a cinder cone shows the lowest <sup>87</sup>Sr/<sup>86</sup>Sr,  $\epsilon_{Nd}$ , Zr/Nb and the highest Zr/Hf and Pb isotopic ratios. The primary magma of this lava is inferred to be picrite. This primary magma composition indicates the extremely high H<sub>2</sub>O fugacity and the existence of refractory peridotite.

These data suggest the existence of slab tear in this region. The slab tear would induce to release the fluid component from the subducting hydrated harzburgite (serpentinite) and to melt the subducting oceanic crust. These effects can be a trigger of alkali basalt and magnesium-rich andesite magmatism behind the volcanic front in this region.

## 5.6 Geochemical evolution of Koolau Volcano, Hawaii

Ryoji Tanaka<sup>1</sup>, Eizo Nakamura<sup>1</sup>, Eiichi Takahashi<sup>2</sup>

<sup>1</sup> PML, ISEI, Okayama Univ., and <sup>2</sup> Dept. Earth Planet. Sci., Tokyo Inst. Tech.

Koolau shield is composed of older Main shield stage and younger Makapuu stage lavas. So-called Koolau-type lavas, as recognized geochemically enriched-endmember component in the Hawaiian shield, are restricted to only the Makapuu stage. In both the subaerial shield and northwestern submarine flank, Main shield stage lavas are buried by Makapuu stage lavas. Only the uppermost part of Main shield stage lavas are exposed in the lowermost subaerial sequences on the cliff, and the majority of the Main shield stage lavas were obtained from the Nuuanu landslide blocks offshore north to the Oahu Island. Main shield stage lavas are characterized by lower Ba/Nb, La/Nb, Pb/Nd, Sr/Nb, Nd/Nb, Zr/Nb, and  $^{87}\text{Sr}/^{86}\text{Sr}$  and higher  $^{143}\text{Nd}/^{144}\text{Nd}$  and  $^{206}\text{Pb}/^{204}\text{Pb}$ , which resemble Loa- or Kea-type compositions, than those of Makapuu stage lavas. Sr-Nd-Pb isotope systematics suggest that Koolau shield lavas were generated from at least three endmember components, such as Enriched Makapuu (EMK), Depleted Makapuu (DMK), and Kea (KEA) components. Both DMK and KEA are similarly depleted in Sr and Nd isotopic compositions ( $^{87}\text{Sr}/^{86}\text{Sr} < 0.7035$ ,  $^{143}\text{Nd}/^{144}\text{Nd} > 0.5130$ ), but the  $^{206}\text{Pb}/^{204}\text{Pb}$  of KEA ( $> 18.80$ ) is distinctively higher than DMK ( $< 17.78$ ). On the other hand, EMK is isotopically enriched in  $^{87}\text{Sr}/^{86}\text{Sr}$  ( $> 0.70427$ ) and  $^{143}\text{Nd}/^{144}\text{Nd}$  ( $< 0.51265$ ) compared with DMK and KEA. The  $^{207}\text{Pb}/^{204}\text{Pb}$  and  $^{208}\text{Pb}/^{204}\text{Pb}$  of EMK ( $> 15.45$  and  $> 37.8$ ) are higher than those of DMK ( $< 15.37$  and  $< 37.2$ , respectively). Higher  $\text{SiO}_2$ ,  $\text{Al}_2\text{O}_3/\text{CaO}$  and incompatible trace elements than other endmembers also characterize EMK. The proportion of these endmember components successively changed from earlier KEA-dominated with an extremely small proportion of EMK, to later EMK-dominated. These observations reveal that the Koolau shield stage lavas span nearly the entire range of the isotopic compositions reported previously for shield stage lavas from all Hawaiian islands, and reveal a secular change in the amount of plume component involved in the generation of Koolau shield magmas. This suggests that it is inadequate to model the evolution and geochemical structure of Hawaiian mantle based only on geochemical investigation of near-surface lavas as is typically done for oceanic island basalts.

### 5.7 A possible discontinuous behavior of melt percolation in partially molten mantle and its implication to compositional layering in orogenic lherzolites.

Masaaki Obata\*, Eiichi Takazawa

\*Department of Geology and Mineralogy, Kyoto University, Kita-shirakawa, Kyoto 606-8502 Japan

Permeability is an important parameter of partially molten rocks that controls the readiness of the migration of partial melts along the grain boundaries. Theoretically the permeability is a function of porosity (or melt fraction) and geometry of the pores (microstructure) of the partially molten rocks. In the upper mantle, high-temperature conditions, textural equilibrium is believed to be maintained or to be closely approached, with the microstructure being controlled by the balancing of the surface energies between the melt and the solids. Several models have been proposed for the permeability function on the basis of percolation experiments and theoretical consideration for a simple and idealized geometries. All the previous models, however, assumes one-to-one relationships between the permeability and the porosity for a given grain size in the matrix. This may be valid only when the melt is not in motion and when the melt pressure is equal to the solid pressure. However, in a dynamical situation where melt is in motion with respect to the solid framework, the melt pressure may deviate from the solid pressure. This inequality of the melt and solid pressures may affect the geometry of the pore and thus the microstructure and thereby affect the permeability even if the melt fraction is kept constant. Quantitatively, in a dynamical situation, a small unbalance in pressure that is generated between the melt and solid may be adjusted through a local recrystallization by the variation of the average curvature between the melt solid interface, which in turn affect the melt connectivity and thus the permeability function. We point out a possibility that a discontinuous topological change may occur at some critical melt fraction that causes a sudden jump of permeability function. Such a discontinuous change of permeability may cause an abrupt motion of melt migration. Abrupt change of composition observed in some orogenic lherzolite mass may be the products of such abrupt behavior of melt percolation in the upper mantle.

We will present a geological example for the products of such a process from a large orogenic lherzolite mass, the Horoman peridotite, Hokkaido, Japan. In the Horoman peridotite, in a 100 meter measured section harzburgite, lherzolite and plagioclase lherzolite occur in this sequence forming a layered structure (Takazawa et al, 2001). Important features are (1) that these rocks define a single colinear trend in compositional space in terms of whole-rock major elements composition and (2) that there are several compositional gaps between the rocks types. The observed compositional collinearity is best explained by the partial melting and melt extraction model (Obata and Nagahara, 1987; Takazawa et al, 2001) but the compositional jump cannot be explained by any conventional model. We interpret the observed compositional gaps is a manifestation of a sudden jump of the permeability function mentioned above.

## 5.8 The role of water in generation of komatiite magma

Yuki Asahara, Eiji Ohtani

Tohoku University

The question whether komatiites were formed under the wet or dry conditions is fundamental for understanding the early thermal history of the Earth. Komatiites are high magnesian volcanic rocks and they were thought to have been formed by partial melting of the dry mantle at high pressures and temperatures [1]. Recently, some workers suggested a possibility that komatiites magmas were generated under hydrous conditions based on the evidence from natural samples [2,3].

Here we reports the results of melting experiments with various H<sub>2</sub>O contents at high pressures and temperatures, and we evaluate possible roles for water in the generation of komatiites magmas.

Hydrous phase relations of primitive mantle compositions in the CaO-MgO-Al<sub>2</sub>O<sub>3</sub>-SiO<sub>2</sub>-H<sub>2</sub>O system with 1, 2, and 5 wt.% H<sub>2</sub>O have been investigated at 4-8 GPa. Compositions of aluminum depleted komatiites are consistent with the liquid formed by more than 30% melting of the primitive mantle containing H<sub>2</sub>O up to 5 wt.% above 8 GPa. Aluminum undepleted komatiite can be formed by more than 50 wt.% melting of dry or wet primitive peridotite with H<sub>2</sub>O up to 2 wt.% at around 4-6 GPa. Variation in chemistry of komatiites might be explained by various depths of partial melting in the primitive mantle under various hydrous conditions, and the variation may reveal dehydration history of Earth's mantle.

### References

- [1] Herzberg, C. (1992), Depth and degree of melting komatiite., *J. Geophys. Res.* 97, 4521 - 4540.
- [2] Parman et al. (1997), Emplacement conditions of komatiites magmas from the 3.49 Ga komati formation, Barberton Greenstone Belt, South Africa. *Earth planet. Sci. Lett.* 150, 303 - 323.
- [3] Shimizu et al. (2001), Cr-spinel, an excellent micro-container for retaining primitive melts - implications for hydrous plume origin for komatiites, *Earth planet. Sci. Lett.* 189, 177 - 188.

## 5.9 Determination of trace element partitioning between majorite and silicate melt in the primitive mantle composition at pressure of 15 GPa

Eizo Nakamura<sup>1</sup>, Toshihiro Suzuki<sup>2</sup>, Katsura Kobayashi<sup>1</sup>, Akio Makishima<sup>1</sup> and Masaki Akaogi<sup>2</sup>

<sup>1</sup> The Pheasant Memorial Laboratory for Geochemistry & Cosmochemistry (PML), Institute for Study of the Earth's Interior, Okayama university at Misasa, Tottori 682-0193, Japan <sup>2</sup> Department of Chemistry, Gakushuin University, Mejiro, Toshima-ku, Tokyo 171-8588, Japan

Majorite, a garnet solid solution containing pyroxene component, is considered as one of the important constituent minerals in the transition zone of the earth's mantle. Thus it has been proposed that majorite played an important role in the chemical fractionation deep in the earth's mantle based on the high-pressure partitioning experiments. However, most of the previous experiments were carried out using starting materials doped by considerably large amounts of small number of key elements (wt. % level available for EPMA) for "trace elements", and the run durations were relatively short as < 10 minutes, making it difficult to apply simply the results to the natural system in the mantle. In order to overwhelm these problems, we undertook melting experiments using a starting material similar to primitive mantle composition both in major and trace elements of McDonough and Sun (1995), and changing run duration from 10 to 120 minutes.

The starting material named PML-PM-1 was prepared by mixing Horoman plagioclase lherzolite and Komuro andesite with approximately 9:1 resulting in primitive mantle composition except for slight depletion of HFSE and slight enrichment of alkaline elements due to the island arc signature of Komuro andesite. Melting experiments were performed under conditions of 15 GPa and 2400°C using a 6-8 type multi-anvil high pressure apparatus installed at Gakushuin University. Details of the experiments are described in Suzuki et al. (2000). Experimental charges were analyzed by a combination of SEM-EDX and ion microprobe (Cameca ims 5f) for major elements and trace elements, respectively. Quantitative analyses of 17 trace elements in majorite and melt with ion microprobe were calibrated using standard materials such as mantle-derived homogeneous clinopyroxene or garnet, and fused MORB glasses using a piston cylinder, respectively, which were precisely characterized by ICP-MS and ion microprobe. The concentration levels of trace elements in the standard materials are similar to those of majorites and melts except for La, reducing matrix effect in the ion probe analyses and thus capable of measuring sub-ppb concentration level of 10  $\mu\text{m}$  spot in diameter. It was difficult to totally avoid a large contamination of La from the surrounding  $\text{LaCrO}_3$  tube, which was used as a thermal insulator, even though the graphite capsule was further enclosed by Re and MgO cylinder and discs. However, the contamination of La was consequently reduced to several tens ppm by this treatment, which is more than two order of magnitude smaller than those in the pervious method.

The D values (Concentration in Majorite/Concentration in Melt) of REE smoothly decrease with increasing ionic radius. D of La very well fits the extrapolation of middle to light REE values in spite of extraordinary large contamination of La. However, the results are largely affected by the run duration. That is, the D values of LREE become smaller with increasing run duration (D=0.07 to 0.003 for La in 10 to 120 minutes runs, respectively), and the LREE/HREE ratios nearly plateau at the run duration more than 60 minutes. Furthermore, the extent of time effect to D values systematically increases with increasing ionic radius. When compared to the previous experiments and one of the present experiment carried out run duration shorter than 10 minutes, D values of extremely incompatible elements such as La and Nb in 60 to 120 minutes runs are more than one order of magnitude smaller. These observations clearly indicate that the D values of trace elements between majorite and melt obtained with shorter experiments (< 10 min.) are out of equilibration so that most of the trace element partitioning experiments especially for incompatible elements must be re-examined. This is supported by the imaging observation of secondary ions performed by high-sensitivity ion microprobe, Cameca ims 1270. That is, the La distribution in majorite grains formed in the shorter run duration show a compositional gradient with lower concentration in the core than the rim, but relatively uniform lower

concentration in the longer runs exceeding 60 minutes. The D values of LREE obtained for majorite are essentially similar to those for garnet formed under condition of 5 Gpa using JB2 as a starting material, basalt from Oshima Island, except for Eu negative anomaly with garnet. However, D values of HREE for garnet are significantly larger than those of majorite exceeding analytical errors. This might be resulted from incorporation of pyroxene component into majorite with increasing pressure. If this is the case, the role of majorite garnet for the HREE fractionation in the deep in the mantle decreases with further increasing pressure.

#### References

- McDonough, W.F. and Sun, S-s., 1995. The composition of the Earth. *Chem. Geol.* 120, 223-253.
- Suzuki, T., Akaogi, M. and Nakamura, E., 2000. Partitioning of major elements between garnet-structured minerals and silicate melt at pressure of 3-15 GPa. *Phys. Earth Planet. Inter.* 120, 79-92.

## 5.10 Melting of peridotite under lower mantle conditions and its implication to differentiation of a deep magma ocean

E. Ito, A. Kubo, T. Katsura, and M. J. Walter

Institute for Study of the Earth Interior, Okayama University, Misasa Tottori-ken 682-0193, Japan

It is generally accepted that the Earth would have been covered by a deep magma ocean in an early stage of its history. Possible heat sources for such extensive melting are (1) the released gravitational energy of accreting planetesimals, (2) that associated with segregation of the central metallic core from the uniform primordial earth material, and (3) a giant impact which might trigger formation of the moon. It is highly likely that some crystal differentiation proceeded in the magma ocean resulting in large scale chemical stratification of the mantle. Melting experiments on mantle material up to pressures corresponding to the deep magma ocean may provide important information to verify the hypothesis. Especially important is proper identification of the liquidus phases and element partitioning between the liquidus phase and melt. In the present study, we have carried out melting experiment on peridotite up to 33 GPa, and propose a working hypothesis for crystal fractionation in deep magma ocean.

High-pressure experiments were performed using a split-sphere type of high-pressure apparatus equipped with sintered diamond (SD) anvils [1]. The SD cubes of 14 mm edge length with truncated corner of 1.5 or 2.0 mm were employed together with an octahedral pressure medium of magnesia mixed with 5%Cr<sub>2</sub>O<sub>3</sub>. Powdered peridotite (KR4003 [2]) sample was put directly into a cylindrical Re heater of 0.7 mm(outer diameter) × 3.8 mm (length), which was set in the octahedron with a LaCrO<sub>3</sub> sleeve. Experimental pressure was determined based on the calibration curve constructed at room temperature using several fixed points: ZnS (15.6 GPa), GaP (22 GPa), and Zr (33 GPa). Effect of sample heating on the generated pressure was minimized by using a sleeve of 0.7 mm thickness, as described elsewhere [1]. The sample was heated to ca. 2500°C for 2-3 min at the prescribed load, and then quenched by shutting off the electric power to the heater. The recovered products were made to polished sections, which were examined by electron microscopy and then analyzed by the electron probe micro analyzer.

The melt was identified under the scanning electron microscope by the presence of dendritic texture. Most of the melt concentrated in the central, high temperature region of the charge, which would have been caused by the dissolution of solid phase components at high temperature and precipitation of those components at lower temperature as a consequence of the saturation gradient due to the steep temperature gradient through the charge (1-2 °C/μm). This makes location of the liquidus very clear in the charge, whereas the solidus is defined more ambiguously in terms of grain size and the presence of pseudomorphs of the starting material. In the super solidus region, phase identification was carried out based on morphology and chemical composition. The temperature gradient in the charge makes it possible to establish the crystallization sequence of different phases with decreasing temperature from the liquidus.

Ferropiclsase (Fp) is the liquidus phase up to about 30 GPa, which is successively followed by magnesian perovskite (Mg-Pv) and calcium perovskite (Ca-Pv). Both Fp and Mg-Pv coexist along the liquidus at 31 GPa, indicating multiple saturation of these phases. At 33 GPa, however, the front of Fp grains moves back from the liquidus to the slightly lower temperature region and Mg-Pv becomes the liquidus phase. Ca-Pv crystallizes at a fairly lower temperature than Fp and Mg-Pv at pressures up to ca. 29 GPa. However the crystallization temperatures of Fp and Ca-Pv become closer with increasing pressure, and the former might be only a few degrees higher than the latter at 33 GPa. The change in liquidus phase in peridotite found in the present study indicates that the composition of the initial melt formed by melting in peridotitic mantle deeper than 900 km should be more basic (or more deficient in silica) than the peridotitic composition.

Remarkable variation in composition was not observed over the central “melt pools” in the run products, which have composition very close to the initial peridotitic. However, both Mg-Pv and Fp on the liquidus have definitely higher Mg/(Mg+Fe) ratios than those located close to the solidus. Partition coefficients between Mg-Pv, Fp, and melt for Si, Mg, Ca, Fe, and Ni do not show prominent pressure dependence compared with those determined at lower pressure [3]. However, Al, Cr, and Ti become “incompatible” in Mg-Pv at 33 GPa. It should be also noted that alkaline (K and Na) and rare earth (La) elements strongly prefer Ca-Pv rather than melt.

Using the compositions of liquidus Mg-Pv, Fp, and Ca-Pv at 33 GPa, we have examined differentiation of these phases from a C1 bulk mantle composition [4] in terms of mass balance regression with respect to Mg, Si, Al, Fe, and Ca. The calculation indicates that preferential subtraction of 34% Mg-Pv and 3% Ca-Pv yields a residual melt close to peridotitic composition, involvement of Fp being negligible. The fractionated perovskites would pile up in the bottom of the mantle to form a layer attaining to a depth ca. 1600 km. Although the perovskite layer may have subsequently interacted with the upper materials, it could stably lie in the lower half of the mantle for a long term because of its intrinsically high density. The layer, on the other hand, is characterized by the high capability of Ca-Pv to accommodate alkaline and rare earth elements as an enriched and heat-producing reservoir [5].

#### References

- [1] Ito, E., A. Kubo, T. Katsura, M. Akaogi, and T. Fujita (1998) *Geophys. Res. Lett.*, 25, 821-824.
- [2] Xue, X., H. Baadsgaard, A. J. Irving, and C. M. Scarfe (1990) *J. Geophys. Res.*, 95, 15879-15891.
- [3] McFarlane, E. a., M. J. Drake, and D. C. Drake (1994) *Geochi. Cosmochi. Acta*, 58, 5161-5172.
- [4] Ohtani, E., T. Kato, and H. Sawamoto (1986) *Nature*, 322, 352-353.
- [5] Kellogg, L. H., B. H. Hager, and R. D. van der Hilst (1999) *Science*, 283, 1881-1884.

### 5.11 Core formation in a reduced magma ocean: new constraints from W, P, Ni and Co

M. Walter

Institute for Study of the Earth's Interior, Okayama Univ., Misasa, Tottori-ken 682-01, Japan;  
walter@misasa.okayama-u.ac.jp

Models for equilibrium core formation in a magma ocean are based on mantle siderophile element (SE) abundances, estimates of bulk Earth SE abundances and a knowledge of metal/silicate partition coefficients,  $D^{met/sil}$ . Equilibrium models must account for the effects of pressure ( $P$ ), temperature ( $T$ ), silicate and metal melt compositions, and oxygen fugacity ( $fO_2$ ) on  $D^{met/sil}$ . The most comprehensive model to date is by Righter and Drake (1999: RD99)<sup>1</sup>, in which all available partitioning data for several SE's are empirically fitted to an equation of the form:

$$\ln D^{met/sil} = a \ln fO_2 + b/T + cP/T + d(nbo/t) + e \ln(1-X_s) + f \ln(1-X_c) + g \quad (5)$$

Based on regressions for five moderately siderophile elements (P, W, Co, Ni and Mo), RD99 concluded that metal-silicate equilibrium may have occurred in a hydrous, magma-ocean at  $\sim 27$  GPa and 2200K. Final equilibration may have occurred when metal ponded at a solid, perovskite-rich magma ocean floor, and this model has arguably become the standard equilibrium magma-ocean core-formation model. In the RD99 model,  $fO_2$  is determined to be about IW-0.4, yielding an FeO content of more than 20 wt% in the residual bulk silicate Earth, more than a factor of two greater than present estimates for the upper mantle. Thus, the RD99 model implicitly requires metal/silicate equilibrium in an oxidized magma ocean, with the mantle having become subsequently more reduced.

Using equation 1 to fit partitioning data can be fraught with danger because the valence state of the SE must be constant over the entire range of conditions being regressed, and  $\ln D$  must be linearly dependent on intensive variables such as  $P$  and  $T$ . Here, we examine new partitioning data for W, which show that valence state is not constant and the pressure effect is non-linear. We also present new partitioning data for P that pressure causes P to become considerably more lithophile, an effect not found previously for this element. We combine our new data for W and P with literature data for Ni and Co to test magma-ocean core-formation models.

The dependence of  $D^{met/sil}$  on  $fO_2$  can be formulated from thermodynamics as:

$$\log D = -x/4 \bullet \log fO_2 + \text{constant} \quad (6)$$

where the slope ( $x/4$ ) is a function of the valence state ( $x$ ) of the metal oxide. This has important implications for modeling core formation because  $fO_2$  is an unconstrained parameter in bulk Earth models, and  $D^{met/sil}$  can be highly dependent on  $fO_2$  especially for high valence cations. Thus, it is critical to know the valence of each SE over a wide range of  $P$  and  $T$ . We have conducted more than 70 experiments to determine  $D^{met/sil}$  for W over a range of conditions from 1 to 18 GPa, 2100 - 3000 K, IW-1 to IW-2.5, and in komatiitic to peridotitic melt compositions. Results for W are summarized as follows: 1) At 1 and 2 GPa, regressions clearly indicate that W occurs in a 5+ oxidation state in the silicate. 2) At 6 - 18 GPa regressions show that W occurs in 4+ oxidation state. 3) The effect of pressure on DW is highly non-linear, with DW increasing up to about 5 GPa, but decreasing monotonically at higher  $P$ . This change if pressure effect is probably related to the change in valence. 4) DW is highly dependent on silicate melt composition. We have conducted 16 experiments to determine  $D^{met/sil}$  for P over a range of conditions from 2 to 18 GPa, 2100 - 2700 K, IW-1.5 to IW-2.5, and in komatiitic to peridotitic melt compositions. Results are summarized as follows: 1) P apparently occurs in a 4+ valence state over the entire range of conditions. 2)  $T$  causes an increase in DP whereas pressure causes a uniform decrease in DP. 3) DP is moderately dependent on silicate composition. In addition, partitioning data for Ni and Co consistently indicate that these elements, like Fe, exist in a 2+ valence state over a wide range of  $P$  and  $T$  at  $fO_2$  below the IW buffer<sup>2</sup>.

We have tested equilibrium core formation in a magma-ocean using our new partitioning data for W and P, the latest literature data for Ni and Co, and a bulk-Earth chemical model<sup>3</sup>. First, in a test of the model conditions of RD99 (27 GPa, 2250 K, IW-0.4, nbo/t=2.7), we find that Ni and Co depletions can be successfully matched within about a factor of 2. However, according to our new data, at the RD99 conditions W would be about a factor of 30 and P about a factor of 700 too lithophile to account for mantle depletions! Even though our modelling is simplified because it does not presently take into account the effects of S or C in the metal, it is extremely unlikely that the effects of these minor components can account for the severe mismatches in predicted and observed depletions.

Using a trial and error approach, a set of conditions is located that can account for the observed depletions of Ni and Co within a factor of 2, and W and P within a factor of about 3. The conditions are: 40 GPa, 4000 K, nbo/t=2.8 (peridotite), and  $fO_2$  of IW-2.6. A similar P - T condition has been determined based on data for Ni and Co in isolation<sup>2</sup>. This result must be considered with caution, however, because the effects of pressure and temperature for all elements have been extrapolated considerably outside the range of the data, requiring further experiments for verification.

Taken at face value this new model indicates core-mantle equilibration in a magma ocean at a depth of about 1200 kms. Such a depth is not too dissimilar to a recent tomographic estimate for the depth of topography in the lower mantle (relic magma ocean floor?)<sup>4</sup>. Further, the relatively low  $fO_2$  predicted in our model would leave a mantle with only about 4 wt% FeO, or about half the estimated value of the present upper mantle, so the mantle would have become subsequently oxidized. The low  $fO_2$  predicted in our model is required in order to make W and P sufficiently siderophile, counteracting the effect of pressure on these elements. Corroborating evidence for a reduced Earth during core formation comes from recent partitioning data, which show that mantle depletions in V and Nb may be due to sequestering of these elements into the core if conditions were highly reduced (i.e.  $\sim$  IW -3)<sup>5</sup>. Further, at such reduced conditions considerable Si can dissolve into the core, accounting at least in part for the light element in the core as well as the sub-chondritic Si/Mg ratio of the upper mantle.

[1] Righter, K. and Drake, M., EPSL, 174, 383, 1999.

[2] Li, J. and Agee, C., GCA, 65, 1821, 2001.

[3] McDonough, W., Chemical Geology, 120, 223, 1995.

[4] van der Hilst, R. and Karason, H., Science, 283, 1885, 1999.

[5] Wade, J., and Wood, B., Nature, 2001.

## 5.12 Mechanisms of metal transport during formation of the earth's core: constraints from the kinetics of metal-silicate reactions

D.C. Rubie<sup>1</sup>, C. Holzappel<sup>1</sup>, J. Reid<sup>1</sup>, S. Fortenfant<sup>1</sup>, H.J. Melosh<sup>2</sup>, B.T. Poe<sup>1</sup>, D.J. Frost<sup>1</sup>, K. Righter<sup>2</sup>

<sup>1</sup> Bayerisches Geoinstitut, Universitaet Bayreuth, D-95440 Bayreuth, Germany

<sup>2</sup> Lunar and Planetary Laboratory, University of Arizona, Tucson, AZ 85721, USA

The concentrations of siderophile elements in the Earth's mantle are believed to have resulted from reactions between liquid metal and silicates/oxides during the early history of the Earth. Based on measured metal-silicate partition coefficients, siderophile element concentrations are too large to be explained by chemical equilibrium during the separation of liquid metal from silicates at low pressures. However, partition coefficients for elements such as Ni and Co decrease with increasing pressure at an oxygen fugacity just below the IW buffer and reach appropriate values at 25-30 GPa. It has therefore been proposed that the concentrations of such elements in the mantle are the result of metal-silicate equilibration at the base of a magma ocean 700-800 km deep (e.g. Li and Agee, 1996; Righter et al., 1997). According to this model, liquid metal ponds at the base of a silicate magma ocean and, after equilibrating chemically, descends as diapirs to form the Earth's core. In the case that a magma ocean stage did not exist on the Earth (e.g. Jones and Palme, 2000), siderophile element concentrations must have resulted from reaction between liquid metal and crystalline silicates/oxides.

The role of reaction kinetics in controlling the partitioning of siderophile elements during core formation has been discussed briefly by Stevenson (1990) and Karato and Murthy (1997). We are investigating kinetics between liquid metal and crystalline mantle phases and between liquid metal and liquid silicate, both experimentally and theoretically. Multianvil experiments on liquid metal-magnesiowüstite at 10 GPa and 2200 K show that equilibration rates are controlled by the diffusion of siderophile elements in the crystalline phase. Diffusion data (e.g. Fe-Mg interdiffusion) for mantle minerals can therefore be used to model rates of metal-silicate reactions during core formation. High-pressure diffusion data for olivine, wadsleyite, magnesiowüstite and (Mg,Fe)SiO<sub>3</sub> perovskite show that rates of reaction must vary strongly with depth. This is because diffusivities differ strongly between these phases: Fe-Mg diffusion is relatively fast in wadsleyite whereas in perovskite it is several orders of magnitude slower than in the other phases. Considering likely rates of grain-scale metal percolation, migration of a large fraction of the liquid metal to the proto-core will occur with very limited chemical exchange with crystalline mantle. Only the last small fraction of metal will percolate slowly enough to allow equilibrium to be reached.

For modeling the kinetics of equilibration between liquid metal and liquid silicate, experimental measurements of viscosity and diffusivity are being performed. Model reaction rates are controlled by chemical diffusion through a silicate liquid boundary layer adjacent to the liquid metal. In the case of reaction between a layer of segregated liquid metal and overlying silicate liquid at the base of a deep magma ocean, the convection velocity of the magma ocean controls both the equilibration rate and the rate at which the magma ocean cools. Results indicate that time scales of chemical equilibration are several orders of magnitude longer than the time scales of cooling and crystallization of the magma ocean. In an alternative model, falling liquid metal droplets and silicate melt react in a convecting magma ocean. In this case, the droplet size and settling velocity are critical parameters. For a typical silicate liquid viscosity at 2600 K, the stable droplet diameter is estimated to be ~1 cm with a settling velocity of ~0.5 m/s. Using such parameters, liquid metal droplets are predicted to equilibrate chemically after settling a distance of <200 m. These models indicate that the concentrations of moderately siderophile elements in the mantle are most likely the result of chemical interaction of a silicate magma ocean with small metal droplets but not with a layer of liquid metal that has already segregated at the base of the magma ocean.

## References

- Jones JH, Palme H (2000) Geochemical constraints on the origin of the Earth and Moon. *In: Origin of the Earth and Moon*, Canup, RM, Righter K (eds), Univ. Arizona Press, Tucson, 197-216.
- Karato S, Murthy VR (1997) Core formation and chemical equilibration in the Earth - I. Physical considerations. *Phys. Earth Plan. Int.* 100, 61-79.
- Li J, Agee CB (1996) Geochemistry of mantle-core differentiation at high pressure. *Nature* 381, 686-689.
- Righter K, Drake MJ, Yaxley G (1997) Prediction of siderophile element/silicate partition coefficients to 20 GPa and 2800°C: the effects of pressure, temperature, oxygen fugacity, and silicate and metallic melt compositions. *Phys. Earth Planet Int.* 100, 115-134.
- Stevenson, DJ (1990) Fluid dynamics of core formation. *In: Origin of the Earth*, Newsom HE, Jones JH (eds), Oxford Univ., New York, 231-249.

### 5.13 Effect of Light Elements on Viscosity of Liquid Iron-Alloy

H. Terasaki<sup>1</sup>, T. Kato<sup>1</sup>, S. Urakawa<sup>2</sup>, K. Funakoshi<sup>3</sup>, A. Suzuki<sup>4</sup>,  
K. Sato<sup>5</sup>, M. Hasegawa<sup>2</sup>

<sup>1</sup>Gescience Inst., Univ. of Tsukuba, <sup>2</sup>Dept. of Earth Sc., Okayama Univ., <sup>3</sup>JASRI,  
<sup>4</sup>Inst. of Mineral. Petrol. Economic geol., Tohoku Univ., <sup>5</sup>Foundation for Advancement of Int. Sc.

#### Introduction

The viscosity of liquid iron-alloy is one of the most fundamental physical properties to investigate the convectational behavior of the Earth's outer core. The outer core consists mainly of liquid Fe-Ni alloy with a significant amount of the light elements such as S, O, C, Si, and H [1]. Dissolved light elements must influence the physical properties of liquid iron under pressure. We have reported the viscosity of liquid Fe [2] and Fe-FeS [3] up to 7 GPa. In this study, we measure the viscosity of the liquid in the system of Fe-Fe<sub>3</sub>C using X-ray radiography falling sphere method and investigate the effect of sulfur and carbon on the viscosity of liquid iron-alloy.

#### Experimental Procedure

High pressure and temperature experiments were performed by MA-8 multianvil press (SPEED-1500) installed at BL04B1, SPring-8, Japan. Starting material was a mixture of Fe (4N) and Fe<sub>3</sub>C (3N) powder. Experimental pressure was determined from the Birch-Murnaghan equation of state for h-BN and MgO [4], which were used as the sample capsule and X-ray window, respectively. Temperature was monitored just above the capsule inside the heater by the W3%Re-W25%Re thermocouple. Detailed cell description was shown in ref. 3. Radiography was observed by the high-speed exposure CCD camera (C4880-80-14A) with resolution of about 5  $\mu\text{m}$  and with the exposure time of 11-21 ms. Images were recorded with computer hard disk at the rate of 30 ms. We used Pt and Pt13%Rh spheres with diameter of 100-150  $\mu\text{m}$ , as viscosity markers. A double layered sample assembly was adopted to avoid influence of the partial melting of the sample during the viscosity measurement. The sphere was set in the silicate layer, which overlay the Fe- Fe<sub>3</sub>C layer in a sample capsule [3]. We used either albite (NaAlSi<sub>3</sub>O<sub>8</sub>) powder as a material in the silicate layer. These spheres were imaged as the dark shadows due to its high X-ray absorption coefficient. Settling velocity of the marker sphere was obtained from the continuous radiographic images (Fig.1), and the viscosity coefficients were calculated using Stokes' equation with wall and end correction.

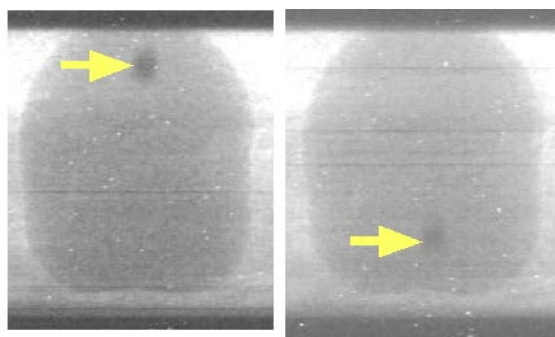


**Fig.1** Continuous radiographic image of falling sphere  
Sphere radius is 64 micron meter, and exposure time is 14 ms.

## Results and Discussion

The viscosity coefficients of the liquid Fe-Fe<sub>3</sub>C are 0.004-0.018 Pa s at 3 GPa, 1605-1923 K. Viscosity coefficient of eutectic Fe-Fe<sub>3</sub>C is smaller than that of liquid Fe and Fe<sub>3</sub>C end member. It seems to take minimum value at the eutectic point (C=4 wt%). This tendency is similar to that of liquid Fe-FeS alloy as shown in Fig.2. In case of the Fe-FeS system, it can be interpreted as the change of near neighbor atomic pair from Fe-Fe pair to Fe-S pair at higher sulfur content [5]. Since it may be explained by the similar structural change of the liquid Fe-Fe<sub>3</sub>C, the structural analysis of liquid Fe-Fe<sub>3</sub>C is required. Pressure effect of viscosity can be estimated from present high pressure viscosity data together with the data measured at ambient pressure. Activation volume (pressure dependence) of liquid iron is larger than that of liquid Fe-FeS and Fe-Fe<sub>3</sub>C.

In the results of radiographic observation, a large deformation of the boundary between the sample iron-alloy and trapper silicate was found during sample melting in the system of Fe and Fe-Fe<sub>3</sub>C. However, such deformation was not observed in the system of Fe-FeS. This phenomenon indicates that surface tension of liquid iron-alloy decreases with increasing sulfur content. On the other hand, addition of carbon shows little influence on the surface tension.

## References

- [1] J.P. Poirier, Phys. Earth Planet. Int. **85**, 319-337 (1994).
- [2] H. Terasaki et al., Submitted
- [3] H. Terasaki et al., Earth Planet. Sci. Lett. **190**, 93 (2001).
- [4] J. C. Jamieson et al., in High-Pressure Research in Geophysics, S. Akimoto, M. H. Manghani, Eds. (Center for Academic Publishing, Tokyo, 1982), pp. 27-48.
- [5] S. Urakawa et al., Rev. High Pressure Sci. Technol. **7**, 286-288 (1998).

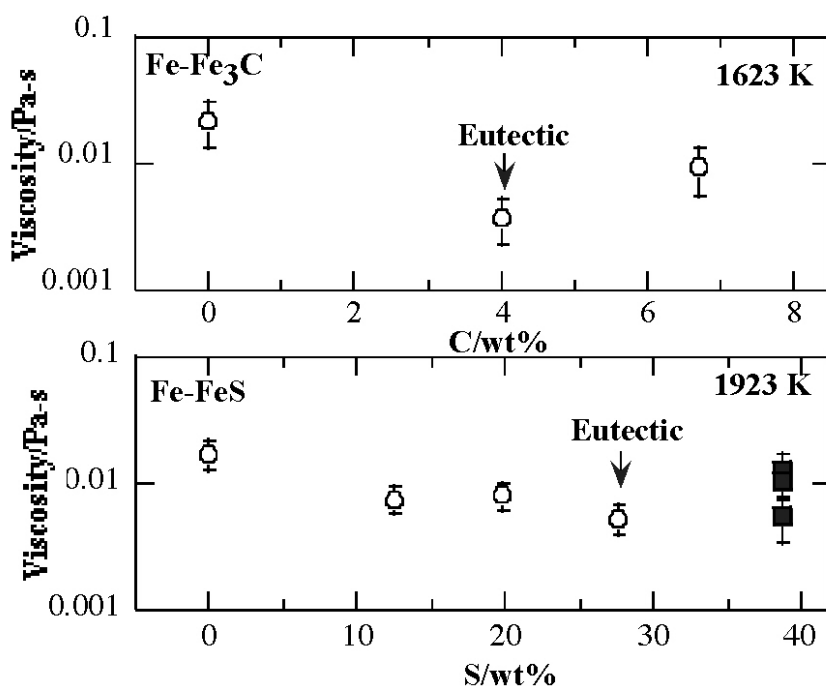


**Fig.2** Compositional variation of viscosity of liquid iron-alloy. Solid squares show viscosity of FeS reported by Dobson et al.(2000). Viscosity coefficients are corrected to the indicated temperatures using arrhenius relation [3].

## 5.14 Critical melt fraction for percolation of core-forming materials

Takashi Yoshino, Michael J. Walter and Tomoo Katsura

Institute for Study of the Earth's Interior, Okayama University

The formation of an iron core and silicate mantle was a major differentiation event in the early history of the Earth. In a homogeneously accreting Earth silicates and metal alloys are initially intimately mixed, so core formation requires a mechanism for separating and mobilizing the iron alloy. For this reason, there has been interest in the wetting properties of liquid iron or alloy melts in silicate mineral matrix. Previous experimental studies concerned with the wetting behavior of alloy melts were based on the determination of dihedral angles under variable conditions. Most of the results show large dihedral angles of over 90 deg for Fe metal in olivine-rich matrix, suggesting a non-wetting property of iron-rich melts. Although it seems reasonable from statistical angle measurements to conclude that iron-rich metallic melts cannot have segregated from an olivine-rich silicate mantle, a certain amount of liquid metal will connect along grain boundary when the dihedral angle is above the critical value of 60 deg. In this case, an excess of melt over the critical melt fraction (CMF) can create permeability and segregate from the silicate matrix leaving residual melts trapped at grain boundaries and as inclusions in silicates. The stranded melts may influence the absolute and relative abundance of siderophile elements in the Earth's mantle. Therefore, it is important to determine the CMF for melt permeability in 3 dimension.

In order to assess the CMF in metal-silicate system and the feasibility of percolation as a core formation process, we performed experiments over a range of metal/alloy mass fraction up to 0.7 in San Carlos olivine + sulfide or San Carlos olivine + iron mixtures. Usage of a starting material composed of San Carlos olivine including variable proportions of synthetic sulfide and metal alloy allows examinations of the CMF with respect to a silicate mineralogy analogous to Earth's upper mantle. Sample materials are packed into graphite capsule. Experiments were performed using a piston cylinder apparatus at 1573-1673K and 1.5GPa. Electrical conductivity of a part of the retrieved sample was measured by digital voltmeter to access metal/sulfide connectivity under room condition. From the above analysis, the lower bound of the CMF was determined.

Run products of olivine-iron mixture are composed of olivine, magnesiowustite (mw) and iron and run products of olivine-sulfide mixture are composed of olivine and sulfide. In both systems, electrical conductivity was lost when percolation drainage had reduced the alloy volume to ~20%, indicating a lack of interconnectivity (Fig. 1). This threshold value corresponds to an interconnection threshold for a nearly 150 deg dihedral angle, based on a prediction for body-centered cubic packing of plane-faced tetrakaidehedra (von Bargen and Waff, 1986). However, the previously reported dihedral angles at the junction of metallosulfide melt with silicate are generally smaller, in the range of 65-115 deg. In addition, the percolation threshold does not change significantly with the sulfur content in the melt, although the dihedral angles are very sensitive to the amount of S in the melt. These inconsistencies may indicate that the system did not establish textural equilibrium during the 3day run duration. Figure 1 shows power law correlation between volume fraction and resistivity. The slope of ~-7 in the olivine+mw+iron system is slightly larger than that in system including sulfide (~-5). Difference in slope may reflect effect of magnesiowustite on bulk resistivity.

The results indicate a critical condition at which the metal segregation process in silicate solid matrix switch from grain boundary percolation to gravitational sinking of molten iron droplets. When metallosulfide fraction is over ~20 vol.%, interconnected molten metal will be able to segregate by porous flow. These considerations may provide new insights into the core formation process in the early history of the Earth and other planetary bodies, and yield important clues for understanding the absolute and relative abundances of siderophile elements in the Earth's mantle.

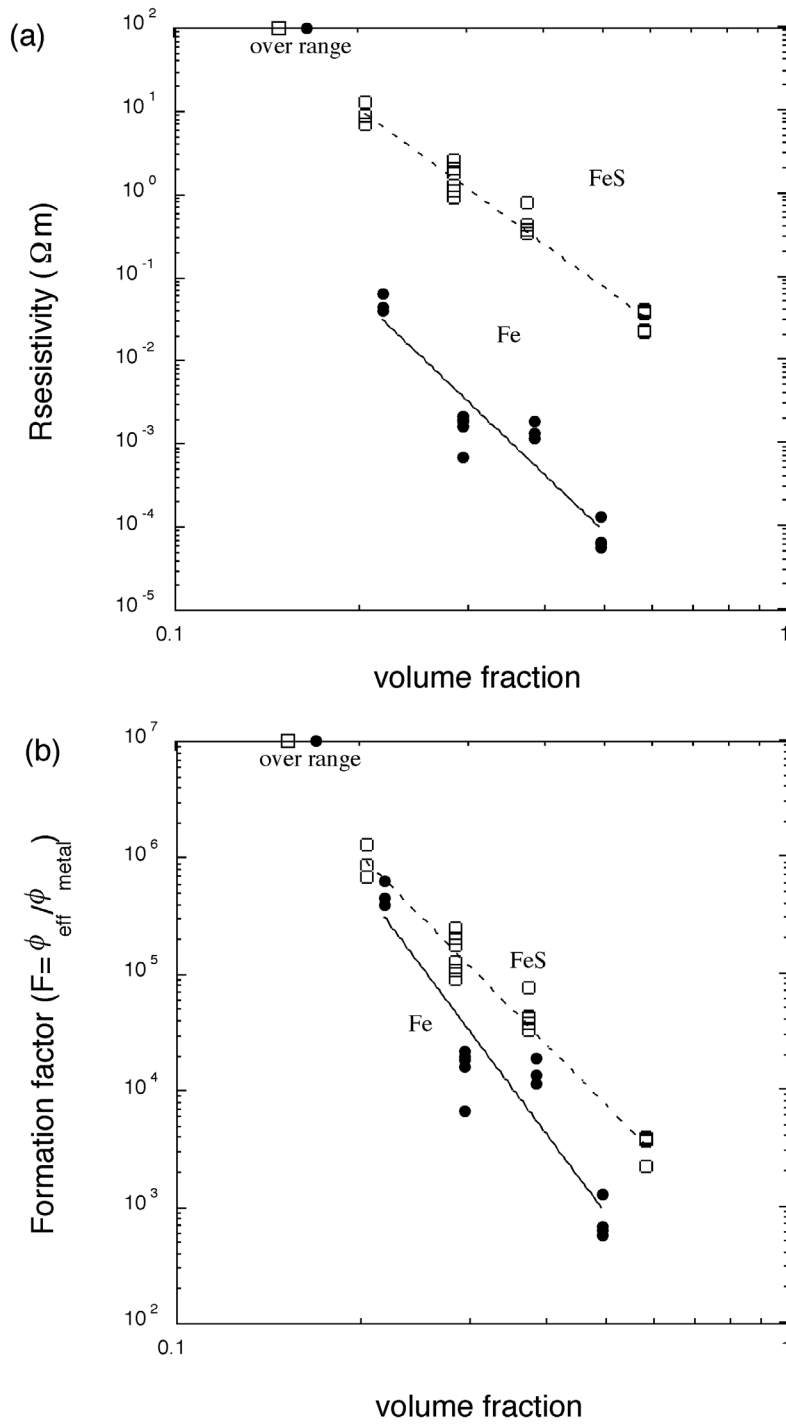


Figure 1. (a) Relation between resistivity and volume fraction of metallosulfide. (b) Relation between resistivity and volume fraction of metallosulfide

## 5.15 Geomagnetic field model for the last 5 my and conditions at core-mantle boundary

Tadahiro Hatakeyama and Masaru Kono

Institute for Study of the Earth's Interior, Okayama University, Japan

We have proposed a geomagnetic field model [1] of stable magnetic periods for the last 5 million years which consists of time-averaged field (TAF) and paleosecular variation (PSV). In this model the TAF and PSV was calculated with considering the nonlinear relationship between model parameters and observations derived from paleomagnetic studies.

The determined TAF models both of normal and reverse geomagnetic polarities show that the geocentric axial quadrupole term,  $g_2^0$ , is significantly larger than other nondipole terms and has same sign as the geocentric axial dipole,  $g_1^0$ . This feature indicates that the geomagnetic equator is shifted northward from the geographic equator and that “the VGP (virtual geomagnetic pole) far-side effect” seen in the paleomagnetic is caused mainly by  $g_2^0$  component in both polarity periods instead of the higher order terms, which is consistent with previous zonal TAF models [2]. When we consider the symmetry with respect to the field ( $\mathbf{B}$ ) in the magnetic induction equations, it is likely that this phenomenon is due to the boundary conditions of the fluid outer core such as heat flows.

On the other hand, the geocentric axial octupole term,  $g_3^0$ , was also thought as a remarkable component in a previous TAF model [3]. However, this term is not excellent in our TAF model because the PSV effect [4] on the mean direction affects mainly this and the effect seems to mislead us into overestimating “apparent”  $g_3^0$  component when it is ignored in the TAF model.

In this study, we will compare the characteristics of the TAF and PSV models derived from paleomagnetic data to the results of the geodynamo simulation with using heterogeneous boundary conditions of heat flux [5] and discuss the role of the condition at the core-mantle boundary region.

### References

- [1] Hatakeyama T. and M. Kono, “A self-consistent time-averaged geomagnetic field and paleosecular variation model for the last 5 My”, *Abst. IAGA-IASPEI joint scientific assembly*, 73, 2001
- [2] Wilson, R. L., “Permanent aspects of the Earth's non-dipole magnetic field over upper tertiary times”, *Geophys. J. R. astr. Soc.*, **19**, 417–437, 1970.
- [3] McElhinny, M. W., P. W. McFadden and R. T. Merrill, “The time-averaged paleomagnetic field 0–5 Ma”, *J. Geophys. Res.*, **101**, 25007–25027, 1996
- [4] Hatakeyama T. and M. Kono, “Shift of the mean magnetic field values: Effect of scatter due to secular variation”, *Earth Planets Space*, **53**, 31–44, 2001
- [5] Glatzmaier, G. A., R. S. Coe, L. Hongre and P. H. Roberts, “The role fo the Earth's mantle in controlling the frequency of geomagnetic reversals”, *Nature*, **401**, 885–890, 1999

**October 5 (Friday) 13:30 – 16:30**

**Session 6**

**Future Perspectives**

Keynote: Dave Mao, Geophysical Laboratory, Carnegie Institution

Chair: Dave Rubie, Bayerisches Geoinstitut, University of Bayreuth



### 6.3 Mantle convection as a tool for understanding the links among the various geological phenomena

S. Honda<sup>1</sup> and M. Yoshida<sup>2</sup>

<sup>1</sup>Hiroshima University <satoru@yesterday.geol.sci.hiroshima-u.ac.jp>

<sup>2</sup>Tokyo University

A successful model of mantle convection must explain observed geological phenomena and, thus, it will clarify their causal links based on physical and chemical principles. Current active research field of mantle convection may be categorized as two major topics, that is, (1) a construction of self-consistent model of mantle convection which shows a plate-like behavior (e.g., Tackley [2000]) and (2) an understanding of the dynamics of deep interior of the Earth (e.g. Forte and Mitrovica [2001]). Both topics have serious difficulties to be overcome. Main difficulties of (1) are an insufficient knowledge and a troublesome numerical treatment of low temperature rheology and those of (2) are the insufficient observational constraints on the deep mantle process. In this presentation, we show our current research efforts related to these topics.

Major features of the plate tectonic movement may be the existence of (1) the rigid plate interior, (2) the transform faults and (3) the asymmetrical subduction. Consider 2D case, that is, ignore (2), the rigid plate movement can be modeled relatively easily. The key point is the weakening mechanism of plate boundaries, which may be caused by a yielding, at least, as a first-order approximation. However, the modeling of the third point turns out to be fairly difficult. This may be caused by the coarse mesh, which cannot resolve the evolution of thin weak zone, and/or the absence of possible asymmetric difference in physical properties around the subduction zones. To achieve the one-sided subduction, we assume the lateral variation of the yield stress (Honda et al. [2000]), in which the yield stress of overlying lithosphere is higher than that of the subducting lithosphere. Generally, we observe an inclined subduction of the cold lithosphere, although the long-existing “favorable” one-sided subduction appears to be difficult. Further modeling efforts like the usage of the finer mesh may be required. We also observe that the lateral variation of yield stress controls the place of future subduction.

A modeling the deep mantle process may be constrained by the present geophysical data, such as the plate movement, gravity and seismic tomography, and the mixing rate inferred from the geochemical data. Recently, we have started the 3D modeling of present mantle convection hoping that we can constrain the whole mantle process (Yoshida et al. [2001]). Plate movements are strongly controlled by the lateral variation of viscosity in the lithosphere. Using the radially stratified viscosity except the lithosphere and the mantle density anomalies inferred from the subduction history, we found that the weak plate margin changes both the plate velocity and geoid substantially as Zhong and Davies [1999] also pointed out. This suggests a trade-off between the rheology of the lithosphere and the viscosity stratification in the lower mantle in explaining the geophysical data. Since the viscosity distribution in the lower mantle is a key to understand the nature of the whole mantle flow (Forte et al. [2001]), the rheology of the lithosphere is also important to clarify the view of mantle-wide process.

#### References

- Forte, A. M., and J. X. Mitrovica, Deep-mantle high-viscosity flow and thermochemical structure inferred from seismic and geodynamic data, *Nature*, **410**, 1049-1056, 2001.
- Honda, S., T. Nakakuki, Y. Tatsumi and T. Eguchi, A simple model of mantle convection including a past history of yielding, *Geophys. Res. Lett.*, **27**, 1559-1562, 2000.
- Tackley, P. J., Self-consistent generation of tectonic plates in time-dependent, three-dimensional mantle convection simulations 1. Pseudoplastic yielding, *Geochemistry Geophysics Geosystem*, **1**, 2000.

- Yoshida, M., S. Honda, M. Kido and Y. Iwase, Numerical simulation for the prediction of the plate motions: Effects of lateral viscosity variations in the lithosphere, *Earth Planets Space*, **53**, 709-721, 2001.
- Zhong, S., and G. F. Davies, Effects of plate and slab viscosities on the geoid, *Earth Planet. Sci. Lett.*, **170**, 487-496, 1999.

### 6.4 High-pressure crystallography in mineral physics

Takamitsu Yamanaka\*, A. Yoshiasa, O. Otaka and N. Nagai

Department of Earth and Space Science Graduate School of Science Osaka University 1-1 Machikaneyama  
Toyonaka, Osaka 560-0043 Japan

#### 1 . Purpose of the high-pressure crystallography

Numerous studies of bulk modulus and equation state (EOS) have been repeatedly carried out for geophysical interests. A dynamical process is one of the significant projects in high-pressure crystallography. Many aspects of structure changes under compression, such as phase transformation, lattice deformation, cation ordering, decomposition, amorphization and solid reactions. Phase transitions under compression due to lattice instability, electronic state change and magnetic spin ordering can be elucidated by X-ray diffractometry, absorption and resonance using diamond anvil cell together with other X-ray optical measurements. Developments of many types of detectors and synchrotron radiation accelerate kinetic studies and dynamical studies of those changes. Hydrostaticity gives an effect on the phase transformation, under shear stress, which does not necessarily gives a thermodynamically stable phase. Nonhydrostaticity of compression brings metastable states or intermediate states, because they are formed in the dynamical process. Besides the stress-strain relation, the crystallite size is an effective parameter of phase transition under compression. Metastable or unstable phases have been formed by the Oswald rule.

Many phase transformations and the phase stabilities have been undertaken under static high-pressure conditions during the last twenty years, Our previous studies related the phase transformation are shown in Table 1.

Table 1. Phase transformation under compression

lattice change	electronic state change	spin-lattice interaction
no coordination change	charge disproportion	Jahn-Teller transition
lattice type change	$Fe^{3+} + Fe^{5+} \leftrightarrow 2Fe^{4+}$	
molecular dissociation	$Au^{1+} + Au^{3+} \leftrightarrow 2Au^{2+}$	
cation order $\leftrightarrow$ disorder	band overlap	high-low spin transition
polyhedral joint	density of state	Mott transition
coordination change	$s \leftrightarrow, f \leftrightarrow$ orbital change	spin-Perierls transition
Martensitic transition	orbital rearrange	

#### 2. Development using synchrotron radiation for structure study

Since synchrotron radiation at Photon Factory (PF) at Tsukuba and SPring-8 in Japan has been utilized, structure study as well as phase study becomes more fashion under high pressure by the extensive studies using DAC or mutianvil apparatus. For example in SPring-8, seven beam lines are available or designed for high-pressure studies by means of XAFS, 7 axes diffractometer for structure analysis, laser heating, low temperature, IR and Mösbauer systems. High-pressure studies often encountered several difficulties for *in situ* observation. Significant progress in *in situ* diffraction studies of earth's interior under compression and high temperature has been made using synchrotron radiation facilities.

#### 3. Time-resolved observation for kinetic study

The transition rate can be determined by profile fitting method. In order to establish the kinetic study of the pressure-induced transformation present devises performed an *in situ* and time dependent measurement of diffraction intensity with high accuracy. Time-resolved and *in situ* diffraction studies using synchrotron radiation give a brilliant light to the dynamical observation of pressure-induced structure changes. Then this system offers more reliable phase identification, lattice constants

and diffraction intensity. Consequently structure information under pressure becomes noticeably improved.

Time resolved diffraction study of the phase transition becomes possible by combination of a strong source with quick photon counting system, because the time dependent structure analysis requires the repeating diffraction measurement with a short time interval.

#### 4. Variety of structure transition with nonhydrostaticity

Phase transformation under compression is not necessary to produce a thermodynamically stable phase. From the viewpoint of statistical process, macroscopic time and space average, of structure transition under pressure, virial theorem proposes the vision of the structure stability under the equilibrium condition between summation of interatomic potential and surrounding pressure  $P_{ext}$  around the crystal.

$$P_{ext} = \frac{Nk_B T}{V} - \frac{1}{3V} \langle \sum \sum (-\frac{\partial \Psi_{ij}}{\partial r_{ij}}) \rangle$$

V:volume N:number of particles  $\Psi_{ij}$ :interatomic potential  $r_{ij}$ :distance between i and j particle

Ostwald step rule indicates that transformation path is not only one. Metastable phase having a small energy barrier, i.e. activation energy lower than that of stable phase is possibly to turn up during the transformation process. Especially anisotropic stress easily accelerates several steps of metastable phases. The shear stress  $P_{ij}$  induced from the nonhydrostatic compression brings a lattice deformation and gliding of slabs such as martensic transition in the random fashion. The phase transition is probable by the non-diffusion transformation mechanism under stress field.

MD calculation reproduces the pressure-induced transformations under any shear stress condition and has an anisotropic property in the structure. Born criterion gives the phase stability from the mutual relation in elastic constants  $C_{ij}$ . MD calculation suggests a mechanism of the pressure-induced modification, which is a precursor atomic movement on the transition process.

#### 5. Charge density distribution analysis.

Crystal structure analyses under nonambient conditions have been significant subjects not only for geosciences but also for material science. Crystal structure and physical properties under extreme conditions have been elucidated by single-crystal diffraction studies. Combined with heating system and DAC, high-temperature and high-pressure measurements have attracted an interest of X-ray crystallography. Synchrotron radiation facilities have accelerated the high-pressure structure study, because of their great advantages for x-ray diffraction studies at nonambient conditions.

Single-crystal structure refinements under high-pressure encountered many difficulties such as nonhydrostaticity, large blind region due to pressure cell, large X-ray absorption and limitation of compression. Our new system solved these difficulties and made it possible to discuss the electron density distribution under pressures up to 50GPa.

Valence electron density distribution as a function of pressure gives a brilliant implication to understand the structure stability and phase transformation mechanism. Localization of valence electron inducing ionic character rather than covalent and less population of bonding electron with elevating pressure up to 30GPa were found by charge density analysis of stishovite. Electron density of state obtained from molecular orbital calculation accords with the above results. Besides the above electron density distribution under pressure, effective charge and dipole moment give insight into the crystal chemistry and bonding character under compression.

### 6.5 Dynamo process in the core under varying energy flow conditions

Masaru Kono

Institute for Study of the Earth's Interior, Okayama University, Misasa, Tottori-ken 682-0193, Japan. email: mkono@misasa.okayama-u.ac.jp

In the outer core of the Earth, thermal or compositional convection takes place. As the electrical conductivity of the fluid core is high enough, the convection induces electric current and thus dynamo action takes place. In the last five years or so, simulation of realistic dynamos became possible. These dynamo models are three-dimensional and fully nonlinear, and do not make any arbitrary assumptions. The parameter range of the models, especially the Ekman number and the Rayleigh number, is not quite that of the Earth (Figure 1). A direct comparison of geomagnetic and paleomagnetic observations with simulation results is therefore not quite satisfactory. In spite of these constraints, comparisons have been made between observations and model calculations, and in many cases very interesting results were obtained. Thus it seems that the results from model studies provide us useful information for considering the real state of the Earth's core.

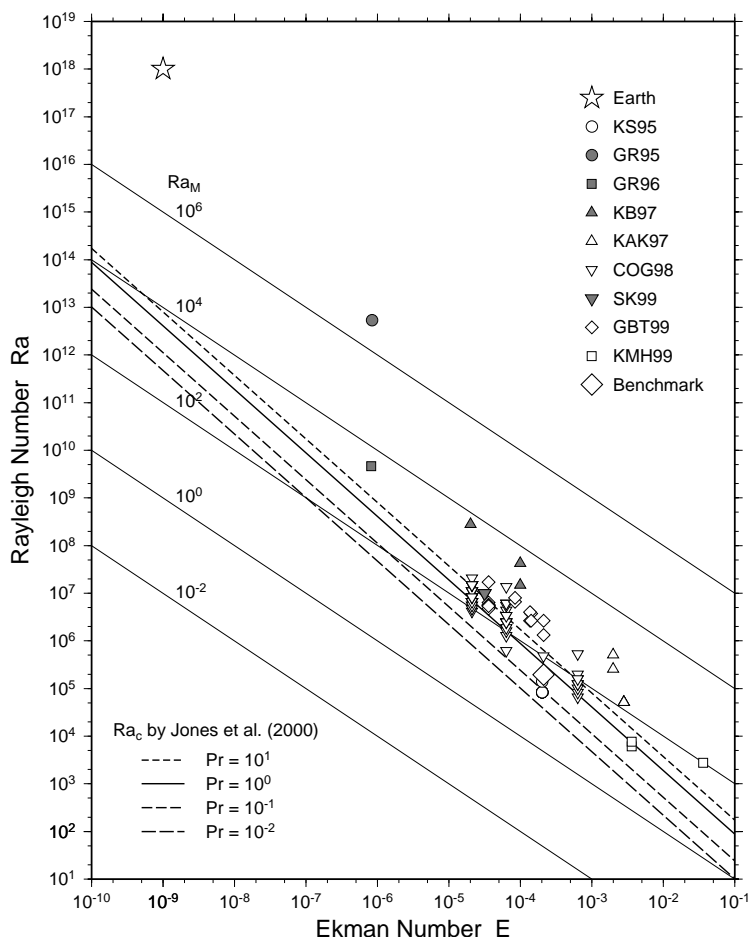


Figure 1. Relation between the Ekman number  $E$  and Rayleigh number  $Ra$  in various MHD dynamo models. Thick lines indicate the theoretical critical Rayleigh numbers, and thin lines show the modified Rayleigh number  $Ra_M = E \cdot Ra$ . The value for the Earth is based on an eddy viscosity of  $1 \text{ m}^2 \text{ s}^{-1}$ .

Through the model studies, it became clear that the Ekman number (which signifies the Coriolis force in comparison with the viscous force) plays the most important role (Figure 2). Also important is the mode of energy transfer. The flow of energy is controlled by the thermal structure of the mantle just above the core-mantle boundary (CMB). Because the thermal diffusion time is very long in the core, while any temperature difference at the CMB will be equilibrated on the core side in very short time, the temperature heterogeneity in the deep mantle will determine the heat flow from the Earth's core. As the lower mantle near the CMB is very heterogeneous (such as  $D''$ ), the heat flow from the core must also be quite inhomogeneous. I will discuss about the possibility of looking for changing energy flow conditions based on these findings.

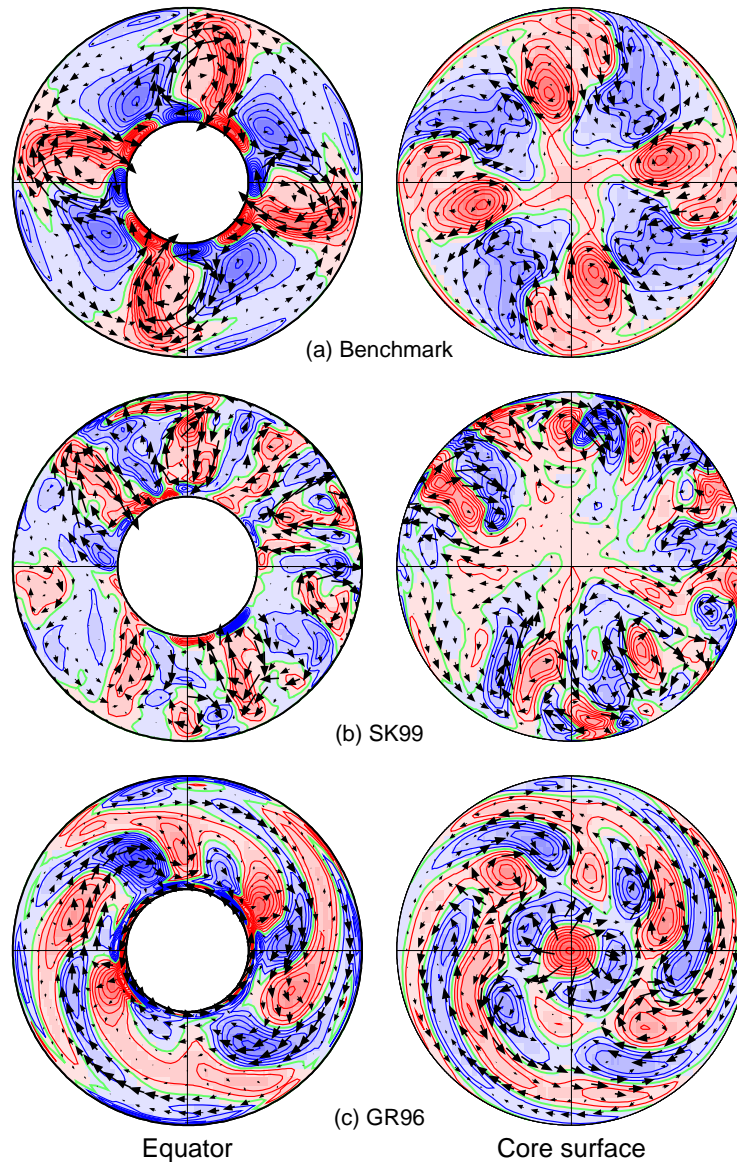


Figure 2. Snapshots of the flow in the equatorial plane (left) and in the Ekman layer below the CMB (right,  $r/r_c = 0.98R_0$ ) in three typical dynamo models. Benchmark is a slow rotator, SK99 (Sakuraba and Kono, 1999) is an intermediate rotator, and GR96 (Glatzmaier and Roberts, 1966) is a fast rotator. Color shade and contours give the flux perpendicular to the plane under consideration ( $V_z$  on the left and  $V_r$  on the right). Arrows show the velocity component in the plane ( $V_s$  and  $V_\phi$  on the left and  $V_\theta$  and  $V_\phi$  on the right).

## 6.6 Comprehensive geochemical analyses of extremely small amounts of terrestrial and extraterrestrial materials for sample-return missions

Eizo Nakamura, Akio Makishima, Takuya Moriguti, Katsura Kobayashi, Chie Sakaguchi, Tetsuya Yokoyama, Ryoji Tanaka, Takeshi Kuritani & Hiroyuki Takei

The Pheasant Memorial Laboratory for Geochemistry and Cosmochemistry (PML), Institute for Study of the Earth's Interior, Okayama University at Misasa, Tottori 682-0193, Japan

We participated in the analytical competition related to the sample-return mission, MUSES-C of the ISAS to be launched in November 2002 and concluded in June 2006. In this competition, we determined as many major and trace element abundances and isotopes as possible, for both two powdered samples provided by ISAS and chondrules separated from Allende meteorite as an additional demonstration to show the analytical capabilities for small fragments.

100 mg of each the samples were split into two fractions of approximately 30 and 70 mg for the determinations of elemental abundances and the isotope analyses, respectively. The bulk concentrations of 55 elements in each 30 mg sample were analyzed using both quadruple-type ICP-MS and sector-type ICP-MS with analytical uncertainties better than 10 % (1?). Boron, Pb, Li, Rb, Sr, Sm and Nd were successively separated from each 70 mg of sample using some nearly developed integrated multi-ion exchange column chemistry, and then these isotopes were determined by TIMS with analytical errors similar to those obtained in our laboratory for terrestrial samples. Strontium, Nd, Re and Os isotopic compositions were also analyzed on remaining aliquots of the sample solutions used for trace element analyses by ICP-MS. The results obtained in this study indicate that samples 1C and 2C are probably ordinary chondrite and the Allende meteorite, respectively. Extreme W, Ta and Nb enrichments in sample 1C were probably caused by contamination during sample preparation.

Chondrules were separated from Allende meteorite and then sliced into three pieces using a dicing saw. The center parts of the slices were used to determine mineral phases by compositional mapping, and to obtain major and trace element compositions (30 elements) by a combination of optical microscopy, SEM-EDX and ion microprobe. The outer slices, for which sample sizes were < 1 mg, were chemically treated to obtain the bulk trace element and isotope compositions of chondrules. For these slices, 24 trace elements and Sr and Nd isotopic compositions were determined with extremely small analytical uncertainties using ICP-MS and TIMS, respectively.

The analytical competition, using extremely small amounts of test samples has allowed a demonstration of the analytical capabilities of our geochemical laboratory, the PML, that could be applied to the samples to be returned from an asteroid by the MUSES-C mission. Most of the mineralogical and chemical data can be obtained for extremely small amounts of samples and with high spatial resolution. Japanese analytical capabilities will be further improved by repeating this type of competition and evaluation, and by incorporating other analytical techniques such as light element isotope analyses and age dating using ion and laser microprobes. Such improvements, aiming to analyze samples with extremely small sample sizes should also make it possible to obtain comprehensive mineralogical and geochemical analyses with high spatial resolution for precious samples returned from Mars.

## 6.7 Zircon age dating by dynamic multi-collection method using high resolution secondary ion mass spectrometer

Katsura Kobayashi, Tomohiro Usui and Eizo Nakamura

Pheasant Memorial Laboratory, Institute for Study of the Earth's Interior, Okayama University at Misasa

We report here development of zircon age dating method using a High Resolution Secondary Ion Mass Spectrometer (HR-SIMS), Cameca ims-1270 with multi-collection system. The zircon dating by an ion microprobe has been mainly developed by SHRIMP group at Australian National University (e.g., Compston *et al.*, 1983). Our method is totally different from their method in two features, i) simultaneous determination of Pb isotope composition by multi-collection system, ii) using of the highly focused primary ion beam. The multi-collection method makes possible to cancel instrumental fluctuations, mainly caused by the instability of the primary beam, and reduce the analytical duration. Our HR-SIMS equips 5 electron multipliers for detection of the secondary ion beam, and it is available to collect  $^{204}\text{Pb}^+$ ,  $^{206}\text{Pb}^+$ ,  $^{207}\text{Pb}^+$  and  $^{208}\text{Pb}^+$  intensities, simultaneously. The configuration of detectors and the analytical condition are shown in Fig. 1. Using this condition, we obtained  $^{207}\text{Pb}/^{206}\text{Pb} = 0.07557 \pm 11$ , corresponding to  $1073 \pm 17$  Ma ( $2\sigma$ ,  $n=10$ ), from Geostandard 91500 Zircon, which has  $^{207}\text{Pb}/^{206}\text{Pb} = 0.07488 \pm 1$  and 1065 Ma by TIMS conventional analyses (Wiedenbeck *et al.*, 1995). We also tried to apply the focused beam with  $(30 \mu\text{m})^2$  pre-spattering substitute for Kohler mode illumination beam, which typically provides over  $\sim 30 \mu\text{m}$  spot diameter (by Cameca ims-1270 at Swedish Museum of National History, Whitehouse *et al.*, 1997). Squared pre-spattering method effectively reduced contamination from surface Pb blank. The identical  $^{207}\text{Pb}/^{206}\text{Pb}$  ratios to those of the Kohler mode were obtained within the analytical errors from natural zircon in Sri Lanka with  $10 \sim 1$  nA range of the primary beam current, corresponding to  $13 \sim 3 \mu\text{m}$  in diameter (Fig. 2). This result indicates that our method is applicable for zircon dating of tiny sample (under  $10 \mu\text{m}$  diameter), which occurs commonly in natural samples, and for more precise analyses of zoned structure formed by episodes of growth and/or recrystallization. In order to support the analysis under high spatial resolution, we have also developed VISUAL STAGE system. This system provides identical spatial coordinates on every image by an optical microscope, SEM, and SIMS. Using this system, we carried on detailed descriptions by these apparatus before the zircon dating by the ion probe.

### References

- Wiedenbeck, M. et al. (1995). Three natural zircon standards for U-Th-Pb, Lu-Hf, trace element and REE analysis, *Geostand. Newslett.*, **19**, 1-23.
- Whitehouse, M. J. et al. (1997). Ion microprobe U-Pb zircon geochronology and correlation of Archaean gneisses from the Lewisian Complex of Gruinard Bay, northwestern Scotland, *Geochim. Cosmochim. Acta*, **61**, 4429-4438.

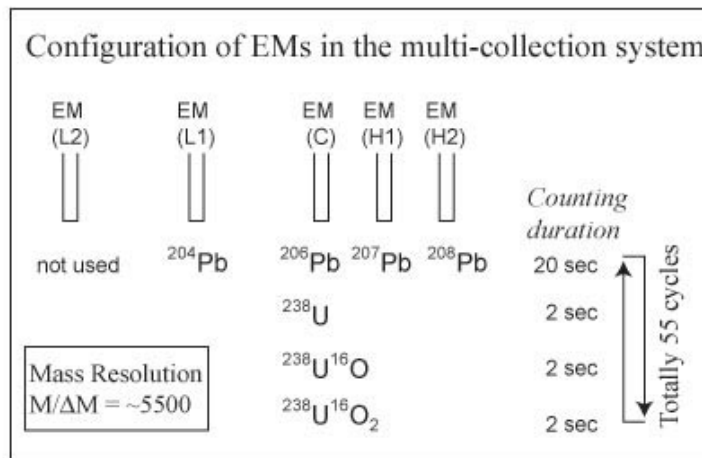
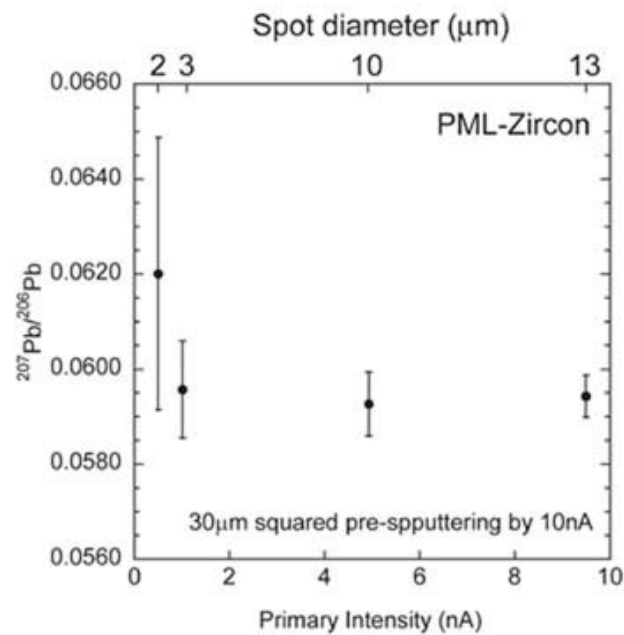


Fig. 1. Configuration of EMs in the multi-collection system and the analytical sequence.



## List of Participants

- Aizawa, Yoshitaka** aizawa@misasa.okayama-u.ac.jp  
Institute for Study of the Earth's Interior, Okayama University  
827 Yamada, Misasa, Tottori 682-0193, Japan
- Akaogi, Masaki** masaki.akaogi@gakushuin.ac.jp  
Department of Chemistry, Gakushuin University  
Mejiro, Tokyo 171-8588, Japan
- Alves, Sophie** salves@pheasant.misasa.okayama-u.ac.jp  
Institute for Study of the Earth's Interior, Okayama University  
827 Yamada, Misasa, Tottori 682-0193, Japan
- Asahara, Yuki** asahara@ganko.tohoku.ac.jp  
Institute of Mineralogy, Petrology and Economic Geology, Tohoku University  
Aoba-ku, Sendai 980-8578, Japan
- Campbell, Ian** Ian.Campbell@anu.edu.au  
Research School of Earth Sciences, Australian National University  
Mills Road, Canberra ACT 200, Australia
- Castillo, Paterno** pcastillo@ucsd.edu  
Scripps Institution of Oceanography, University of California, San Diego  
9500 Gilman Drive, La Jolla, CA 92093-0212, USA
- Chiba, Hitoshi** hchiba@misasa.okayama-u.ac.jp  
Institute for Study of the Earth's Interior, Okayama University  
827 Yamada, Misasa, Tottori 682-0193, Japan
- Faul, Ulrich** uli.faul@anu.edu.au  
Research School of Earth Sciences, Australian National University  
Canberra ACT 200, Australia
- Fei, Yingwei** fei@gl.ciw.edu  
Geophysical Laboratory, Carnegie Institution of Washington  
5251 Broad Branch Rd., NW, Washington DC 20015, USA
- Fujino, Kiyoshi** fujino@ep.sci.hokudai.ac.jp  
Division of Earth and Planetary Sciences, Hokkaido University  
Kita 10 Nishi 8, Kita-ku, Sapporo 060-0810, Japan
- Fukao, Yoshio** fukao@eri.u-tokyo.ac.jp  
Earthquake Research Institute, University of Tokyo  
Yayoi, Bunkyo, Tokyo, 113-0032, Japan
- Green, Harry, II** harry.green@ucr.edu  
Institute of Geophysics and Planetary Physics, University of California, Riverside  
University Ave., Riverside, CA 92521, USA
- Hanyu, Takeshi** hanyu@eri.u-tokyo.ac.jp  
Earthquake Research Institute, University of Tokyo  
Yayoi 1-1-1, Bunkyo-ku, Tokyo 113-0032, Japan
- Hart, Stanley** shart@whoi.edu  
Department of Geology, Woods Hole Oceanographic Institution  
Woods Hole, MA 02543, USA
- Hatakeyama, Tadahiro** hatake@misasa.okayama-u.ac.jp  
Institute for Study of the Earth's Interior, Okayama University  
827 Yamada, Misasa, Tottori 682-0193, Japan
- Hemley, Russell J.** hemley@gl.ciw.edu  
Geophysical Laboratory, Carnegie Institution of Washington  
5251 Broad Branch Rd., NW, Washington DC 20015, USA
- Higo, Yuji** higo@sci.ehime-u.ac.jp  
Department of Earth Sciences, Ehime University  
Bunkyo-cho 2-5, Matsuyama 790-8577, Japan

- Hirao, Naohisa** hirao@ganko.tohoku.ac.jp  
Faculty of Science, Tohoku University  
Aoba, Aramaki, Aoba-ku, Sendai 980-8578, Japan
- Hirato, Takafumi** hrt1@geo.titech.ac.jp  
Department of Earth and Planetary Sciences, Tokyo Institute of Technology  
O-okayama 2-12-1, Meguro, Tokyo 152-8551, Japan
- Honda, Satoru** satoru@yesterday.geol.sci.hiroshima-u.ac.jp  
Department of Earth and Planetary Systems Science, Hiroshima University  
1-3-1 Kagami-yama, Higashi Hiroshima 739-8526, Japan
- Iguchi, Tomohiro** tiguchi@geo.titech.ac.jp  
Department of Earth and Planetary Sciences, Tokyo Institute of Technology  
2-12-1 Ookayama, Meguro-ku, Tokyo 152-8551, Japan
- Inoue, Toru** inoue@sci.ehime-u.ac.jp  
Geodynamics Research Center, Ehime University  
2-5 Bunkyo-cho, Matsuyama, Ehime 790-8577, Japan
- Irifune, Tetsuo** irifune@dpc.ehime-u.ac.jp  
Geodynamics Research Center, Ehime University  
2-5 Bunkyo-cho, Matsuyama, Ehime 790-8577, Japan
- Ito, Eiji** eiito@misasa.okayama-u.ac.jp  
Institute for Study of the Earth's Interior, Okayama University  
827 Yamada, Misasa, Tottori 682-0193, Japan
- Iwamori, Hikaru** hikaru@eps.s.u-tokyo.ac.jp  
Department of Earth and Planetary Sciences, University of Tokyo  
Hongo, Tokyo 113-0033, Japan
- Kagi, Hiroyuki** kagi@eqchem.s.u-tokyo.ac.jp  
Laboratory for Earthquake Chemistry, Graduate School of Science, University of Tokyo  
Hongo 7-3-1, Bunkyo-ku, Tokyo 113-0033, Japan
- Kanzaki, Masami** mkanzaki@misasa.okayama-u.ac.jp  
Institute for Study of the Earth's Interior, Okayama University  
827 Yamada, Misasa, Tottori 682-0193, Japan
- Kato, Mamoru** mkato@gaia.h.kyoto-u.ac.jp  
IHS/Earth Science, Kyoto University  
Yoshida-Nihonmatsu, Sakyo, Kyoto 606-8501, Japan
- Katsura, Tomoo** tkatsura@misasa.okayama-u.ac.jp  
Institute for Study of the Earth's Interior, Okayama University  
827 Yamada, Misasa, Tottori 682-0193, Japan
- Kawakatsu, Hitoshi** hitosi@eri.u-tokyo.ac.jp  
Earthquake Research Institute, University of Tokyo  
1-1-1 Yayoi, Bunkyo-ku, Tokyo 113-0032, Japan
- Kawamoto, Tatsuhiko** kawamoto@bep.vgs.kyoto-u.ac.jp  
Institute for Geothermal Sciences, Kyoto University  
Noguchibaru, Beppu 874-0903, Japan
- Kobayashi, Katsura** katsura@pheasant.misasa.okayama-u.ac.jp  
Institute for Study of the Earth's Interior, Okayama University  
827 Yamada, Misasa, Tottori 682-0193, Japan
- Koga, Kenneth T.** ktkoga@misasa.okayama-u.ac.jp  
Institute for Study of the Earth's Interior, Okayama University  
827 Yamada, Misasa, Tottori 682-0193, Japan
- Kondo, Tadashi** tdkondo@mail.cc.tohoku.ac.jp  
Faculty of Science, Tohoku University  
Aoba, Aramaki, Aoba-ku, Sendai 980-8578, Japan
- Kono, Masaru** mkono@misasa.okayama-u.ac.jp  
Institute for Study of the Earth's Interior, Okayama University  
827 Yamada, Misasa, Tottori 682-0193, Japan

- Kubo, Atsushi** akubo@misasa.okayama-u.ac.jp  
Institute for Study of the Earth's Interior, Okayama University  
827 Yamada, Misasa, Tottori 682-0193, Japan
- Kuritani, Takeshi** kuritani@misasa.okayama-u.ac.jp  
Institute for Study of the Earth's Interior, Okayama University  
827 Yamada, Misasa, Tottori 682-0193, Japan
- Kusakabe, Minoru** kusakabe@misasa.okayama-u.ac.jp  
Institute for Study of the Earth's Interior, Okayama University  
827 Yamada, Misasa, Tottori 682-0193, Japan
- Li, Jie** jieli@gl.ciw.edu  
Geophysical Laboratory, Carnegie Institution of Washington  
5251 Broad Branch Rd., NW, Washington DC 20015, USA
- Mao, Ho-kwang (Dave)** mao@gl.ciw.edu  
Geophysical Laboratory, Carnegie Institution of Washington  
5251 Broad Branch Rd., NW, Washington DC 20015, USA
- Masters, Guy** gmasters@ucsd.edu  
IGPP, Scripps Institution of Oceanography, University of California, San Diego  
9500 Gilman Drive, La Jolla, CA 92093-0225, USA
- Matsui, Masanori** m.matsui@sci.himeji-tech.ac.jp  
Faculty of Science, Himeji Institute of Technology  
Kouto, Kamigoricho, Akogun, Hyogo 678-1297, Japan
- Matsumoto, Naoko** matsu@pheasant.misasa.okayama-u.ac.jp  
Institute for Study of the Earth's Interior, Okayama University  
827 Yamada, Misasa, Tottori 682-0193, Japan
- Mayama, Norihito** mayama1@mail7.dddd.ne.jp  
Department of Earth Science, Okayama University  
Tsushimannishizaka2-14-30, Okayama 700-0086, Japan
- Mibe, Kenji** mibe@magma.eri.u-tokyo.ac.jp  
Geophysical Laboratory, Carnegie Institution of Washington  
5251 Broad Branch Rd., NW, Washington DC 20015, USA
- Miyajima, Nobuyoshi** Nobuyoshi.Miyajima@uni-bayreuth.de  
Bayerisches Geoinstitut Universität Bayreuth  
Universitätstr.30, Bayreuth D-95440, Germany
- Moreira, Manuel** moreira@ipgp.jussieu.fr  
Géochimie-Cosmochimie, Institut de Physique du Globe de Paris  
4 place Jussieu, Paris 75005, France
- Moriguti, Takuya** moriguti@misasa.okayama-u.ac.jp  
PML, Institute for Study of the Earth's Interior, Okayama University  
827 Yamada, Misasa, Tottori 682-0193, Japan
- Morishita, Tomoaki** moripta@kenroku.kanazawa-u.ac.jp  
Earth Sciences, Kanazawa University  
Kakuma, Kanazawa, Ishikawa 920-1192, Japan
- Moriyama, Takeru** takeru@pheasant.misasa.okayama-u.ac.jp  
Institute for Study of the Earth's Interior, Okayama University  
827 Yamada, Misasa, Tottori 682-0193, Japan
- Mysen, Bjorn** mysen@gl.ciw.edu  
Geophysical Laboratory, Carnegie Institution of Washington  
5251 Broad Branch Rd., NW, Washington DC 20015, USA
- Nagai, Takaya** nagai@ess.sci.osaka-u.ac.jp  
Department of Earth and Space Science, Osaka University  
1-1 Machikaneyama, Toyonaka, Osaka 560-0043, Japan
- Nakamura, Eizo** eizonak@misasa.okayama-u.ac.jp  
PML, Institute for Study of the Earth's Interior, Okayama University  
827 Yamada, Misasa, Tottori 682-0193, Japan

- Nakayama, Keisuke** knakayam@geo.titech.ac.jp  
Earth and Planetary Sciences, Tokyo Institute of Technology  
Ookayama 2-12-1, Meguroku, Tokyo 152-8551, Japan
- Nishihara, Yu** yuu@geo.titech.ac.jp  
Magma Factory, Earth and Planetary Sciences, Tokyo Institute of Technology  
2-12-1 Ookayama, Meguro-ku, Tokyo 152-8551, Japan
- Nishikawa, Osamu** nisikawa@misasa.okayama-u.ac.jp  
Institute for Study of the Earth's Interior, Okayama University  
827 Yamada, Misasa, Tottori 682-0193, Japan
- Obata, Masaaki** obata@kueps.kyoto-u.ac.jp  
Department of Geology and Mineralogy, Kyoto University  
Kita-shirakawa, Kyoto 606-8502, Japan
- Ohtaka, Osamu** ohtaka@ess.sci.osaka-u.ac.jp  
Earth and Space Science, Osaka University  
Machikaneyama 1-1, Toyonaka, Osaka 560-0043, Japan
- Ohtani, Eiji** ohtani@mail.cc.tohoku.ac.jp  
Institute of Mineralogy, Petrology, and Economic Geology, Tohoku University  
Aza-Aoba, Aramaki, Aoba-ku, Sendai 980-8578, Japan
- Ono, Shigeaki** sono@jamstec.go.jp  
Institute for Frontier Research on Earth Evolution, Japan Marine Science and Technology  
Center  
2-15 Natsushima-cho, Yokosuka, Kanagawa-ken 237-0061, Japan
- Osako, Masahiro** sako@kahaku.go.jp  
Division of astronomy and geophysics, National Science Museum  
3-23-1 Hyakunin-cho, Shinjuku-ku, Tokyo 169-0073, Japan
- Presnall, Dean** presnall@gl.ciw.edu  
Geophysical Laboratory, Carnegie Institution of Washington  
5251 Broad Branch Rd., NW, Washington DC 20015, USA
- Prewitt, Charles T.** prewitt@gl.ciw.edu  
Geophysical Laboratory, Carnegie Institution of Washington  
5251 Broad Branch Rd., NW, Washington DC 20015, USA
- Rapp, Robert P.** rapp@sbmp04.ess.sunysb.edu  
Department of Geosciences and Mineral Physics Institute, State University of New York  
ESS Building, Stony Brook, New York 11794-2100, USA
- Ren, Zhong-Yuan** ren@geo.titech.ac.jp  
Earth and Planetary Sciences, Tokyo Institute of Technology  
2-12-1 Ookayama, Meguro-ku, Tokyo 152-8551, Japan
- Richard, Guillaume** Guillaume.Richard@cnes.fr  
UMR 5562, Terrestrial and Planetary dynamics Laboratory, Observatoire Midi-Pyrenees  
14, Avenue E. Belin, Toulouse 31400, France
- Rose, Estelle F.** erose@pheasant.misasa.okayama-u.ac.jp  
Institute for Study of the Earth's Interior, Okayama University  
827 Yamada, Misasa, Tottori 682-0193, Japan
- Rubie, David C.** dave.rubie@uni-bayreuth.de  
Bayerisches Geoinstitut, Universität Bayreuth  
Universitätstr. 30, Bayreuth D-95440, Germany
- Sakaguchi, Chie** csaka@misasa.okayama-u.ac.jp  
Institute for Study of the Earth's Interior, Okayama University  
827 Yamada, Misasa, Tottori 682-0193, Japan
- Sakamoto, Daisuke** dai@esstop.ess.sci.osaka-u.ac.jp  
Earth and Space Science, Graduate School of Science, Osaka University  
Machikaneyama-1, Toyonaka, Osaka 560-0043, Japan

- Sanloup, Chrystele** sanloup@gl.ciw.edu  
Geophysical Laboratory, Carnegie Institution of Washington  
5251 Broad Branch Rd., NW, Washington DC 20015, USA
- Schmidt, Max W.** max.schmidt@erdw.ethz.ch  
Institute for Mineralogy and Petrology, ETH  
Sonneggstr. 10, Zürich 8092, Switzerland
- Shirasaka, Miki** sirasaka@geo.titech.ac.jp  
Department of Earth and Planetary Sciences, Tokyo Institute of Technology  
2-12-1 Ookayama, Meguro-ku, Tokyo 152-8551, Japan
- Smyth, Joseph** joseph.smyth@colorado.edu  
Department of Geological Sciences, University of Colorado  
2200 Colorado Avenue, Boulder CO 80309-0399, USA
- Song, Maoshung** song@misasa.okayama-u.ac.jp  
Institute for Study of the Earth's Interior, Okayama University  
827 Yamada, Misasa, Tottori 682-0193, Japan
- Stacey, Frank D.** f.stacey@cat.csiro.au  
CSIRO, Exploration and Mining  
Kenmore QLD 4069, Australia
- Sueda, Yuichiro** sueday@sci.ehime-u.ac.jp  
Department of Earth Sciences, Ehime University  
Bunkyo-cho, Matsuyama, Ehime 790-8577, Japan
- Takahashi, Eiichi** etakahas@geo.titech.ac.jp  
Earth and Planetary Sciences, Tokyo Institute of Technology  
2-12-1 Ookayama, Meguro-ku, Tokyo 152-8551, Japan
- Takei, Hiroyuki** htakei@misasa.okayama-u.ac.jp  
Institute for Study of the Earth's Interior, Okayama University  
827 Yamada, Misasa, Tottori 682-0193, Japan
- Tanaka, Ryoji** ryoji@misasa.okayama-u.ac.jp  
Institute for Study of the Earth's Interior, Okayama University  
827 Yamada, Misasa, Tottori 682-0193, Japan
- Tange, Yoshinori** tan@issp.u-tokyo.ac.jp  
Institute for Study of the Earth's Interior, Okayama University  
827 Yamada, Misasa, Tottori 682-0193, Japan
- Tanimoto, Masaaki** tanimoto@pheasant.misasa.okayama-u.ac.jp  
Institute for Study of the Earth's Interior, Okayama University  
827 Yamada, Misasa, Tottori 682-0193, Japan
- Tatsumi, Yoshiyuki** tatsumi@jamstec.go.jp  
IFREE, JAMSTEC  
Natsushima, Yokosuka, Kanagawa 237-0061, Japan
- Terasaki, Hidenori** tera@luna.riko.tsukuba.ac.jp  
Geoscience Institute, University of Tsukuba  
Tennoudai 1-1-1, Tsukuba, Ibaraki 305-8571, Japan
- Tsuchiya, Taku** takut@geo.titech.ac.jp  
Earth and Planetary Science, Tokyo Institute of Technology  
Ookayama 2-12-1, Meguro, Tokyo 152-8551, Japan
- Tsujimura, Tomoyuki** tomoyuki@ganko.tohoku.ac.jp  
Department of Mineralogy, Petrology and Economic Geology, Tohoku University  
Aoba, SendaiMiyagi, 980-8578, Japan
- Urakawa, Satoru** afeg0320@cc.okayama-u.ac.jp  
Department of Earth Science, Okayama University  
3-1-1 Tsushima naka, Okayama700-8530, Japan
- Usui, Tomohiro** tusui@misasa.okayama-u.ac.jp  
Institute for Study of the Earth's Interior, Okayama University  
827 Yamada, Misasa, Tottori 682-0193, Japan

- Van Orman, James** [j.van-orman@gl.ciw.edu](mailto:j.van-orman@gl.ciw.edu)  
Geophysical Laboratory, Carnegie Institution of Washington  
5251 Broad Branch Rd., NW, Washington DC 20015, USA
- Van Westrenen, Willem** [w.van-westrenen@gl.ciw.edu](mailto:w.van-westrenen@gl.ciw.edu)  
Geophysical Laboratory, Carnegie Institution of Washington  
5251 Broad Branch Rd., NW, Washington DC 20015, USA
- Venkataramaiah, Ganesh Atni** [ganmysore@hotmail.com](mailto:ganmysore@hotmail.com)  
Department of Geology, Mysore University  
Manasagangotri, Mysore, Karnataka 570 006, India
- Walter, Michael** [walter@misasa.okayama-u.ac.jp](mailto:walter@misasa.okayama-u.ac.jp)  
Institute for Study of the Earth's Interior, Okayama University  
827 Yamada, Misasa, Tottori 682-0193, Japan
- Watada, Shingo** [watada@eri.u-tokyo.ac.jp](mailto:watada@eri.u-tokyo.ac.jp)  
Earthquake Research Institute, Tokyo University  
1-1-1 Yayoi, Bunkyo-ku, Tokyo 113-0032, Japan
- Wood, Bernard J.** [b.j.wood@bris.ac.uk](mailto:b.j.wood@bris.ac.uk)  
Department of Earth Sciences, University of Bristol  
Queens Road, Bristol, BS8 1RJ, U.K.
- Xue, Xianyu** [xianyu@dbmac1.misasa.okayama-u.ac.jp](mailto:xianyu@dbmac1.misasa.okayama-u.ac.jp)  
Institute for Study of the Earth's Interior, Okayama University  
827 Yamada, Misasa, Tottori 682-0193, Japan
- Yagi, Takehiko** [yagi@issp.u-tokyo.ac.jp](mailto:yagi@issp.u-tokyo.ac.jp)  
Institute for Solid State Physics, University of Tokyo  
5-1-5 Kashiwanoha, Kashiwa, Chiba 277-8581, Japan
- Yamada, Hitoshi** [hyamada@misasa.okayama-u.ac.jp](mailto:hyamada@misasa.okayama-u.ac.jp)  
Institute for Study of the Earth's Interior, Okayama University  
827 Yamada, Misasa, Tottori 682-0193, Japan
- Yamanaka, Takamitsu** [b61400@center.osaka-u.ac.jp](mailto:b61400@center.osaka-u.ac.jp)  
Dept. Earth and Space Science, Osaka University  
1-1 Machikaneyama, Toyonaka, Osaka 560-0043, Japan
- Yamashita, Shigeru** [shigeru@misasa.okayama-u.ac.jp](mailto:shigeru@misasa.okayama-u.ac.jp)  
Institute for Study of the Earth's Interior, Okayama University  
827 Yamada, Misasa, Tottori 682-0193, Japan
- Yamazaki, Daisuke** [yamaz002@issp.u-tokyo.ac.jp](mailto:yamaz002@issp.u-tokyo.ac.jp)  
Institute for Solid State Physics, University of Tokyo  
5-1-5 Kashiwanoha, Kashiwa, Chiba 277-8581, Japan
- Yokoyama, Tetsuya** [yokoyama@misasa.okayama-u.ac.jp](mailto:yokoyama@misasa.okayama-u.ac.jp)  
Institute for Study of the Earth's Interior, Okayama University  
827 Yamada, Misasa, Tottori 682-0193, Japan
- Yoneda, Akira** [yoneda@misasa.okayama-u.ac.jp](mailto:yoneda@misasa.okayama-u.ac.jp)  
Institute for Study of the Earth's Interior, Okayama University  
827 Yamada, Misasa, Tottori 682-0193, Japan
- Yoshino, Takashi** [tyoshino@misasa.okayama-u.ac.jp](mailto:tyoshino@misasa.okayama-u.ac.jp)  
Institute for Study of the Earth's Interior, Okayama University  
827 Yamada, Misasa, Tottori 682-0193, Japan
- Zhao, Dapeng** [zhao@sci.ehime-u.ac.jp](mailto:zhao@sci.ehime-u.ac.jp)  
Geodynamics Research Center, Ehime University  
Bunkyo-cho 2-5, Matsuyama, Ehime 790-8577, Japan

## Author Index

- Aizawa, Yoshitaka** ..... 76  
**Akaogi, Masaki** ..... 63, 148  
**Allègre, Claude J.** ..... 57  
**Alves, Sophie** ..... 57  
**Aoki, K.** ..... 104  
**Arai, Shoji** ..... 118  
**Asahara, Yuki** ..... 147  
  
**Bebout, Gray E.** ..... 51  
**Bourdon, Bernard** ..... 57  
  
**Campbell, Ian H.** ..... 15  
**Castillo, P.R.** ..... 16  
**Chakraborty, S.** ..... 88  
  
**Davies, Gareth R.** ..... 17  
**Dunai, Tibor J.** ..... 17  
  
**Faul, Ulrich** ..... 142  
**Fortenfant, S.** ..... 154  
**Frost, Daniel J.** ..... 13, 88, 96, 126, 154  
**Fujihisa, H.** ..... 104  
**Fujino, Kiyoshi** ..... 67  
**Fujita, Kiyoshi** ..... 133  
**Fukao, Yoshio** ..... 3  
**Funakoshi, Ken-ichi** ..... 71, 75  
**Funakoshi, Kenichi** ..... 61, 72, 156  
  
**Green, Harry W.** ..... 114  
  
**Hanyu, Takeshi** ..... 17  
**Hart, Stanley R.** ..... 11  
**Hasegawa, M.** ..... 156  
**Hasegawa, Masayuki** ..... 75  
**Hatakeyama, Tadahiro** ..... 160  
**Helmstaedt, Herwart** ..... 46  
**Higo, Yuji** ..... 71, 128  
**Hirao, Naohisa** ..... 80  
**Hirose, Kei** ..... 132  
**Hirschmann, M.** ..... 13  
**Holzappel, Christian** ..... 88, 154  
**Honda, S.** ..... 163  
  
**Iguchi, Tomohiro** ..... 79, 103  
**Inoue, Toru** ..... 71, 128  
**Irifune, Tetsuo** ..... 71, 128  
**Ito, Eiji** ..... 61, 63, 69, 72, 83, 150  
**Iwamori, Hikaru** ..... 117  
  
**Kagi, Hiroyuki** ..... 120  
**Kaneoka, Ichiro** ..... 17  
**Kanzaki, Masami** ..... 93, 99–101  
  
**Kato, Mamoru** ..... 5  
**Kato, T.** ..... 156  
**Katsura, Tomoo** ..... 61, 72, 77, 133, 150, 158  
**Kawakatsu, Hitoshi** ..... 5, 6  
**Kawamoto, T.** ..... 99  
**Kawamoto, Tatsuhiko** ..... 121  
**Kawamura, Katsuyuki** ..... 81  
**Kikegawa, Takumi** ..... 79, 80  
**Kitakaze, A.** ..... 101  
**Kitamura, Masao** ..... 24  
**Kittaka, Koichi** ..... 78  
**Kobayashi, Katsura** ... 21, 22, 43, 46, 47, 90, 148, 169, 170  
**Koga, KT** ..... 90  
**Kogiso, T.** ..... 13  
**Kondo, Tadashi** ..... 80  
**Kono, Masaru** ..... 160, 167  
**Kubo, Atsushi** ..... 61, 72, 150  
**Kudoh, Y.** ..... 101  
**Kuritani, Takeshi** ..... 23, 43, 50, 141, 169  
  
**Langenhorst, Falko** ..... 88, 96  
**Laske, Gabi** ..... 4  
  
**Makishima, Akio** . 32, 35, 37, 39, 54, 55, 148, 169  
**Maruyama, Shigenori** ..... 30, 46  
**Masters, Guy** ..... 4  
**Matsui, Masanori** ..... 66  
**Matsukage, Kyoko** ..... 79, 121  
**Matsumoto, Naoko** ..... 24  
**Mayama, N.** ..... 77  
**Melosh, H.J.** ..... 154  
**Miyajima, Nobuyoshi** ..... 67, 96  
**MonnerEAU, M.** ..... 130  
**Moreira, Manuel** ..... 18  
**Moriguti, Takuya** ..... 22, 25–27, 169  
**Morishita, Tomoaki** ..... 118  
**Murakami, Motohiko** ..... 132  
  
**Nagai, Takaya** ..... 78, 165  
**Naka, Hisanobu** ..... 71  
**Nakajima, K.** ..... 137  
**Nakamura, Eizo** 21–23, 25–27, 29, 30, 32, 33, 35, 37, 39, 41, 43, 46, 47, 49–51, 53, 54, 55, 90, 137, 144, 145, 148, 169, 170  
**Nakanishi, Mayumi** ..... 54  
**Nakano, Toshio** ..... 49, 53  
**Nakashima, Satoru** ..... 132  
**Nakayama, Keisuke** ..... 79  
**Nishihara, Yu** ..... 79, 103  
**Nishikawa, Osamu** ..... 61, 72, 92

- Nohda, Susumu** ..... 17  
**Obata, Masaaki** ..... 146  
**Odawara, Reki** ..... 67  
**Ogawa, Hisayuki** ..... 67  
**Ohno, I.** ..... 77  
**Ohtaka, O.** ..... 95  
**Ohtani, Eiji** ..... 80, 111, 147  
**Ono, S.** ..... 69  
**Osako, Masahiro** ..... 83  
**Ota, K.** ..... 95  
**Otaka, O.** ..... 165  
  
**Poe, B.T.** ..... 154  
**Punongbayan, R.S.** ..... 16  
  
**Rapp, Robert P.** ..... 122  
**Reid, J.** ..... 154  
**Ren, Zhang-Young** ..... 137  
**Richard, G.C.M.** ..... 130  
**Richter, K.** ..... 154  
**Rose, Estelle F.** ..... 55  
**Rubie, Dave** ..... 88, 154, 96  
  
**Sakaguchi, Chie** ..... 29, 169  
**Sakamoto, D.** ..... 95  
**Sakashita, M.** ..... 104  
**Sanehira, Takeshi** ..... 71  
**Sasaki, Yohei** ..... 67  
**Sata, Nagayoshi** ..... 67  
**Sato, K.** ..... 156  
**Schiano, Pierre** ..... 57  
**Schmidt, Max W.** ..... 109  
**Shimizu, Kenji** ..... 22, 30  
**Shimizu, N.** ..... 122  
**Shinmei, Toru** ..... 61, 72  
**Shinoda, Keishi** ..... 133  
**Shinozaki, K.** ..... 137  
**Shirasaka, Miki** ..... 79, 124  
**Smyth, Joseph R.** ..... 126  
**Solidum, R.U.** ..... 16  
**Song, M.** ..... 104  
**Song, Maoshuang** ..... 61, 72  
**Stacey, Frank D.** ..... 7  
**Sueda, Yuichiro** ..... 71  
**Suzuki, A.** ..... 156  
**Suzuki, I.** ..... 77  
**Suzuki, Toshihiro** ..... 148  
  
**Takahashi, Eiichi** ..... 79, 103, 124, 137, 145  
**Takazawa, Eiichi** ..... 146  
**Takeguchi, R.** ..... 137  
**Takei, Hiroyuki** ..... 32, 33, 169  
**Tamura, Akihiro** ..... 118  
**Tanaka, Akira** ..... 63  
  
**Tanaka, Ryoji** ..... 22, 137, 144, 145, 169  
**Tanimoto, Masaaki** ..... 50  
**Tanimoto, Yasutika** ..... 128  
**Tareen, J.A.K.** ..... 112  
**Terasaki, H.** ..... 156  
**Tsuchiya, Taku** ..... 81  
**Tsujimura, T.** ..... 101  
  
**Ueda, Takayuki** ..... 71, 128  
**Urakawa, Satoru** ..... 75, 156  
**Usui, Tomohiro** ..... 46, 47, 170  
**Uto, Kozo** ..... 17  
**Utsumi, Wataru** ..... 71, 75  
  
**Venkatramiah, Ganesha Atni** ..... 112  
  
**Walter, Michael J.** ..... 90, 150, 152, 158  
**Wood, B.J.** ..... 140  
  
**Xue, X.** ..... 99–101  
  
**Yagi, Takehiko** ..... 67, 96  
**Yamada, Hitoshi** ..... 61, 72  
**Yamakawa, Junji** ..... 75  
**Yamanaka, Takamitsu** ..... 78, 95, 165  
**Yamashita, Shigeru** ..... 102  
**Yamawaki, H.** ..... 104  
**Yokoyama, Tetsuya** ..... 32, 35, 37, 39, 41, 43, 169  
**Yoneda, Akira** ..... 77, 83, 86  
**Yoshiasa, A.** ..... 95, 165  
**Yoshida, M.** ..... 163  
**Yoshikawa, Masako** ..... 50  
**Yoshino, Takashi** ..... 158  
**Yurimoto, Hisayoshi** ..... 132  
  
**Zhao, Dapeng** ..... 8, 116